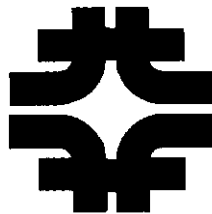


# **KTeV Design Report**

Physics Goals, Technical Components, and Detector Costs



**Fermi National Accelerator Laboratory  
Batavia, Illinois**

Operated by Universities Research Association Inc.  
Under Contract with the United States Department of Energy

# KTeV DESIGN REPORT

*January 22, 1992*

*K. Arisaka<sup>3</sup>, A. Barker<sup>4</sup>, G. Bock<sup>1</sup>, E. Cheu<sup>4</sup>, S. Childress<sup>1</sup>, S. Cihangir<sup>1</sup>, R. Coleman<sup>1</sup>, M. Crisler<sup>1</sup>, R. Currier<sup>1</sup>, P. Czarapata<sup>1</sup>, J. Enagonio<sup>1</sup>, R. Fast<sup>1</sup>, R. Ford<sup>1</sup>, W. Freeman<sup>1</sup>, G. Gollin<sup>2</sup>, D. Goloskie<sup>1</sup>, P. Haas<sup>7</sup>, W. Hogan<sup>7</sup>, Y.B. Hsiung<sup>1</sup>, D. Jensen<sup>1</sup>, J. Kilmer<sup>1</sup>, S. Kim<sup>7</sup>, A. Malensek<sup>1</sup>, S. Myung<sup>7</sup>, G. Ping<sup>7</sup>, J. Quackenbush<sup>3</sup>, E. Ramberg<sup>1</sup>, R. Ray<sup>1</sup>, A. Roodman<sup>4</sup>, R. Schmitt<sup>1</sup>, S. Schnetzer<sup>7</sup>, P. Shawhan<sup>4</sup>, W. Slater<sup>3</sup>, S. Somalwar<sup>4</sup>, E. Swallow<sup>4,5</sup>, A. Szymulanski<sup>1</sup>, G. Thomson<sup>7</sup>, R. Tschirhart<sup>1</sup>, J. Volk<sup>1</sup>, Y. Wah<sup>4</sup>, B. Wands<sup>1</sup>, M. Weaver<sup>3</sup>, A. Wilson<sup>4</sup>, B. Winstein<sup>4</sup>, R. Winston<sup>4</sup>, T. Yamanaka<sup>1,6</sup>*

We would like to thank the following people for many useful contributions  
suggestions and discussions:

*L. Beverly<sup>1</sup>, R. Briere<sup>4</sup>, P. Cooper<sup>1</sup>, R. DeMaat<sup>1</sup>, C. Federowicz<sup>1</sup>, J. Hackemer<sup>1</sup>, S. Hansen<sup>1</sup>, H. Hillman<sup>1</sup>, K. Knickerbocker<sup>1</sup>, J. Krider<sup>1</sup>, J. Kubic<sup>3</sup>, T. Lackowski<sup>1</sup>, J. Matthews<sup>7</sup>, A. Lee<sup>1</sup>, W. Nestander<sup>1</sup>, T. Nurczyk<sup>1</sup>, G. Oleynik<sup>1</sup>, T. Pawlak<sup>1</sup>, R. Pordes<sup>1</sup>, S. Pordes<sup>1</sup>, D. Roberts<sup>3</sup>, T. Sager<sup>1</sup>, H. Sanders<sup>4</sup>, R. Stanek<sup>1</sup>, R. Tokarek<sup>1</sup>, E. Villegas<sup>1</sup>, A. Visser<sup>1</sup>*

Special thanks to:

*Terry Grozis, Mary Hill and Patty Conlon for their effort in the  
preparation of this report, and to Kristen Ford for the  
cover design.*

---

<sup>1</sup> Fermilab

<sup>2</sup> Univ. of Illinois

<sup>3</sup> Univ. of California at Los Angeles

<sup>4</sup> Univ. of Chicago

<sup>5</sup> Elmhurst University

<sup>6</sup> Osaka University

<sup>7</sup> Rutgers University

# TABLE OF CONTENTS

INTRODUCTION.....	1
1. PHYSICS MOTIVATION.....	3
1.1 Tests of CP and CPT Symmetry.....	3
1.1.1 Measurement of $\text{Re}(\epsilon'/\epsilon)$ .....	5
1.1.2 Tests of CPT Symmetry Using $K \rightarrow \pi\pi$ Decays.....	8
1.1.3 Studies of CP Violation Using Rare $K_L$ Decays.....	10
1.2 Other Rare $K_L$ and $\pi^0$ Decay Modes.....	13
1.2.1 Searches for Lepton Flavour Violation .....	13
1.2.2 Radiative $K_{\pi 2}$ Decays, $K_{L,S} \rightarrow \pi^+\pi^-\gamma$ .....	14
1.2.3 $K_L \rightarrow \pi^0\gamma\gamma$ .....	16
1.2.4 Four-Prong Decays of the $K_L$ and $\pi^0$ .....	17
1.2.5 Lepton-Pair and Dalitz Decays of the $K_L$ and $\pi^0$ .....	18
2. SPECTROMETER OVERVIEW .....	21
2.1 Beam .....	21
2.2 Detectors .....	22
2.3 Sensitivities and Backgrounds .....	28
2.3.1 P832: Measurement of $\text{Re}(\epsilon'/\epsilon)$ .....	28
2.3.2 Comparison with the CERN NA48 Experiment.....	35
2.3.3 E799II: Search for Rare $K_L$ Decays .....	36
3. BEAM DESIGN .....	49
3.1 General KTeV Beam Requirements .....	49
3.2 Primary Beam Transport.....	53
3.2.1 Beam Trajectory .....	53
3.2.2 Final Focusing and Target AVB System .....	54
3.2.3 Beam Direction Correction .....	57
3.3 Kaon Production Target.....	58
3.4 Secondary Kaon Beam.....	62
3.4.1 General Collimator Design Considerations .....	64
3.4.2 Elevation View Collimator Specifications .....	66

## TABLE OF CONTENTS

3.4.3	Plan View Collimator Specifications.....	72
3.4.4	Slab Collimator .....	74
3.4.5	Numerical Results, Validity of Approximations.....	77
3.4.6	Collimator Tolerances.....	79
3.4.7	Alignment System.....	80
3.4.8	Collimator Halo Contributions .....	83
3.5	Primary Proton Dump.....	91
3.6	Muon Flux Simulations .....	94
3.6.1	Simulation Layout.....	94
3.6.2	CASIMU Muon Flux Simulation and Code Validation.....	97
3.6.3	Preliminary Simulation Results.....	100
4.	TECHNICAL DESIGN OF THE DETECTORS .....	101
4.1	KTeV Detector Configuration and Acceptance .....	102
4.2	Vacuum Decay Region and Photon Vetoes .....	106
4.2.1	Vacuum System .....	106
4.2.2	Photon Vetoes .....	109
4.3	Active Regenerator, Active Mask, and Absorber Mover (P832).....	114
4.4	Chambers .....	119
4.4.1	Drift Chamber Preamps/Amplifiers .....	119
4.4.2	Drift Chamber and TRD Gas Studies .....	121
4.5	KTeV Spectrometer Magnet.....	123
4.5.1	Geometry and Field Requirements .....	123
4.5.2	KTeV Spectrometer Magnet Mapping .....	126
4.6	Transition Radiation Detectors .....	127
4.6.1	TRD Upgrades.....	128
4.6.2	Recirculating Xenon Gas System .....	133
4.7	CsI Electromagnetic Calorimeter.....	136
4.7.1	General Requirements .....	136
4.7.2	CsI Crystal Specifications.....	145
4.7.3	CsI Phototubes.....	151
4.7.4	CsI PMT Bases.....	157



## TABLE OF CONTENTS

4.7.5	CsI High Voltage Power Supply .....	159
4.7.6	Laser Calibration System for CsI Calorimeter .....	160
4.7.7	CsI Calorimeter Blockhouse .....	167
4.7.8	CsI Calibration.....	168
4.7.9	Splitting Magnets for $e^+e^-$ Calibration.....	173
4.7.10	Simulation of Radiation Dosage in CsI Calorimeter.....	174
4.8	CsI Test Results.....	175
4.8.1	CsI Test Array Results .....	175
4.8.2	Radiation Damage Test Results.....	182
4.9	Beam Hole Veto .....	189
4.9.1	Collar Anti.....	190
4.9.2	Back Anti .....	190
4.10	Trigger Hodoscopes, Hadron Veto and Muon System.....	197
4.10.1	Trigger Counters .....	197
4.10.2	Hadron Veto.....	197
4.10.3	Muon Detection.....	198
4.11	Trigger and Electronics .....	202
4.11.1	Trigger System Design .....	202
4.11.2	CsI ADC Design and Readout Considerations.....	213
4.11.3	Front End Electronics.....	219
4.11.4	Hardware Cluster Finder II .....	223
4.11.5	Track Processor Upgrade .....	239
4.12	Data Acquisition System and Third Level Filter.....	242
4.12.1	Overview .....	242
4.12.2	DAQ Specifications .....	244
4.12.3	Architecture .....	246
4.12.4	R&D .....	252
4.13	Offline Computing.....	253
5.	COSTS, MANPOWER, AND TIMELINE .....	255
5.1	Detector Costs.....	255
5.2	Manpower Availability .....	262

## TABLE OF CONTENTS

5.3	Beam Technical Costs.....	265
5.4	Detector Timeline .....	268
APPENDIX A. EXPERIMENT SITING AND ENVIROMENTAL SAFETY .....		270
A.1	Experiment Siting.....	270
A.2	ES&H Issues.....	273
A.2.1	Radiation Safety .....	273
A.2.2	Conventional/Occupational Safety.....	275

# INTRODUCTION

We present here the Design Report for the new Kaons at the TeVatron (KTeV) program of two upcoming (1994-95) fixed target Tevatron experiments: E799 Phase-II (E799II), a search for "direct" CP violation in rare neutral kaon decays; and the proposed experiment P832, a precision measurement on the "direct" CP-violation parameters  $\epsilon'/\epsilon$  in the  $2\pi$  decay mode of the neutral kaon system. Both experiments need new high-performance detectors and better neutral kaon beams to reach their design goals. With the new beam and detectors, it will be possible to probe the fundamental questions of CP violation and rare decays with much greater precision and sensitivity.

In this Design Report, we discuss the physics motivations, sensitivities and backgrounds, beam design, and technical design of the spectrometer, including costs, manpower and time-line requirements. These experiments require a new neutral kaon beam and new detector facility in place of the MCenter facility used previously for E731, E773 and E799 Phase-I (E799I). As of the writing of this report, the details of site selection (new or existing experimental hall) and the corresponding design for the civil construction are unavailable to us. We have therefore placed the present discussion of target areas and experimental halls in an appendix.

We have exercised substantial care in our design efforts to maintain a high level of compatibility with the Kaons at the Main Injector (KAMI) program<sup>1</sup>. On the other hand, we have not included components or costs in this report which are needed solely for KAMI; for example, the construction of large, ultra-high-rate drift chambers is not envisioned here.

The general physics motivation for KTeV is presented in Section 1. Studies of CP violation in rare kaon decays and  $2\pi$  decays, tests of CPT symmetry, and searches for other rare decays of neutral kaons and  $\pi^0$ s are discussed. Current results are presented for comparison. An overview of the beam and spectrometer is presented in Sections 2.1 and 2.2. Experimental sensitivities and backgrounds are discussed in Section 2.3 including comparisons with competing experiments.

---

<sup>1</sup>K. Arisaka, *et al.*, *Conceptual Design Report: Kaons at the Main Injector*, Fermilab Report FN-568 (June, 1991).

Technical details of primary beam targeting, secondary beam collimation and muon halo simulations are presented in Section 3, the beam design part of the report. The detector design, including trigger, electronics and data acquisition, is discussed in Section 4.

The proposed high-resolution CsI electromagnetic calorimeter is discussed in detail in Section 4.7, including the specifications on CsI crystals, phototubes and bases, high voltage power supplies, flasher monitoring system, and calibration procedures. Our recent results from a CsI test array and from an *in situ* beam study of radiation hardness are presented in Section 4.8. These R&D efforts have shown that the proposed CsI calorimeter will provide our required detector sensitivity and that pure CsI can be produced with the required radiation hardness.

Costs, manpower and scheduling are summarized in Section 5. It is, of course, the goal of this program to be ready to do physics at the start of the upcoming fixed target run in 1994-95.

In an appendix, we outline the progress on site selection and the design of the civil construction for the target area and experimental hall along with a study of ES&H issues.

We emphasize that excellent and timely physics results from the KTeV program depend on the timeliness of necessary approvals and choice of the ultimate site. Once the experiment is approved and finds a new home, we will be able to proceed with more detailed preparation for the exciting physics to come.

# 1. PHYSICS MOTIVATION

Though the neutral kaon system has been studied for many years, it remains a rich hunting ground for the performance of incisive studies and for possible new discoveries. In this hunt, KTeV will be armed with an intense source of high-energy kaon decays together with a state-of-the-art detector capable of very high precision measurements. We will be able to extract the value of the CP-violation parameter  $\text{Re}(\epsilon'/\epsilon)$  with an uncertainty of  $1 \times 10^{-4}$ , nearly an order of magnitude better than at present. We will also be able to observe rare four-body  $K_L$  decays with branching fractions as small as  $10^{-11}$ , an improvement of two orders of magnitude over today's sensitivity. In this section, we discuss a few of the many physics topics which can be addressed by KTeV. In Section 2, we make this more concrete with a general discussion of the design of the KTeV spectrometer. Then we estimate the sensitivity of the proposed detector to some of the effects mentioned here and consider the limitations imposed by a variety of background processes.

## 1.1 Tests of CP and CPT Symmetry

In 1964 the study of CP violation was born with the discovery<sup>1</sup> of the  $2\pi$  decay mode of the  $K_L$  in the famous experiment of Christenson, Cronin, Fitch and Turlay. The impact of their observation on elementary particle physics has been profound. Here, for the first time, was a mechanism that could distinguish matter from antimatter. Such an interaction is an essential ingredient in most explanations of the striking asymmetry between the abundance of matter and antimatter in the universe. The connection with baryogenesis has led to strong cosmological interest in the origins of CP violation.

Today it is thought that the Standard Model, with three generations, can account for this phenomenon. In this model CP violation arises from a non-zero phase in the  $V_{ub}$  transition matrix element through the now-familiar box diagram shown in Figure 1.1.1. In the Wolfenstein parameterization  $V_{ub} = \lambda^3 (\rho + i\eta)$ . The phase of  $V_{ub}$  is conveniently displayed in the so-called Unitarity Triangle, shown in Figure 1.1.2. In the Standard Model, the value of  $\eta$  governs the size of *all* CP-violating phenomena. Current fits to

---

<sup>1</sup>J. H. Christenson, J. W. Cronin, V. L. Fitch, and R. Turlay, Phys. Rev. Lett. 13, 138 (1964).

weak interaction processes place  $\eta$  in the range of about 0.2 to 0.7. If this explanation is correct, then the Fitch-Cronin effect, which was discovered only a year after the introduction of the quark hypothesis by Gell-Mann and Zweig, was in fact the first evidence for the existence of the third generation of quarks and leptons, including the top quark! If, on the other hand, the origin of CP violation lies *outside the Standard Model*, then its importance as a manifestation of new physics would be greater still. It is therefore imperative that we push forward the effort to either verify or disprove the idea that the Standard Model describes the source of CP violation.

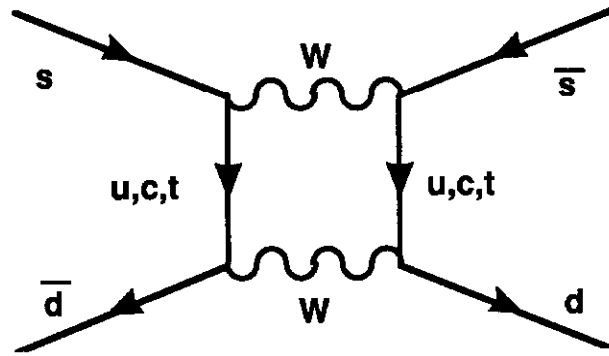


Figure 1.1.1: The  $\Delta S=2$  Box Diagram in the Standard Model.

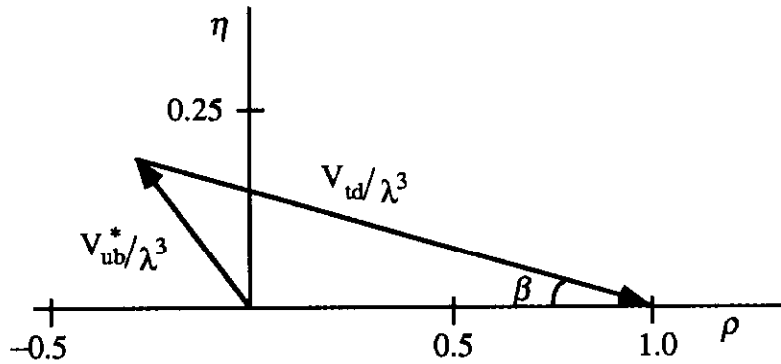


Figure 1.1.2: The Unitarity Triangle, scaled by  $\lambda^3$ .

### 1.1.1 Measurement of $\text{Re}(\epsilon'/\epsilon)$

The CP-violating decay  $K_L \rightarrow 2\pi$  and the semileptonic charge asymmetry in  $K_{e3}$  and  $K_{\mu 3}$  decays arise largely from one mechanism: an asymmetry in the rate of particle-antiparticle transitions. This effect, parameterized by  $\epsilon$ , corresponds to transitions with  $\Delta S=2$ . A Superweak model<sup>2</sup> maintains that the fundamental interaction responsible for CP violation is a  $\Delta S=2$  coupling, and that there are no  $\Delta S=1$  manifestations of the effect. That is to say, that the CP-odd eigenstate,  $K_2$ , never decays to  $2\pi$ , and that the  $K_L$  does so only because it includes an admixture of the CP-even eigenstate,  $K_1$ . By contrast, the Standard Model predicts the existence of "direct" CP violation: a  $\Delta S=1$  transition in which the  $K_2$  decays to two pions. This transition is described in part by the strong penguin diagram shown in Figure 1.1.3, and by its electroweak counterparts, in which the gluon is replaced by a photon or a Z boson. The relative importance of the various diagrams, and the extent of constructive or destructive interference between them, depends on the mass of the top quark.

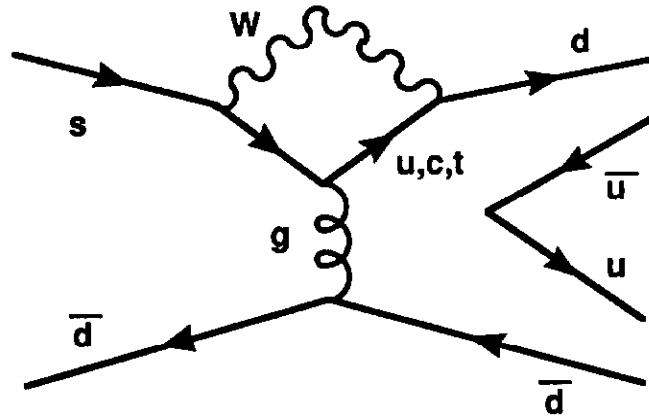


Figure 1.1.3: Strong Penguin Diagram contributing to  $K_2 \rightarrow \pi^+ \pi^-$ .

<sup>2</sup>L. Wolfenstein, Phys Rev, Lett. 13, 562 (1964).

The strength of this transition is conventionally expressed by means of the parameter  $\epsilon'$ , defined by the expression

$$\epsilon' = \frac{i}{\sqrt{2}} e^{i(\delta_2 - \delta_0)} \text{Im}\left(\frac{A_2}{A_0}\right),$$

where the  $\delta_j$  are the  $\pi\pi$  phase shifts at the  $K^0$  mass for a state with isospin  $j$  and the  $A_j$  are defined in terms of the  $K^0$  decay amplitudes by

$$\langle I=j | T | K^0 \rangle = A_j e^{i\delta_j}.$$

With these definitions, the ratios of  $K_L$  to  $K_S$  decay amplitudes for the  $\pi^+\pi^-$  and  $\pi^0\pi^0$  final states are given by

$$\eta_{+-} = \epsilon + \epsilon' \text{ and } \eta_{00} = \epsilon - 2\epsilon',$$

assuming that CPT invariance holds. In this case, the value of  $\text{Re}(\epsilon'/\epsilon)$  can be found by measuring the double ratio of the four  $K_{L,S} \rightarrow 2\pi$  decay rates. This double ratio is equal to the squared magnitude of the ratio  $\eta_{+-}/\eta_{00}$ , which is related in turn to  $\text{Re}(\epsilon'/\epsilon)$ :

$$\frac{\Gamma(K_L \rightarrow \pi^+\pi^-) / \Gamma(K_S \rightarrow \pi^+\pi^-)}{\Gamma(K_L \rightarrow \pi^0\pi^0) / \Gamma(K_S \rightarrow \pi^0\pi^0)} = \left| \frac{\eta_{+-}}{\eta_{00}} \right|^2$$

$$\left| \frac{\eta_{+-}}{\eta_{00}} \right|^2 = \left| \frac{\epsilon + \epsilon'}{\epsilon - 2\epsilon'} \right|^2 \approx \left| 1 + 3 \frac{\epsilon'}{\epsilon} \right|^2 \approx 1 + 6 \text{Re}\left(\frac{\epsilon'}{\epsilon}\right).$$

Until about 15 years ago, the best available measurement put  $\text{Re}(\epsilon'/\epsilon) < 0.02$ . Then, in 1977, the  $b$  quark was discovered, and it became possible to make Standard Model predictions for the value of  $\epsilon'$ . This in turn provided renewed motivation for a new round of experiments, including Fermilab's E731 and CERN's NA31. The final result<sup>3</sup> from the NA31 group, averaging the results from data collected in 1986, 1988, and 1989, and combining statistical and independent systematic errors in quadrature, is

---

<sup>3</sup>A. C. Schaffer (NA31 Collaboration), to appear in *Proceedings of the APS Division of Particles and Fields Meeting*, Vancouver, Canada, August 1991. See also Lydia Ikonomidou-Fayard (NA31 Collaboration), preprint LAL-91-05, March 1991, presented at the Rencontres de Moriond, Les Arcs, France, January 1991.



$$\text{Re}(\epsilon'/\epsilon) = (23 \pm 7) \times 10^{-4},$$

a three-sigma deviation from zero. However, E731 finds<sup>4</sup> instead

$$\text{Re}(\epsilon'/\epsilon) = (6.0 \pm 5.8 \text{ (Stat.)} \pm 3.2 \text{ (Syst.)} \pm 1.8 \text{ (M.C.)}) \times 10^{-4},$$

consistent with a Superweak model. There is thus a qualitative difference in the conclusions to be drawn from the two results, despite the fact that the significance of the numerical difference is only  $1.7\sigma$ . The question of the origin of CP violation is left unanswered by these results.

Although the Standard Model generally predicts a non-zero result of order  $10^{-3}$ , there are large uncertainties and possible cancelling effects. A simple expression, used by J.M. Gerard in his summary talk at the 1991 Lepton-Photon Conference is:

$$\epsilon'/\epsilon = 30 \eta f (1 - \Omega) \times 10^{-3}.$$

Here  $f$  represents the fraction of the strong penguin in  $K \rightarrow 2\pi$ , and  $\Omega$  represents isospin breaking effects, such as the electromagnetic penguin. Using values of 0.5 and 0.3 for  $f$  and  $\Omega$  respectively, we then have

$$\begin{aligned} \eta &= 0.21 \pm 0.07 \text{ NA31,} \\ \eta &< 0.14 \text{ (90\% confidence) E731.} \end{aligned}$$

Even considering the theoretical uncertainties, the E731 measurement is beginning to contradict the favored region in the  $(\rho, \eta)$  plane from all other measurements – which analysis, of course, assumes that the value of  $\epsilon$  arises from the box diagram.

---

<sup>4</sup>E. C. Swallow (E731 Collaboration), to appear in the *Proceedings of the APS Division of Particles and Fields Meeting*, Vancouver, Canada, August 1991. See also the summary talk by B. Winstein, Enrico Fermi Institute preprint EFI-91-52, to appear in the *Proceedings of the APS Division of Particles and Fields Meeting*, Vancouver, Canada, August 1991

### 1.1.2 Tests of CPT Symmetry Using $K \rightarrow \pi\pi$ Decays

The E731 group has also fit for a number of other parameters describing the neutral kaon system using the  $2\pi$  data samples. The reported results<sup>5</sup>, where both statistical and systematic errors are included, are:

$$\begin{aligned}\tau_S &= (0.8912 \pm 0.0013) \times 10^{-10} \text{ sec}; \\ \Delta m &= (0.5339 \pm 0.0020) \times 10^{10} \text{ sec}^{-1}; \\ \phi_{+-} &= (43.2 \pm 1.6)^\circ; \\ \Delta\phi &= \phi_{+-} - \phi_{00} = (-0.6 \pm 1.6)^\circ.\end{aligned}$$

Here  $\phi_{+-}$  and  $\phi_{00}$  are the phases of the amplitude ratios  $\eta_{+-}$  and  $\eta_{00}$ . If CPT invariance is not violated, then  $\phi_{+-}$  and  $\phi_{00}$  must be equal to within about  $0.2^\circ$ . These results are either comparable to or exceed in precision the best previous determinations. All of these measurements are necessary inputs in tests of CPT symmetry. In addition, E731 expects to have a measurement of the semileptonic charge asymmetry,  $\delta_e$ , more precise than the current world average. Since P832 will use essentially the same analysis methods as E731, but with increased statistics and improved understanding of systematic errors, the KTeV measurements of some of these quantities will be even more precise. One important combination of these measurements is the Superweak phase,

$$\phi_{SW} = \tan^{-1}[2(\Delta m)/(\Gamma_S - \Gamma_L)],$$

which can be shown to be the phase of the mixing parameter  $\epsilon$ . We expect to determine this phase with a precision of  $0.05^\circ$  from KTeV data. In the absence of CPT violation, we have the relation  $\delta_e = 2 \text{Re } \epsilon$ , so measuring both  $\phi_{SW}$  and  $\delta_e$  yields a measurement of both the real and imaginary parts of  $\epsilon$ . P832 will also measure  $\Delta\phi$  with a precision of approximately  $0.2^\circ$ . Together with our measurement of  $\text{Re } (\epsilon'/\epsilon)$ , this will give us a precise measurement of the imaginary part of  $\epsilon'/\epsilon$  as well, and will constitute a sensitive test of CPT symmetry.

There are many possible modes of CPT violation, and the complicated problem of untangling all the various possibilities is best dealt with by tagging experiments like those

---

<sup>5</sup>See footnote 4.

that will be performed at  $\phi$  factories<sup>6</sup>. Nevertheless, high-statistics KTeV measurements of various parameters can put significant bounds on certain combinations of CPT-violating amplitudes, and can be useful inputs in tests performed by other experiments. For example, if CPT is violated in the kaon mass matrix, then the effective values of the mixing parameter  $\epsilon$  may differ for  $K_L$  and  $K_S$ . One may define  $\epsilon_L = \epsilon + \Delta$  and  $\epsilon_S = \epsilon - \Delta$ , such that  $\Delta$  parameterizes the CPT violation in mixing. In this case, (assuming that the  $\Delta S = \Delta Q$  rule holds) we would have

$$\delta_e = 2 \operatorname{Re} \epsilon_L = 2(\operatorname{Re} \epsilon + \operatorname{Re} \Delta).$$

The KTeV measurement of  $\eta_{+-}$  will also yield a precise measurement of this combination of  $\epsilon$  and  $\Delta$ . To extract CPT-violation limits, these measurements must be compared to a different combination of parameters, such as that given by the Bell-Steinberger relation:

$$\operatorname{Re} \epsilon + i \operatorname{Im} \Delta = e^{-i\phi_{SW}} \frac{[\sum_f A(K_S \rightarrow f)^* A(K_L \rightarrow f)]}{\sqrt{[4(\Delta m)^2 + (\Gamma_S + \Gamma_L)^2]}}.$$

If the amplitudes on the right-hand side of this relation can be determined with sufficient accuracy, then limits on the real and imaginary parts of  $\Delta$  can be extracted by subtracting this equation from the expression for  $\epsilon_L$  given above, assuming that the only source of CPT violation is in the mass matrix. Our knowledge of the right-hand side of the Bell-Steinberger Relation is presently limited in part by the lack of a precise determination of the phases  $\phi_{SW}$ ,  $\phi_{+-}$ , and  $\phi_{00}$ . The cancellation between these is important since the latter two are present in the leading  $K \rightarrow 2\pi$  contributions to the decay amplitude sum. The value of  $\operatorname{Re} \epsilon$  is currently known with a relative accuracy of 4 to 5%. The error on  $\operatorname{Im} \Delta$  is also about 4% of  $\epsilon$ .

---

<sup>6</sup>C. Buchanan, *et al.*, University of California, Los Angeles preprint UCLA/91/TEP/44, November, 1991.

### 1.1.3 Studies of CP Violation Using Rare $K_L$ Decays

Historically, the  $\pi\pi$  decays of the  $K_S$  and the  $K_L$  have provided the only window on the phenomenon of CP violation. But more recently, considerable attention has focussed on the possibility of extracting the value of the Wolfenstein parameter  $\eta$  from a measurement of CP-violating amplitudes for a variety of rare  $K_L$  decays. Because the  $K_L$  is so long-lived, it may be possible to observe the effects of even highly suppressed CP-violating decay diagrams within the Standard Model, or to detect very rare  $K_L$  decays forbidden by the Standard Model or inconsistent with its predictions. In this section, we discuss three rare decays of the  $K_L$  the study of which will yield information regarding the value of  $\eta$  within the Standard Model. Later, we will consider a variety of other rare  $K_L$  decays that can be studied with the KTeV detector.

#### $K_L \rightarrow \pi^0 e^+ e^-$

The decay which has been most discussed in the literature and which is probably the most promising as a window on Standard Model CP violation is  $K_L \rightarrow \pi^0 e^+ e^-$ . The amplitude for  $K_L \rightarrow \pi^0 e^+ e^-$  has both a CP-conserving and a CP-violating part. In terms of the CP eigenstates  $K_1$  (even) and  $K_2$  (odd), one may describe the three principal contributions to the  $K_L \rightarrow \pi^0 e^+ e^-$  decay amplitude as follows: (a) the CP-conserving amplitude via two photon exchange  $K_2 \rightarrow \pi^0 \gamma^* \gamma^*$ , where  $\gamma^*$  is an off-shell photon; (b) the mass matrix “indirect” CP violation amplitude which comes from the small  $K_1$  component of the  $K_L$ ; and (c) the “direct” CP violation amplitude  $\epsilon'_{\pi ee}$  from the 1-photon exchange  $K_2 \rightarrow \pi^0 \gamma^*$  and Z-exchange  $K_2 \rightarrow \pi^0 Z^*$  amplitudes. Within the Standard Model, contribution (c) can be described by the ‘electromagnetic penguin’ diagram shown in Figure 1.1.4 (and its counterpart with the photon replaced by a Z boson) and is comparable to or larger than (b) in magnitude.

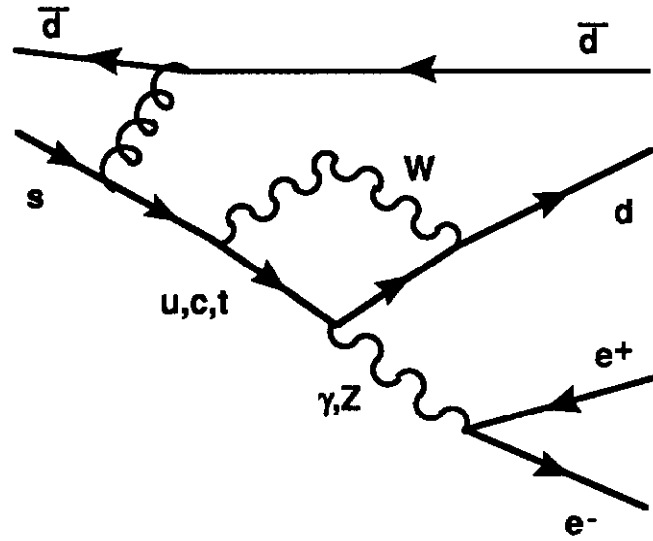


Figure 1.1.4: The Electromagnetic Penguin diagram contributing to  $K_2 \rightarrow \pi^0 e^+ e^-$ .

The three contributions can be untangled by measuring (a) the branching ratio and  $\gamma\gamma$  invariant mass distribution<sup>7</sup> of the rare decay  $K_L \rightarrow \pi^0 \gamma\gamma$ , (b) the branching ratio and  $e^+e^-$  invariant mass distribution<sup>8</sup> of  $K^+ \rightarrow \pi^+ e^+ e^-$ . The existing measurements of both decay modes favor small contributions to  $K_L \rightarrow \pi^0 e^+ e^-$ . If this is so, and the origin of CP violation lies within the Standard Model, then  $\epsilon'_{\pi ee}/\epsilon$  will be of order unity, compared to  $10^{-3}$  for  $\epsilon'_{\pi\pi}/\epsilon$ .

### $K_L \rightarrow \pi^0 \mu^+ \mu^-$

The related mode  $\pi^0 \mu\mu$  is of interest for the same reasons. In the context of the Standard Model, the CP-violating amplitudes, both direct and indirect, for  $K_L \rightarrow \pi\mu\mu$  are expected to be nearly the same as for  $K_L \rightarrow \pi ee$ . The  $K_L \rightarrow \pi\mu\mu$  branching ratio is however suppressed due to phase space which would give  $BR(K_L \rightarrow \pi\mu\mu)/BR(K_L \rightarrow \pi ee) = 0.212$  in the absence of CP-conserving contributions. Unfortunately, the CP-conserving contributions to  $K_L \rightarrow \pi\mu\mu$  may be significantly greater than those to  $K_L \rightarrow \pi ee$ , because the helicity-suppression of the amplitude in which the  $\pi^0$  and the dilepton system are in a relative S-wave is much weaker than in the electron case.

<sup>7</sup> G. Barr, *et al.*, Phys. Lett., **242B**, 523 (1990); V. Papadimitriou, *et al.*, Phys. Rev **D44**, 573 (1991).

<sup>8</sup> A result from BNL E777 has been accepted and will be published soon in PRL.

## $K_L \rightarrow \pi^0 \nu \bar{\nu}$

The decay,  $K_L \rightarrow \pi^0 \nu \bar{\nu}$  has received considerable attention<sup>9</sup>. Unlike  $K_L \rightarrow \pi^0 e^+ e^-$ , this decay mode is essentially purely direct-CP-violating in the Standard Model: the contributions from indirect CP violation and CP-conserving terms are totally negligible. Furthermore, the branching ratio is expected to be about six times larger than for  $K \rightarrow \pi^0 e^+ e^-$ . The only diagram contributing to the decay is the one shown in Figure 1.1.4, where the  $e^+ e^-$  pair is replaced by a  $\nu \bar{\nu}$ , and of course only the Z propagator contributes. Theoretical predictions of the branching fraction for  $K_L \rightarrow \pi^0 \nu \bar{\nu}$  range from  $10^{-12}$  to  $10^{-10}$  with a central value of about  $4 \times 10^{-11}$ . Within the context of the Standard Model, the rate for  $K_L \rightarrow \pi^0 \nu \bar{\nu}$  is directly proportional to  $\eta^2$ . Free of the complications that attend the analysis of the  $K_L \rightarrow \pi^0 e^+ e^-$  and  $K_L \rightarrow \pi^0 \mu^+ \mu^-$  modes, this decay provides a uniquely direct probe into the structure of the CKM matrix. Experimentally, since one observes only a single  $\pi^0$ , a search for this mode poses some formidable challenges. The approach taken in the analysis of E731 data has been to look for events in which the  $\pi^0$  undergoes Dalitz decay, so the  $e^+$  and  $e^-$  tracks can be used to establish the location of the event vertex, and so determine the missing transverse momentum in the event. Unfortunately this strategy entails the loss of nearly two orders of magnitude in sensitivity since the branching ratio for  $\pi^0 \rightarrow \gamma e^+ e^-$  is only 1.2%.

---

<sup>9</sup>L. Littenberg, Phys. Lett. D39, 3322 (1989); T. Inagaki, *et al.*, Letter of Intent, *Experiment to search for the decay  $K_L^0 \rightarrow \pi^0 \nu \bar{\nu}$  at KEK 12 GeV Proton Synchrotron*, November, 1991.

## 1.2 Other Rare $K_L$ and $\pi^0$ Decay Modes

In addition to the three rare  $K_L$  decays sensitive to Standard Model CP violation, the KTeV facility will have the capability to perform sensitive searches for a variety of other rare and forbidden decays. As a bonus, we will be able to search for rare decays of the  $\pi^0$  using mesons produced in the copious  $3\pi^0$  decay of the  $K_L$ . Some of the modes we will search for are exotic, Standard-Model-forbidden processes involving the violation of Lepton Flavour conservation; others, like  $\pi^0 \rightarrow e^+e^-$  or  $K_L \rightarrow \mu^+\mu^-e^+e^-$ , are heavily suppressed in the Standard Model, so that they provide "windows" where new physics might be observed. Still others, like  $K_L \rightarrow \pi^+\pi^-\gamma$  and  $K_L \rightarrow \pi^0\gamma\gamma$ , will allow us to study details of  $K_L$  and  $\pi^0$  couplings which must be understood in order correctly analyze more exotic modes, and which in themselves provides valuable tests of models such as Chiral Perturbation Theory.

### 1.2.1 Searches for Lepton Flavour Violation

A number of searches have been made for the Lepton-Flavour-violating decay modes  $K_L \rightarrow \mu e$  and  $K^+ \rightarrow \pi^+\mu^+e^-$ , resulting in stringent limits on the existence of horizontal gauge bosons. At KTeV, we can perform a complementary searches for the mode  $K_L \rightarrow \pi^0\mu e$ . As in the case of the charged K search, this decay is sensitive to vector couplings; however, there is an advantage over the  $K^+ \rightarrow \pi^+\mu^+e^-$  mode because of the longer lifetime of the  $K_L$ , and because we will be sensitive to both  $K_L \rightarrow \pi^0\mu^+e^-$  and  $K_L \rightarrow \pi^0\mu^-e^+$ . Furthermore, we will be able to search for the  $\Delta S=0$  mode  $\pi^0 \rightarrow \mu e$ . The sensitivity of the latter decay to Lepton-Flavour-violating couplings is of course reduced due to the relatively short  $\pi^0$  lifetime.

It is also possible to search for Lepton Flavour violation in rare decays of B mesons. Somewhat model dependent comparisons of the sensitivities of rare B decay searches with rare K decay searches have been made. Marciano<sup>10</sup> considers the branching ratio sensitivity for each decay into either  $\mu e$  or into  $X\mu e$  and he estimates

---

<sup>10</sup>W. J. Marciano, *Rare Decay Symposium*, Vancouver, Canada, edited by D. Bryman, J. Ng, T. Numao, J. M. Poutissou, World Scientific, 1988.

$$\frac{\text{BR}(B \rightarrow \mu e)}{\text{BR}(K_L \rightarrow \mu e)} \approx \frac{\tau_B}{\tau_K} \frac{m_B}{m_K} \left(\frac{C_B}{C_K}\right)^2 ,$$

$$\frac{\text{BR}(B \rightarrow X \mu e)}{\text{BR}(K \rightarrow \pi \mu e)} \approx \frac{1}{10} \frac{\tau_B}{\tau_K} \left(\frac{m_B}{m_K}\right)^5 \left(\frac{C_B}{C_K}\right)^2 .$$

The assumption here is that the amplitudes responsible for these flavor violating decays are proportional to  $C/M^2$  where  $M$  is the scale of new physics and  $C_{B,K}$  represents the effects of couplings and mixing angles. The factor of  $1/10$  is an estimate of the suppression for the disfavored few-body final states in B decay.

For equal couplings, one finds

$$\frac{\text{BR}(B \rightarrow \mu e)}{\text{BR}(K_L \rightarrow \mu e)} \approx 2 \times 10^{-4} ,$$

$$\frac{\text{BR}(B \rightarrow X \mu e)}{\text{BR}(K \rightarrow \pi \mu e)} \approx 1 .$$

The couplings may in fact favor the K decay if the generation number is involved. In any event, even current sensitivity in the K system appears to have far greater reach than anything anticipated in the B system.

With a similar analysis, one finds that the sensitivity to  $M$ , the scale of the new physics, is in the range of 50 TeV. However, a  $10^4$  improvement in a BR will correspond to only a factor of 10 in the scale.

### 1.2.2 Radiative $K_{\pi 2}$ Decays, $K_{L,S} \rightarrow \pi^+ \pi^- \gamma$

The radiative two pion decay of the neutral kaon system, or  $K_{L,S} \rightarrow \pi^+ \pi^- \gamma$ , has several features which make a high statistics study worthwhile. There are two ways in which this process can occur: the direct emission (DE) decay and the inner bremsstrahlung (IB) decay<sup>11</sup>. These have opposite CP characteristics. A recent analysis of E731 data, in which approximately 4000 examples of both  $K_L$  and  $K_S$  decays were identified, has

---

<sup>11</sup>G. Costa and P.K. Kabir, Nuovo Cimento A51, 564 (1967).



demonstrated for the first time that  $K_L - K_S$  interference occurs in this channel, as shown in Figure 1.2.1. The CP violation parameters for this process have been measured to be<sup>12</sup>:

$$\eta_{+-\gamma} = (2.60 \pm 0.54 \pm 0.21) \cdot 10^{-3} ,$$

$$\phi_{+-\gamma} = (41 \pm 28 \pm 11)^\circ .$$

This same data has shown that the DE photon energy spectrum exhibits a shift from the spectrum predicted by the simplest magnetic dipole amplitude.

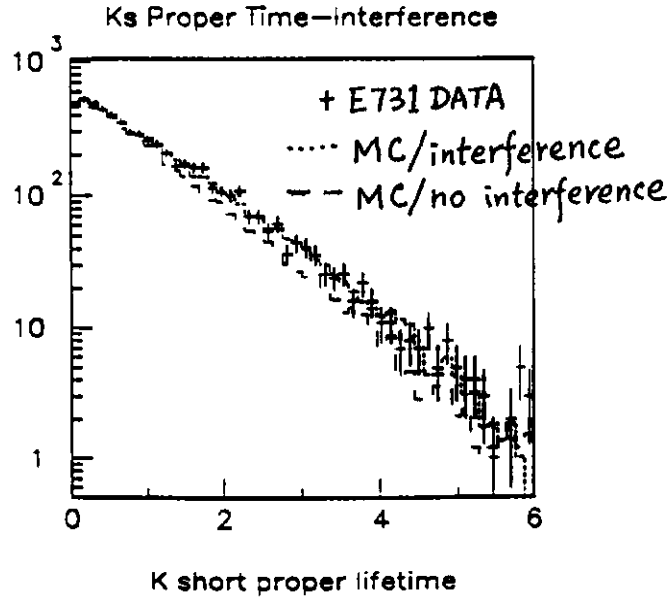


Figure.1.2.1: Proper time distribution of  $K_{L,S} \rightarrow \pi^+\pi^-\gamma$  events.

At KTeV, further study of this mode will enable us to check with greater precision the degree to which  $\eta_{+-\gamma}$  and  $\phi_{+-\gamma}$  are identical to  $\eta_{+-}$  and  $\phi_{+-}$ . It is possible that an unexpectedly large direct CP-violating amplitude in the radiative decay could lead to a difference. In addition, we will be able to study in detail the DE photon energy spectrum and angular distributions, which will allow us to search for quadrupole contributions to the DE amplitude and to check predictions based on different models for the hadronic couplings involved. Direct CP violation may also manifest itself as a charge asymmetry in the Dalitz plot.

<sup>12</sup>E. Ramberg (E731 Collaboration), Fermilab preprint CONF-91/258, presented at 3rd Topical Seminar on Heavy Flavours, San Miniato, June, 1991.

### 1.2.3 $K_L \rightarrow \pi^0 \gamma \gamma$

The decay  $K_L \rightarrow \pi^0 \gamma \gamma$  is of current interest<sup>13</sup> within the context of both Chiral Perturbation Theory (ChPT) and the Vector Meson Dominance (VMD) model as well as for its contribution to the decay  $K_L \rightarrow \pi^0 e^+ e^-$  as a CP-conserving intermediate state. Predictions for its branching ratio vary from  $6.3 \times 10^{-7}$  to  $6.2 \times 10^{-6}$  and the expected  $\gamma \gamma$  invariant mass distributions vary considerably. At the one-loop level in Chiral Perturbation Theory, the branching ratio is estimated to be  $6.8 \times 10^{-7}$  with a characteristic  $M_{\gamma \gamma}$  distribution peaking at about  $325 \text{ MeV}/c^2$ . Recently, the NA31 group reported the first observation of the signal; their measurement was confirmed by the E731 group at Fermilab. The published<sup>14</sup> branching ratios are:

CERN: NA31	$(2.1 \pm 0.6) \times 10^{-6}$
FNAL: E731	$(2.2 \pm 1.0) \times 10^{-6}$ .

These numbers are calculated using events with  $M_{\gamma \gamma} > 280 \text{ MeV}/c^2$ . The observed  $M_{\gamma \gamma}$  spectra are peaked around  $300 \text{ MeV}/c^2$  and strongly favor the ChPT prediction. On the other hand, the central value of the measured branching ratio is about a factor of three higher than that predicted by ChPT and so prefers the VMD model. A more precise measurements of both the branching ratio and the  $M_{\gamma \gamma}$  spectrum are necessary to constrain the theoretical models.

The large uncertainty in the branching ratio is due ultimately to the sizeable background from  $K_L \rightarrow 3\pi^0$ , where two photons escape or fuse with other photons, so that only four clusters are observed in the EM calorimeter. NA31 removed this background by imposing tight cuts, but this procedure reduces the size of their signal. A preconverter detector was constructed in order to reduce the background from fusions in E799I, which ran in late 1991. Analysis of the data collected has just begun, but an ultimate signal on the order of 100 events is expected. In order to calculate accurately the expected CP-conserving contribution to  $K_L \rightarrow \pi^0 e^+ e^-$ , a still larger data sample will be required. This is one of the goals of the KTeV experiments.

---

<sup>13</sup>G. Ecker, A. Pich and E. De Rafael, Phys. Lett. **189B**, 363 (1987); P. Ko and J. L. Rosner, Phys. Rev. **D40**, 3775 (1989); T. Morozumi and H. Iwasaki, *Proceedings of the Second Meeting on Physics at TeV Energy Scale*, May 1988; L. M. Sehgal, Phys. Rev. **D41**, 161 (1990); P. Ko, Phys. Rev. **D41**, 1531 (1990); G. Ecker, A. Pich and E. De Rafael, UWThPh-1989-65, FTUV 89-44.

<sup>14</sup>G. Barr, *et al.*, Phys. Lett., **242B**, 523 (1990); V. Papadimitriou, *et al.*, Phys. Rev **D44**, 573 (1991).

### 1.2.4 Four-Prong Decays of the $K_L$ and $\pi^0$

In KTeV, we expect to observe three different four-track decay modes of the  $K_L$ . Two of these,  $K_L \rightarrow e^+e^-e^+e^-$  and  $K_L \rightarrow e^+e^-\mu^+\mu^-$ , are rare electromagnetic decays, while the third,  $K_L \rightarrow \pi^+\pi^-e^+e^-$ , is an interesting hadronic mode. At present, a handful of  $e^+e^-e^+e^-$  events have been observed at Brookhaven<sup>15</sup> and CERN<sup>16</sup>, while the other two modes have never been seen<sup>17</sup>. We will also be sensitive to the double Dalitz decay of the  $\pi^0$ , by using  $\pi^0$ 's produced in the  $3\pi^0$  decay of the  $K_L$ . The best existing measurement of  $\pi^0 \rightarrow e^+e^-e^+e^-$  is based on 146 events seen in a 1962 bubble chamber experiment<sup>18</sup>. We will also be able to observe the decay  $K_L \rightarrow \mu^+\mu^-\mu^+\mu^-$ , but only if the branching ratio is significantly larger than the QED prediction<sup>19</sup> based on  $K_L \rightarrow \gamma\gamma$ , which is below  $10^{-12}$ .

The  $e^+e^-$  and  $\mu^+\mu^-$  invariant mass distributions in the electromagnetic modes provide a direct probe of the structure of the  $K_L \gamma^*\gamma^*$  and  $\pi^0 \gamma^*\gamma^*$  couplings for positive  $Q^2$ , the invariant mass-squared of the virtual photons. These form factors are necessary ingredients in the calculation of the branching ratios for dilepton decays in which two-photon intermediate states are possible, such as  $K_L \rightarrow \mu^+\mu^-$ ,  $K_L \rightarrow e^+e^-$ , and  $\pi^0 \rightarrow e^+e^-$ . In the case of the  $\pi^0$ , knowledge of the  $\pi^0 \gamma^*\gamma^*$  form factor would allow the branching ratio for  $\pi^0 \rightarrow e^+e^-$  to be more accurately calculated within QED. This would in turn make the measurement of the branching ratio for this mode, which is another goal of E799, be a more stringent test of the Standard Model than is currently the case. Moreover, the  $\pi^0 \gamma^*\gamma^*$  form factor is a necessary ingredient in a calculation of the CP-conserving component of the  $\pi^0 e^+e^-$  decay of the  $K_L$ , together with the branching ratio for the  $\pi^0 \gamma\gamma$  mode.

As for the kaon decays to  $e^+e^-e^+e^-$  and  $e^+e^-\mu^+\mu^-$ , a more precise knowledge of the two-photon contribution<sup>20</sup> to  $K_L \rightarrow \mu^+\mu^-$  would allow the short-distance, weak-interaction part of that amplitude to be more accurately determined, yielding information about the effects of virtual top quarks. If the top quark mass is measured by CDF,

---

<sup>15</sup>W. Morse, *et al.*, Brookhaven National Laboratory preprint BNL-46282, May, 1991.

<sup>16</sup>G. D. Barr, *et al.*, Phys. Lett. **B259**, 389 (1991).

<sup>17</sup>M. Ya. Balats, *et al.*, Sov. J. Nucl. Phys. **38**, 556 (1983).

<sup>18</sup>N. P. Samios, *et al.*, Phys. Rev. **126**, 1844 (1962).

<sup>19</sup>T. Miyazaka and E. Takasugi, Phys. Rev. **D8**, 2051 (1973).

<sup>20</sup>G. Belanger and C. Q. Geng, Phys. Rev. **D43**, 140 (1991).

precision measurements of the short-distance part of the amplitude for  $K_L \rightarrow \mu^+\mu^-$  would allow the value of the real part of  $V_{ub}$  to be determined. The two-photon contribution to the dimuon amplitude depends on the three inputs: the partial width for  $K_L \rightarrow \gamma\gamma$ , the  $K_L \gamma^*\gamma^*$  form factor measured using four-lepton decays, and the  $K_L \gamma^*\gamma$  form factor (where one photon is on the mass shell) measured using the Dalitz and muonic Dalitz decays of the  $K_L$ .

More detailed examination of the kinematic structure of the  $e^+e^-e^+e^-$  and  $e^+e^-\mu^+\mu^-$  final states can provide information about possible CP-violating effects in the  $K_L \rightarrow \gamma\gamma$  decay, which require knowledge of the photon polarizations. Not directly observable in the two photon decay, the polarization structure can be inferred from the angular distributions in the four-lepton modes<sup>21</sup>.

Finally, we expect to observe the decay  $K_L \rightarrow \pi^+\pi^-e^+e^-$ . There are several different contributions to this decay, of which the most interesting is a diagram involving the radiative transition between a  $K_1$  and a  $K_2$  with the emission of a longitudinal photon<sup>22</sup>. A measurement of this component of the amplitude would yield a value for the charge radius of the neutral kaon. Estimates for the  $\pi^+\pi^-e^+e^-$  branching ratio range from  $5 \times 10^{-8}$  to  $5 \times 10^{-7}$ . A fairly large sample of data will be needed to untangle contributions of the various amplitudes.

## 1.2.5 Lepton-Pair and Dalitz Decays of the $K_L$ and $\pi^0$

The KTeV detector will also be sensitive to the GIM- and helicity-suppressed lepton-pair decay modes of the  $K_L$ ,  $K_L \rightarrow \mu^+\mu^-$  and  $K_L \rightarrow e^+e^-$ . Large samples of the  $\mu^+\mu^-$  mode have now been collected, containing well over 1000 events<sup>23</sup>. In E799II, we will be able to make another high-precision measurement of the branching fraction for this mode. The comparison of our results with those of the Brookhaven experiments will provide a valuable check on our Monte Carlo acceptance calculations. Also, as  $K_L \rightarrow \mu^+\mu^-$  is the only well-measured decay mode of the  $K_L$  with two muons in the final

<sup>21</sup>Zenaida E.S. Uy, Phys. Rev. **D43**, 1572 (1991).

<sup>22</sup>L. A. Kondratyuk, L. A. Ponomarev, and V. I. Zakharov, Phys. Lett. **27B**, 655 (1968); D. P. Majumdar and J. Smith, Phys. Rev. **187**, 2039 (1969).

<sup>23</sup>T. Shikawa, to appear in *Proceedings of the APS Division of Particles and Fields Meeting*, Vancouver, Canada, August, 1991; S. Kettell, to appear in *Proceedings of the APS Division of Particles and Fields Meeting*, Vancouver, Canada, August, 1991.

state, this mode may well be used to normalize other decays, examples of which will also be collected using a dimuon trigger: these will include  $K_L \rightarrow \mu^+\mu^-\gamma$ ,  $K_L \rightarrow \mu^+\mu^-\gamma\gamma$ , and  $K_L \rightarrow \mu^+\mu^-e^+e^-$ .

Because of the strong helicity suppression of  $K_L \rightarrow e^+e^-$ , and the very high trigger rate for two-track events without dimuons or additional photons, we will probably not search for that mode. However, we will search for the related decay  $\pi^0 \rightarrow e^+e^-$  using  $3\pi^0$  decays of the  $K_L$ . This decay is described by the QED box diagram shown in Figure 1.2.2.

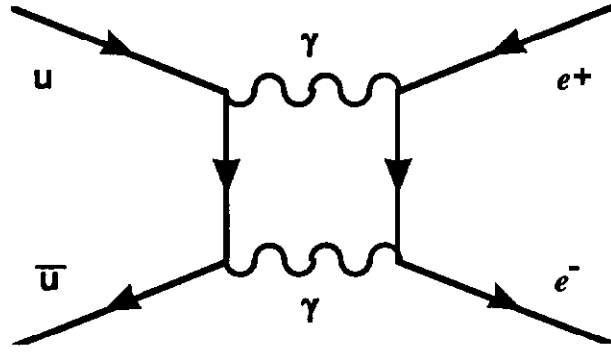


Figure 1.2.2: QED Feynman diagram for  $\pi^0 \rightarrow e^+e^-$ .

There are several somewhat contradictory results concerning this mode. Most recently the SINDRUM experiment reported<sup>24</sup> an upper limit of  $1.3 \times 10^{-7}$  for this mode at the 90% confidence level. Fairly reliable Standard Model calculations can be made for this branching ratio. Current expectations<sup>25</sup> are in the range of  $6$  to  $7 \times 10^{-8}$ . The predictions depend on the  $\pi^0 \gamma^* \gamma^*$  form factor, which (as mentioned in the preceding section) we will be able to accurately measure in some regions of  $Q^2$  using the  $\pi^0$  double Dalitz decay. Because the Standard Model prediction for this mode is very small and can be calculated with reasonable accuracy, deviations from the expected rate may signal interesting new physics.

<sup>24</sup>C. Niebuhr, *et al.* (SINDRUM Collaboration), Phys. Rev. D **40**, 2796 (1989).

<sup>25</sup>A. N. Kamal and Lo Chong-Huah, Phys. Rev. D **32**, 1744 (1985); L. Bergstrom, Z. Phys. C **14**, 129 (1982); L. Bergstrom, E. Masso, L. Ametller, and A. Bramon, Phys. Lett. **126B**, 117 (1983).

In addition to the dilepton modes, we will measure the branching fractions and dilepton mass distributions for the  $K_L$  Dalitz decay,  $K_L \rightarrow e^+e^-\gamma$ , and its muonic counterpart  $K_L \rightarrow \mu^+\mu^-\gamma$ . These modes allow the  $K_L \gamma^*\gamma$  form factor to be measured; this form factor is a measure of the deviation of the differential cross section from the Kroll-Wada form, in which the form factor is taken to be constant. Both the  $K_L \gamma^*\gamma^*$  and  $K_L \gamma^*\gamma$  form factors describe how the coupling between the  $K_L$  and photon fields is affected by the hadronic character of the kaon; for example, they parameterize the contribution to the amplitude of virtual vector mesons. Recent measurements<sup>26</sup> of the electronic  $K_L$  Dalitz decay have already begun to probe these contributions. As discussed in the preceding section, the measurement of the  $K_L \gamma^*\gamma$  form factor is an essential ingredient in the extraction of the short-distance part of the  $K_L \rightarrow \mu^+\mu^-$  amplitude.

The most problematic background to the important  $K_L \rightarrow \pi^0\mu^+\mu^-$  and  $K_L \rightarrow \pi^0e^+e^-$  modes is that due to radiative Dalitz decays,  $K_L \rightarrow \mu^+\mu^-\gamma\gamma$  and  $K_L \rightarrow e^+e^-\gamma\gamma$ , since these decays contain the identical final state particles, the only difference being the continuum of  $\gamma\gamma$  invariant masses allowed<sup>27</sup>. Kinematic cuts can reduce these backgrounds, but it is still highly desirable to search for and reconstruct these radiative decays in order to check that they occur at the predicted level and that the cuts used to remove them from the  $\pi^0\mu^+\mu^-$  and  $\pi^0e^+e^-$  samples have the predicted effect.

---

<sup>26</sup>K. E. Ohl, *et al.*, Phys. Rev. Lett. **65**, 1407 (1990); G. D. Barr, *et al.*, Phys. Lett. **240B**, 283 (1990).

<sup>27</sup>H. B. Greenlee, Phys. Rev. **D42**, 3724 (1990).

## **2. SPECTROMETER OVERVIEW**

The new KTeV facility will be used to perform the rare decay search experiment E799II and the precision  $\epsilon'/\epsilon$  measurement experiment P832. For the purpose of discussion in this design report, the KTeV spectrometer will be divided into Beam and Detector sections. A brief overview of each will be described below. Detailed design considerations will be given in the Section 3 and Section 4 of this report.

Although the setup of the two experiments are alike, one is a search experiment that requires a high flux of kaon beam, while the other is a precision experiment that requires moderate flux, but a very clean and stable kaon beam. The design of the KTeV spectrometer must be compatible with the requirements of each experiment.

### **2.1 Beam**

Neutral kaon beams will be produced by the primary Tevatron proton beam with an intensity up to  $5 \times 10^{12}$  per spill. The nominal targeting angle will be 4.2 mrad for the 900 GeV Tevatron beam on a 1.1 interaction length target in the '94-'95 run. Two side by side secondary neutral kaon beams are defined by a set of collimators and sweeping magnets. The size of the neutral beam is constrained by the size of the beam holes in the electromagnetic calorimeter. The neutral beam including the halo tail should be well contained in the calorimeter beam holes to minimize possible radiation damage to the detector. The neutral beam size should be as big as the current E731/773/799I beam at MCenter beamline which is about 0.31  $\mu$ steradian per beam. The highest kaon flux of each beam for the experiment E799II will be  $2 \times 10^8$  per spill. The useful kaon momentum will be between 20-220 GeV with a mean momentum about 70 GeV.

Substantial improvements in the stability of the primary and secondary beams and in the muon halo singles rate in the spectrometer are expected from the study of the beam design as described in Section 3 of this report.

## 2.2 Detectors

The detector spectrometer consists of a vacuum decay space and detection system. The two neutral beams after collimation emerge into a large evacuated decay volume which is surrounded by an annular photon veto system. The decay products exit through a thin vacuum window to a detection apparatus consisting of calorimetry, tracking and magnetic spectrometer, veto counters and particle identification.

Figures 2.2.1 and 2.2.2 show the plan and elevation views of the KTeV spectrometer layout for E799II and P832. We now briefly describe each detector element. Detectors common to both E799II and P832 experiment will be described first. Other detector elements will be used in P832 only are described last.

### Decay Region

A 60 meter vacuum decay space begins at 99 m downstream of target. A 1.8 meter diameter thin window composed of Kevlar and metalized mylar terminates the vacuum volume at the end of decay region. This long decay region is required by the rare decay search experiment E799II to achieve very high flux of kaon decays. The vacuum requirement is  $10^{-4}$  torr to minimize the neutron interaction background and the multiple scattering on the charged particles from the neutral kaon decay.



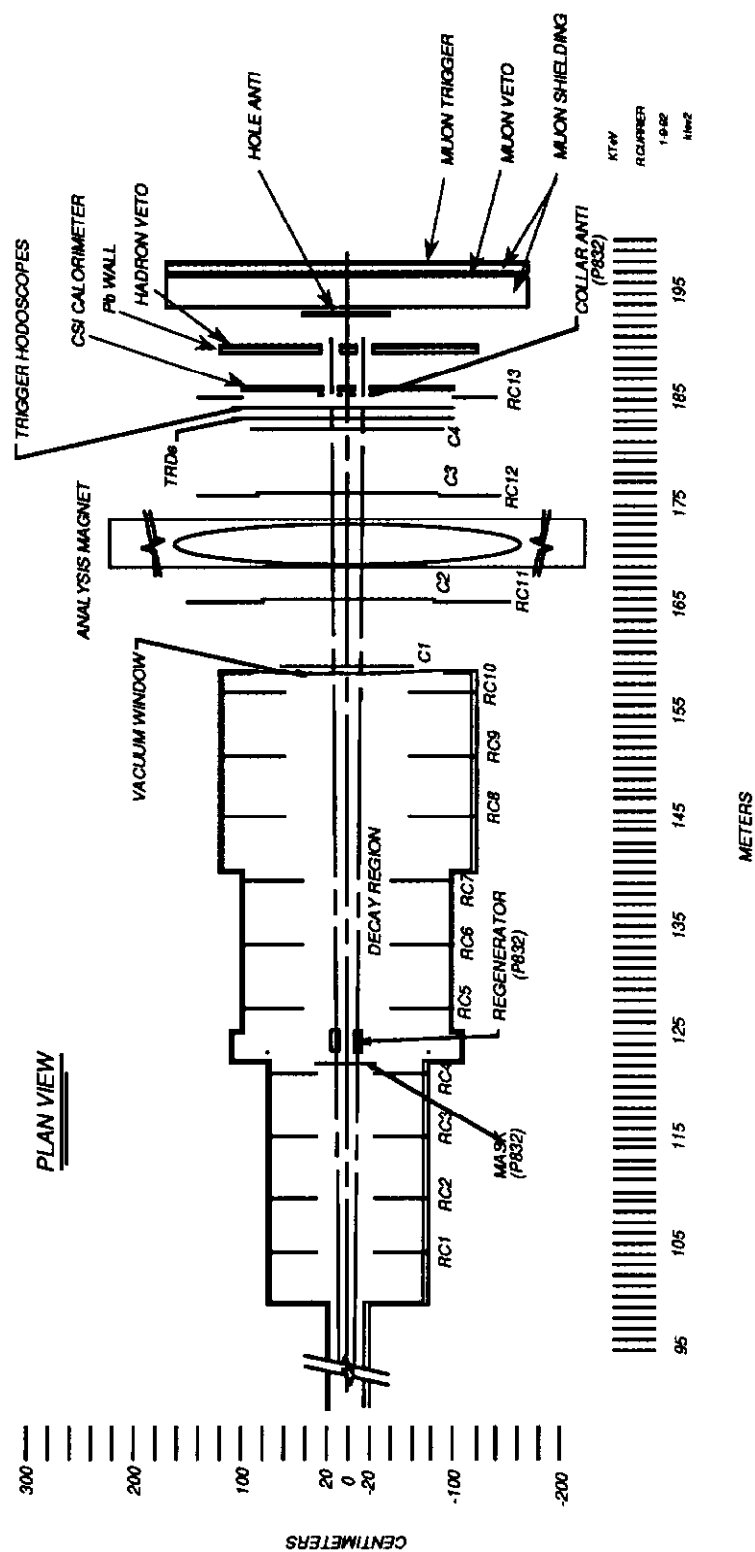


Figure 2.2.1: Plan view of KTeV spectrometer layout showing decay space and apparatus.

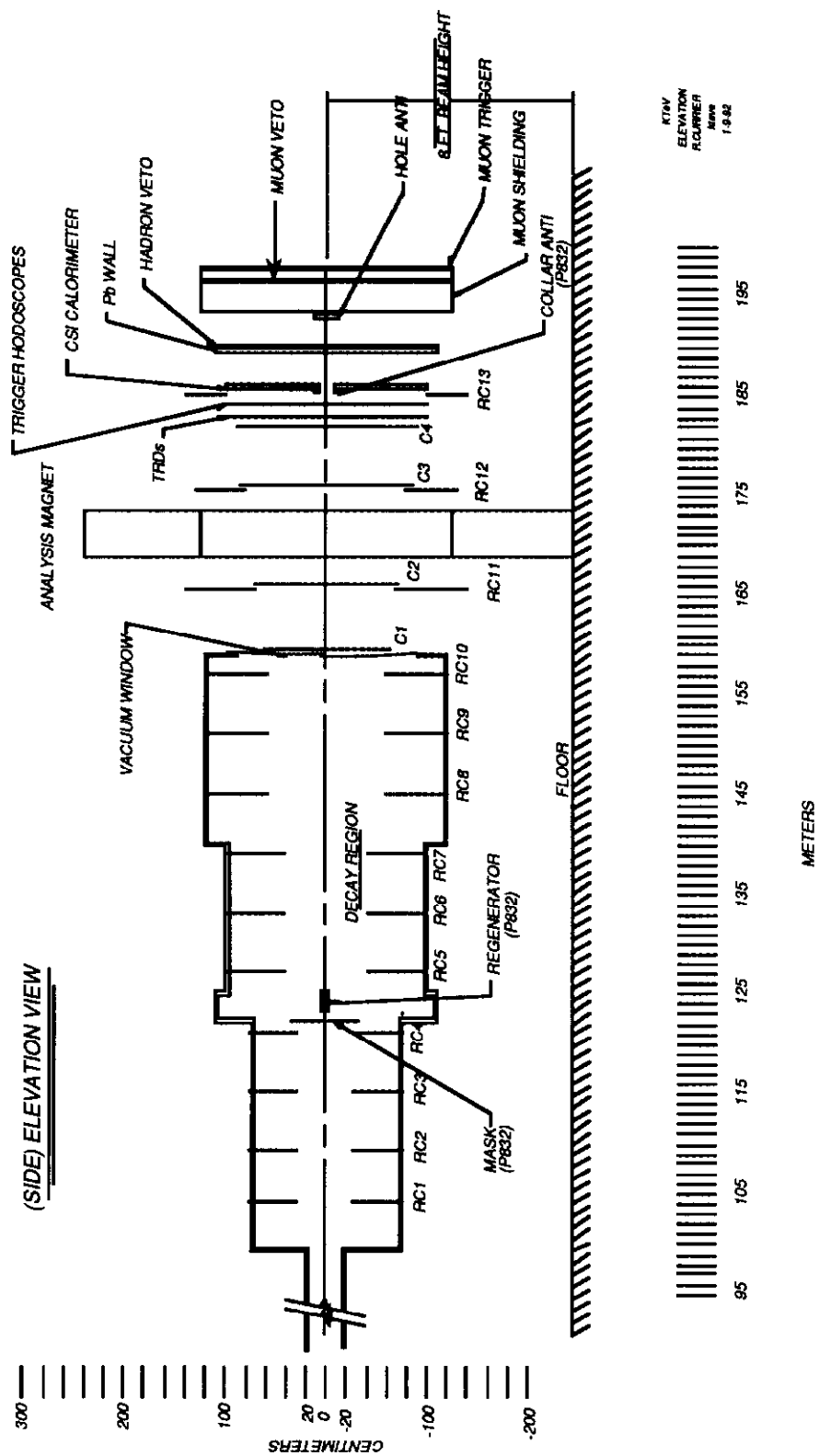


Figure 2.2.2: KTeV spectrometer layout in elevation view.

## Drift Chambers, Analysis Magnet and Trigger Hodoscopes

Four sets of drift chambers and an analyzing magnet placed downstream of the vacuum window will measure the momenta and the decay vertex of the charged particles from the neutral kaon decay. The field integral of the magnet is nominally 200 MeV/c. Each chamber has two horizontal planes (x and x') and two vertical planes (y and y') offset by half a wire spacing to resolve the left-right ambiguity. The existing E731 chambers will be used with fast chamber gas and new pre-amplifiers. Recent studies of fast gas mixtures have indicated that we can decrease the maximum drift time of our existing chambers by a factor of two, to less than 100 nsec. Beam tests of a new prototype pre-amplifier have shown that it is possible for the chambers to run at a significantly lower gas gain, thereby postponing the onset of space charge effects that are associated with high rate environments. The typical resolution for these chambers is 100  $\mu\text{m}$  per plane. The momentum resolution will be better than 0.6% at 35 GeV. Two 2 m  $\times$  2 m scintillation trigger hodoscopes will be placed downstream of the last drift chamber as a fast trigger device for charged particles.

## CsI Electromagnetic Calorimeter

A crucial detector for the KTeV experiments is a 2 m by 2 m, high-resolution electromagnetic (EM) calorimeter. It is located 1.5 m downstream of the trigger hodoscope for the detection of photons and electrons. This calorimeter is the sole detector for reconstructing neutral mode kaon decays, such as  $2\pi^0$  and  $3\pi^0$ , by measuring the energy and position of photons from  $\pi^0$  decays. Better than 1% energy resolution for photon energies greater than 1 GeV can be achieved with a 50 cm long, 27 radiation length pure CsI crystal array. Such resolution can be compared with the 3% resolution obtained with the E731 lead glass calorimeter. In addition, the spatial resolution of neutral clusters in the CsI calorimeter array will be less than 2 mm, as compared with 3-4 mm achieved with the E731 lead glass calorimeter. This will greatly improve the  $\pi^0$  mass resolution, the background rejection for the CP-violating  $K_L \rightarrow 2\pi^0$  mode and the rare  $K_L \rightarrow \pi^0 e^+ e^-$  mode, as well as the decay vertex resolution in the  $2\pi^0$  decay mode for the  $\epsilon'/\epsilon$  measurement.

Recent test results from the CsI test array show that good energy and position resolution can be achieved. The results are discussed in Section 4.8 together with the encouraging beam test results of radiation hardness studies on the pure CsI crystals.

There will be two beam holes in the CsI calorimeter for the neutral beam to pass through. The beam is then dumped in the muon filter behind the calorimeter.

### **Photon Vetoes**

In the vacuum decay region, 10 annular photon veto ring counters are placed every 5 to 6 meters along the vacuum tank. These photon veto ring counters are designed to catch wide angle photons from background  $3\pi^0$  decays down to a threshold of 100 MeV. Three additional photon veto counters downstream of the vacuum window will cover the gaps between the drift chambers and the gap outside the EM calorimeter. Since photons out to a laboratory angles of 80 mrad will be detected, the photon veto system will be nearly hermetic. A beam hole veto calorimeter ("Back Anti") will be placed 7 m downstream of the CsI calorimeter to tag forward decay photons and electrons that escape the calorimeter down the beam hole.

### **Transition Radiation Detectors**

Our  $e/\pi$  separation is enhanced by a set of transition radiation detectors (TRDs) just downstream of the last drift chamber. The transition radiation material and chambers amount to an additional 4-5% of a radiation length in front of the CsI calorimeter. This is acceptable according to a GEANT simulation. The expected  $\pi/e$  rejection is about  $\times 100$  off-line and  $\times 5$  on-line as a second level trigger element. The TRDs, which were tested in E799I, will be modified to reduce the charge collection time to less than 100 nsec. This will significantly reduce the trigger bias introduced by accidental charged particles.

### **Hadron Veto and Muon System**

Downstream of the calorimeter, a scintillator hodoscope behind a lead brick wall will serve as a hadron veto for purely electromagnetic decay triggers. There will be a beam hole in the hadron veto and lead wall for the two beams to pass through. The muon detection and veto systems will be downstream of the beam hole veto. It will consist of 4

meters of iron muon filter instrumented with planes of scintillator hodoscope and resistive plate chambers. The muon filter also serves as the neutral beam dump.

### **Regenerator, Mask Anti and Collar Anti (for P832)**

For the experiment P832, in addition to the above detector system, a 2 m long fully active regenerator will be placed 24 meters downstream of the beginning of the vacuum decay region to provide side by side  $K_S$  and  $K_L$  beams. The regenerator will be moved from one beam to the other every spill to cancel systematic effects. An absorber just downstream of the primary collimator will move synchronously with the regenerator to attenuate the beam incident on the regenerator. Upstream of the regenerator, a lead mask and anti counters around the two beam holes chokes off the acceptance for the upstream decays and serves as a well-defined aperture for acceptance calculations in  $\epsilon'/\epsilon$ . Another instrumented defining aperture (the "Collar Anti") is located just upstream of the CsI calorimeter beam holes, and partially covers the CsI blocks surrounding the beam holes. The Collar Anti will also provide a well defined aperture for acceptance calculations. These three detectors can easily be installed or removed to switch between E799II and P832, so tests for one experiment can be quickly performed during running periods for the other.

### **Acceptance**

A typical two-body decay acceptance, such as for  $K_L \rightarrow \pi^+\pi^-$  for the P832 configuration, is 50% over the kaon momentum range 40 to 160 GeV with pion momentum greater than 5 GeV. A four-body decay acceptance, such as for  $K_L \rightarrow \pi^0\pi^0$  in the same momentum range, is 20% with photon energy greater than 1 GeV. This large acceptance and long decay region will give us an  $\epsilon'/\epsilon$  statistical error of less than  $1 \times 10^{-4}$  for a 6 month run. The typical acceptance for  $K_L \rightarrow \pi^0 e^+ e^-$  in E799II is 8.3% averaged over the useful kaon momentum range from 20 to 220 GeV and the entire 60 m decay region. A 6-body decay mode, such as  $K_L \rightarrow \pi^0\pi^0\pi^0$  with one  $\pi^0 \rightarrow e^+e^-$  (very cleanly tagged), will have a 3.3% acceptance. Therefore, our reach in single event sensitivity for 4-body rare  $K_L$  decays is expected to be about  $10^{-11}$  in E799II.

## 2.3 Sensitivities and Backgrounds

### 2.3.1 P832: Measurement of $\text{Re}(\epsilon'/\epsilon)$

#### $\epsilon'/\epsilon$ Experimental Technique

The techniques used to measure  $\epsilon'/\epsilon$  are well known and are the same as used in E731. Hence, the experimental design makes heavy use of the experience gained in the earlier effort and attempts to make improvements where necessary. In this section, we will discuss these improvements particularly as they impact the understanding of the systematic uncertainties. The reader is referred to the proposal for this experiment and to the publications from E731; however, the essential points will be given here.

First, we must obtain a significant increase in statistics over E731. Using the full fiducial region, we collected 110,000 CP-violating  $2\pi^0$  decays for our “G” data set where we recorded all four modes simultaneously. We need about 6M in P832, collected in the same manner, to reach a statistical sensitivity below  $10^{-4}$ . This factor of 50 increase is obtained as follows. The G set was 3 weeks and we anticipate running for 26 weeks for P832; the intensity was  $0.7 \times 10^{12}$  protons per pulse and we anticipate running at  $3.5 \times 10^{12}$  ppp; the live time was 50% and this will be improved to 80%; these factors combined give a factor of about 80 providing some safety. We note that during the 3 week G set, we did perform the usual calibration runs so that that running was “typical”. Also, for the bulk of E731, where the modes were recorded separately, we ran at  $2.0 \times 10^{12}$  ppp so that the increase is only a factor of 1.7 over where we typically ran. We fully expect the beam and associated accidentals to be cleaner in P832 than in E731 as described in subsequent sections. A Trigger and Data Acquisition system capable of 80% live time is also described later in this document.

#### Systematic Errors

We now turn to systematic uncertainties. In the following Table, we list the size of the most important corrections and their contributions to the systematic errors, both for E731 and for P832 and then we will explain how the improvement arises.

### Systematic Errors for $\epsilon'/\epsilon$

Effect	E731 Correction [%]	E731 Syst. Error [%]	Expected P832 Correction [%]	Expected P832 Syst. Error [%]
$\pi e \nu$	0.35	0.014	0.03	0.005
$3\pi 0$	0.45	0.03	0.02	0.01
"cross-over"	4.66	0.07	0.35	0.01
incoherent regeneration (neutral)	2.58	0.05	1.0	0.01
accidental effects (charged)	-	0.04	-	0.01
accidental effects (neutral)	0.07	0.05	-	0.01
energy scale (neutral)	-	0.10	-	0.02
acceptance charged		0.05		0.02
acceptance neutral		0.05		0.02
<b>TOTAL</b>		<b>0.17</b>		<b>0.04</b>

Our overall goal is to keep the systematic uncertainty to the level of 0.04% on the double ratio; this is a factor of about four better than we have already achieved in E731. To reach this goal, we need to keep each contribution to the systematic uncertainty in the double ratio at the level of 1 or 2 x 10<sup>-4</sup>.

### Semileptonic Background

In E731, this background was at the level of 0.35% and was due to residual  $\pi e \nu$  decays where the electron was mis-identified as a pion. The systematic uncertainty is already at nearly the acceptable level. In the new experiment, we expect this background to be reduced by a factor of about 10 as a result of the much better electron energy resolution in the CsI calorimeter, the better kinematic reconstruction from the uniformly high analysis magnetic field, and the (off-line) use of the TRDs for particle identification.

## $\pi^0\pi^0\pi^0$ Background

Here the background is a bit less than 0.5% with a systematic uncertainty, determined after a great deal of effort, at the level of 0.03%. The background is severely reduced by first vetoing events in which there is an extra gamma outside the acceptance of the calorimeter and second by the ability to recognize merged clusters in the calorimeter. The new detector will have a much better veto system and, because of the finer granularity, better ability to resolve overlapping clusters. In addition, because of the better resolution of the device, we can cut more tightly on kinematic quantities thereby further reducing the background.

We have done a simulation of this background, resulting in an expected background level of  $2 \times 10^{-4}$ . An uncertainty at the  $10^{-4}$  level should be attainable with very little attention. Figure 2.3.1 shows the vacuum beam  $\pi^0\pi^0$  mass spectrum obtained in E731. The background is primarily due to  $\pi^0\pi^0\pi^0$  events. On the same figure we show a simulated spectrum for P832, scaled by  $10^{-3}$ . The figure shows both the improvement in mass resolution and the reduced background level expected in P832 due to the new calorimeter and photon veto system.



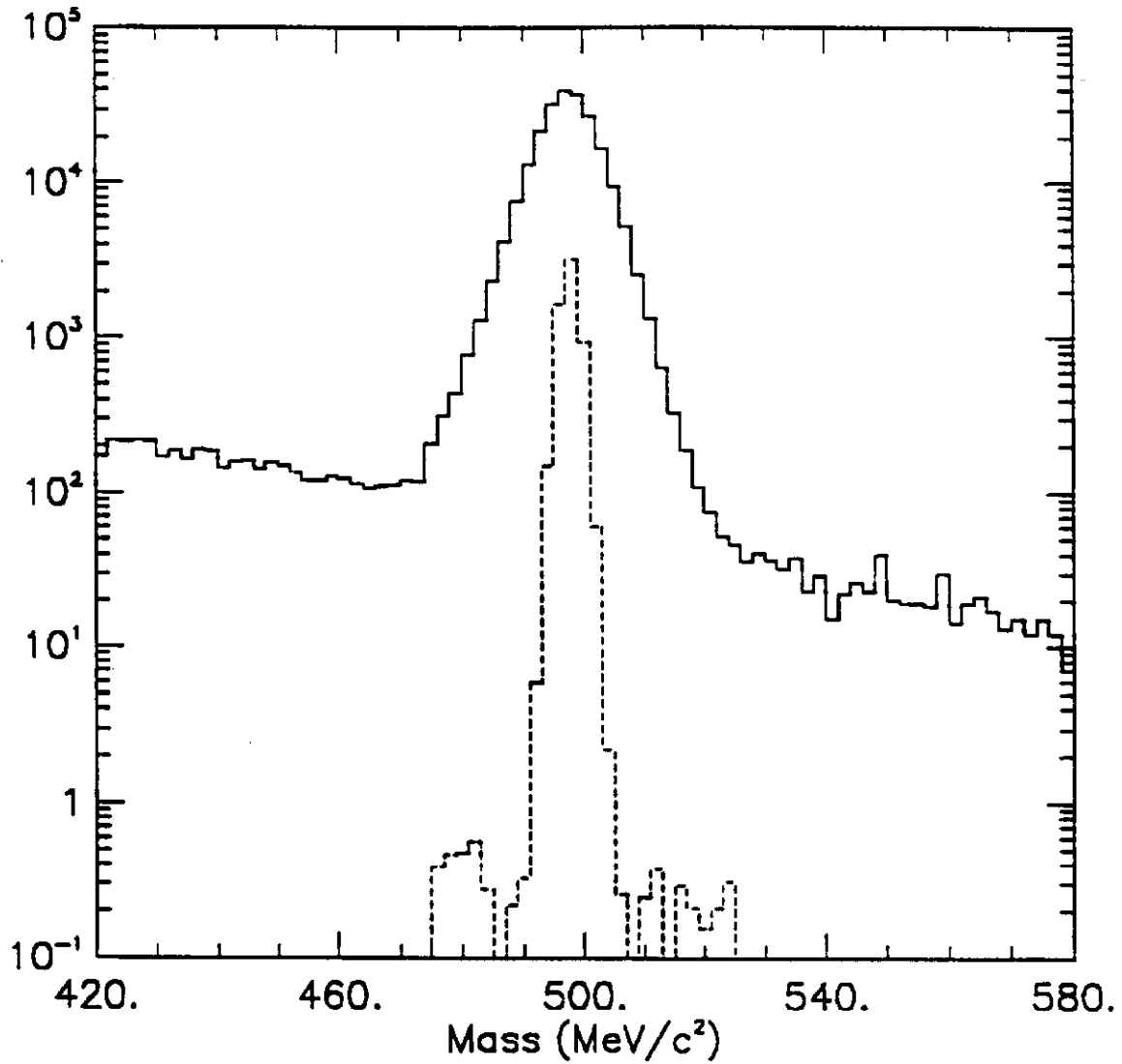


Figure 2.3.1: The vacuum beam  $\pi^0\pi^0$  invariant mass spectrum from E731, showing the level of  $\pi^0\pi^0\pi^0$  background. Superimposed is the corresponding spectrum produced by a simulation of the KTeV detector between 475  $\text{MeV}/c^2$  and 525  $\text{MeV}/c^2$ . The normalization of the KTeV histogram is arbitrary, but is approximately 0.1% of the number of events we expect to collect.

## **Background from Incoherent Regeneration**

The largest correction in E731 was due to incoherent regeneration. Here events can scatter in the regenerator and remain within the cuts in the regenerator beam, or worse, travel across the beams and wind up in the vacuum beam. Because the charged events, taken at the same time, will have precisely the same distribution in scattering angle, this correction can be made with good reliability based solely upon the data itself. Nevertheless, it is clear that a substantial reduction in systematic uncertainty is required.

This reduction is accomplished by the use of a fully active regenerator described later in this document. We have built and used such a regenerator in E-773 so our estimates of reduction of background are based upon a real device. For that regenerator, made solely of plastic scintillator, we achieved a further reduction of a factor of 6.6. For P832, the crossover is expected to be about 0.35% (the decay region is a factor of two longer increasing the vacuum signal relative to the regenerated one). Our goal is to understand this correction to about 3% of itself whereas in E731 our understanding is already better than that. The incoherent events in the regenerated beam will be at the 1% level, and we would like to understand these to 1% of themselves. This should be possible with the greatly increased statistics and using the simultaneously collected charged mode events.

## **Accidentals**

Accidental activity in the detector can potentially cause a bias in that it can shift events from bin to bin and such might be different for  $K_L$  vs.  $K_S$  events. We are very careful to record accidental events with the proper distribution in intensity and then these events are overlaid upon Monte Carlo ones, fully reconstructed to determine the losses and effect of shifts in reconstructed quantities.

Because of our technique of recording all events simultaneously, such effects cancel in first order but may not in second order. For E731, the determined shifts in the ratio of  $K_L$  over  $K_S$  decays for both modes are given in the above table. In the neutral mode, there was barely a  $1\sigma$  effect and in the charged mode, no effect seen. The systematic errors were taken to be the statistical errors in the (rather time consuming) simulation. This will clearly be improved in the new experiment. In addition, as most of the accidental events arose from beam halo, the expected dramatic reduction in this will result in similarly reduced

effects due to accidental activity in the detector. Thus a factor of 4–5 reduction in systematic uncertainty can be expected.

## Energy Scale

The energy scale in the neutral mode must be accurately known. This is because of the close relationship between the reconstructed vertex position and the energy of clusters: if the cluster energies are systematically off by one part in 1000, then so is the reconstructed vertex and then ( $K_L$ ) events will be lost as vertex cuts are made to produce the final sample. Currently, we have an assigned uncertainty in energy scale of 0.05% in E731 leading to a systematic uncertainty in the double ratio of 0.1%. We plan to reduce this uncertainty to 0.02%.

We need to discuss a few details of our calibration scheme. We have recorded in E731 every  $K_{e3}$  decay simultaneous with the  $2\pi$  modes. This very large sample provides refined calibration constants. The calibration for each lead glass block includes fitting for an overall gain constant and a non-linearity, arising from the rather large absorption of light in the crystals as described later in this report. With this electron sample, and the effectively two parameter fit to the energy vs momentum plot for each block, we end up with the mean of  $E/p$  flat to better than 0.1% over the full momentum range (2 GeV/c to 80 GeV/c).

However, photons are not electrons and when we determine and check the photon response, we are typically about 0.2% off. The photon response (typically 3% higher than the electron response) is determined from two sources. The first is a sharp edge in the reconstructed regenerator beam  $z$ -distribution for  $2\pi^0$  events and the second is from  $\pi^+\pi^-\pi^0$  events where the vertex is known from the charged decay products. This means that from a calibration sample, we can determine the photon energy scale to about 0.2%, but that the final adjustment is made using the data itself. The uncertainty of 0.05% is then a measure of the possible uncertainties in this procedure.

We are anticipating a factor of 5 improvement for the new experiment. This arises mainly from the improved characteristics of the new calorimeter: it will be 27 radiation lengths deep, in contrast to the lead glass which was about 19 radiation lengths deep, and it will have significantly better light transmission. As a result, the difference in electron to photon response is expected to be less than 0.001 or a factor of 30 improvement. This will

also mean that the linearity of the device will be much better so that it is likely that one can take all calibration constants directly from the electron sample. Planned calibration procedures are discussed in more detail in Section 4.7.8.

### Acceptance Corrections

The final systematic to be discussed is associated with the acceptance of the apparatus. This acceptance is different for  $K_L$  and  $K_S$  decays because of their different lifetimes, and hence  $z$  distributions, and an adjustment must be made. The acceptance for both modes is determined by Monte Carlo. The important inputs to the Monte Carlo, the ones that effect the relative acceptance for the  $K_L$  and  $K_S$  decays, are the apertures of the detection elements. In E731, these are first input from survey information and then they are finally determined using the independent high statistics modes:  $\pi e\nu$  and  $3\pi^0$  decays.

The final systematic uncertainties are estimated as follows. In the charged mode, we looked at the  $z$  distributions for the vacuum beam in the data and Monte Carlo in momentum bins and took as a most conservative estimate, the bin with the worst agreement. This disagreement was still consistent within statistics but yielded an 0.05% shift in the  $K_S$  to  $K_L$  acceptance ratio. In the neutral mode, we used the far more copious  $3\pi^0$  decays, comparing data to Monte Carlo to look for any systematic effects in the reconstructed  $z$  distributions. Here to be very conservative, we took 10 times the discrepancy seen in  $3\pi^0$  decays and found that this caused also an 0.05% shift in the ratio of  $K_S$  to  $K_L$  decays.

We are confident that this technique can be improved to yield the required factor of 2 to 3 improvement. In all likelihood, this could already be obtained with the E731 data sample but clearly there is not the motivation in that already the systematic error is much better than the statistical one. For 832, we will have a sample of  $K_{e3}$  and  $3\pi^0$  decays of about  $10^9$  each, allowing more than enough precision in acceptance checks.

### **2.3.2 Comparison with the CERN NA48 Experiment**

In this section we briefly compare our experiment with that in CERN, the NA48 experiment.

While P832 relies upon the techniques developed in E731, NA48 is going to use a design completely different from that in NA31. They will use a liquid Kr calorimeter and a double beam arrangement with a close target and a far target struck simultaneously by primary protons. Decays observed in the detector are associated with one or the other of the beams on the basis of tagging counters in the primary beam incident upon the close target.

We list here what we believe to be the key differences in the two approaches.

1. Approximately 1% resolution is needed for the electromagnetic calorimeter. In principle, both devices can achieve this. The liquid Kr is slower than the CsI which will result in somewhat greater pileup. It may, however, be easier to calibrate than the CsI. The Molier radius is significantly greater in the Kr leading to broader showers and probably poorer ability to resolve close by gammas. This may be partially compensated in that the NA48 sampling is currently at 2 cm by 2 cm, compared to 2.5 cm by 2.5 cm for our CsI detector. However, many more channels need to be added together in the liquid Kr detector leading to a higher noise level. The ratio of radiation length to interaction length is more favorable for the CsI, leading to better pion-electron separation. Finally, the liquid Kr calorimeter is almost certainly more expensive.

2. While both groups have a double beam arrangement, in P832 the roles of the beams will be interchanged every accelerator pulse as in E731. In NA48, the beams cannot be interchanged so, if there is a bias in the detector favoring one of the beams over the other, it may be hard to untangle.

3. The use of the regenerator in P832 insures that the two beams are identical in shape and divergence, unlike the two NA48 beams. In P832 (as in E731), all selection criteria and kinematic cuts are done blind with respect to which beam the kaon decayed in. For NA48, we believe that they will be making different cuts. However, the ambient singles rate is greater in P832 because of interactions in the regenerator, and there will be a

small number of diffracted events which "cross-over". Given our experience, we strongly favor using the regenerator although NA48 would make the opposite claim.

4. The NA48 tagging counters in the close beam have rates of about 10 MHz, so rather precise timing with a signal in the detector is required. While accidental false tags will only dilute a possible signal rather than generating one, a great deal of attention still must be paid to possible biases in this timing signal for charged vs neutral events.

5. NA48 will obtain the same precision in three runs that P832 will obtain in one. The difference stems mainly from the fact that we believe that we can calculate the acceptance sufficiently accurately to use a larger fiducial region.

### **2.3.3 E799II: Search for Rare $K_L$ Decays**

$$K_L \rightarrow \pi^0 e^+ e^-$$

#### **Single-Event Sensitivity**

We have estimated the sensitivity of E799II to  $K_L \rightarrow \pi^0 e^+ e^-$  by scaling the published limit obtained from the last 20% of the data collected by E731. This data set was used because the running conditions were comparable to those planned for E799II. Based on the 20% sample of E731 data, we reported a 90% confidence level upper limit  $BR(K_L \rightarrow \pi^0 e^+ e^-) < 4 \times 10^{-8}$ . In Table 2.3.1, we list the various factors used to estimate the overall factor by which the E731 result should be scaled:

**Table 2.3.1: Sensitivity Estimate for  $K_L \rightarrow \pi^0 e^+ e^-$**

Limiting Factor	E731 20%	E799II	Factor Gained
Run time	3 weeks	24 weeks	8
Proton intensity	0.7E12	5E12	7.1
Be absorber	in	out	2.5
Decay /Acceptance	18m	60m	2.6
Live time	50%	70%	1.4
Beam size	100cm <sup>2</sup>	290cm <sup>2</sup>	2.2
Collar Anti	yes	no	2
<b>Combined Effect</b>			<b>2300</b>

The single-event sensitivity for E799II is estimated on the basis of this table to be some 2300 times smaller than the  $1.8 \times 10^{-8}$  achieved using the E731 20% data sample. This implies a single-event sensitivity of  $8.0 \times 10^{-12}$  for E799II. However, as we will discuss in the next section, we expect that unless the  $\pi^0 e^+ e^-$  branching fraction is much larger than the Standard Model predicts, the upper limit obtained by E799II on  $BR(K_L \rightarrow \pi^0 e^+ e^-)$  will in fact be limited by the radiative Dalitz decay background,  $K_L \rightarrow e^+ e^- \gamma \gamma$ .

### Radiative Dalitz Decay Background

As found by H. Greenlee, the radiative Dalitz decay,  $K_L \rightarrow e e \gamma \gamma$ , will be a serious background in this search. We have done a full detector simulation for the KTeV detector configuration using the correct  $K_L \rightarrow e e \gamma \gamma$  matrix element which we obtained from Dr. Greenlee. Except for the requirement that the  $e^+ e^-$  invariant mass be greater than 135 MeV/c<sup>2</sup>, we first applied the same cuts mentioned in the E799 proposal. We then applied a cut to the four body  $e e \gamma \gamma$  phase space in order to maximize the signal to background ratio. Figure 2.3.2 shows the resulting single event sensitivities (solid curves) and background levels (dashed curves) as a function of signal efficiency, relative to the efficiency prior to the phase-space cut. The relevant curves for E799II are those labeled "Phase II" and "CsI". For comparison, the corresponding curves for the sensitivity of E799I and the Lead Glass calorimeter used in that experiment are also shown. The reduced background level

for the CsI calorimeter is a consequence of the greatly improved energy resolution, which allows us to select a narrower  $\gamma\gamma$  invariant mass region around the nominal  $\pi^0$  mass. Here we have assumed that we will be able to require that  $M_{\gamma\gamma}$  be within  $2 \text{ MeV}/c^2$  of  $M_{\pi^0}$  when using the CsI, compared to  $10 \text{ MeV}/c^2$  with the Lead Glass.

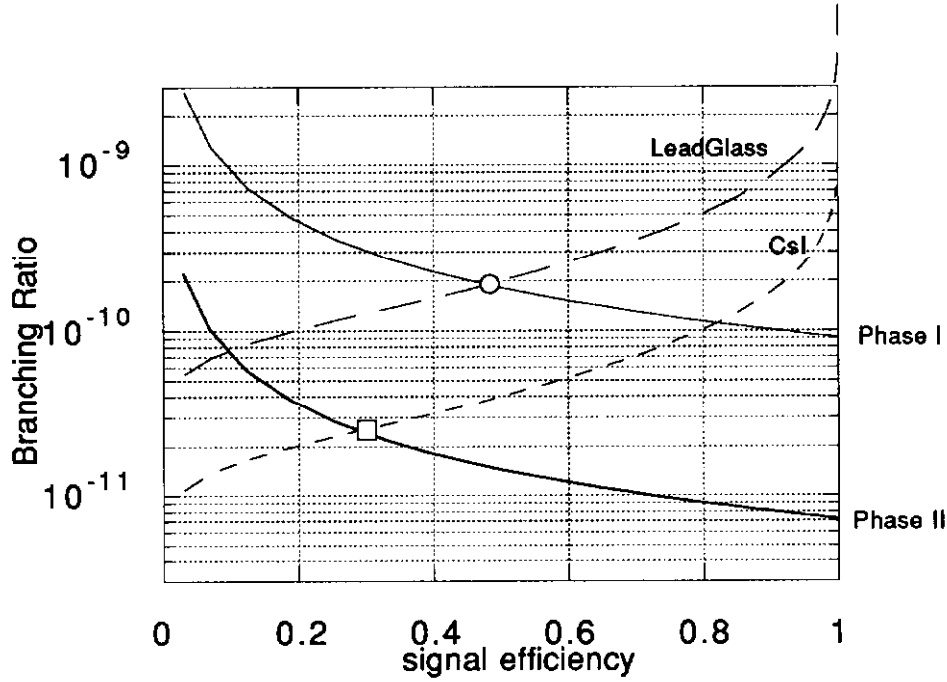


Figure 2.3.2: Sensitivity to  $K_L \rightarrow \pi^0 e^+ e^-$  vs. expected  $ee\gamma\gamma$  background.

The end point of the Phase I and Phase II curves at a relative signal efficiency of unity correspond to the sensitivity quoted in the previous table. We expect to see one background event at the point where the sensitivity and background curves cross. We can optimize the phase-space cut to give the best 90% confidence-level upper limit on the branching fraction for  $K_L \rightarrow \pi^0 e^+ e^-$  by assuming that we will see exactly the number of events expected from the  $ee\gamma\gamma$  background and then finding the point where the phase-space cut results in the best limit after background subtraction. In Phase II with the CsI calorimeter, it turns out that the optimum value of the cut corresponds to a signal efficiency of 0.7. At this level, the single-event sensitivity is  $1 \times 10^{-11}$  and the background level is  $7 \times 10^{-11}$ , so we would expect to see 7 events. The 90% confidence level is then obtained by asking how large the total number of expected events (background plus signal) would



have to be in order for the probability of observing 7 events or fewer to be less than 10%; this turns out to be about 14 events, corresponding to an upper limit of 7 signal events, for a branching ratio upper limit of  $7 \times 10^{-11}$ . In the absence of the radiative Dalitz background, we would obtain an upper limit of about  $2 \times 10^{-11}$ , so the Greenlee background costs us about a factor of 3.5 in sensitivity.

### Other Backgrounds to $K_L \rightarrow \pi^0 e^+ e^-$

Other backgrounds to the  $K_L \rightarrow \pi^0 e^+ e^-$  decay arise from combinations of three effects, namely: 1) missing final state photons; 2) particle mis-identification; and 3) overlaps with accidentals. In this section, we will summarize the various background sources and the levels at which they fake a  $K_L \rightarrow \pi^0 e^+ e^-$  signal, as predicted by Monte Carlo calculations. The Monte Carlo program used was the same one used in the E731  $\text{Re}(\epsilon'/\epsilon)$  measurement and incorporates detailed simulations of detector responses and resolutions. We assumed a  $\pi/e$  rejection ratio of 100 from E/p, and another 100 with four modules of Transition Radiation Detector. The cuts applied to define a good event are the same as used in the acceptance calculation. The energy resolution assumed here is that of lead glass, and with the new CsI calorimeter, the background levels should be much less than the numbers shown below.

Backgrounds involving accidentals were simulated by superimposing a Monte Carlo event with an “accidental trigger” event taken during the E731 run. These triggers reflected the true detector response to accidental activity and were weighted by the instantaneous proton intensity.

The various background levels given below were determined using the relation

$$\text{BR}_{\text{bg}} = (\text{Events}_{\text{pass}} / \text{Events}_{\text{gen}}) \times \prod (\text{BR}_i) \times (\text{MisID})^n / \text{Acc}_{\text{sig}}.$$

In this equation,  $\text{BR}_{\text{bg}}$  is the apparent  $\pi^0 e^+ e^-$  branching ratio from a particular background source,  $\text{Events}_{\text{gen}}$  is the number of events generated by the Monte Carlo and  $\text{Events}_{\text{pass}}$  is the number of events passing all analysis cuts; the  $\text{BR}_i$  are the branching ratios involved in the background process; MisID is the estimated probability of misidentifying a pion as an electron (taken to be 0.01%) and  $n$  is the number of pions so misidentified in the background process under consideration; finally,  $\text{Acc}_{\text{sig}}$  is the approximately 10% acceptance for  $K_L \rightarrow \pi^0 e^+ e^-$  signal events predicted by the Monte Carlo simulation. The

following table shows the resulting values of  $BR_{bg}$  for various backgrounds that were considered. Note that this table does *not* include the radiative Dalitz background, which is discussed in the preceding section. “Less-than” signs indicate a 90% confidence-level upper limit on  $BR_{bg}$

Background Source: $K_L$ decay products plus any accidentals.	Comments: How does this type of event result in a background to $K_L \rightarrow \pi^0 e^+ e^-$ ? Which particles are lost or misidentified?	$BR_{bg}$
$\pi^0 \pi^0 (\pi^0 \rightarrow \gamma e^+ e^-)$ $\pi^0 (\pi^0 \rightarrow \gamma e^+ e^-)$	Two $\pi^0$ Dalitz decays; both Dalitz photons missed or fused; one electron and one positron lost.	$< 2.2 \times 10^{-11}$
$\pi^0 \pi^0 (\pi^0 \rightarrow \gamma e^+ e^-)$	Missing or fused Dalitz $\gamma$ .	$< 1.0 \times 10^{-15}$
$\pi^0 (\pi^0 \rightarrow \gamma e^+ e^-)$ $\pi^0 (\pi^0 \rightarrow \gamma e^+ e^-)$	Two $\pi^0$ Dalitz decays; one electron and one positron lost; two Dalitz photons accidentally form fake $\pi^0$ .	$< 3.3 \times 10^{-12}$
$\pi^0 \pi^0 (\pi^0 \rightarrow e^+ e^- e^+ e^-)$	Double Dalitz decay; one electron and one positron lost.	$< 4.0 \times 10^{-13}$
$\pi^0 \pi^0 \pi^0 (\pi^0 \rightarrow \gamma e^+ e^-)$ $\pi^0 \pi^0 \pi^0 (\pi^0 \rightarrow e^+ e^- e^+ e^-)$	Missing $\pi^0$ and missing or fused Dalitz $\gamma$ ; also includes missing $\pi^0$ and missing Dalitz $e^+ e^-$ pair.	$< 1.0 \times 10^{-15}$
$\pi^0 \pi^0 (\pi^0 \rightarrow e^+ e^-)$	Can be removed by cutting on mass of $e^+ e^-$ pair.	0
$\pi^+ \pi^- \pi^0$	Double Misidentification.	$< 1.0 \times 10^{-13}$
$\pi^+ \pi^0 e^- \nu$	Misidentified pion.	$< 1.6 \times 10^{-13}$
$\gamma e^+ e^- + 1 \text{ or } 2 \text{ Accid. } \gamma$	Two photons accidentally form fake $\pi^0$ .	$5.3 \times 10^{-12}$
$\pi^+ \pi^- \gamma + 1 \text{ Accid. } \gamma$	Double Misidentification and a fake $\pi^0$ .	$2.2 \times 10^{-13}$
$\pi^+ e^- \nu \gamma + 1 \text{ Accid. } \gamma$	Single Misidentification and a fake $\pi^0$ .	$2.2 \times 10^{-13}$
$\pi^+ e^- \nu + 2 \text{ Accid. } \gamma$	Single Misidentification and a fake $\pi^0$ .	$< 7.3 \times 10^{-12}$

### Current Experimental Situation

Current published limits are  $BR(K_L \rightarrow \pi^0 e^+ e^-) < 5.5 \times 10^{-9}$  (90% C.L.) from BNL E-845, and  $< 7.5 \times 10^{-9}$  (90% C.L.) from FNAL E731. Currently there are two experiments whose primary purpose is to search for this decay mode. KEK E162 is planning to start taking data in the fall of 1992, and their goal is to achieve  $1 \times 10^{-10}$  single event sensitivity. Our Fermilab E799-I finished taking data in January of 1992 and we anticipate improvements on  $K_L \rightarrow \pi^0 e^+ e^-$ ,  $K_L \rightarrow e^+ e^- \gamma \gamma$ , and  $K_L \rightarrow \pi^0 \gamma \gamma$ .

$$K_L \rightarrow \pi^0 \mu^+ \mu^-$$

We estimate that the acceptance for this mode in E799II will be about 8%. This will correspond to a single-event sensitivity of  $1.0 \times 10^{-11}$ . Triggering will be easy for this mode, as we found in E799I that the rate for a simple dimuon trigger is very low.

By far the most important backgrounds to  $K_L \rightarrow \pi^0 \mu^+ \mu^-$  originate with the common  $\pi^+ \pi^- \pi^0$  mode. There are three possible backgrounds: (a) both pions decay in flight; (b) both pions punch through the muon steel; and (c) one pion decays and the other punches through. In this discussion, “decay in flight” is defined to mean that the pion decayed upstream of the CsI calorimeter, while “punch-through” means that the pion survived to the CsI; it may then have generated a hadronic shower containing decaying pions, or it may have decayed prior to reaching the muon filter. The level of such “punch-through” has been simulated using the GEANT Monte Carlo.

A Monte Carlo simulation indicates that the expected background level from double-decay is *less than*  $2.3 \times 10^{-11}$  at the 90% confidence level. The goal for the muon filter design in KTeV, which seems reasonable in view of the GEANT simulation results, is to keep the pion punch-through probability at less than 0.3%. If this is achieved, the the double-punch-through background level will be  $2 \times 10^{-12}$ , small compared to the single-event sensitivity. Based on the same assumption, the background from source (c) will also be *less than*  $2.3 \times 10^{-11}$  at the 90% confidence level. For both pion-decay backgrounds, there were no Monte Carlo events found which passed all cuts, so the background levels are likely to be significantly lower than the upper limits given above.

$$K_L \rightarrow \pi^0 \nu \bar{\nu}$$

Experimentally, this process is extremely challenging, since only the  $\pi^0$  in the final state is detectable and enormous backgrounds are expected to come from the copious  $K_L \rightarrow \pi^0 \pi^0$  and  $K_L \rightarrow \pi^0 \pi^0 \pi^0$  decays in which only two clusters are detected in the CsI calorimeter due to escaping or fusing photons. Thus far, there has been no serious attempt at a measurement. A limit is *not even listed* in the Particle Data Table.

At KTeV, the large momentum of the produced kaons will be an advantage, since the decay photons are boosted far forward, making it difficult for them to escape both the CsI calorimeter and the photon veto system. In addition, the fine segmentation of the CsI will reduce the number of fused photon pairs.

We are planning to search for this decay at KTeV by examining events in which the  $\pi^0$  has undergone a Dalitz decay. In a later dedicated run, we might be able to use the  $\gamma\gamma$  decay. Although the branching fraction for the Dalitz decay is just 1.2%, the additional kinematical constraints provided by the charged tracks are important tools in reducing the backgrounds, since they permit reconstruction of the  $\pi^0$  mass and the  $K_L$  decay vertex. Most importantly for the elimination of backgrounds, they can be used to determine the missing transverse momentum in the  $K_L$  decay. Because both neutrinos are massless, the missing transverse momentum can be larger in the  $\pi^0\nu\bar{\nu}$  decay than is possible in the background processes involving missing  $\pi^0$ 's.

In the next section, we discuss the sensitivity and backgrounds of the Dalitz decay analysis at KTeV. Subsequently, we consider the possibility of a dedicated experiment using the  $\pi^0 \rightarrow \gamma\gamma$  decay.

### **Dalitz Decay Analysis of $K_L \rightarrow \pi^0\nu\bar{\nu}$**

The geometrical acceptance for this mode is approximately 19%; however, cuts that must be imposed (for example, requiring a large missing transverse momentum) reduce the acceptance by an order of magnitude. Taking into account the branching fraction for the required Dalitz decay, we estimate that the KTeV single event sensitivity will be approximately  $3 \times 10^{-9}$ .

A major source of background is, of course,  $\pi^0$  + "something", where "something" is undetected. For example, neutron interactions with residual gas in a vacuum decays tank could produce  $\pi^0$ 's. To reduce this type of background to manageable level, the KTeV vacuum will have to be better than  $10^{-4}$  Torr.

Once this background is reduced, more serious backgrounds come from the decay of neutral particles such as  $K_L \rightarrow \pi^0\pi^0$ ,  $K_L \rightarrow \pi^0\pi^0\pi^0$  and  $\Lambda^0 \rightarrow \pi^0n$ . Among them,  $K_L \rightarrow \pi^0\pi^0\pi^0$  and  $\Lambda^0 \rightarrow \pi^0n$  can be rejected mainly by using the missing transverse

momentum. The maximum missing  $P_T$  from  $K_L \rightarrow \pi^0\pi^0\pi^0$  and from  $\Lambda^0 \rightarrow \pi^0 n$  are 139 MeV/c and 104 MeV/c respectively, whereas the missing  $P_T$  from  $K_L \rightarrow \pi^0\psi\psi$  extends up to 231 MeV/c. By only accepting events with missing  $P_T > 160$  MeV/c, virtually all the background events can be removed.

On the other hand, the missing  $P_T$  from  $K_L \rightarrow \pi^0\pi^0$  can be as large as 209 MeV/c. Since only 5% of the phase space for  $K_L \rightarrow \pi^0\psi\psi$  lies above 209 MeV/c, it is important that we be able to obtain adequate rejection against the  $K_L \rightarrow \pi^0\pi^0$  background by means of a the photon veto system, rather than requiring missing transverse momentum beyond the  $\pi^0\pi^0$  end point. Hermeticity and detection efficiency of photon veto detectors have been carefully optimized for this purpose. Extensive Monte Carlo simulation has been done based on the proposed detector geometry, and a rejection factor of  $5 \times 10^4$  has been estimated for this background based only on counting the number of photons. With optimized cuts, our Monte Carlo simulations result in an expected background level of less than 0.1 event with a single-event sensitivity of  $3 \times 10^{-9}$ .

### **Purely Neutral Analysis of $K_L \rightarrow \pi^0\psi\psi$**

If we could avoid the need to use the Dalitz decay of the  $\pi^0$  in order to adequately reduce the backgrounds to  $K_L \rightarrow \pi^0\psi\psi$  we could gain nearly two orders of magnitude in sensitivity. But the discussion of the previous section makes it clear that a fairly accurate measure of the transverse momentum of the  $\pi^0$  is essential if the backgrounds are to be reduced by the necessary amount. This could be achieved using the  $\gamma\gamma$  decay *only* by a dedicated run in which the neutral beam is made extremely narrow, so that the transverse position of the kaon decay would be known. The required beam size is under study, but we estimate that its transverse size would have to be at least an order of magnitude smaller than that of the KTeV neutral beam described in this report. The incident proton intensity would have to be as high as possible: if we were able to take  $10^{13}$  protons per pulse, we estimate that a single-event sensitivity of  $3 \times 10^{-10}$  could be achieved. This would also require an upgrade to the photon veto system in order to improve its efficiency for the detection of soft photons.

$$K_L \rightarrow \pi^0 \mu^+ e^- \text{ and } K_L \rightarrow \pi^0 \mu^- e^+$$

We estimate that our acceptance for these exotic Lepton-Flavour-violating modes will be comparable to that for  $K_L \rightarrow \pi^0 \mu^+ \mu^-$ , which was discussed above. The best limit on the related charged mode  $K^+ \rightarrow \pi^+ \mu^+ e^-$  is currently  $2.1 \times 10^{-10}$ . At a single-event sensitivity of  $10^{-11}$ , KTeV will be considerably more sensitive to a Flavour-violating amplitude. Indeed, taking into account the factor of 4 difference in the  $K_L$  and  $K^+$  lifetimes, we will be competitive with the proposed upgrade of the BNL experiment, which plans to reach a single-event sensitivity of  $3 \times 10^{-12}$ . Backgrounds to this mode at KTeV are expected to be small but need further study.

$$K_L \rightarrow \pi^+ \pi^- \gamma$$

Based on our E731 acceptance, we will collect about one million examples of this radiative decay during P832. This will allow us to measure the CP-violation parameter  $\eta_{+-\gamma}$  with a statistical precision of 1%, and to extract its phase  $\phi_{+-\gamma}$  to within about  $1.5^\circ$ . We expect the level of background under the mass peak will be quite small, perhaps 1%, coming primarily from accidental activity in the CsI calorimeter. The purity of the sample, combined with the high statistics, will make it possible for us to identify a higher-multipole contribution to the amplitude as small as 5% of the total, and to perform a sensitive search for asymmetries in the Dalitz plot which may signal direct CP violation.

$$K_L \rightarrow \pi^0 \gamma \gamma$$

The uncertainty in the E731 measurement of this mode was due primarily to the large background arising from fusions of four photons to form just two energy clusters in the lead glass. Because of the smaller block size in the central region of the CsI calorimeter, we estimate that the background due to double fusions will be reduced by at least an order of magnitude at KTeV. Based on a Monte Carlo simulation, we estimate our overall acceptance for this mode to be about 1%, including the effect of kinematic cuts used to improve the background rejection. Assuming that the branching fraction for this decay is about  $2 \times 10^{-6}$ , as measured by the NA31 and E731 groups, and that we will analyze only data in the farthest upstream 20 m of the decay volume in order to reduce the residual

double-fusion background, we expect to reconstruct roughly 10,000 examples of this decay during E799II. The estimated background from  $\pi^0\pi^0\pi^0$  events is about 20%.

### Four-Prong Rare Decays

Our acceptance for  $K_L \rightarrow e^+e^-e^+e^-$  in E799II is estimated from Monte Carlo simulations to be about 4.4% for decays between 100 and 160 meters from the target. With an effective flux of  $1.25 \times 10^{12}$   $K_L$  decays, this implies a single-event sensitivity of  $1.8 \times 10^{-11}$ . Neglecting the effect of the  $K_L \gamma^*\gamma^*$  form factor, and assuming that CP-violating effects are absent, the QED prediction for the  $K_L \rightarrow e^+e^-e^+e^-$  branching ratio is  $3.5 \times 10^{-8}$ . At this level, we would expect to see nearly 2000 events, more than enough to perform detailed studies of the kinematical distributions. The corresponding prediction for the  $e^+e^-\mu^+\mu^-$  branching ratio is  $1.1 \times 10^{-8}$ . The estimated acceptance for this mode is slightly smaller, yielding a single-event sensitivity of  $2.2 \times 10^{-11}$ . We would thus expect to see about 50 examples of the  $e^+e^-\mu^+\mu^-$  decay, enough for an accurate measurement of the branching ratio, and enough to take a first look at the kinematics.

We do not yet have a good estimate of the E799II sensitivity to the  $\pi^0$  Double Dalitz decay,  $\pi^0 \rightarrow e^+e^-e^+e^-$ . Nevertheless, a total of  $8.0 \times 10^{11}$   $\pi^0$ 's will decay in  $K_L \rightarrow \pi^0\pi^0\pi^0$  events, so that even if the acceptance is as poor as 0.1%, we would have a single-event sensitivity of  $1.25 \times 10^{-9}$  for this mode. The branching ratio has been measured to be  $3.2 \times 10^{-5}$ , so we would expect no fewer than 25,000  $\pi^0 \rightarrow e^+e^-e^+e^-$  events, an increase of more than two orders of magnitude compared to the bubble chamber sample.

Finally, we expect to observe the decay  $K_L \rightarrow \pi^+\pi^-e^+e^-$ . Estimates for the  $\pi^+\pi^-e^+e^-$  branching ratio range from  $5 \times 10^{-8}$  to  $5 \times 10^{-7}$ . The acceptance will depend on the form of the matrix element. If we take the 4% value found for the  $e^+e^-e^+e^-$  and  $e^+e^-\mu^+\mu^-$  modes, then we would expect to see 2500 to 25,000 events with an unprescaled four-track trigger. If the trigger for this mode must be prescaled by 10, as it was in E799I, then these numbers would be correspondingly reduced to 250 to 2500. Even so, this should be enough to begin to untangle the various contributions to the matrix element, and should also provide an interesting test of Chiral Perturbation Theory calculations.

Backgrounds to four-track decays are expected to be fairly small, and fall generally into two classes. The first is radiative decays in which the photon converts in the vacuum

window or in the first drift chamber. For example,  $K_L \rightarrow e^+e^-\gamma$  with a photon conversion could fake  $K_L \rightarrow e^+e^-e^+e^-$ . The probability of a photon conversion is about 0.1%. This background will manifest itself as an excess of events at small  $e^+e^-$  invariant masses (below 20 MeV/c<sup>2</sup>). We will be able to measure the level of such conversions using the  $\pi^0$  Dalitz decay, because the  $e^+e^-$  mass distribution of that decay is well known, and we will see a small-mass excess there due to conversions, as well. Once the conversion probability has been measured, we will be able to simulate the background to  $e^+e^-e^+e^-$ , which should be comparable to the number of real  $e^+e^-e^+e^-$  events. The same comments apply to the  $e^+e^-\mu^+\mu^-$  background from  $\mu^+\mu^-\gamma$ , and to the  $\pi^+\pi^-e^+e^-$  background from  $\pi^+\pi^-\gamma$ .

The second major class of backgrounds consists of real four-track decays with additional, missed, photons. For example,  $K_L \rightarrow \pi^0\pi^0$  followed by both  $\pi^0$ 's undergoing Dalitz decay, for which the effective branching ratio is  $1.3 \times 10^{-7}$ , followed by the loss of both Dalitz photons due to escape or fusion with electron clusters. In this case the  $e^+e^-$  invariant masses will not always be small. A background to  $e^+e^-\mu^+\mu^-$  could come from  $K_{\mu 4}$  decays,  $K_L \rightarrow \mu^+\pi^-\pi^0\nu$ , in which the  $\pi^0$  undergoes a Dalitz decay, the photon is lost, and the charged pion is misidentified as a muon due to decay or punch-through. Another possibility is  $K_L \rightarrow \pi^+\pi^-\pi^0$ , with both charged pions misidentified as muons and a  $\pi^0$  Dalitz decay with a missing photon. These backgrounds to  $e^+e^-\mu^+\mu^-$  should be small, because one must simultaneously have pion misidentification, Dalitz decay, and lost particles.

The dominant background to the  $\pi^+\pi^-e^+e^-$  mode will come from  $K_L \rightarrow \pi^+\pi^-\pi^0$ , followed by  $\pi^0 \rightarrow e^+e^-\gamma$  with loss of the photon. All of these backgrounds involving missing final state particles will be reduced by the requirement that there be no missing transverse momentum in the observed four-track state, and that the total invariant mass of the four charged particles be equal to the kaon mass. Furthermore, backgrounds due to photon escapes will be smaller than in E799I by virtue of the improved photon veto system, and backgrounds due to photons hiding under electron clusters in the CsI will be smaller because the improved energy resolution of the CsI will allow us to cut more tightly in E/p.

## $K_L \rightarrow \mu^+\mu^-\gamma$

As mentioned in Section 1, E799II will be sensitive to a variety of dilepton and Dalitz decays of both the  $K_L$  and the  $\pi^0$ . Detailed simulations have yet to be performed to



estimate the sensitivity to and backgrounds expected for these decays. One mode that has been studied in some detail is  $K_L \rightarrow \mu^+\mu^-\gamma$ . To give a flavour for the considerations involved, we consider that mode in the remainder of this section.

The acceptance for the muonic Dalitz decay in KTeV has been estimated from Monte Carlo simulations to be about 10%. The relatively low acceptance for a three-body mode is due to tight cuts required in order to reject backgrounds which will be mentioned below. Nevertheless, with this acceptance we expect to collect perhaps 5000 examples of this decay during E799II (based on the Kroll-Wada cross section), a considerable improvement over the largest extant sample, which consists of one event.

There are three important backgrounds to this mode: (a)  $K_L \rightarrow \pi^+\mu^-\nu$  plus an accidental photon, followed by pion decay or punch-through, (b)  $K_L \rightarrow \pi^+\mu^-\nu\gamma$ , followed by pion decay or punch-through, and (c)  $K_L \rightarrow \pi^+\pi^-\pi^0$ , with both pions decaying or punching through to the muon counters, and one of the photons from the  $\pi^0$  decay lost or fused.

The combination of hermetic photon veto coverage in KTeV together with the internal kinematic constraint of background source (c) make that background contribution very small, and hence no effort has been made to simulate that background in detail. Of course the internal kinematic constraint is defeated if the pion decays inside the spectrometer, that is, between the most upstream and most downstream chambers. Detailed Monte Carlo studies of background (a) have shown that events where the pion decays inside the spectrometer are very strongly rejected by track quality cuts. The radiative decay in background (b) has never been observed, but the expected branching fraction is  $5 \times 10^{-4}$ , for radiated photon energies greater than 30 MeV. This branching fraction together with the pion decaying and the internal kinematic constraint in background (b) keep this background below  $1 \times 10^{-8}$ .

The most serious background of the above three is background (a). We have studied this background in detail using the technique of overlaying accidental events in the E731 Monte Carlo. We find that by making tight cuts, we can reduce the background branching fraction from background (a) to about  $1.5 \times 10^{-7}$ , compared to the expected signal branching fraction of  $2 \times 10^{-7}$ . While this does not seem promising, we hope to achieve a significant reduction in accidental activity at KTeV compared to that observed in E731 due to an improved beam design. If we can reduce the accidental neutral cluster

background by a factor of ten in KTeV, it should be possible to make a precise measurement of the  $K_L \rightarrow \mu^+ \mu^- \gamma$  branching fraction with background at the 10% level. With the accidental background reduced, it may even be possible to relax the strict cuts mentioned above, so that the number of events observed could be as large as 10 or 15 thousand.

### 3. BEAM DESIGN

In this section, we discuss major design issues relating to creation of the required neutral kaon beams for E799II and P832. This KTeV beam facility consists of the primary beam transport, secondary beam production system, primary beam dump, neutral beam collimation system, filter and absorbers.

#### 3.1 General KTeV Beam Requirements

Here we specify the general KTeV beam requirements including the primary proton beam, the target, the secondary neutral kaon beam, absorbers and muon halo. These specifications are based on studies performed to understand our beam stability, neutral beam halo and muon halo in E731 and E799I (run in the MCenter beam line) and to improve them for E799II and P832. These experiments require higher primary proton beam intensities than the  $2 \times 10^{12}$  permitted in MCenter with significantly lower muon background rates.

The current experimental location in MCenter is not a viable location for a higher intensity KTeV facility. Fundamental shielding problems exist due to the above-grade beam location, without reasonable options for solution. Hence, the requirement exists for another experimental facility for the KTeV program. Further discussion of this requirement is presented in Appendix A.

Improved beam stability for both the primary and secondary beam is required for P832. To achieve a systematic error contribution  $\delta(\epsilon'/\epsilon)$  well below the  $5 \times 10^{-5}$  level, effects due to drift or walk of the primary proton beam on the production target (typically 0.3 mm in MCenter) and the sinking or misalignment of the neutral beam collimator system (typically 1 to 1.5 mm in MCenter) must be reduced. In E731 the value of  $\delta(\epsilon'/\epsilon)$  due to primary beam instability and neutral beam misalignment is less than  $7 \times 10^{-5}$  (mostly cancelled out with the double beam, double ratio technique). An improvement by a factor 3-5 is therefore needed to ensure that these effects are not major sources of systematic error for KTeV.

Neutral beam halo in E731 and E799I was the major source of radiation damage to the lead glass calorimeter around the beam holes. Scaled to  $10^{12}$  incident protons per spill, an average radiation dose of 30 (55) rads per week was observed in the 24 lead glass blocks bordering the beam holes during E731 (E799I), corresponding to a light output decrease of about 6% (11%) per week in those blocks. Most of the damage occurred in the region between the two beams and near the vacuum beam. The beam halo arose primarily from scattering of neutrons in the Be absorber and Pb gamma filter placed in the neutral beams downstream of the initial collimator. Simulations<sup>1</sup> using the E731 collimator geometry and tolerances in GEANT reproduce the general radiation pattern and indicate that the halo intensity is quite sensitive to the location of the absorber and filter and to the alignment and construction tolerances of the beam collimation system. This neutral beam halo is also a source of accidental clusters in the calorimeter. Therefore significant improvement in the neutral beam halo is necessary for the KTeV experiments.

Muon halo is the major singles rate in the MCenter detector. In E731, the rate exceeded 1 MHz for  $10^{12}$  incident protons per spill, about 2/3 of the total counting rate in the trigger planes and drift chambers. Improvements to reduce the muon halo to less than a few percent of the kaon decay rate and the interaction rate in the regenerator is needed. The muon halo in MCenter reached the detectors mainly as a result of the non-magnetic nature of the primary beam dump. A study to reduce such muon halo was done for the KAMI conceptual design report, where a combination of a target sweeping magnet (vertical bend) and a dump magnet (horizontal bend) reduce the muon halo rate at the spectrometer and experimental counting room dramatically. A similar design study is currently in progress for the KTeV experiment with the goal of reducing the muon halo rate in the KTeV spectrometer to less than 100 kHz at  $5 \times 10^{12}$  incident protons per spill.

The following specifications summarize our beam requirements.

---

<sup>1</sup>W. Slater, KAMI-57 and KAMI-55, internal notes (1991).

### Primary Proton Beam Specifications

- a. Proton beam energy: 800/900 GeV
- b. Proton intensity:  $5 \times 10^{12}$  per spill (see proposals)
- c. Targeting angle: 4.2 mrad (vertical)  
0.0 mrad (horizontal)
- d. Targeting angle variability: 3.5 mrad to 5.0 mrad (vertical)
- e. Beam size on target ( $\sigma$ ):  $\leq \pm 250 \mu\text{m}$  (horizontal and vertical)
- f. Beam spot stability:  $\leq \pm 50 \mu\text{m}$  (horizontal and vertical)
- g. Beam divergence:  $\pm 0.5$  mrad (horizontal and vertical)
- h. Beam angle stability:  $\leq \pm 0.1$  mrad (horizontal and vertical)

### Secondary Neutral Kaon Beam Specifications

- a. Two side by side well collimated neutral kaon beams, separated by 30 cm at the CsI calorimeter. Each beam has  $12 \text{ cm} \times 12 \text{ cm}$  beam area at 185.2 m from target.
- b. Half separation angle:  $\pm 0.810$  mrad
- c. Neutral beam divergence:  $\pm 0.278$  mrad to  $\pm 0.324$  mrad  
(the same for both beams)
- d. Beam tail or halo:  $< 1$  cm around each beam at CsI calorimeter
- e. Neutron:Kaon ratio:  $< 1.5 : 1$
- f. Kaon flux per beam:  $\geq 5 \times 10^7$  for P832  
 $\sim 2 \times 10^8$  for E799II

### Production Target:

- a. Material: low Z, high density, short interaction length: BeO or Be.
- b. Length: about 1.1-1.4 interaction lengths
- c. Width:  $\leq 1.5$  mm, with proton beam well contained in target.
- d. Height: as large as structural needs dictate, if beam spot is stable.

### **Neutron and Photon Absorbers:**

- a.      Common absorber:    to reduce the photon and neutron to kaon ratio in the beam, 3" Pb (E799II) plus additional 10"- 18" of Be (P832). Placement should be upstream of the primary two-hole collimator to reduce beam halo.
  
- b.      Movable absorber:    to reduce beam intensity incident on regenerator for P832 only, 20" Be. It must move from one beam to the other every spill, synchronized with regenerator. An out-of-beam position is required for E799.

### **Muon Halo:**

The singles rate from muon halo in the KTeV detector should be less than 100 kHz at  $5 \times 10^{12}$  incident protons per spill. The radiation dosage at the experimental counting room should also be well within specified personnel safety levels.

## **3.2 Primary Beam Transport**

The most demanding requirements in the KTeV primary beam design are set by P832, the precision measurement of  $\epsilon'/\epsilon$ . This experiment will use two separate neutral kaon beams which must be identical at the 1% level. To insure that the two beams are identical in rate and momentum spectrum, it is essential that the primary beam position and direction at the production target be controlled precisely. The experiment is sensitive to very small changes in beam position at the target because these affect the secondary beam profiles leading to changes in acceptance. Sensitivity to the beam direction arises through the targeting angle seen by each of the beams. Differences in the targeting angles affect the relative rates and momentum spectra of the two beams which must be simulated in the data analysis. Primary beam requirements for P832 are summarized in Section 3.1.

It should be noted that beam position stability and beam direction stability can be conflicting goals. Focussing optics designed to ensure a stable beam spot generally work by converting the variations in the extracted beam phase space into beam direction variations at the target. We propose here an optical configuration that generates a stable spot on the target while allowing a mechanism to correct the beam direction.

### **3.2.1 Beam Trajectory**

A detailed description of the proton beam transport to the KTeV primary target is dependent on final site selection for the KTeV program. Details on pre-target focusing and beam direction correction, presented in Sections 3.2.2 and 3.2.3, are based on a beam transported from the Switchyard NMuon beam line. However, similar techniques could also be employed for another primary beam transport. Beam focus achievable at the kaon production target as described in 3.2.2 should be relatively independent of experimental location.

### 3.2.2 Final Focusing and Target AVB System

In order to produce a small stable beam spot on target, a quadrupole triplet focusing system is desirable. Transport studies show that if we use a triplet comprising 8 4Q120 quadrupoles operating with field gradients less than 5 kGauss/inch a suitable focus can be attained 60 feet downstream from the end of the last quad. For a typical proton beam emittance of  $140\pi$  mm  $\mu$ rad, such a system produces a spot with  $\sigma < 300 \mu$  in both views. A smaller beam spot could be attained in principle but this would require a shorter focal length and would push the 4Q's nearer to the current limit. In addition one is limited by depth of field effects in which the spot size isn't maintained over the entire target length. Figure 3.2.1 shows the beam  $\sigma$  as a function of  $z$  near the target for the nominal quad currents and for currents varied by  $\pm 1$  amp. The variation of the spot size over the target length is clearly visible, as is the conclusion that the quad currents must be regulated to 1 - 2 amps.

The 60 foot space between the last quad and the target is the natural location for the B2 dipoles that set the targeting angle. These two magnets form the target angle varying bend or AVB system. By varying the relative currents of the two dipoles, targeting angles from 3.5 to 4.8 milliradians can be attained while preserving a fixed target position. The arrangement of magnets in the final focus and targeting region is shown in Figure 3.2.2 along with details of the action of the target AVB system. Typical operating specifications for the target AVB magnets are listed in Table 3.2.2.

$\vartheta$ tgt	$\vartheta_1$	$\vartheta_2$	B <sub>1</sub>	B <sub>2</sub>	I <sub>1</sub>	I <sub>2</sub>
mrad	mrad	mrad	kGauss	kGauss	amp	amp
3.5	0.2	3.3	1.0	16.0	223	4143
4.2	2.3	1.9	11.3	9.0	2938	2339
4.8	3.3	1.5	16.0	7.4	4143	1891

Table 3.2.2 Operating properties of target AVB system



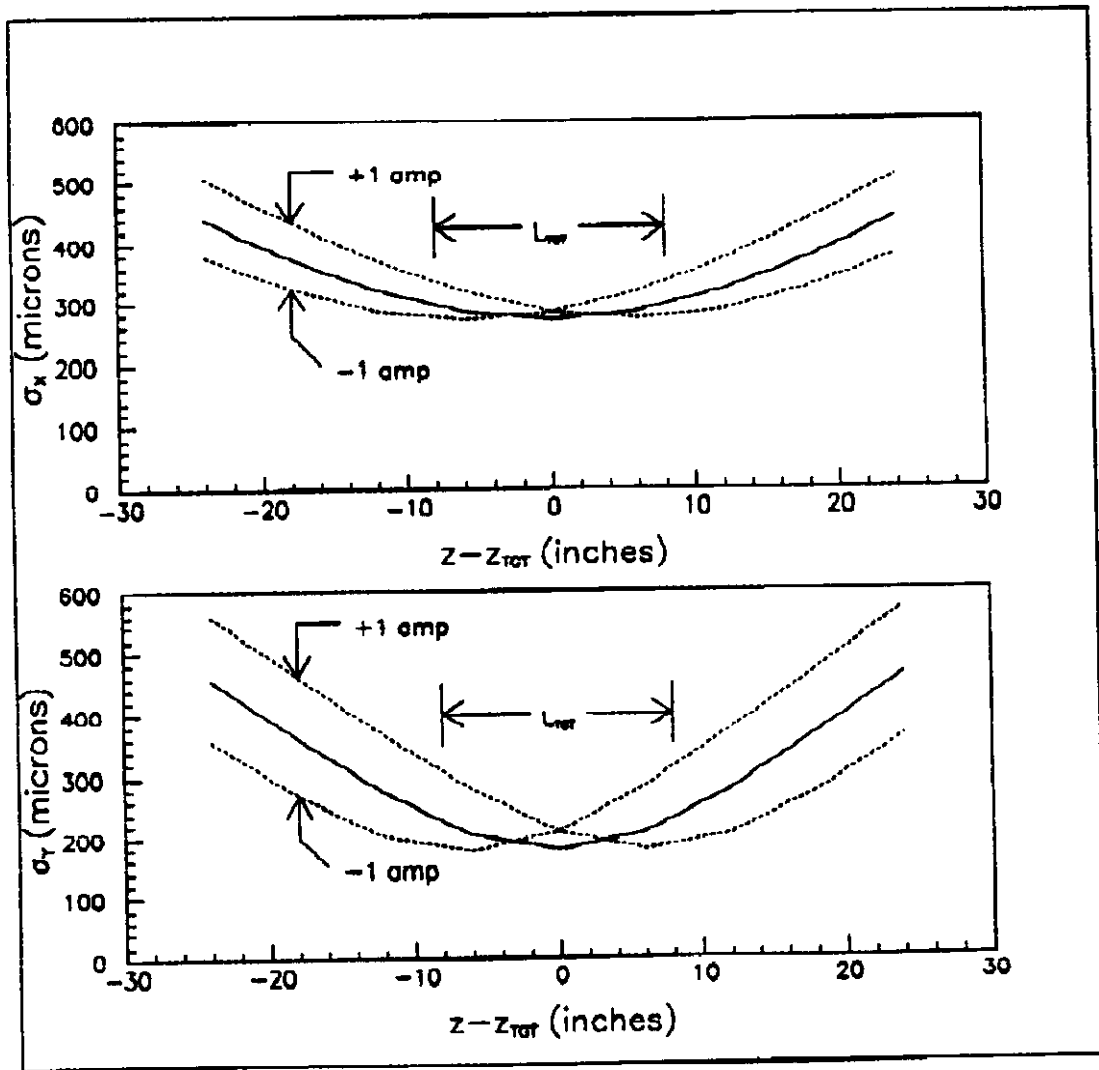


Figure 3.2.1: Beam spot size as a function of  $z$  near target showing effect of variation in quad current

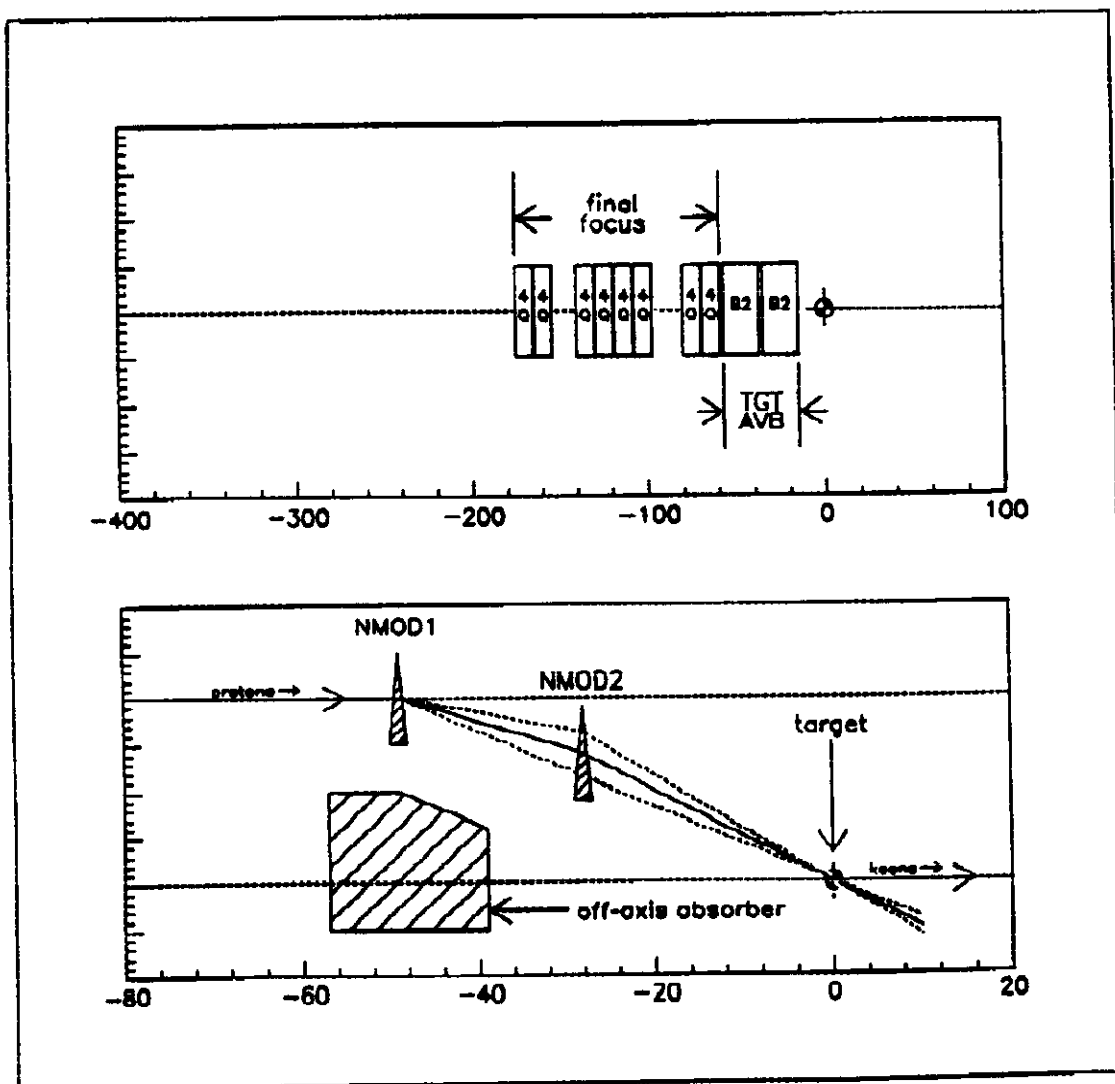


Figure 3.2.2 The upper plot is a layout of magnets in the targeting and final focus region. Below is a detail showing the action of the target AVB system.

### 3.2.3 Beam Direction Correction

Figure 3.2.3 illustrates the action of the focusing system to preserve the beam spot against variations in the extracted beam. Changes in the initial phase space population or  $\delta p/p$  effects are all converted to variations in beam angle through the target. If we employ trim magnets at an intermediate focus, then we can directly modify the beam direction at target without affecting the focal condition. The required correction is easily determined by looking at the beam profile near the final focus quads where the beam is largest. Given the 120 foot focal length of the quads, the beam position at that point needs only be controlled to the few millimeter level to attain the required 0.1 mrad beam direction control.

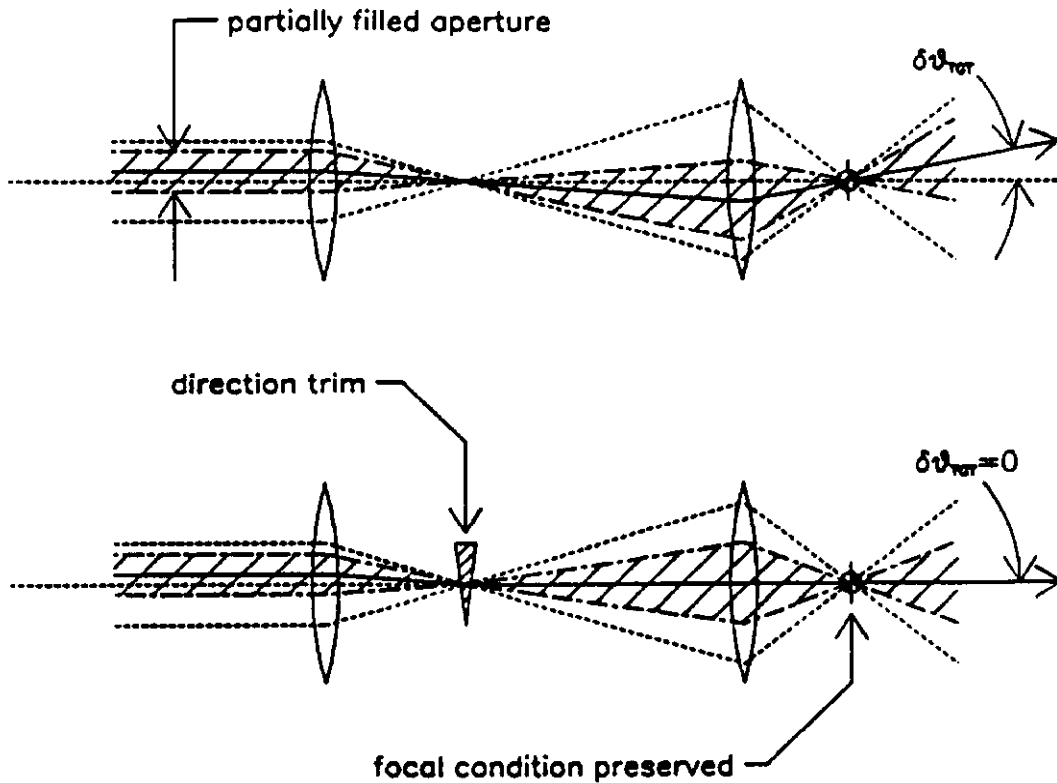


Figure 3.2.3 The upper figure shows how an incompletely filled aperture results in a change in effective targeting angle. The lower figure shows how a direction trim magnet located at an intermediate focus can be used to correct the targeting angle without affecting the focal condition.

### 3.3 Kaon Production Target

Any KTeV target must be designed to take the full accelerator energy and about 1/3 of the full intensity (*i.e.*,  $1 \times 10^{13}$  at 900 GeV). Under these conditions, target heating is a serious problem. To definitively limit the kaon source size in the critical dimension, the horizontal size of the target needs to be small, but the vertical dimension can be much larger. In addition to shape, the target material, length, and cooling mechanism must be chosen. In this section, we limit the range of choices by considering the thermal and mechanical characteristics of various materials. This information combined with flux and background measurements from the E799I run and muon Monte Carlo results will be used to make a final decision about target length and material.

In any case, several targets which can be remotely moved in and out of the proton beam need to be available. The targets will be plates, small horizontally and large vertically, successively placed on a precision horizontal slide. In addition to the horizontal motion of the slide, there will be the capability to rotate the entire slide so that the angle of the target can be made to match the incoming beam angle. Each target will be separately isolated electrically so that "charge depletion" can be used to monitor targeting efficiency.

The designed optics of the beamline gives an expected spot size on the target of  $\sigma(x) \cong \sigma(y) \cong 0.25$  mm. For structural purposes, the minimum full width of the target can be as small as 1.0 mm. Making its full width equal to 1.0 mm means that about 90% of the beam hits the target. A reasonable height of 2.54 cm, supported on top and bottom, will hold and keep the 1.0 mm dimension aligned. As shown in Figure 3.3.1, kaon production peaks at a target length of 1.3-1.4 interaction lengths ( $\lambda$ ) and varies slowly on either side of this region. Since practical considerations favor a shorter target length, we tentatively choose a length of  $1.1\lambda$ . There will be two such principal targets (1 mm x 2.54 cm x  $1.1\lambda$ ), one to serve as a backup. In addition there will be three other targets: two of the same material as the principal target, and one short copper target. Assuming beryllium as the principal target material, the setup is shown in Figure 3.3.2. The copper target will be  $\lambda/10$  and 0.005 inches in full width. One of the secondary beryllium targets will have the same cross-section as the principle target, but a length of  $\lambda/10$ ; the other will have the same length and height, but a full width of 3.0 mm.

### Target Efficiency vs L/Lambda

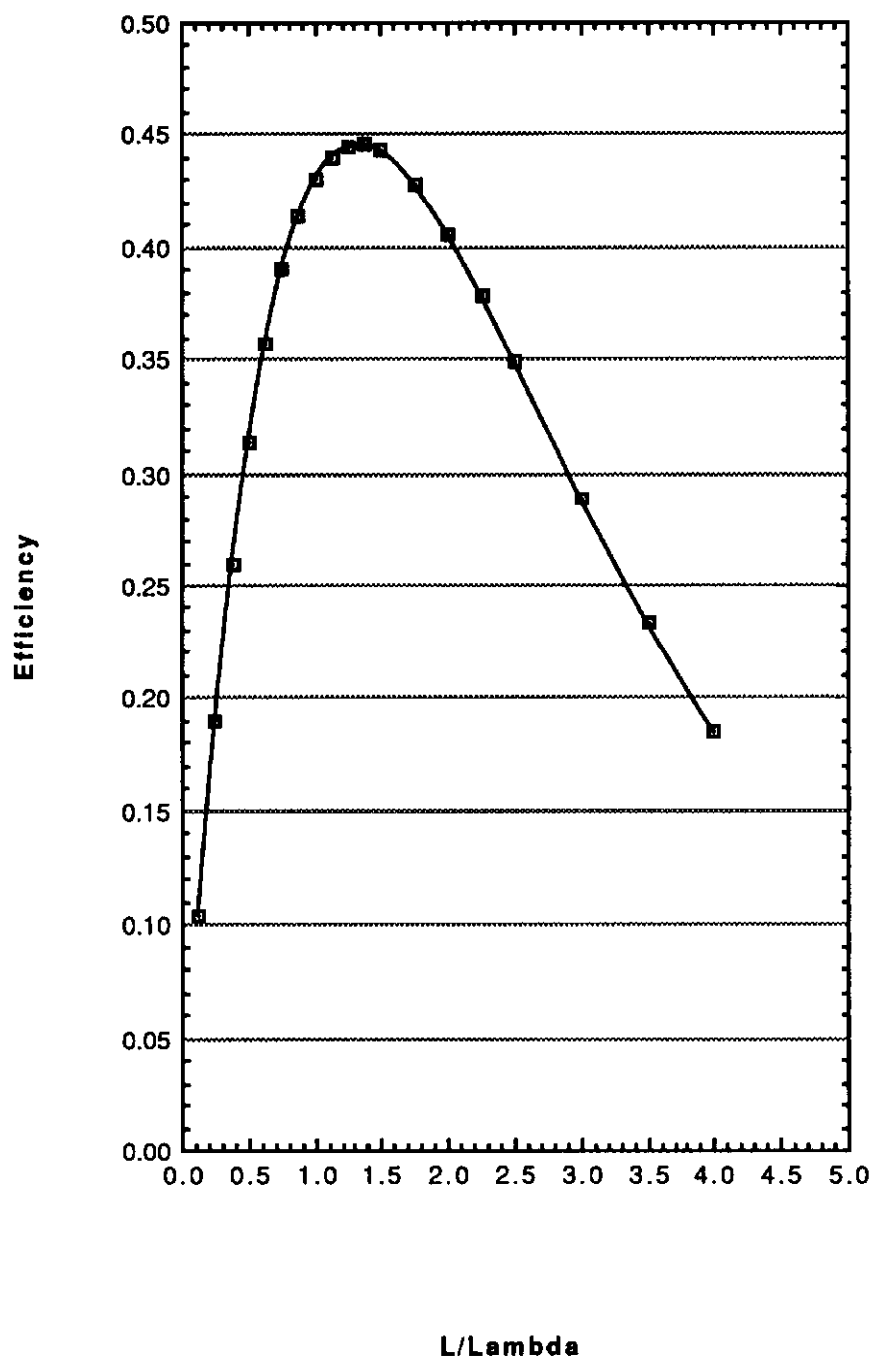


Figure 3.3.1 Variation of kaon production efficiency with target length (expressed in interaction lengths).

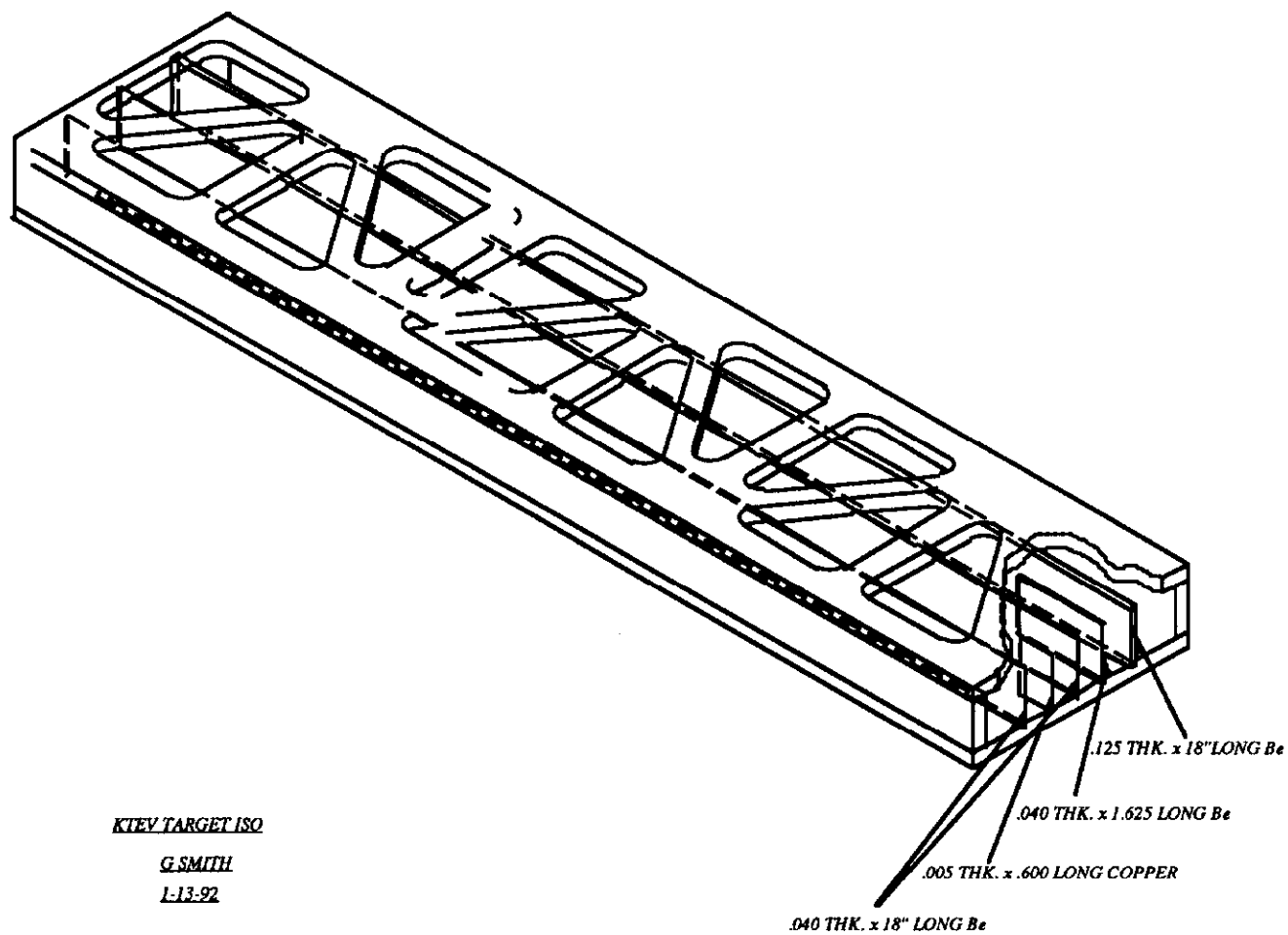


Figure 3.3.2 Schematic drawing of kaon target assembly.

For 900 GeV protons incident on a 1.1  $\lambda$  target, CASIM<sup>2</sup> gives the following energy depositions (EBAR is the average energy deposition and EMAX is the maximum energy deposition, both in GeV/cm<sup>3</sup>-incident proton. TMELT is the melting temperature of the material.):

<u>MATERIAL</u>	<u>L(cm)</u>	<u>EBAR</u>	<u>EMAX</u>	<u>TMELT(°C)</u>
Be	45	0.046	1	1280
BeO	32	0.3	4	2500
Cu	17	3.6	30	1080

For normal slow spill operation, the spill times are large compared to the diffusion time of the target material, so both the so called "dynamic" stresses (shock) and the "quasi-static" stresses are negligible. Thus melting, not fracture, is the main issue. Both Be and BeO can be adequately cooled via radiation and forced convection at a modest flow rate. Dry nitrogen gas at a flow rate of 1 meter/second perpendicular to the targets is used for the convection mechanism and will keep the temperatures well below TMELT. Be is kept below 40 °C and BeO is kept below 125 °C for normal operation. On the other hand, radiation and forced convection even at high flow rates are insufficient to keep a long copper target safely below the melting point, necessitating cooling by conduction. Even cooling by conduction is inadequate to keep tungsten targets below their melting point under these conditions. Clearly Be and BeO are the materials of choice because water cooling introduces other problems.

While KTeV uses slow spill (20 seconds), it may be the case that other experiments need fast spill (1 millisecond). Should a single fast spill pulse of full intensity be accidentally put onto the KTeV principal target, Be reaches  $T \cong 475$  °C, BeO is marginal at  $T \cong 2235$  °C, and copper will fail due to "quasi-static" stresses coming from the non-uniform temperature distribution within the target. Here Be seems preferable as the primary target material, if the additional target length can be tolerated.

---

<sup>2</sup>CASIM, A. Van Ginneken & M. Awschalom, *High Energy Particle Interactions in Large Targets*, (1975); A. Van Ginneken, Fermilab Report FN-272 (1975).

## 3.4 Secondary Kaon Beam

As discussed in Section 3.1, it is crucial to the KTeV experiments that the neutral beam collimation system prevent beam halo from causing radiation damage to the CsI electromagnetic calorimeter. Of course, it must also provide beams with the required acceptance, size, and intensity. Simulations indicate that scattering of beam particles (particularly neutrons) in filters and absorbers used to reduce the non-kaon component of the neutral beam was the primary source of this halo in E731.

For all anticipated KTeV experiments, a Pb filter will be used to attenuate the photon component of the beam. In P832, there will be an additional Be filter to enhance the kaon to neutron ratio by preferentially removing neutrons. There will also be a movable Be absorber to attenuate the regenerator beam. The KTeV neutral beam design must allow for the use of these filters, so *the collimator system must insure that no neutral particle scattered from the neutral beam itself can hit the calorimeter*. This must be done with achievable construction and alignment tolerances. Secondly, the less intense halo contribution from interactions in the collimator faces should be studied and minimized. In this section, we deal with these design considerations in turn.

Figure 3.4.1 illustrates the essential features of the KTeV secondary beam. Primary protons are targeted at 4.2 mrad (900 GeV) to avoid the large neutron flux at zero degrees. A sweeping magnet deflects the transmitted primary beam into a beam dump and charged secondaries into absorbers. The neutral collimation scheme involves a *primary* collimator 7.6 m downstream from the target and a *defining* collimator at 85 m. The CsI electromagnetic calorimeter is located 185 m downstream from the target.

The defining collimator provides the principle definition of the edges of the neutral beam. To obtain sharp edges, it is located as far downstream as possible, while still allowing for clean up sweeping magnets before the start of the instrumented decay region. The primary collimator is located as close as possible to the target. There will be a filter station close to its upstream end, and another close to its downstream end. The optimum distribution of filters has not yet been determined. It may well be somewhat different for E799II and P832. In any case, the function of the primary collimator is to limit the lateral size of the beam at the scattering source. The combination of the primary and secondary



collimators then defines the maximum deviation of a scattered neutral particle from the beam axis at the z position of the CsI calorimeter. The idea is to constrain all such scattered tracks to lie within the beam holes, missing the calorimeter.

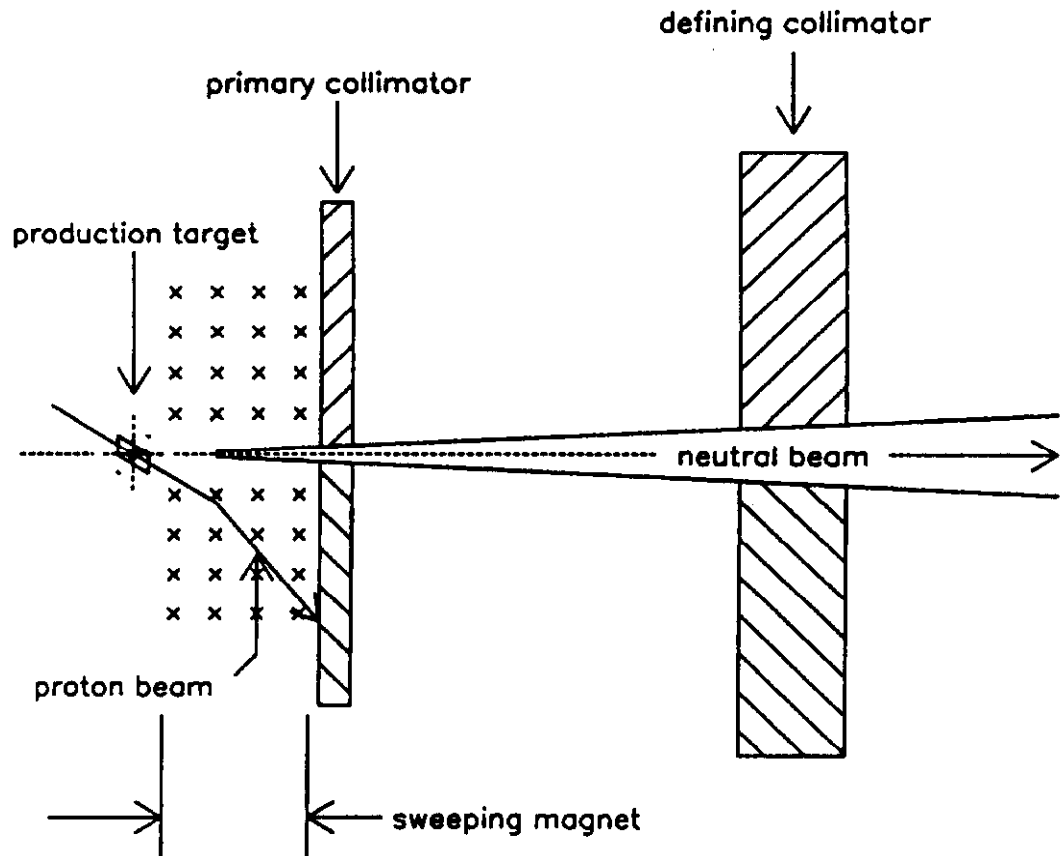


Figure 3.4.1. Schematic layout of the experiment showing the target and collimators.

We now show that collimators can be specified which satisfy these requirements while still providing the required kaon flux for E799II and P832.

### 3.4.1 General Collimator Design Considerations

If it were possible to run the experiment with a point-like target, then the collimators would simply be cut so that the collimator jaws pointed directly at the target. All neutral tracks emanating from the target would either be cleanly absorbed by the collimator walls or would pass cleanly through the hole. As discussed in Section 3.3, a practical target length for efficient neutral kaon production is 1.1 interaction lengths ( $\lambda$ ). For Be this corresponds to 45 cm; for BeO, 32 cm. Coupled with the 4.2 mrad targeting angle and the finite beam spot size, the physical target must be viewed as an extended source. This affects the design of the collimators. When the target size is non-negligible, the walls of the collimator should be tapered to point to an apex downstream of the target. The target should lie entirely within a cone extending upstream from the apex as shown in Figure 3.4.2. Allowing the collimator walls to "see" the target can have undesirable consequences. The relative merits of different collimator tapers are not addressed further here. It is assumed that all collimator surfaces must be tapered to satisfy the apex condition described above.

Our purpose here is to write down, with all approximations made explicit, the equations specifying collimators, and to develop the constraints necessary to ensure that *no particles scattered directly from the beam hit the CsI calorimeter*. As long as the calorimeter clearance constraints are satisfied, the collimator taper only affects the content of the beam within the beam hole, and the decision between various options must be based on further detailed simulation. In practice, the difference in collimator tapers is small for the defining collimator. For the primary collimator it is not.

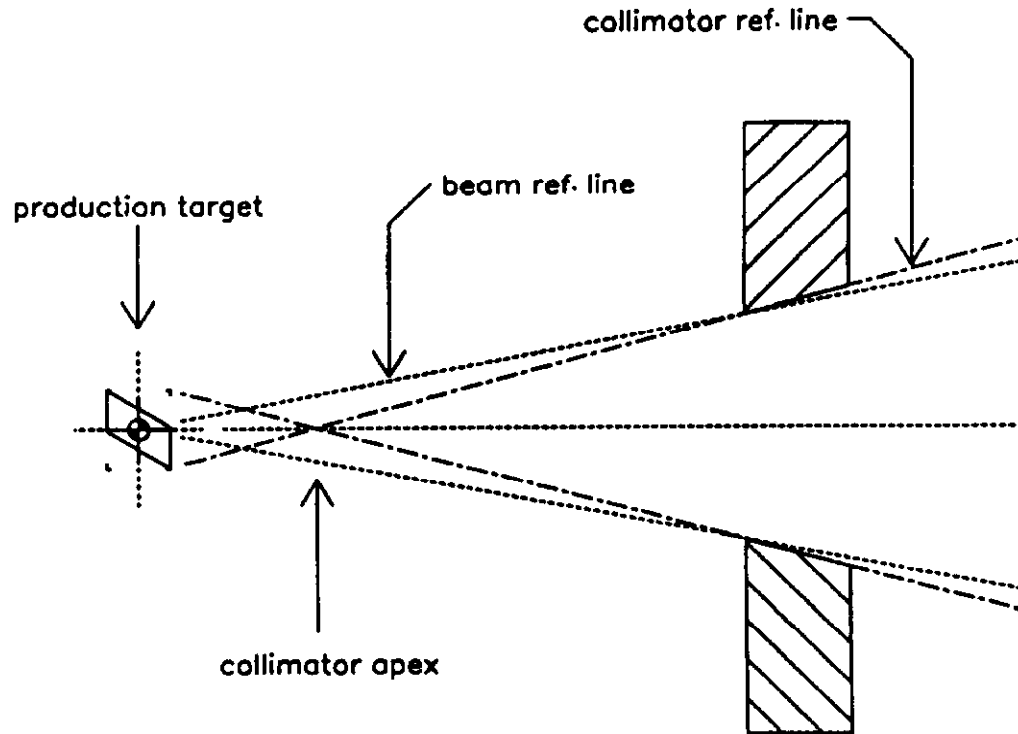


Figure 3.4.2. The walls of the collimator lie on lines that, projected forward, cross at a point called the *collimator apex*. If the target lies entirely upstream of the apex within the cone defined by these lines, then no neutral track emanating from the target can strike the inner walls of the collimator aperture.

### 3.4.2 Elevation View Collimator Specifications

In the elevation view, where the situation is not complicated by the presence of two beams, the upstream aperture of the defining collimator is given, *by definition*, by

$$\delta y_{du} \equiv z_d \delta \vartheta_y.$$

The downstream end of the defining collimator depends on the upstream end and on the apparent target height  $\delta y_{tgt}$ . As shown in Figure 3.4.3, the apparent target height is a function of the targeting angle  $\vartheta_{tgt}$ , the target length  $L_{tgt}$ , and the physical half-height of the target  $h_{tgt}$ . The target height is given by

$$\delta y_{tgt} = h_{tgt} + \frac{L_{tgt} \vartheta_{tgt}}{2}$$

For the target to lie entirely in the cone upstream from the collimator apex, the upper collimator wall must be tapered to lie on a line connecting the lower corner of downstream end of the target to the upper corner of the upstream end of the defining collimator aperture. This defining collimator reference line is illustrated in Figure 3.4.4, and is given exactly by

$$y_{dc}(z) = -\delta y_{tgt} + \frac{z + \frac{1}{2} L_{tgt}}{z_d} (\delta y_{du} + \delta y_{tgt}).$$

Terms of the form  $\frac{1}{2} L_{tgt}$  contribute at the  $1\mu$  level to the defining collimator and at the  $40\mu$  level to the primary collimator and will be dropped. With that simplification, the expression reduces to

$$y_{dc}(z) = \left(\frac{z}{z_d} - 1\right) \delta y_{tgt} + z \delta \vartheta_y.$$

The aperture at the downstream end of the defining collimator is then given by

$$\delta y_{dd} = \frac{L_d}{z_d} \delta y_{tgt} + (z_d + L_d) \delta \vartheta_y$$

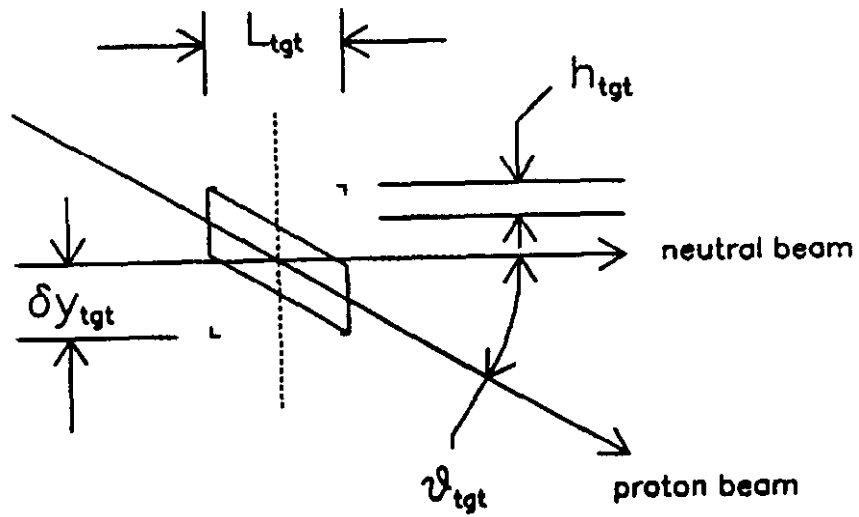


Figure 3.4.3. Elevation view of the target showing the relationship between the target half-height and length, the targeting angle, and the apparent height of the target as seen from the apparatus.

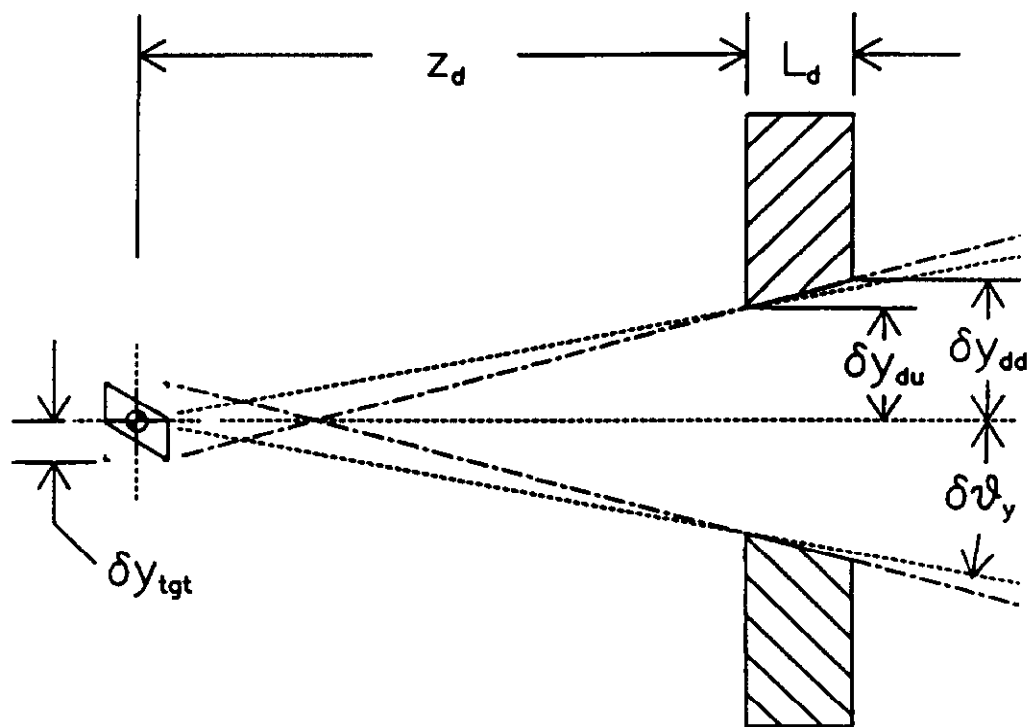


Figure 3.4.4. Elevation view of the defining collimator showing the reference lines that determine the collimator walls, and illustrating the variables used to describe the problem.

The reference lines for the primary collimator are shown in Figure 3.4.5. Its upstream aperture is defined by lines connecting the top of the target to the top of the defining collimator aperture and the bottom of the target to the bottom of the defining collimator. The equation for this reference line is

$$\begin{aligned} y_{pc}(z) &= +\delta y_{tgt} + \frac{z}{z_d} (\delta y_{du} - \delta y_{tgt}) \\ &= (1 - \frac{z}{z_d})\delta y_{tgt} + z\delta\vartheta_y \end{aligned}$$

The upstream aperture is then given by

$$\delta y_{pu} = (1 - \frac{z_p}{z_d})\delta y_{tgt} + z_p\delta\vartheta_y$$

The taper of the primary collimator wall is specified by a second reference line

$$\begin{aligned} y'_{pc}(z) &= -\delta y_{tgt} + \frac{z}{z_p} (\delta y_{pu} + \delta y_{tgt}) \\ &= (\frac{2z}{z_p} - \frac{z}{z_d} - 1)\delta y_{tgt} + \delta\vartheta_y \end{aligned}$$

From this we determine the downstream aperture of the primary collimator

$$\delta y_{pd} = (1 - \frac{z_p + L_p}{z_d} + \frac{2L_p}{z_p}) \delta y_{tgt} + (z_p + L_p)\delta\vartheta_y$$

The final step is to consider the limits imposed by the collimators on scattered rays. If we assume that the worst case scattering comes from a filter of length  $L_f$  located immediately downstream from the primary collimator, then the starting point of the most extreme scattered ray is determined by projecting the primary collimator reference line to a position  $Z_{max} = Z_p + L_p + L_{filter}$  as shown in Figure 3.4.6. The offset at this point,  $\delta y_s$ , is given by

$$\delta y_s = (1 - \frac{z_{max}}{z_d} + \frac{2(L_p + L_f)}{z_p}) \delta y_{tgt} + z_{max}\delta\vartheta_y$$

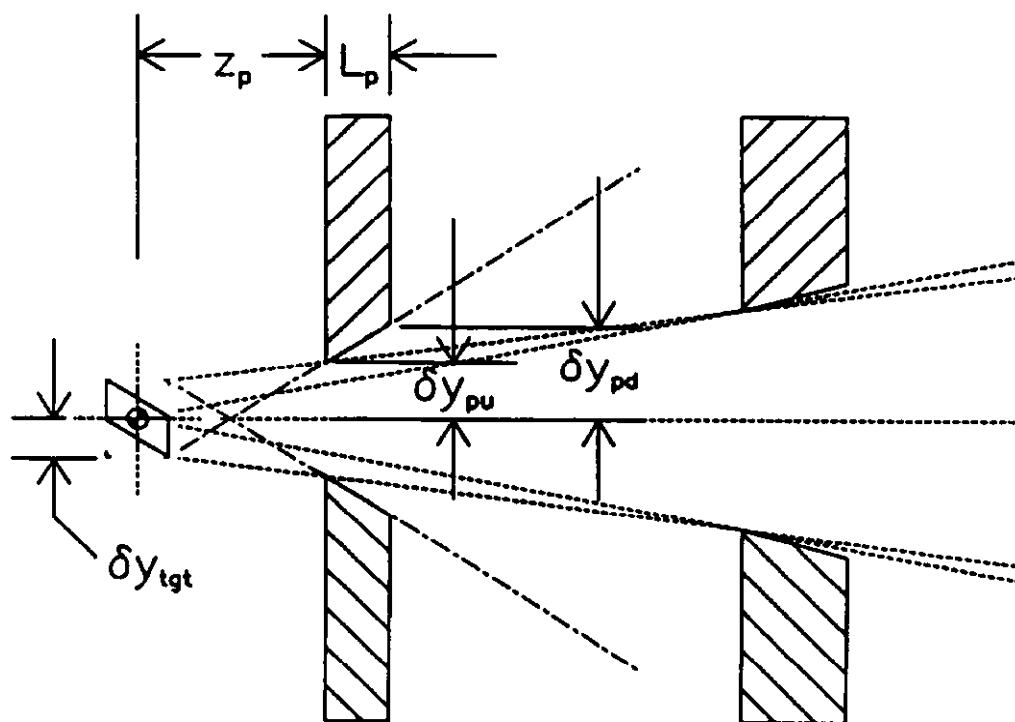


Figure 3.4.5. Elevation view showing reference lines which define the primary collimator.



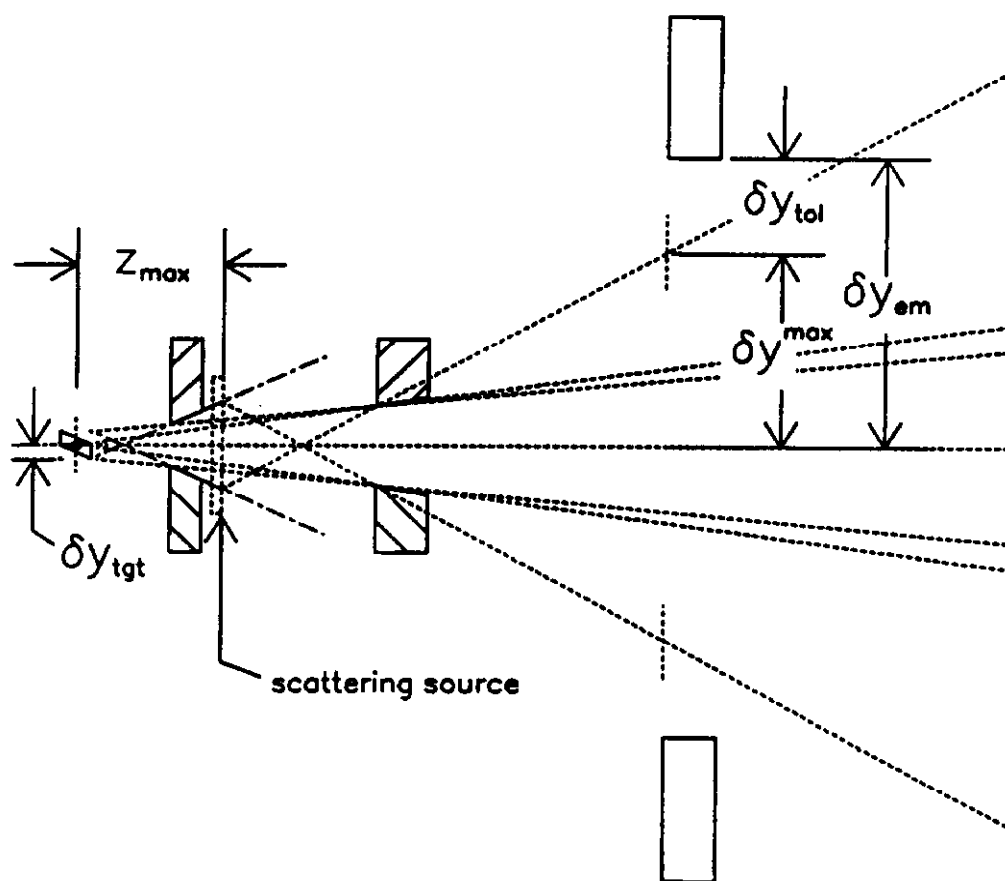


Figure 3.4.6. Elevation view of the collimator system showing the downstream most filter location and illustrating the clearance between the calorimeter and the scattered rays.

The scattering reference line connecting this point to the lower lip of the defining collimator is given by

$$y_s(z) = -\delta y_s + \frac{z - z_{\max}}{z_d - z_{\max}} (\delta y_{du} + \delta y_s).$$

If we project this line to the  $z$  position of the electromagnetic calorimeter,  $z_{em}$ , then we find that the maximum deviation of a scattered ray from the beam axis is given by

$$\delta y_{\max} = \left[ \left( \frac{z_{em} - z_d}{z_d - z_{\max}} \right) \left( \frac{2z_{\max}}{z_p} - \frac{z_{\max}}{z_d} - 1 \right) \right] \delta y_{tgt} + \left[ \frac{z_{em} (z_d + z_{\max}) - 2z_d z_{\max}}{z_d - z_{\max}} \right] \delta \vartheta_y$$

$$\equiv \alpha \delta y_{tgt} + \rho \delta \vartheta_y$$

This relationship is useful because given an effective target height,  $\delta y_{tgt}$ , we can immediately determine the maximum allowable beam acceptance

$$\delta \vartheta_y^{\max} \equiv \frac{1}{\rho} (\delta y_{em} - \delta y_{tolerance} - \alpha \delta y_{tgt})$$

where  $\delta y_{tolerance}$  is the minimum clearance required between a scattered track and the electromagnetic calorimeter hole.

### 3.4.3 Plan View Collimator Specifications

In the plan view there are two beams, separating from the symmetry plane of the experiment by  $\pm \vartheta_x$  as shown in Figure 3.4.7. The equations for the elevation view carry over if we substitute  $\vartheta_x$  for the targetting angle  $\vartheta_{tgt}$  and view the apertures as deviations from the nominal beamlines  $x = z\vartheta$ . With the additional equations expressing the beam center-line separations,  $\Delta x_i$ , at the various  $z$  stations, we have

$$\delta x_{tgt} = w_{tgt} + \frac{L_{tgt} \vartheta_x}{2}$$

$$\Delta x_{du} = z_d \vartheta_x, \quad \delta x_{du} = z_d \delta \vartheta_x$$

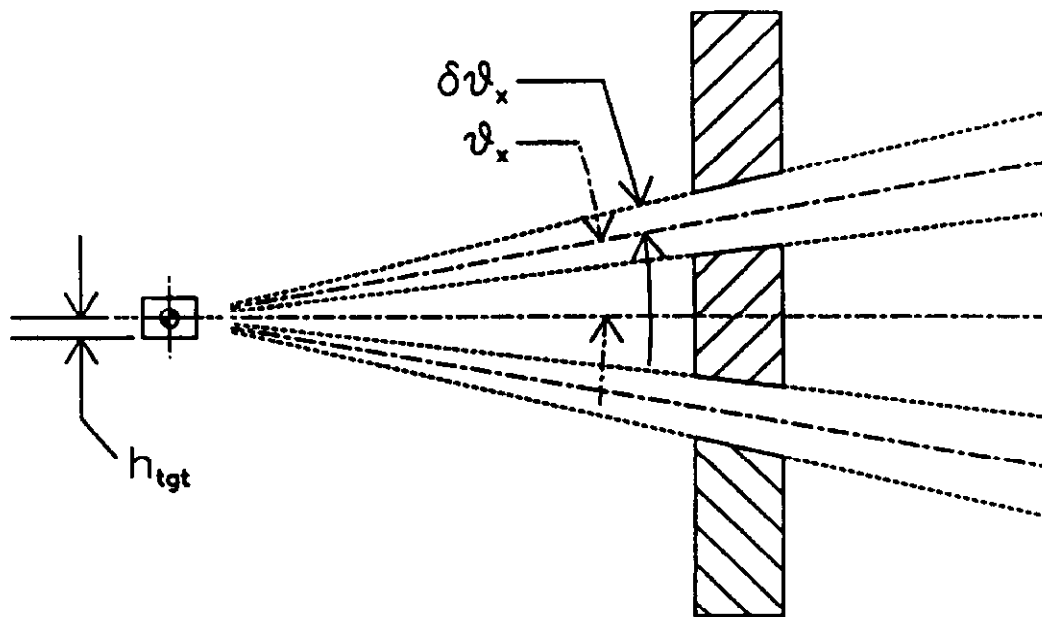


Figure 3.4.7. Plan view showing the two beams and the defining angles.

$$\Delta x_{dd} = (z_d + L_d)\vartheta_x, \quad \delta x_{dd} = \frac{L_d}{z_d}\delta x_{tgt} + (z_d + L_d)\delta\vartheta_x$$

$$\Delta x_{pu} = z_p\vartheta_x, \quad \delta x_{pu} = (1 - \frac{z_p}{z_d})\delta x_{tgt} + z_p\delta\vartheta_x$$

$$\Delta x_{pd} = (z_d + L_p)\vartheta_x, \quad \delta x_{pd} = (1 - \frac{z_p + L_p}{z_d} + \frac{2L_p}{z_p})\delta x_{tgt} + (z_p + L_p)\delta\vartheta_x$$

$$\delta x_s = (1 - \frac{z_{max}}{z_d} + \frac{2(L_p + L_f)}{z_p})\delta x_{tgt} + z_{max}\delta\vartheta_x$$

$$\delta x^{max} = [(\frac{z_{em} - z_d}{z_d - z_{max}})(\frac{2z_{max}}{z_p} - \frac{z_{max}}{z_d} - 1)]\delta x_{tgt} + [\frac{z_{em}(z_d + z_{max}) - 2z_d z_{max}}{z_d - z_{max}}]\delta\vartheta_x$$

$$\delta x^{max} \equiv \alpha\delta x_{tgt} + \rho\delta\vartheta_x$$

$$\delta\vartheta_x^{max} \equiv \frac{1}{\rho}(\delta x_{em} - \delta x_{tolerance} - \alpha\delta x_{tgt})$$

### 3.4.4 Slab Collimator

The mechanism that prevents scattered tracks from hitting the calorimeter is clearly violated in the plan view because tracks scattered out of one beam can hit the calorimeter by passing through the *other* beam hole in the defining collimator. To alleviate this problem, we incorporate a *slab collimator* into the design to separate the two beams. Figure 3.4.8 shows the arrangement. In order to stop tracks scattered from one beam to the other but not interfere with either unscattered beam, the corners of the slab collimator must lie within a triangle specified by the reference lines *AB*, *CD*, and *EF* as shown in the figure. In describing the slab collimator, it is most convenient to switch to a coordinate system with its *x* origin at *x*=0 and its *z* origin at *z*<sub>max</sub>. We define

$$c_s = z_{max}\vartheta_x - \delta x_s$$

$$d_s = z_{max}\vartheta_x + \delta x_s$$

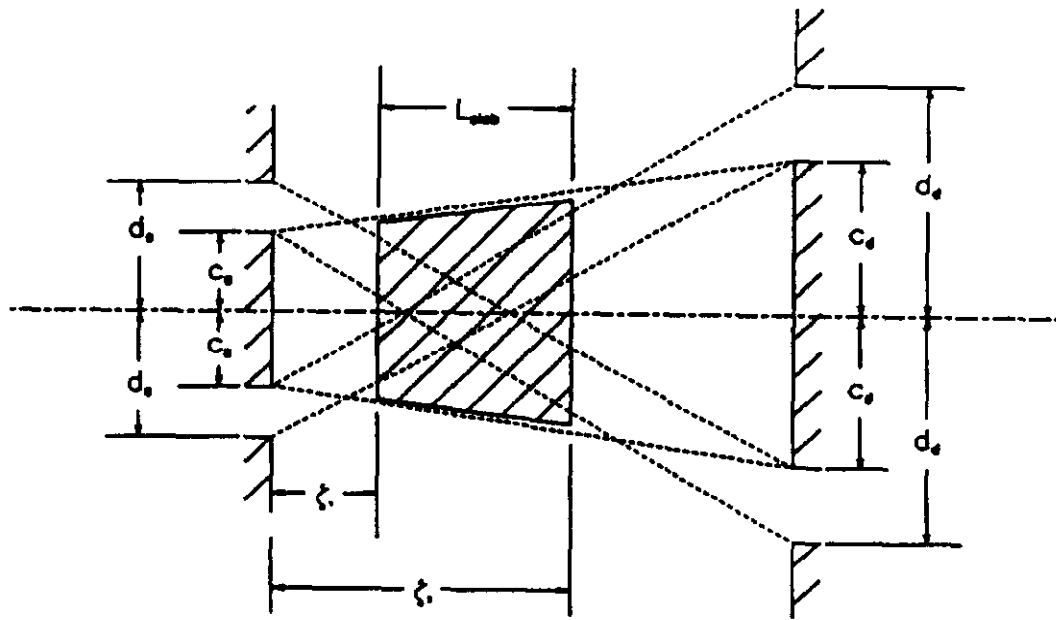


Figure 3.4.8. Plan view illustrating the use of the slab collimator to solve the cross-over problem.

$$c_d = z_d \vartheta_x - \delta x_{du}$$

$$d_d = z_d \vartheta_x + \delta x_{du}$$

$$\zeta = z - z_{\max}$$

$$\zeta_d = z_d - z_{\max}$$

In these coordinates, the reference lines are given by

$$AB(\zeta) = \frac{\zeta}{\zeta_d} (c_s + d_d) - c_s$$

$$CD(\zeta) = d_s - \frac{\zeta}{\zeta_d} (d_s + c_d)$$

$$EF(\zeta) = c_s + \frac{\zeta}{\zeta_d} (c_d - c_s)$$

If we specify a mechanical tolerance,  $t$ , to which the slab collimator can be manufactured and aligned, then its upstream end can be no farther upstream than the point at which  $EF$  and  $CD$  are separated by  $2t$ .

$$c_s + \frac{\zeta_1}{\zeta_d} (c_d - c_s) - d_s + \frac{\zeta_1}{\zeta_d} (d_s + c_d) = 2t$$

$$\Rightarrow \zeta_1 = \left( \frac{d_s - c_s + 2t}{d_s - c_s + 2c_d} \right) \zeta_d$$

similarly its downstream end is constrained by the point where  $EF$  and  $AB$  are separated by  $2t$

$$c_s + \frac{\zeta_2}{\zeta_d} (c_d - c_s) - \frac{\zeta_2}{\zeta_d} (c_s + d_d) + c_s = 2t$$

$$\Rightarrow \zeta_2 = \left( \frac{2c_s - 2t}{2c_s + d_d - c_d} \right) \zeta_d$$

The maximum length of the slab collimator is then given by

$$L_{\text{slab}}^{\text{max}} = \zeta_2 - \zeta_1$$

Substituting these results back into the expressions for  $AB$ ,  $CD$ , and  $EF$  and switching back to our normal coordinates, we have

$$z_s = z_{\text{max}} + \zeta_1$$

$$L_s = \zeta_2 - \zeta_1$$

$$\delta x_{su} = \frac{(c_d - t)(c_s + d_s)}{2c_d - c_s + d_s}$$

$$\delta x_{sd} = \frac{(c_s - t)(c_d + d_d)}{2c_s - c_d + d_d}$$

### 3.4.5 Numerical Results, Validity of Approximations

The equations developed in the previous sections specify the lateral dimensions of collimator apertures in terms of the apparent target height and beam solid angle and coefficients that depend only on the lengths and  $z$  positions of the various devices. To examine typical numerical values, we use the set of nominal  $z$  positions and lengths listed in the table below.

target length	$L_{\text{tgt}}$	30.0 cm
primary collimator Z position	$z_p$	960 cm
primary collimator length	$L_p$	200 cm
filter assembly length	$L_f$	75 cm
Z of last scattering source	$z_{\text{max}}$	1235 cm
defining collimator Z position	$z_d$	8500 cm
defining collimator length	$L_d$	300 cm
CsI calorimeter Z position	$z_{\text{em}}$	18500 cm

The expressions are all derived in the approximation that neglects the various  $L_{tgt}/2$  terms that arise from whether reference lines connect to the upstream end of the target or the downstream end. To validate this approximation, the values of the various apertures were calculated exactly and compared to the values obtained from the approximate analytic expressions, using the nominal value  $\delta\vartheta_x = \delta\vartheta_y = 0.278$  mrad for the beam divergence. The table below shows the comparison.

			Exact	Approximate	Difference
Defining Collimator	upstream end	$\delta y_{du}$	2.3630 cm	2.3630 cm	1 $\mu$ 1 $\mu$
		$\delta x_{du}$	2.3630 cm	2.3630 cm	
		$\Delta x_{du}$	6.8935 cm	6.8935 cm	
	downstream end	$\delta y_{dd}$	2.4505 cm	2.4505 cm	
		$\delta x_{dd}$	2.4487 cm	2.4486 cm	
		$\Delta x_{dd}$	7.1368 cm	7.1368 cm	
Primary Collimator	upstream end	$\delta y_{pu}$	0.3706 cm	0.3671 cm	35 $\mu$
		$\delta x_{pu}$	0.3256 cm	0.3220 cm	35 $\mu$
		$\Delta x_{pu}$	0.6164 cm	0.6164 cm	
	downstream end	$\delta y_{pd}$	0.4730 cm	0.4671 cm	58 $\mu$
		$\delta x_{pd}$	0.4077 cm	0.4021 cm	56 $\mu$
		$\Delta x_{pd}$	0.7786 cm	0.7786 cm	
Beam Size at CsI		$\delta y^{\max}$	6.319 cm	6.310 cm	90 $\mu$
		$\delta x^{\max}$	6.219 cm	6.210 cm	90 $\mu$
Slab Collimator	upstream end	$\delta x_{su}$	0.9106 cm	0.9118 cm	12 $\mu$
	downstream end	$\delta x_{sd}$	1.2967 cm	1.3089 cm	122 $\mu$
	z position	$z_s$	1894.6 cm	1886.1 cm	8.5 cm
	maximum length	$L_s$	706.9 cm	728.3 cm	21.4 cm

Clearly the accuracy is quite good for the primary and defining collimators. The slab collimator, however, requires a more thorough analysis. In the following sections the mechanical tolerances on each of the collimators will be addressed.



### 3.4.6 Collimator Tolerances

In order to specify the tolerances for the collimators, three criteria were adopted.

1. The size of the beam at the calorimeter, including scattered rays must be less than 6.5 cm. This provides a minimum of 1 cm clearance between the beam and the calorimeter edges.
2. The sizes and alignments of the various collimator apertures must be such that the beam size and position at the calorimeter is affected by less than 1 mm.
3. The areas of the two beams must be equal to within 1%.

For the beam areas to be equal to 1%, the the fabrication tolerances must be 1% of the hole size. To evaluate the second criterion, the beam solid angles were varied until the beam spot was changed by 1 mm at the CsI calorimeter. The changes produced in each collimator aperture by that same variation in beam solid angle were then taken to be the required alignment and fabrication tolerances, which are tabulated below.

	$\delta x_{pu}$	$\delta y_{pu}$	$\delta x_{pd}$	$\delta y_{pd}$	$\delta x_{du}$	$\delta y_{du}$	$\delta x_{dd}$	$\delta y_{dd}$
Equal Area	44 $\mu$	44 $\mu$	53 $\mu$	53 $\mu$	386 $\mu$	386 $\mu$	400 $\mu$	400 $\mu$
1 mm Beam Tolerance	33 $\mu$	37 $\mu$	41 $\mu$	47 $\mu$	240 $\mu$	240 $\mu$	249 $\mu$	249 $\mu$

Based on this conservative analysis, the defining collimator presents no extraordinary mechanical problems. It must be fabricated and aligned to better than about 250  $\mu$ . The primary collimator, however, presents a potential problem since 50  $\mu$  tolerances are not easily attained for a 2 meter long collimator. It is important to recognize that the tolerances for the primary collimator would become even more demanding if it were made the defining collimator with the second collimator serving only to reduce beam halo.

### 3.4.7 Alignment System

Maintaining the alignment of the neutral beam elements to the required tolerances is crucial to the KTeV program, and the ultimate measure of alignment comes from studying the beam itself. We propose a system of tungsten masks that can be used to align each collimator in the system using a photon beam. The idea is illustrated in Figure 3.4.9. Each end of each collimator is fitted with a tungsten mask that can be flipped into the beam or retracted. Each mask has three holes. The center hole of the upstream mask subtends exactly the same solid angle as the center hole of the downstream mask and is aligned with the center of the collimator. The outer holes are the same area, but the upstream pair is closer to the center than the downstream pair such that only the inner half of each downstream hole overlaps with the outer half of each upstream hole. When the collimator ends are properly aligned the resulting beam pattern at the downstream end of the experiment consists of a central beam spot flanked by a spot on each side having half the area of the central spot. Since the spots are cleanly resolved, this can be determined using only *the total count rate* in each beam. The detector used to monitor the beam does not need very good spatial resolution to detect very small changes in position. Figure 3.4.10 shows a simulated beam profile using masks on the ends of the primary collimator for proper alignment and for a  $50\text{ }\mu$  shift of the upstream end. The shift is easily detected with 20,000 detected photons.

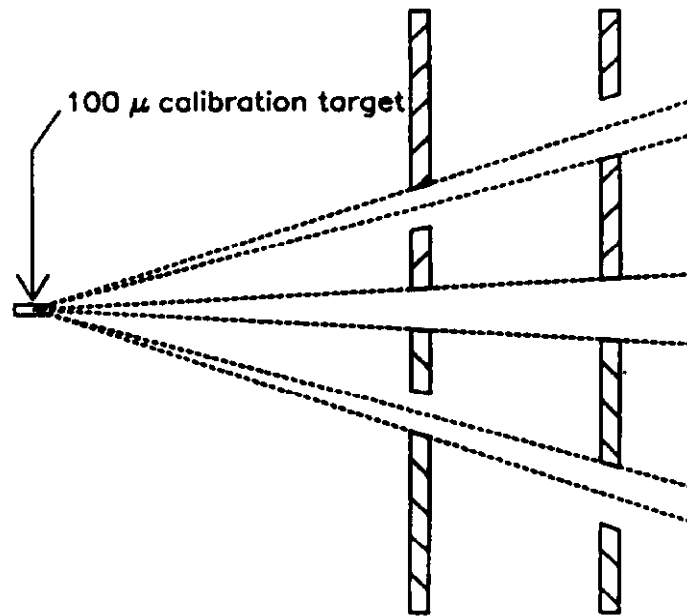


Figure 3.4.9. Illustration of the collimator alignment masks. The relative alignment of the holes is such that very small changes in alignment produce large variations in the count rates in the three beams.

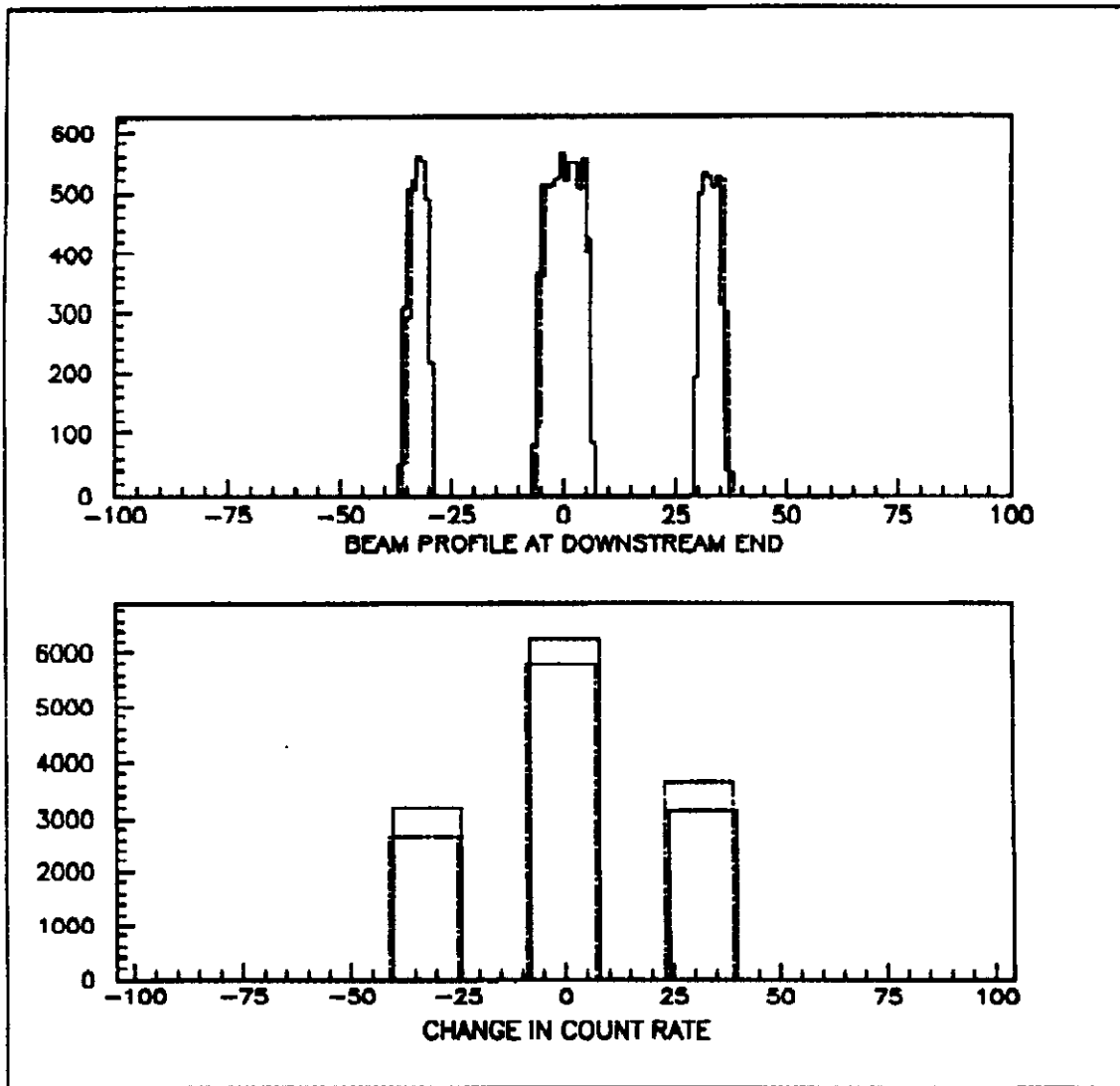


Figure 3.4.10. Simulated photon beam profiles created by the mask system showing the effect of a  $50\ \mu$  misalignment of the upstream end of the primary collimator.

### 3.4.8 Collimator Halo Contributions

The previous sections dealt with collimator design and our primary beam halo concern: particles (particularly neutrons) scattered from filters placed in the neutral beam. The next most significant source, down by roughly an order of magnitude, is neutron interactions in the collimator faces. For an initial exploration of this subject, two collimator and filter configurations have been investigated. A comparison of these two concepts is done with a GEANT simulated neutron beams produced with 900 GeV protons incident on a Be target. Only a single beam was simulated with collimators centered on the beam axis.

The essential difference between the two configurations is whether the downstream collimator (C2) is "beam defining" (BD) as discussed in the previous sections, in which case it intrudes on the direct line of sight to the target, or whether it is farther out transversely than the edges of the neutral beam so that it only removes halo debris ("halo cutting" or HC) generated in the photon filter. In the latter case, the initial primary collimator defines the neutral beam. These two geometries for the simulations are shown schematically in Figures 3.4.11 and 3.4.12.

It is clear that the upstream face of C2 receives a larger flux of beam particles for the BD geometry. It is also the case that elastically scattered neutrons make a larger contribution at C2 because more filter area is seen at the C2 plane than in the HC design. Figure 3.4.13a shows separately the direct neutron beam and that which is scattered in the filter (dashed histogram). The filter length of  $\Delta z = 10$  centimeters is expected to contribute a fraction of approximately  $\exp(-\lambda \Delta z)$  where

$$\frac{1}{\lambda} = \frac{1}{\lambda_T} + \frac{1}{\lambda_I} = \frac{1}{116.2} + \frac{1}{194} = \frac{1}{290} \text{ cm}^2/\text{gm}$$

This gives  $\lambda = 25$  centimeters, so the elastic scatters are expected at a level of about  $1 - e^{-4} \approx 30\%$ , and the Monte Carlo result is of this order. The background that arrives at the CsI is normalized to the number of neutrons that go through the CsI beam hole which are shown in the energy distribution of Figure 3.4.13b. Figure 3.4.13c shows the x-distribution of all background particle hits at the CsI for the BD geometry. The ratio of CsI hits to neutrons through the beam hole is .069, corresponding to one CsI hit for every 30 *rf* buckets at  $5 \times 10^8$  secondary beam neutrons per spill.

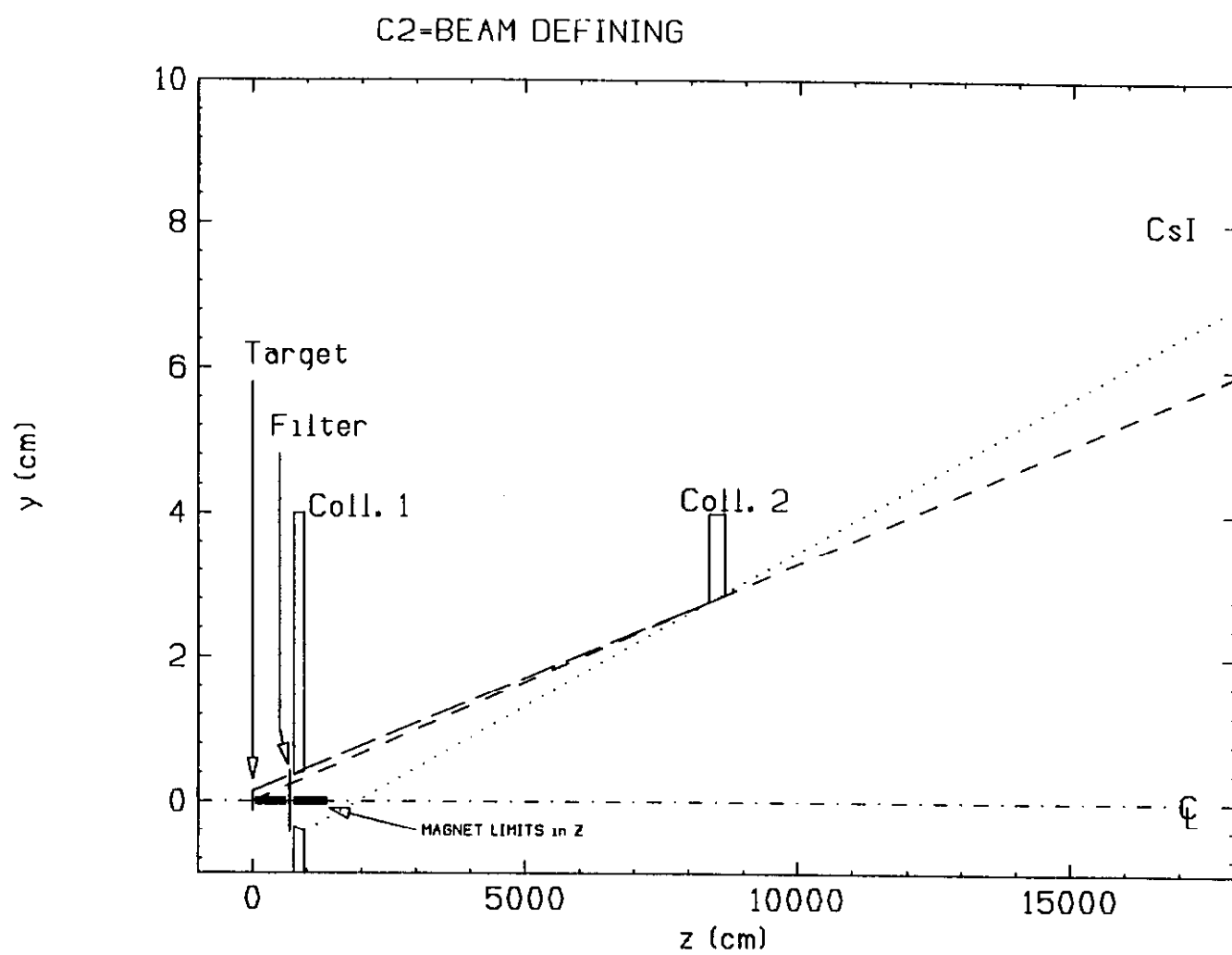


Figure 3.4.11: Elevation view of collimator system for BD geometry simulation.

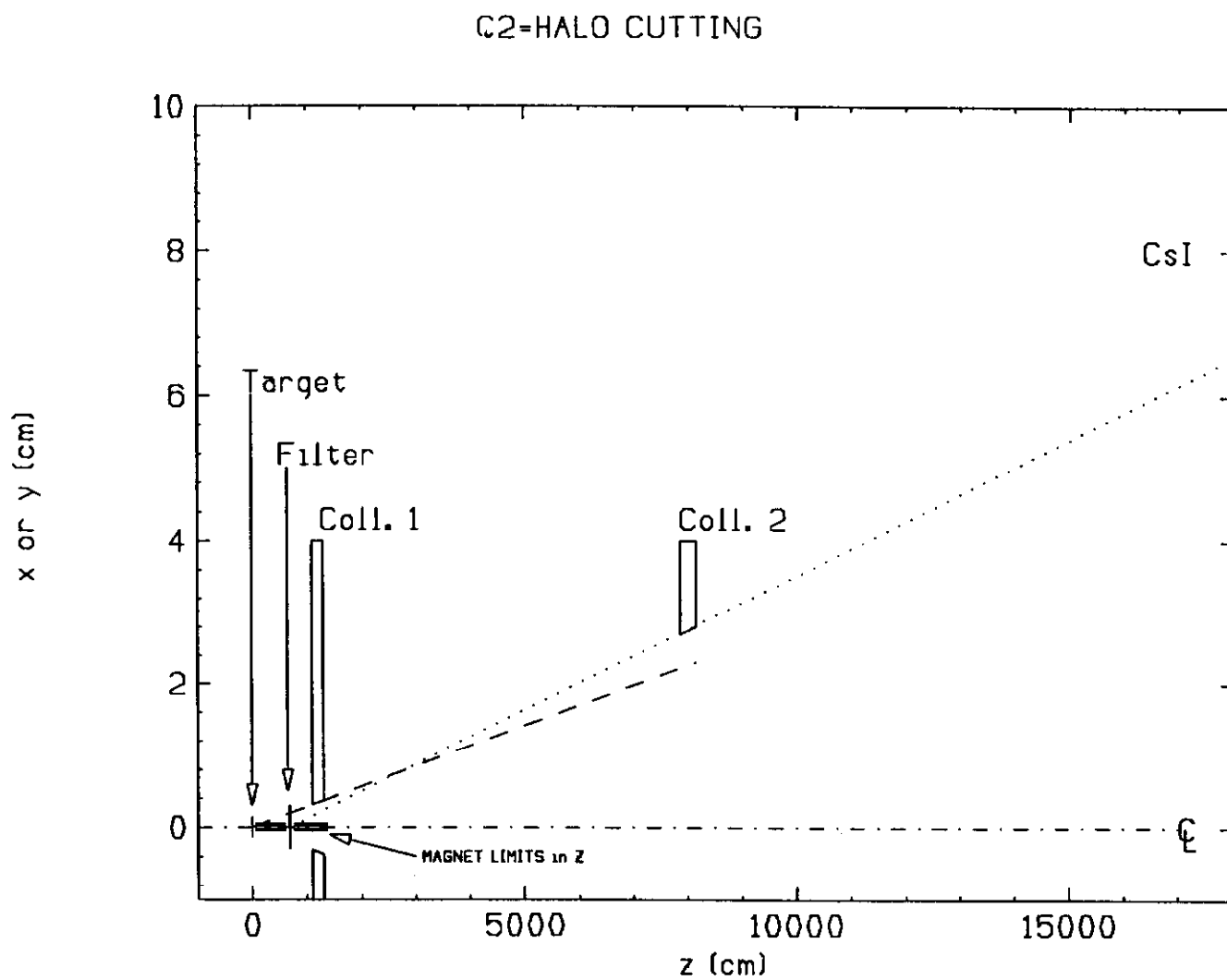


Figure 3.4.12: Elevation view of collimator system for HC geometry simulation.

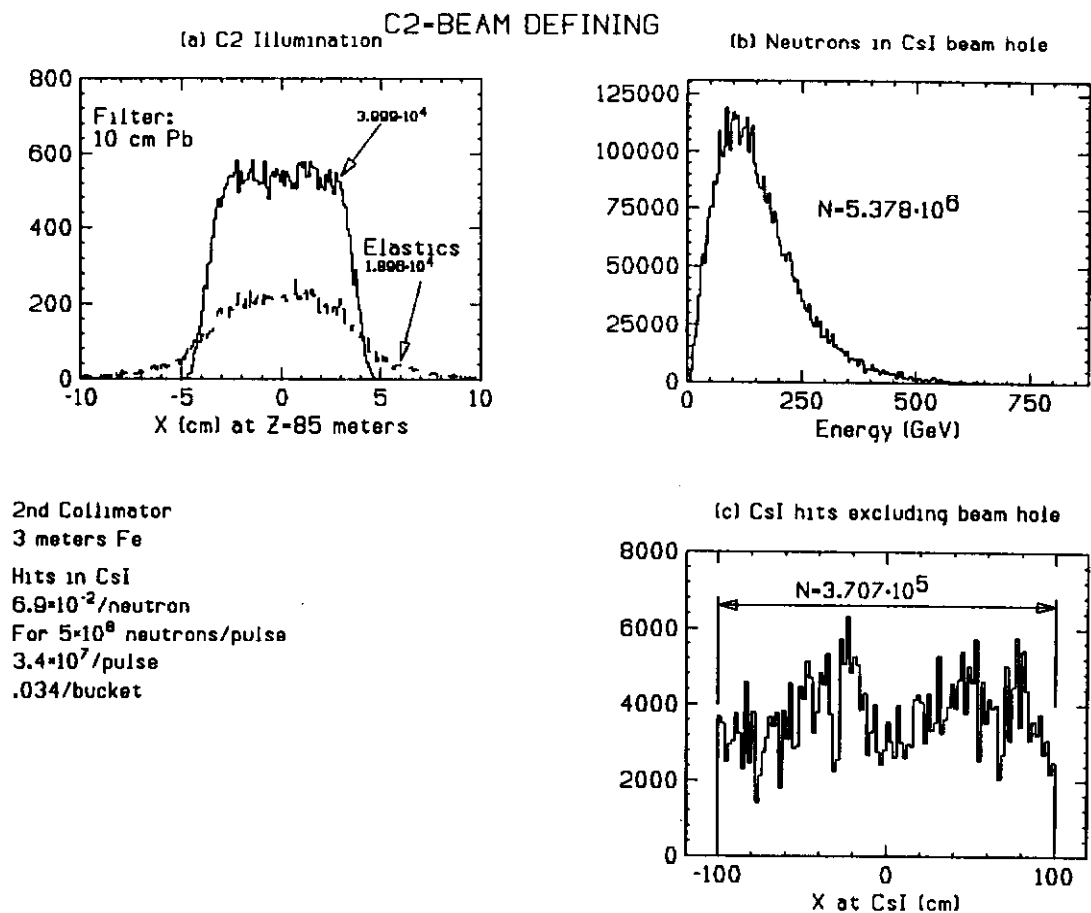


Figure 3.4.13: (a) Neutron illumination at C2; (b) Energy spectrum for neutrons passing through CsI beam hole; (c) Illumination for background particle hits at CsI, all for BD simulation geometry.



Figure 3.4.14 presents the same information for the HC configuration. The smaller C1 aperture produces a narrower beam, and the smaller amount of visible filter volume produces a slightly reduced fraction of elastically scattered neutrons. Here the C2 aperture begins at  $x=2.7$  cm and cuts practically no direct neutrons, but it removes the tail of those scattered in the filter. The resulting noise in the CsI is 0.0016 hits per neutron, down by a factor of 43 from the BD geometry.

Figure 3.4.15a(16a) shows particle identification for the BD(HC) geometry. There is no significant difference. In both cases most of the background is due to photons. The energy distributions for selected particle types are shown in the remaining parts of Figures 3.4.15 and 3.4.16. Event propagation was halted for any particle that fell below 100 MeV kinetic energy, as can be seen in the Figure 3.4.15b and 3.4.16b inserts where the photons are cut for  $E<100$  MeV.

The main point of the HC geometry is to mask the C2 walls from the target, and to some extent from the filter. Most of the CsI background originates in these walls. The main problem with the HC geometry is that alignment and construction tolerances for C1 become unreasonably stringent.

In summary, we have shown that a viable collimator design meeting our basic requirements exists. While the statistical precision of our initial simulations is low in the regions of interest, they still show that further CsI background reduction may well be possible in a final optimized design. It remains at this point to use the insights and tools presented here to carefully examine the trade-offs between construction and alignment tolerances (with their impact on background coming directly from scattering in beam filters), background originating in C2, useful beam intensity, and general muon counting rates.

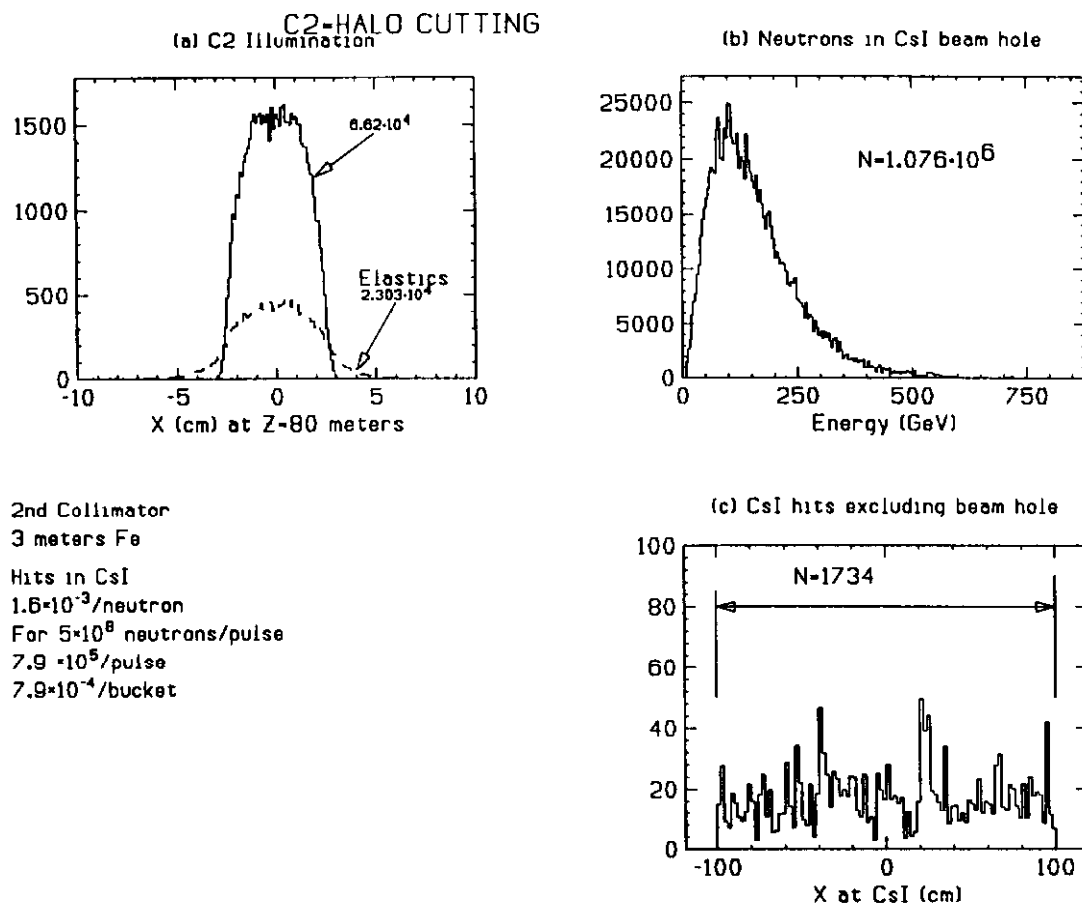


Figure 3.4.14: (a) Neutron illumination at C2; (b) Energy spectrum for neutrons passing through CsI beam hole; (c) Illumination for background particle hits at CsI, all for HC simulation geometry.

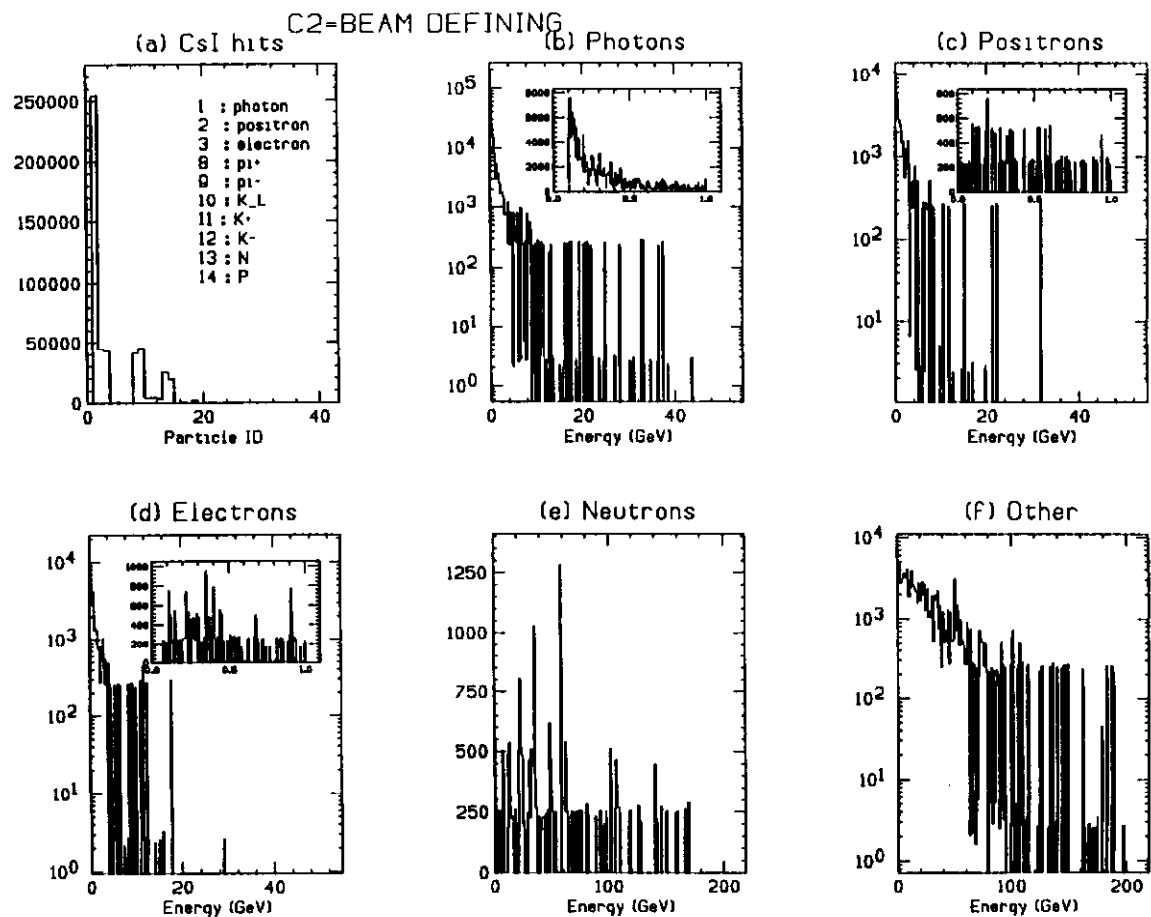


Figure 3.4.15: Particle identification and energy spectra for BD simulation geometry.

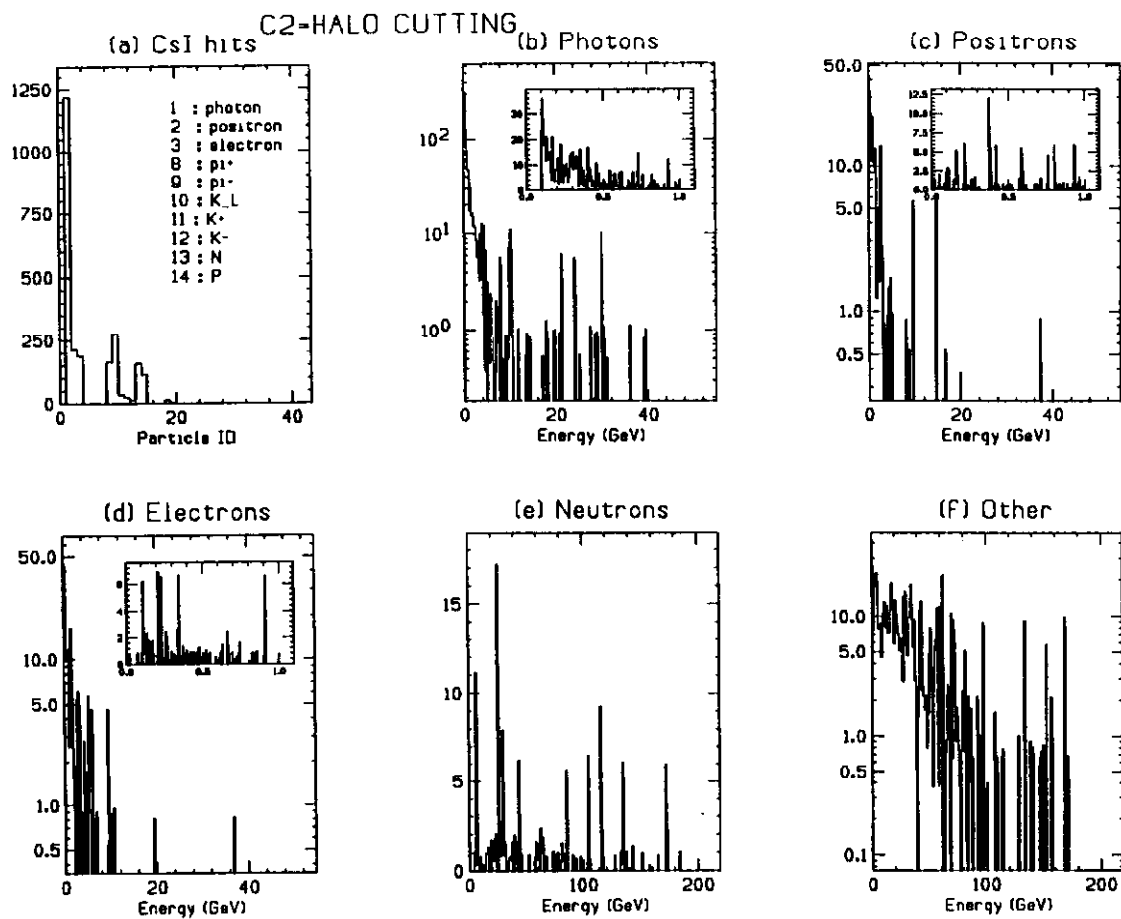


Figure 3.4.16: Particle identification and energy spectra for HC simulation geometry.

### 3.5 Primary Proton Dump

Two magnets follow the target: the so-called Hyperon Magnet and a Dump Magnet. The Hyperon Magnet, with its high magnetic field, sweeps charged particles outside the acceptance of the neutral channel. In addition, it bends the primary protons towards the dump. The Dump Magnet is a conventional "H" dipole shown in Figure 3.5.1. The beam dump is a copper section located within the gap of the upstream 5 feet of the Dump Magnet. The second 5 feet has the same cross-section, except the large hole near the center is replaced by a 2-hole tungsten collimator.

Thermally the 20 feet Dump Magnet is divided into 3 sections. They are (1) the upstream 5 feet which is water-cooled, (2) the second 5 feet which contains the tungsten collimator, and (3) the downstream 10 feet (see Figure 3.5.2). Because the tungsten collimator requires precision alignment, it follows the first section which is water-cooled and which absorbs most of the beam power. In this way, temperature variations which will tend to move the tungsten will be minimized. In addition to water-cooling the copper in the first section, the magnet iron may need a few water paths. The third section does not need as large a gap as the first two because only collimators, not dumps, are located there. It might be advantageous to fill part of it with magnet quality steel to give the largest possible  $\int B dl$  for bending muons produced in the dump away from the detector.

CASIM was used to evaluate local energy deposition as well as total power dissipation for each dump section. Figure 3.5.2 shows the thermal loads in each region for  $1 \times 10^{13}$  protons at 900 GeV every 60 seconds.

Even if the beam is focused on the beam dump with the same spot size as the target ( $\sigma \cong 0.25$  mm), the stresses and temperatures in the copper are acceptable for slow spill. Some means will have to be implemented to ensure that the fast (millisecond) spill will not be taken on the dump. The temperature rise during a single fast accident pulse is well above the melting point of copper.

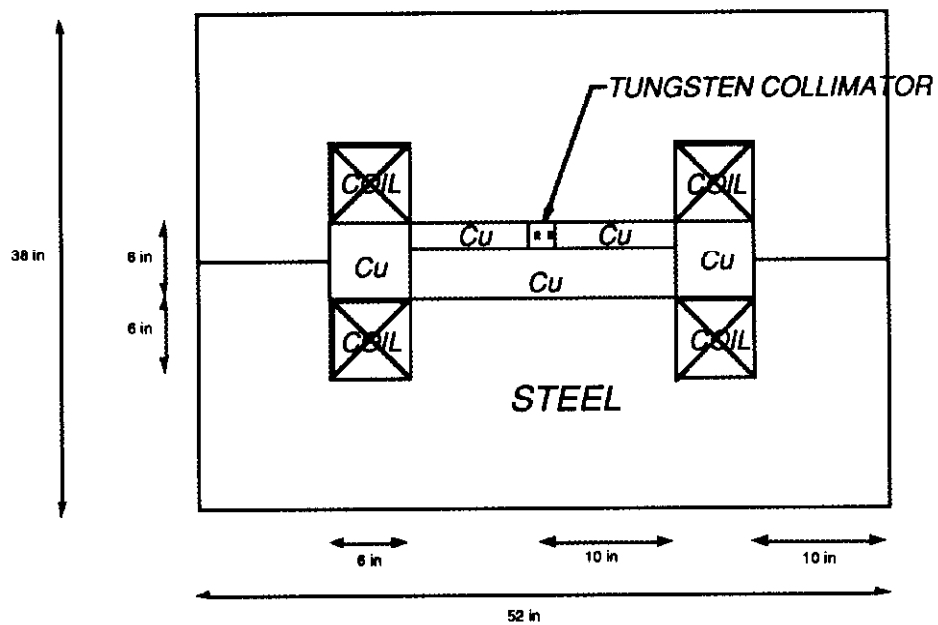


Figure 3.5.1: Schematic drawing of the KTeV primary proton beam Dump Magnet.

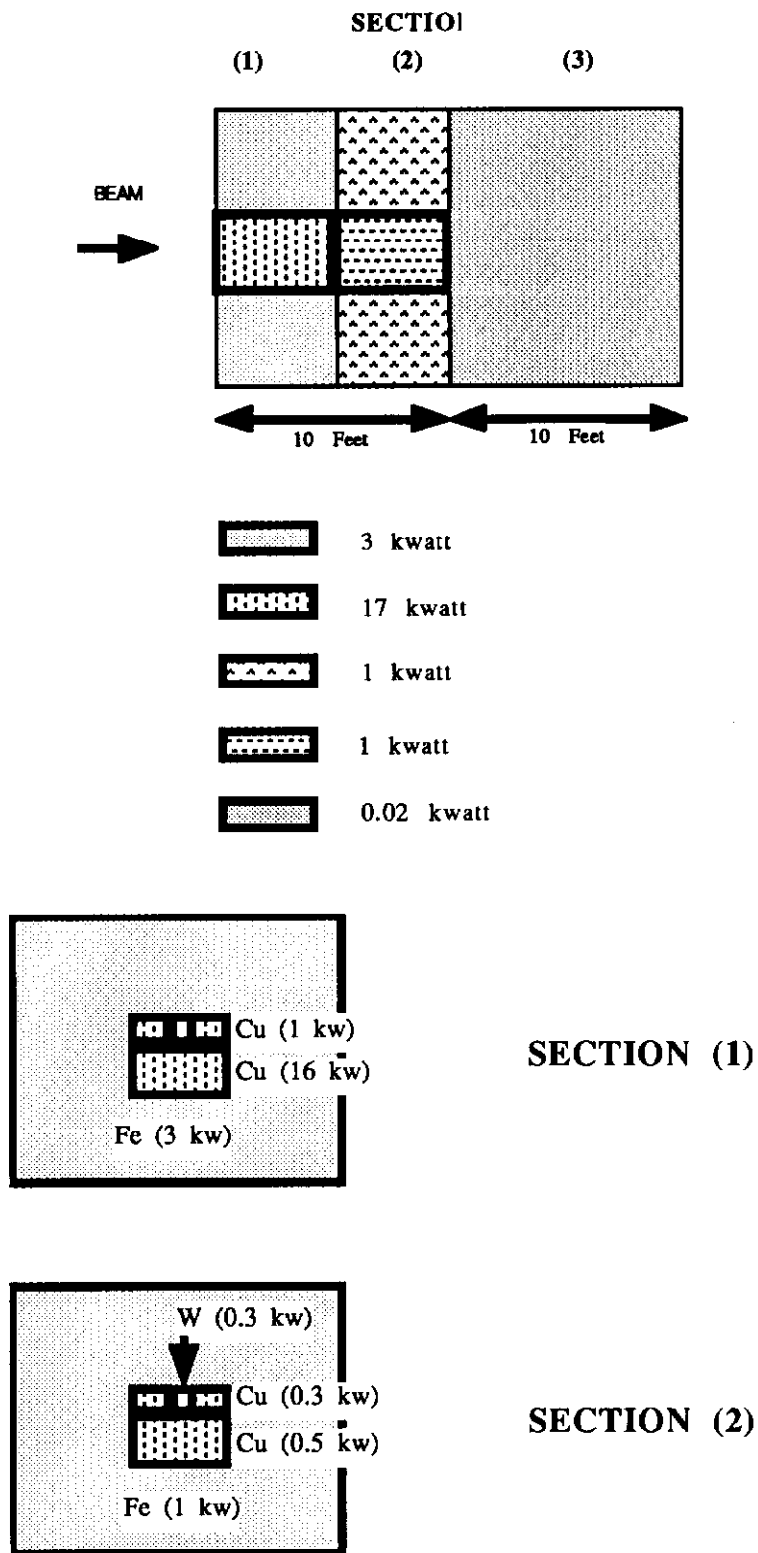


Figure 3.5.2: Thermal loads in various portions of the KTeV primary proton beam dump.

## 3.6 Muon Flux Simulations

Operation of the KTeV program with a primary intensity of  $5 \times 10^{12}$  protons on target will require substantial care to protect the experimental apparatus and counting room areas from the intense muon fluxes generated. Muons dominated the singles rate for the experiments conducted in MCenter, exceeding 1MHz for  $10^{12}$  incident protons in E731. Additionally, muon rates in both counting rooms and external areas near MCenter would preclude the beam intensity requirements for KTeV.

The design study currently in progress has the goal of reducing detector muon rates for KTeV to less than 100 kHz for  $5 \times 10^{12}$  incident protons per spill. Additionally, use is made of below-grade shielding available in a new experimental area to provide personnel protection from the intense muon fluxes. A key design feature is the addition of a magnetized beam dump system.

This section describes the status of efforts to calculate the KTeV muon flux using the program CASIMU. Anticipating the need to perform several design iterations on the target hall, magnets, and experimental site, new software tools have been developed which will allow us to easily vary magnet designs and incorporate these magnet modifications into the simulation geometry. In addition, Quality Assurance code has been developed to validate the geometry simulation routines. Work is in progress to connect the CASIMU geometry simulations to terrain map data. This, when complete, will facilitate studies of muon fluxes at ground level and at the site boundary. An immediate objective of the effort has been to simulate in detail one specific, realistic KTeV target hall layout and obtain initial muon flux profiles.

### 3.6.1 Simulation Layout

The geometry of the target/beam-dump/muon-sweeping system considered is shown in plan view in Figure 3.6.1. The primary proton beam is targeted downward at 4.2 mrad. The target sweeping magnet bends the primary beam and positive secondaries further down. Negative secondary particles are pitched upward. We have taken the target sweeping magnet to be the currently unused E8 hyperon magnet with a tapered pole tip



insert to concentrate the field near the central axis. With this modification, a field in excess of 30 kGauss can be attained over a one inch gap. The primary beam is transported through a channel in the target sweeping magnet and dumped 25 feet downstream from the target in a water-cooled copper beam dump insert located in the beam dump magnet. This geometry enables the beam dump to be considerably separated from the neutral kaon channel, providing a significant reduction in background.

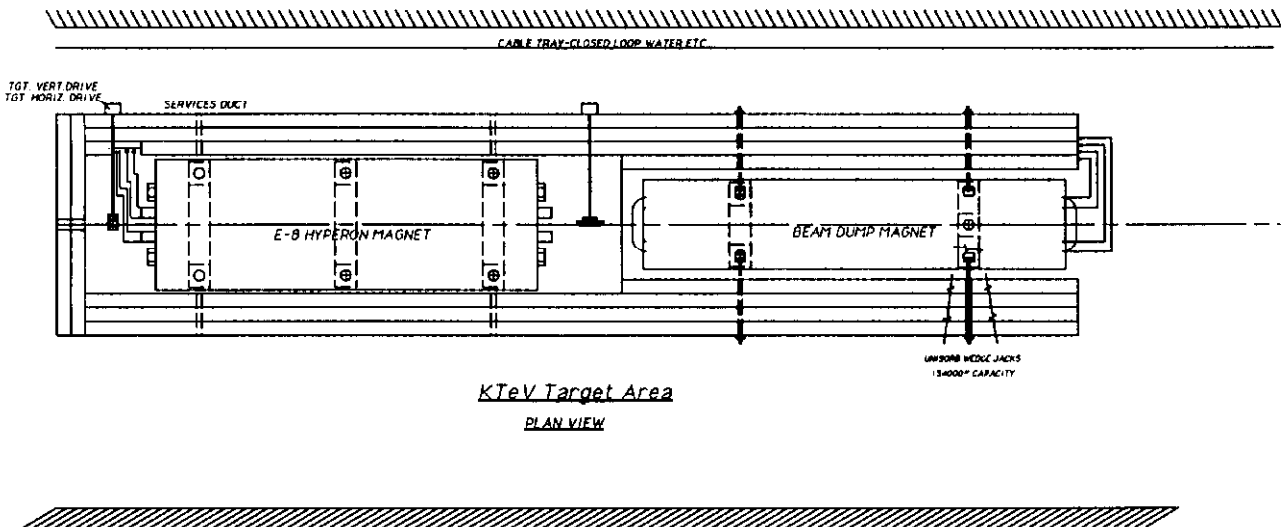


Figure 3.6.1: Plan view target hall layout showing the target sweeping and beam dump magnets.

Combining the effects of the targeting angle and the target sweeping magnet, the unused primary protons are aimed 10 mrad downward when they strike the beam dump. The beam dump magnet bends horizontally, and sweeps positives to the east. Perpendicular arrangement of the two magnets is necessary because of the separation between the target and the beam dump. Primary protons that fail to interact in the target are bent significantly downward before they hit the beam dump. If the beam dump magnet had the same orientation, then negative secondaries produced at that point would be deflected back upward. For negative secondaries produced in the beam dump, the action of the

target and beam dump magnets would then tend to cancel, resulting in a muon lobe aimed at the apparatus. By orienting the magnets perpendicular to each other, the net  $P_{\perp}$  of the system is somewhat less, but the bending is always away from the apparatus. Approximately, if  $\vartheta_1$  is the deflection produced by the target sweeping magnet, and  $\vartheta_2$  the deflection produced by the beam dump magnet, then in a parallel magnet orientation the deflections of positive and negative muons are given by

$$\vartheta^+ = \vartheta_1 + \vartheta_2$$

$$\vartheta^- = \vartheta_1 - \vartheta_2$$

where, in the perpendicular orientation,

$$\vartheta^+ = \vartheta^- = \sqrt{(\vartheta_1)^2 + (\vartheta_2)^2}.$$

The perpendicular magnet arrangement produces three primary muon lobes.

- *Below grade, east:* positive muons produced in the target or in the beam dump are swept down and to the east.
- *Below grade, west:* negative muons produced in the beam dump are swept down and to the west.
- *Above grade, west:* negative muons produced in the target are swept up and to the west.

The fourth quadrant, above grade and east, has no direct muon lobe. This is the appropriate location for the counting rooms. The beam dump magnet is considered to be a new magnet which will be designed explicitly for this application.

The target sweeping magnet modeled, the E8 hyperon magnet, is larger in cross section than would be necessary for this application. However, several motivating factors encourage the use of this magnet.

- 1) *Shielding.* A design input requirement is that the target and beam dump areas must be surrounded by five feet of steel for environmental shielding. By using the E8 magnet, the bulk of the required shielding is provided.

will be dumped directly into the magnet coils leading to the concern of a radiation damage problem. Using a large magnet like the E8, there is enough shielding between the center-line and the coil to absorb the bulk of the radiation in passive material.

3) *Availability.* The iron yoke of the E8 hyperon magnet is currently being used as muon shielding upstream from the MCenter portacamps. Its coils are in storage in the meson detector building. The magnet should be available for KTeV use.

### 3.6.2 CASIMU Muon Flux Simulation and Code Validation

A significant development process has been underway to enable a detailed and accurate simulation of muon fluxes using the program CASIMU<sup>3</sup>.

Benchmarking of the program CASIMU for muon simulations was carried out during the KAMI Conceptual Design<sup>4</sup> using results from the E613 beam dump experiment.

POISSON<sup>5</sup> two dimensional field calculations for the magnets utilized were performed to provide detailed field maps for the particle tracking in CASIMU.

Development of new code to efficiently incorporate these POISSON magnet maps into the CASIMU simulations in a flexible way has been carried out.

To provide additional validation for the CASIMU simulation, including accurate input of material boundaries, programs have been developed for KTeV that generate a comparison between the output of the CASIMU geometry routine and accurate line drawings of the simulated apparatus.

---

<sup>3</sup> CASIMU is a modified version of the hadronic cascade program CASIM; see A. Van Ginneken, Fermilab Report FN-272 (1975).

<sup>4</sup>K. Arisaka, *et al.*, *Conceptual Design Report: Kaons at the Main Injector*, Fermilab Report FN-568 (June, 1991).

<sup>5</sup>R. F. Holsinger and C. Iselin, CERN Program Memo PM-0054.

Histograms of magnet fields as a function of location can be displayed with a routine which generates magnetic field histograms superimposed on scale drawings of the actual magnets. Coincidence of the field features with features in the magnet verifies the accuracy of the input simulation code.

Finally, still under development is a terrain map subroutine which will interface these geometry simulations to site survey data about the ground surface. This will enable realistic and accurate modeling of the impact of a particular site geometry on residual muon fluxes.

Figures 3.6.2 thru 3.6.4 illustrate some outputs of the code validation process. Figure 3.6.2 shows a POISSON field map for the E8 hyperon magnet. X and Y components of the field along the Y axis of the magnet are displayed in Figure 3.6.3. Similarly, Figure 3.6.4 shows the transverse components of the field along the X axis of the beam dump magnet.

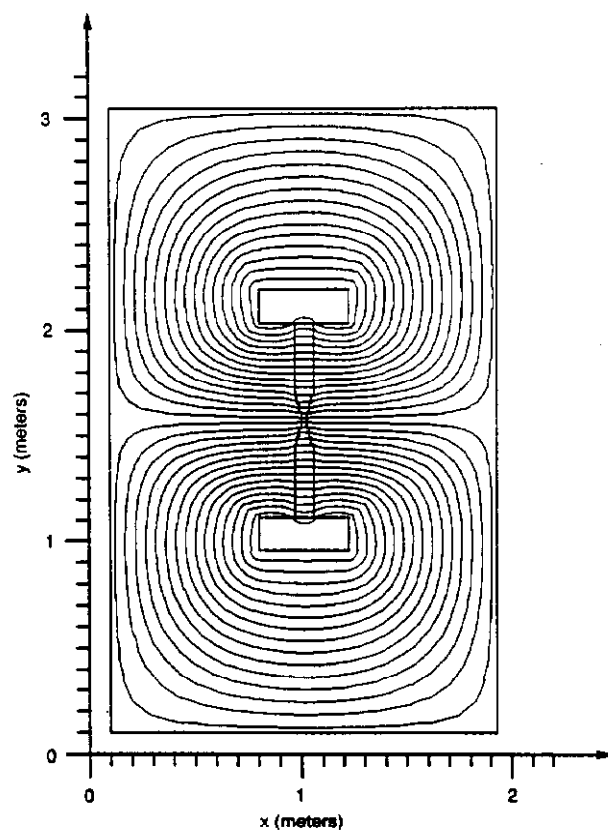


Figure 3.6.2: POISSON field map for the E8 hyperon magnet.

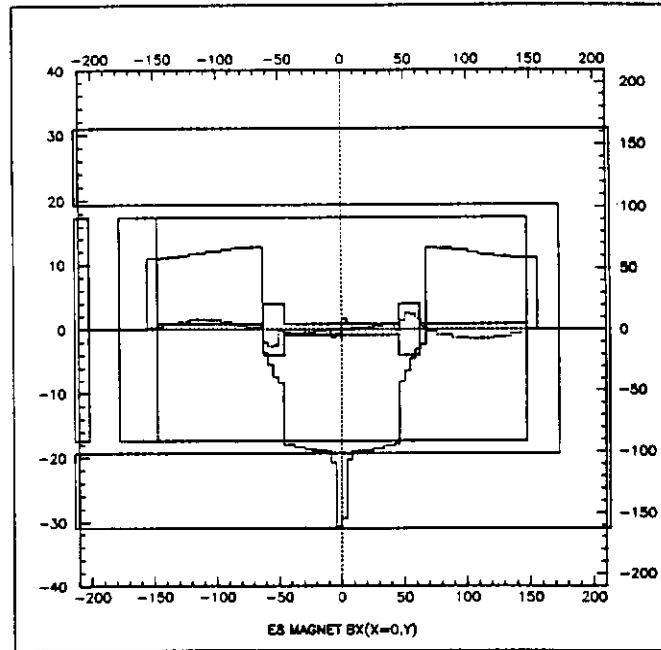


Figure 3.6.3: X and Y field components along the Y axis of the E8 hyperon magnet.

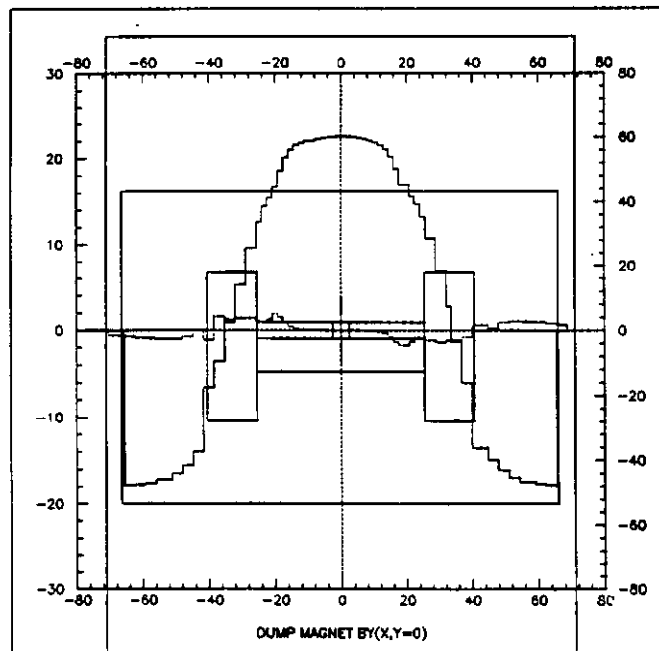


Figure 3.6.4: X and Y field components along the X axis of the modeled beam dump magnet.

### 3.6.3 Preliminary Simulation Results

Shown in Figure 3.6.5 is a plot of the transverse distribution of muons predicted at the Z location of the CsI electromagnetic calorimeter with the active beam dump as described. Superimposed on the plot is a cross section outline of the detector region and a projected experimental hall and detector region. The perspective is along the beamline, looking upstream. [For this projection, the NMuon hall was used.]

Several aspects of the basic design look very good in that the apparatus region and counting room areas are largely free of muons. Additionally, the bulk of the muon flux remains below grade, and will not pose a shielding concern. The major remaining concern with this design is the above grade lobe of negative muons [from interactions in the target] to the west of the detector.

More detailed simulations are ongoing to quantitatively understand the flux normalizations in each muon lobe, as well as possible design variations which could maintain the solid muon rejection at the detector while providing better control of the negative target associated lobe.

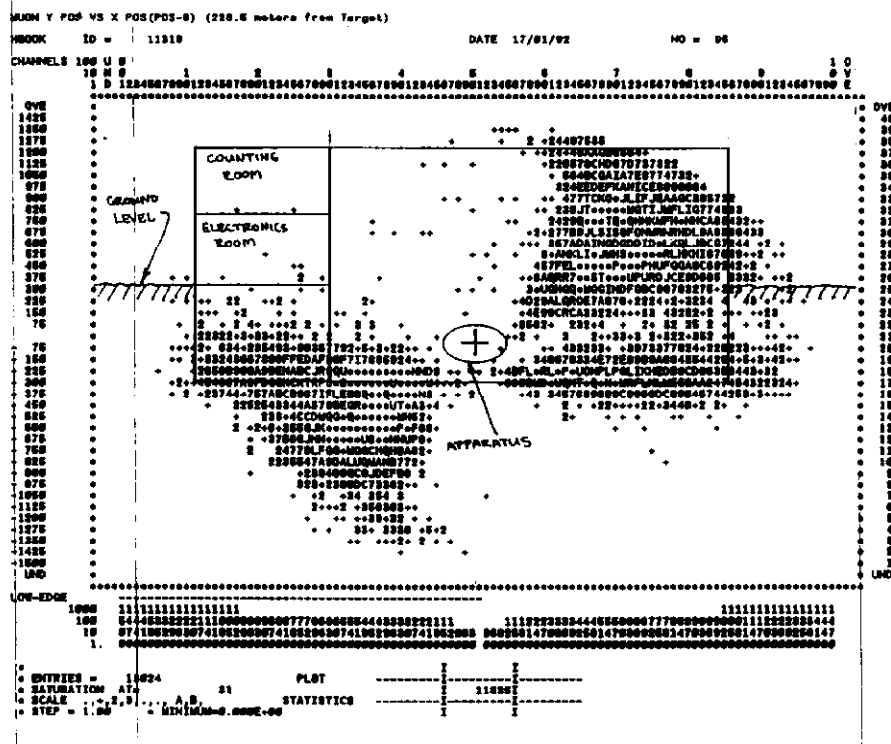


Figure 3.6.5: Projected X-Y distribution of muon hits at the Z location of the CsI array.

## **4. TECHNICAL DESIGN of the DETECTORS**

In this section, we will give the detector configuration and detailed specifications of the detector that will address the physics for the KTeV experiments E799II and P832. At this stage, some first order engineering designs on various detector elements will be presented for the purpose of cost estimate. The cost estimates, manpower and timeline of various detector elements will be summarized in Section 5 of this Design Report.

The detector consists of tracking chambers, analyzing magnet, CsI electromagnetic calorimetry, nearly hermetic photon veto systems, particle identification (TRDs for electrons, hadron veto and muon shielding and counters for muons), a trigger system of several levels, front end electronics, and finally a data acquisition system and 3rd level filter. We also address the estimated offline computing needs at the end of this section.

The spectrometer detectors will be discussed in the following order (roughly following the "beam order", from upstream to downstream):

- Vacuum Decay Regions and Photon Vetoes
- Active Regenerator, Active Mask and Absorber Mover (P832)
- Chambers
- KTeV Spectrometer Magnet
- Transition Radiation Detectors
- CsI Electromagnetic Calorimeter
- CsI Crystals Test Results
- Beam Hole Vetoes
- Trigger Hodoscope, Hadron Veto and Muon System
- Trigger and Electronics
- Data Acquisition and 3rd Level Filter
- Offline Computing

New equipment to be added for the KTeV running period from '94 to '95 will be emphasized in this section, especially for the new CsI electromagnetic calorimeter which is described in section 4.7. Test results from a CsI test array and a radiation damage study of CsI crystals in a hadron beam are also included in section 4.8.

## 4.1 KTeV Detector Configuration and Acceptance

The detector configuration and layout has been shown in Fig. 2.2.1 and Fig. 2.2.2 in the spectrometer overview section 2.2. A list of the KTeV detector elements and proposed geometry is in Table 4.1.1.

Table 4.1.1: KTeV (E799II/P832) Detector Configuration

Detector Element	z from Target	Transverse Dimensions (x × y)
Start of Decay Region	99.212 m	Vacuum pipe i.d.= 1.5 m
Photon Veto RC1	104.212 m	inner x&y = ± 28 cm, o.d.=1.5 m
RC2	109.212 m	inner x&y = ± 28 cm, o.d.=1.5 m
RC3	115.212 m	inner x&y = ± 28 cm, o.d.=1.5 m
RC4	121.212 m	inner x&y = ± 28 cm, o.d.=1.5 m
Mask Anti (P832)	122.212 m	x & y = ± 33 cm with two beam holes 9 cm × 9 cm each
Regenerator (P832)	123.212-125.212 m	10 cm × 10 cm (beam size 8 cm × 8 cm)
Photon Veto RC5	127.212 m	inner x&y = ± 42 cm, o.d.=2.0 m
RC6	133.212 m	inner x&y = ± 42 cm, o.d.=2.0 m
RC7	139.212 m	inner x&y = ± 42 cm, o.d.=2.0 m
Photon Veto RC8	145.212 m	inner x&y = ± 59 cm, o.d.=2.4 m
RC9	151.212 m	inner x&y = ± 59 cm, o.d.=2.4 m
RC10	157.212 m	inner x&y = ± 59 cm, o.d.=2.4 m
Vacuum Window	159.212 m	o.d.= 1.8 m
Drift Chamber C1	159.712 m	1.251 m × 1.251 m
Photon Veto RC11	165.712 m	inner x= ± 80 cm, outer x= ± 1.4 m inner y= ± 70 cm, outer y= ± 1.4 m
Drift Chamber C2	166.212 m	1.607 m × 1.403 m
Analyzing Magnet	171.212 m	Gap 2.4 m
Photon Veto RC12	175.712 m	inner x= ± 85 cm, outer x= ± 1.4 m inner y= ± 80 cm, outer y= ± 1.4 m



Drift Chamber C3	176.212 m	1.708 m $\times$ 1.607 m
Drift Chamber C4	182.212 m	1.759 m $\times$ 1.759 m
TRDs	183.212 m	2.0 m $\times$ 2.0 m
Trigger Hodoscope	184.212 m	2.0 m $\times$ 2.0 m
Photon Veto RC13	185.212 m	inner x= $\pm$ 98 cm, outer x= $\pm$ 1.4 m inner y= $\pm$ 98 cm, outer y= $\pm$ 1.4 m
Collar Anti (P832)	185.412 m	2.5 cm around each beam hole
CsI Calorimeter	185.712 m	2.0 m $\times$ 2.0 m with two beam holes each 15 cm $\times$ 15 cm in size and separated by 30 cm center-to-center
Hadron Veto	190.212 m	2.4 m $\times$ 2.2 m
Back Anti	193.212 m	60 cm $\times$ 24 cm
Muon Filter	193.712-196.712 m	3.4 m $\times$ 2.5 m
Muon Veto	196.8 m	3.4 m $\times$ 2.5 m
Muon Filter	197.212-198.212 m	3.4 m $\times$ 2.5 m
Muon Counter	198.3 m	3.4 m $\times$ 2.5 m

The geometric acceptance in P832 for the  $\epsilon'/\epsilon$  measurement has been studied based on the above detector geometry. The acceptances versus decay vertex  $z$  for  $K_L \rightarrow \pi^+\pi^-$  and  $\pi^0\pi^0$  are shown in Fig. 4.1.1 and Fig. 4.1.2 in the kaon momentum range 40 to 160 GeV/c for a 40 m decay region.

The geometric acceptance for four-body decay, such as  $K_L \rightarrow \pi^0 e^+ e^-$ , in E799II with a 60 m decay region and 20 to 220 GeV/c kaon momentum range is shown in Fig. 4.1.3.

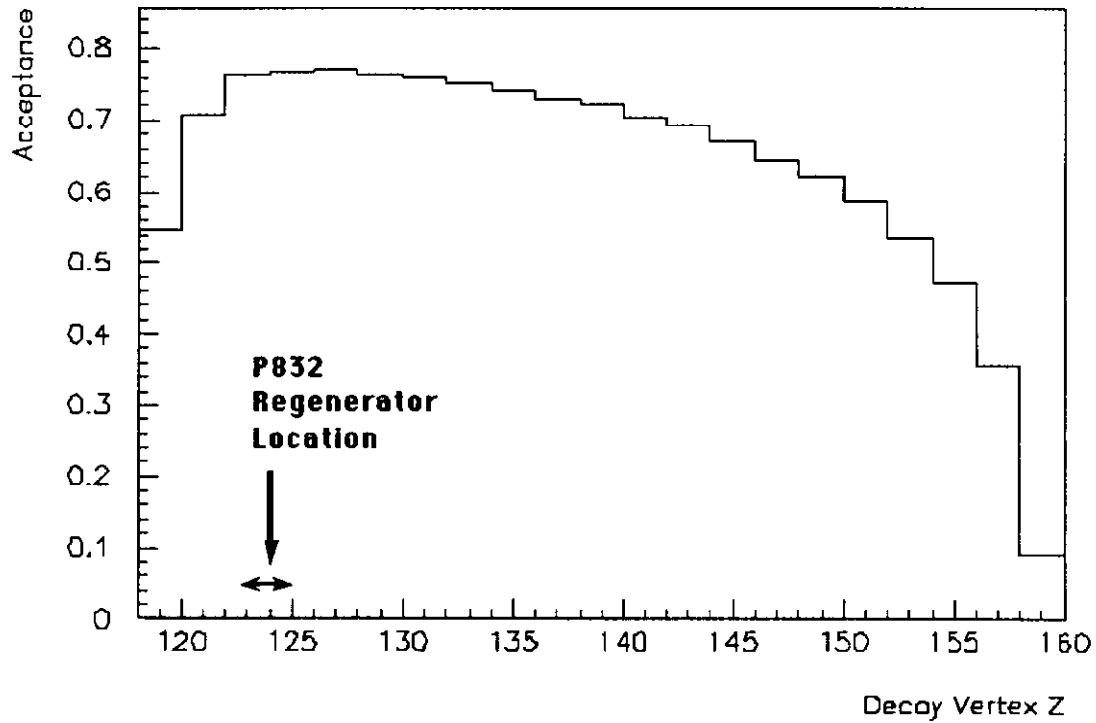


Fig. 4.1.1: Acceptance versus decay vertex for  $K_L \rightarrow \pi^+\pi^-$  in the kaon momentum range 40 to 160 GeV/c and in a 40 m decay region for P832.

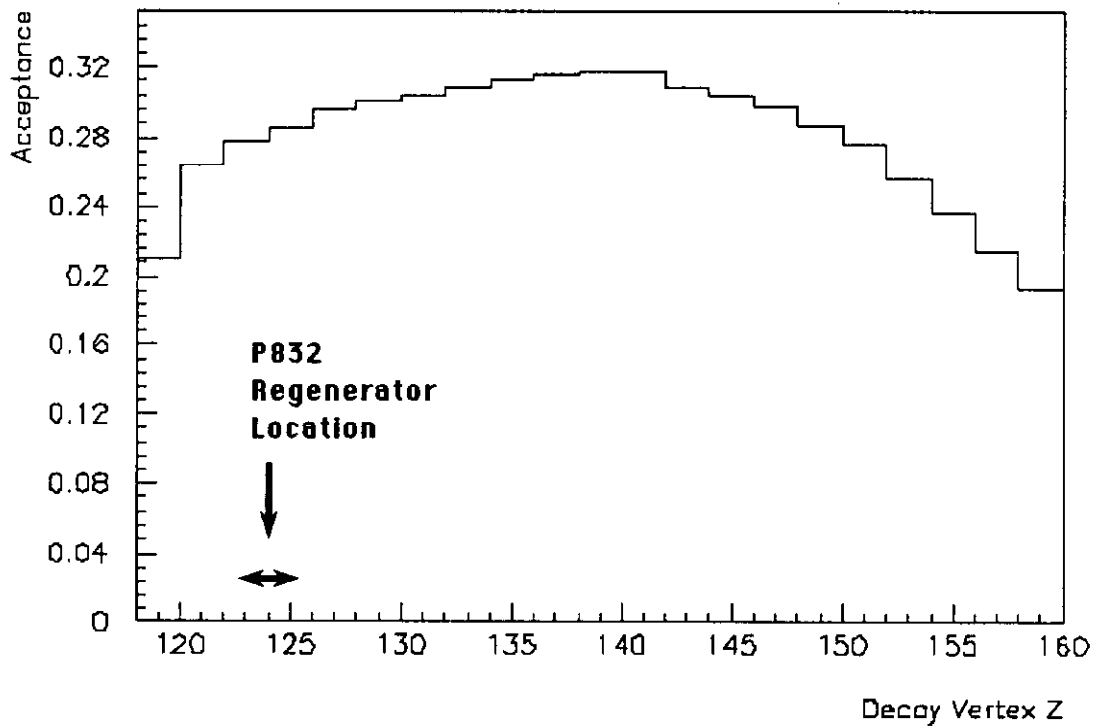


Fig. 4.1.2 : Acceptance versus decay vertex for  $K_L \rightarrow \pi^0\pi^0$  in the kaon momentum range 40 to 160 GeV/c and in a 40 m decay region for P832.

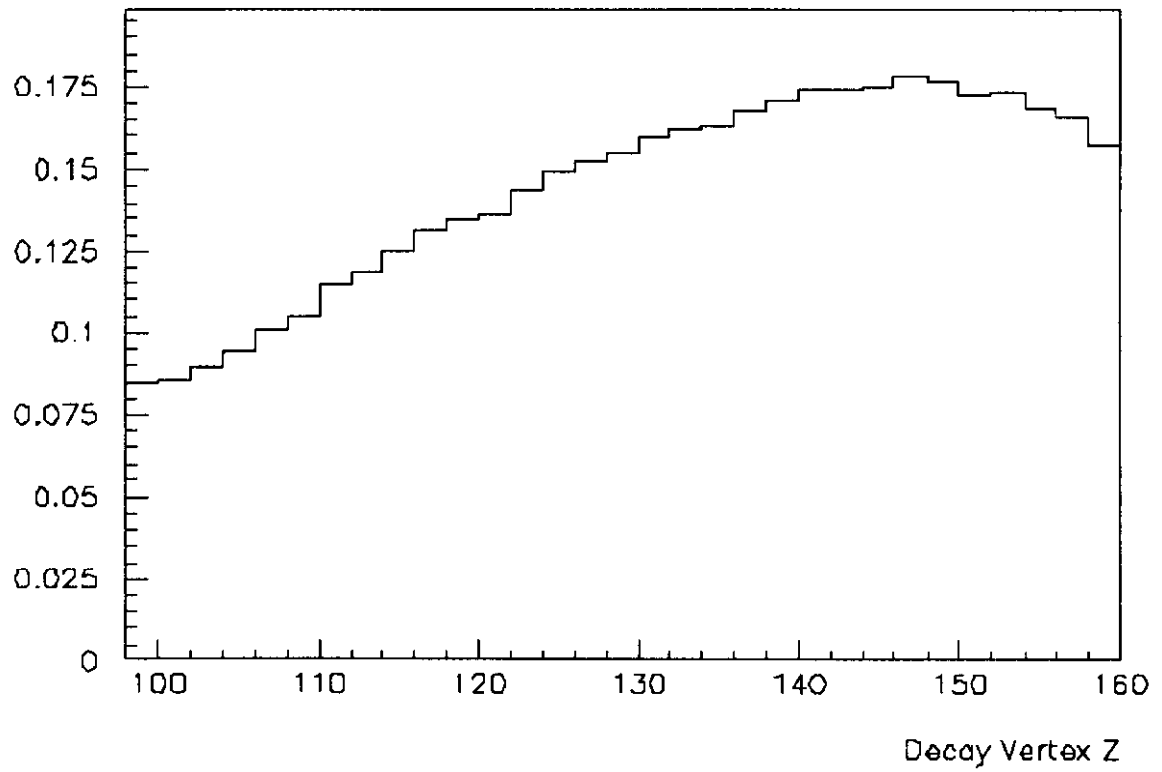


Fig. 4.1.3: Acceptance versus decay vertex for  $K_L \rightarrow \pi^0 e^+ e^-$  in the kaon momentum range 20 to 220 GeV/c and in a 60 m decay region for E799II.

## 4.2 Vacuum Decay Region and Photon Vetoes

The vacuum decay region begins 99.2 m from the target and ends 60 m later at the large vacuum window at  $z=159.2$  m. In this decay region approximately 3% of the  $K_L$  decays which can be reconstructed by the downstream detector to measure the decay particles, momenta and vertex. Photon veto ring counters will be spaced out inside the vacuum decay region and in the downstream detector region to reject wide angle low energy photons escaping the downstream electromagnetic calorimeter. A regenerator box which houses the regenerator and its mover in vacuum for P832 will be inserted between vacuum tanks at  $z=124$  m. In this section we will discuss the requirements for the vacuum system and photon vetoes as well as the design considerations. The regenerator will be discussed in section 4.3 of this report.

### 4.2.1 Vacuum System

In order to minimize backgrounds due to interactions of the neutral beam with residual material, the decay region, and as much of the neutral beam transport line as possible, should be evacuated. As discussed in the physics sections above, the vacuum should be  $\leq 10^{-4}$ .

This vacuum can be achieved by building a steel vacuum tank similar to that used in the previous kaon experiments that were carried out in MCenter. The vacuum tank must be constructed in sections in order to insert various pieces of experimental apparatus - viz, the photon veto ring counters, the regenerator, and the lead mask anti ( see the specific sections that discuss each of these subsystems ). A unified support system for all of these devices is also planned. Fig. 4.2.1 shows the overall view of the engineering design of the vacuum tank system.

The pumps for the vacuum system exist. That system consists of two 18,000 liter/sec diffusion pumps with backup blower and roughing pumps. One additional right angle valve must be purchased so that the two pumping systems can run independently (thus allowing for maintenance/dealing with difficulties ). It is a standard device readily available.

A preliminary cost for the vacuum tank was estimated at about \$250 k. Since then, it has been decided to support the vacuum vetoes from the vacuum pipes. This will require some additional material. Using thicker material should escalate the cost only to about \$300 k. Other costs are included in the tables in section 5. The total cost to build the vacuum system is estimated to be \$475 k including windows.

### **Vacuum Window Design**

There will be a 1.8 meter diameter vacuum window at the downstream end of the decay region. The present requirements for a vacuum window are that it is larger than the solid angle created by the kaon decay space and that the interaction length is minimized. Fermilab already has good experience in this design and has successfully used a 1.8 m and a 1.2 m window for E617 and E731, respectively. The E731 1.2 m window uses a Kevlar/Mylar sandwich. Kevlar was chosen because it provides the greatest tensile strength to density ratio while providing minimal elongation. This provides an interaction length of 0.2% using Kevlar 29 Type 964 1500 Denier with a  $2 \times 2$  basket weave and 5 mils of Mylar.

The KTeV window design will be 1.8 m in diameter and use aluminized Mylar to reduce the water vapor permeation rate. A finite element method (ANSYS) analysis has been done on this 1.8 m vacuum window design. It shows that at this window diameter a safety factor of two can be maintained. The window and flange have been designed by the Fermilab Research Division. The fabric clamping method is well understood. Soft aluminum round wire is clamped into an O-ring groove to prevent slippage. A safety review is in progress. In order to confirm the safety of the design, a test fixture will be constructed to test the windows. Three windows will be assembled and tested to destruction. Measurements will be made to confirm the distortion of the window under vacuum.

The upstream vacuum window is small and is a standard 'off the shelf' item. No special tests are planned.

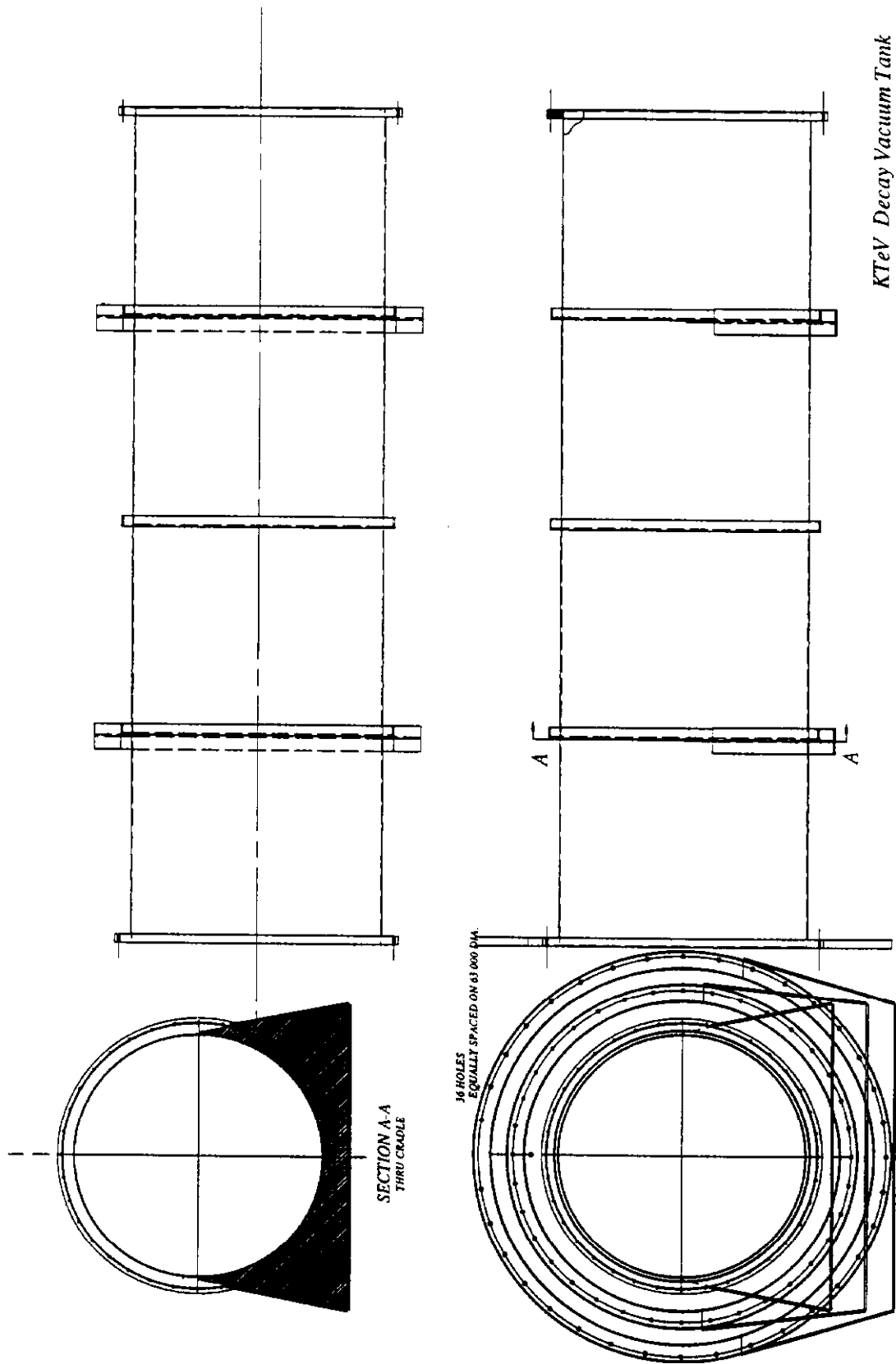


Fig. 4.2.1: Overall engineering design of the KTeV vacuum tanks.

## 4.2.2 Photon Vetoes

As shown in Fig. 2.2.1 ring veto counters (RC1-RC13) will be spaced evenly in  $z$  around the neutral beam. These counters will be used both on-line in the trigger and offline in analysis to reduce backgrounds which can be  $\sim 10^3$  to  $\sim 10^8$  times larger than the expected signal. In P832 ( $\epsilon'/\epsilon$ ) a major background to the  $K_L \rightarrow 2\pi^0$  decays are  $K_L \rightarrow 3\pi^0$  decays in which two of the photons are lost. The improved hermeticity of the photon veto ring counter system in P832 over E731 should increase the rejection of  $K_L \rightarrow 3\pi^0$  decays from a factor of 130 to a factor of 1000. Combined with an improvement in mass resolution, the systematic uncertainty in  $\epsilon'/\epsilon$  should be  $\sim 10^{-5}$ . See section 2.3.

The photon veto is also necessary in certain rare decay modes, for example,  $K_L \rightarrow \pi^0 \nu \bar{\nu}$ . The standard model prediction for  $K_L \rightarrow \pi^0 \nu \bar{\nu}$  is of the order  $10^{-11}$  and would only be attainable in E799 if the  $\pi^0 \rightarrow 2\gamma$  decays were used. Rejection of background  $K_L \rightarrow 2\pi^0 \rightarrow 4\gamma$  would require truly hermetic coverage at a level of  $10^{-8}$  which is beyond what we propose. We are constrained to use the Dalitz mode for the signal,  $K_L \rightarrow \nu \bar{\nu} \pi^0$ ,  $\pi^0 \rightarrow \gamma e^+ e^-$  which costs a factor of 80 in sensitivity. The projected running time will not permit us to approach the prediction. The experimental goal is to reduce all instrumental limits well below the sensitivity limit. Less rare modes like  $K_L \rightarrow \pi^0 \gamma \gamma$  will also have backgrounds from  $3\pi^0$ .

The structure of the photon veto will be roughly doughnut shaped in 13 modules, of which 10 are inside the vacuum (RC1 – RC10). Simulation of the background events mentioned above has shown that complete coverage of the decay volume is not required, rather hermeticity for a kaon decay angular region of  $\theta < 80$  milliradians will either reduce the background below  $10^{-4}$  or else force it into a kinematically unfavored region where an easy energy cut will remove it. The photon lower energy limit for which this must be achieved is approximately 250 MeV.

For the first 10 ring counters, the outer circular boundaries of the modules contained in the vacuum volume, are between .75 meters and 1.2 meters radius, depending on their location along the beam. The inner square boundaries are determined by the requirement that the veto system not be a limiting aperture in the spectrometer; i.e., any decay particle that projects to the CsI or through any drift chamber must not be vetoed.

Achieving the rejection factor of 1000 for  $K_L \rightarrow 3\pi^0$  in  $\epsilon'/\epsilon$  measurement requires

single photon veto inefficiency better than  $10^{-4}$  including both cracks in geometric coverage and counter performance itself. This is attainable with a lead/scintillator sandwich structure. To provide a slight safety factor, at least  $14X_0$  of Pb will be needed having a longitudinal segmentation of about  $0.5X_0$ . From GEANT simulations of the ring counter system, a longitudinal sampling of  $0.5 X_0$  allows photon detection with high efficiency down to 100 MeV.

The construction details are yet to be fully specified; at this time the choice of using an embedded wavelength shifting fiber or an edge-abutted clear fiber has not been made. Deficiencies of the wavelength-shifter include low signal level, and longer time structure than is present in the scintillator. On the other hand, a wavelength-shifter is not so critical in its coupling to the scintillator as is a passive fiber. Either of these two options will be more cost effective and trouble free than machined or thermally shaped light guides.

Lateral segmentation is determined by a tradeoff between requiring no gaps, which argues for large scintillator segments, and the conflicting requirements that time jitter be well below the RF structure of the Tevatron and the occupancy be low enough that an event can not be killed by remnants from another separate event; dimensions of order  $50 \text{ cm} \times 50 \text{ cm}$  will meet these bounds. Layers will be rotated with respect to the preceding layer so that cracks between scintillator segments will not be aligned. This will lead to a topological problem of how to gang the overlapping scintillators which probably means odd layers go in one gang and even ones in a different gang. The final design will need further simulation and prototyping.

While the sensitive volumes must be located inside the vacuum region, the phototubes and bases must be replaceable from outside. A suitably transparent window will be used to which the PMT can abut. The inside structure must be such that the vacuum can be maintained  $\sim 10^{-4}$  torr. Therefore the sandwich and fiber structure must either be isolated so as not to make a virtual leak, or else the vacuum pumps must be able to handle this problem. If there is to be a separate dirty vacuum to house each veto module, its inside walls must be as thin as possible consistent with not being prone to pin-holes. Any dead material on the beam-side of the module will reduce sensitivity and increase the possibility of geometric veto inefficiency.

A particularly important angular gap to eliminate is the one just outside the CsI (RC13). Since the CsI will be located inside a light tight room, and this will probably force



a gap of at least a meter in  $z$  between it and the nearest veto module, that module will intrude slightly on the outer angular bound of the CsI. Simulations have shown that the greatest losses in E731 occurred at this point.

First level mechanical design on these photon veto counters has been done at Fermilab Physics Department. Three similar designs have been done for the photon vetoes RC1-RC10 in the vacuum tank. Fig. 4.2.2 and Fig. 4.2.3 show the design of annular and longitudinal segmentation for the module RC1. A design for the downstream spectrometer veto has also been done. The cost estimate to build RC1-RC10 is \$406 k, and for RC11-RC13 is \$164 k. A total of \$570 k has been estimated.

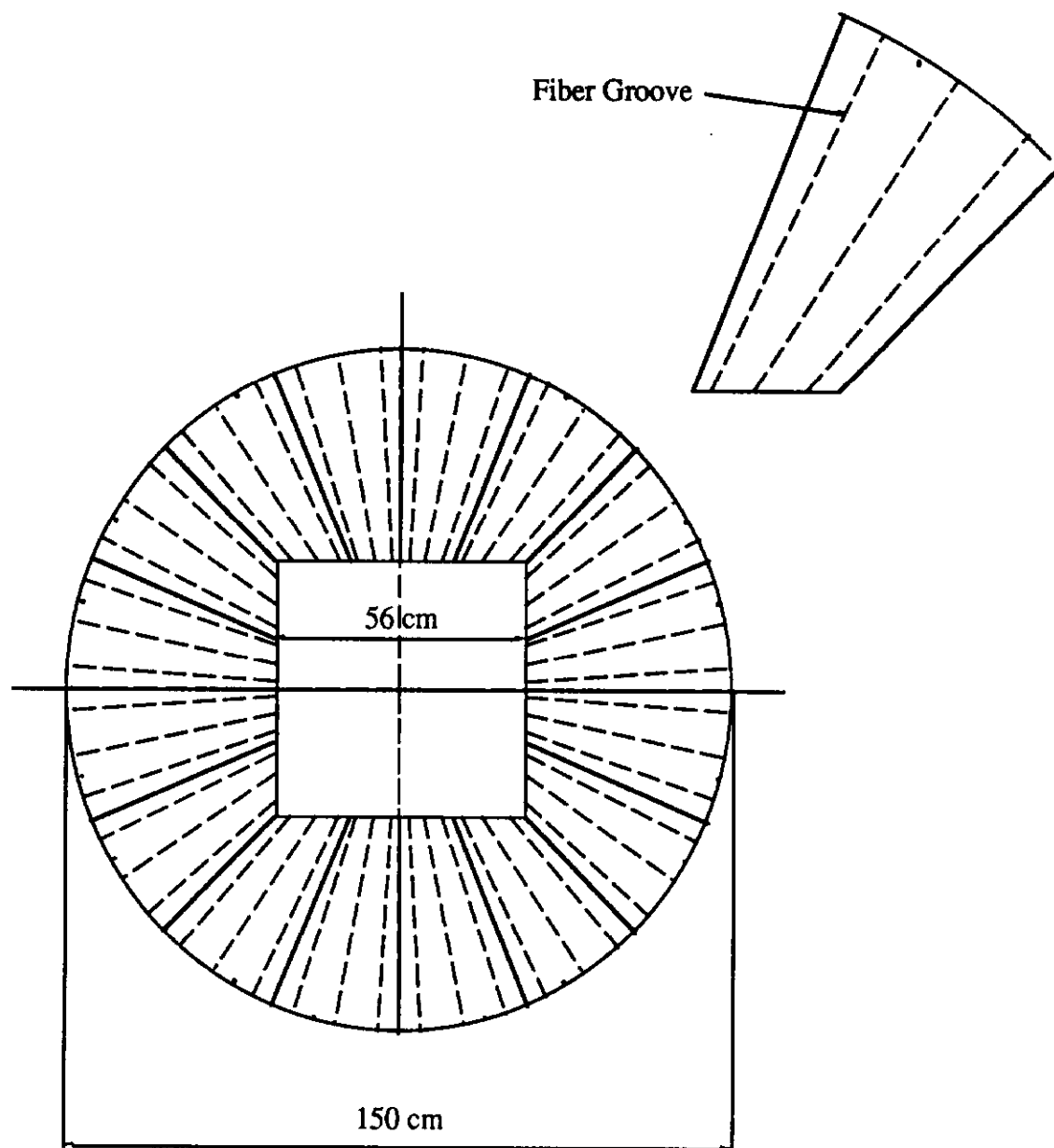


Fig. 4.2.2: Design of the annular segmentation for RC1-RC4. The annular ring veto consists of a total 16 wedge shape counters. Each wedge counter consists of 24 layers scintillator and  $0.5 X_0$  lead sheet sandwich. Wavelength shift fibers will be inserted into the groove for the scintillation light collection to the phototube view port.

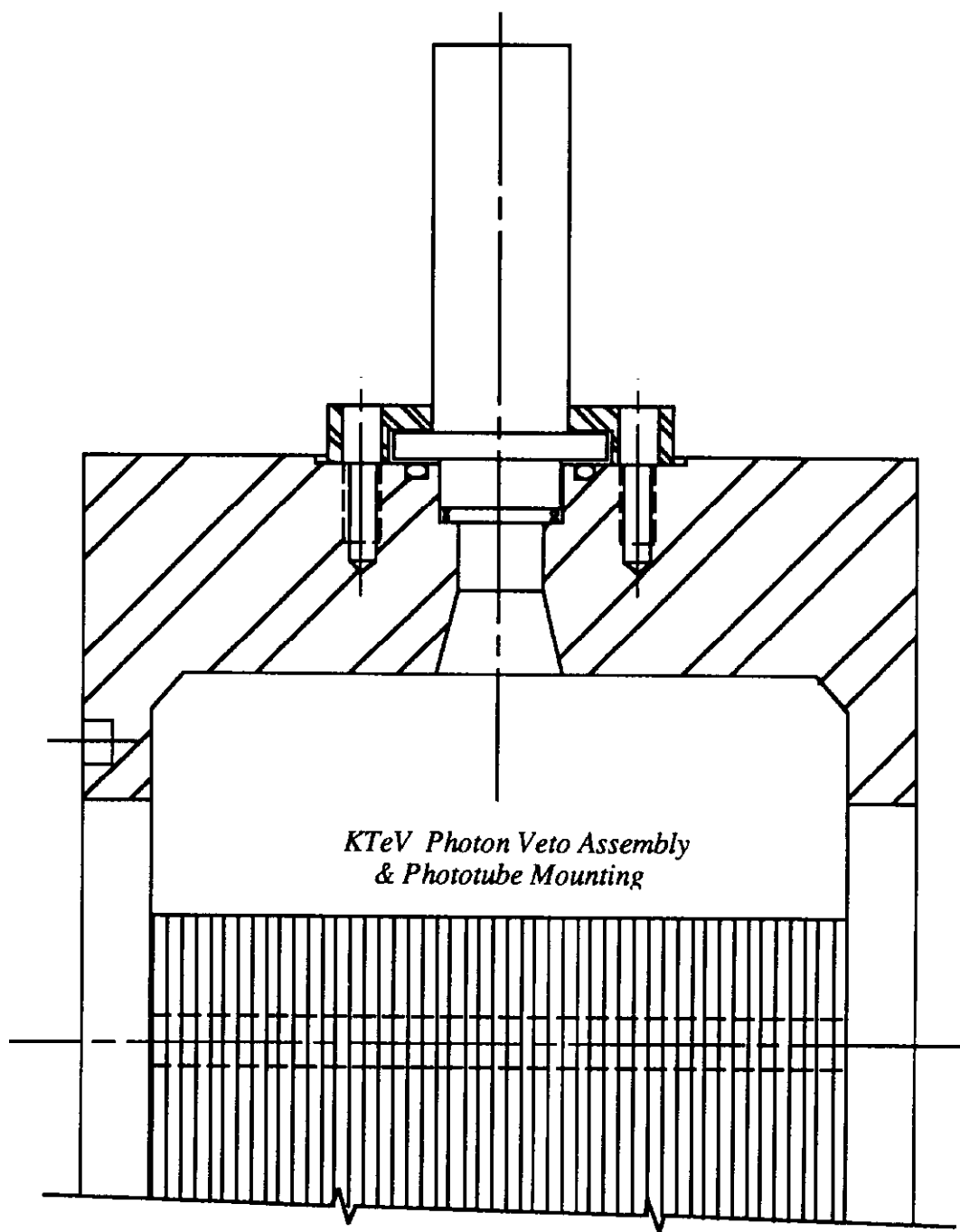


Fig. 4.2.3: Design of the longitudinal segmentation (along the beam direction) and phototube mounting for RC1–RC4.

### 4.3 Active Regenerator, Active Mask, and Absorber Mover (P832)

#### The Active Regenerator

The role of the regenerator in an  $e'/e$  experiment is to provide a  $K_S$  beam from the  $K_L$  beam. The proposed active regenerator is two interaction lengths long so as to maximize the coherent regeneration and minimize the background due to diffractively regenerated  $K_S$ 's. In order to significantly reduce the inelastic regeneration background (see Fig. 4.3.1), we propose to make the regenerator completely active, i.e., it will be made out of fast scintillator viewed by photomultiplier tubes. E773 successfully employed a completely active 0.4 interaction length regenerator in the 1991 fixed target run. The proposed regenerator differs from the E773 device in two respects. First, the new device will be five times as long, and second, it will operate in vacuum. As in E731 and E773, the new regenerator will alternate between the two beams every spill. The physical dimensions of the scintillator part of the device will be  $10\text{ cm} \times 10\text{ cm} \times 200\text{ cm}$  (see Fig. 4.3.2 and Fig. 4.3.3).

Since the regenerator will sit in the hadron beam, the accidental rate in it will tend to be high. In E731 as well as E773, the intensity of the  $K_S$  beam was effectively lowered by a factor of approximately 2.5 with the aid of an upstream shadow absorber. The absorber had its own mover which moved synchronously with the regenerator mover. The effect of the accidental activity in P832 can be estimated from that in the E773 'upstream' regenerator. This partially active device was 1.2 interaction length long, and was able to see the minimum-ionizing signal at the cost of approximately 10% accidental loss at the E773 intensity. For P832, in comparison with E773, the intensity will be approximately 2.5 times more, but since the regenerator will be shadowed by the movable absorber which will have an attenuation of 2.5, the effective intensity will be the same. However, since the P832 regenerator will be two interaction lengths, there is effectively twice as much activity in the P832 regenerator. The remaining factor of two reduction in the accidental activity can be brought about by using  $\times 10$  shaping amplifier which will drive the long cables to ADC, and protect the PMT's from losing gain due to excessive anode current. These amplifiers were used in the E773's completely active regenerator successfully.

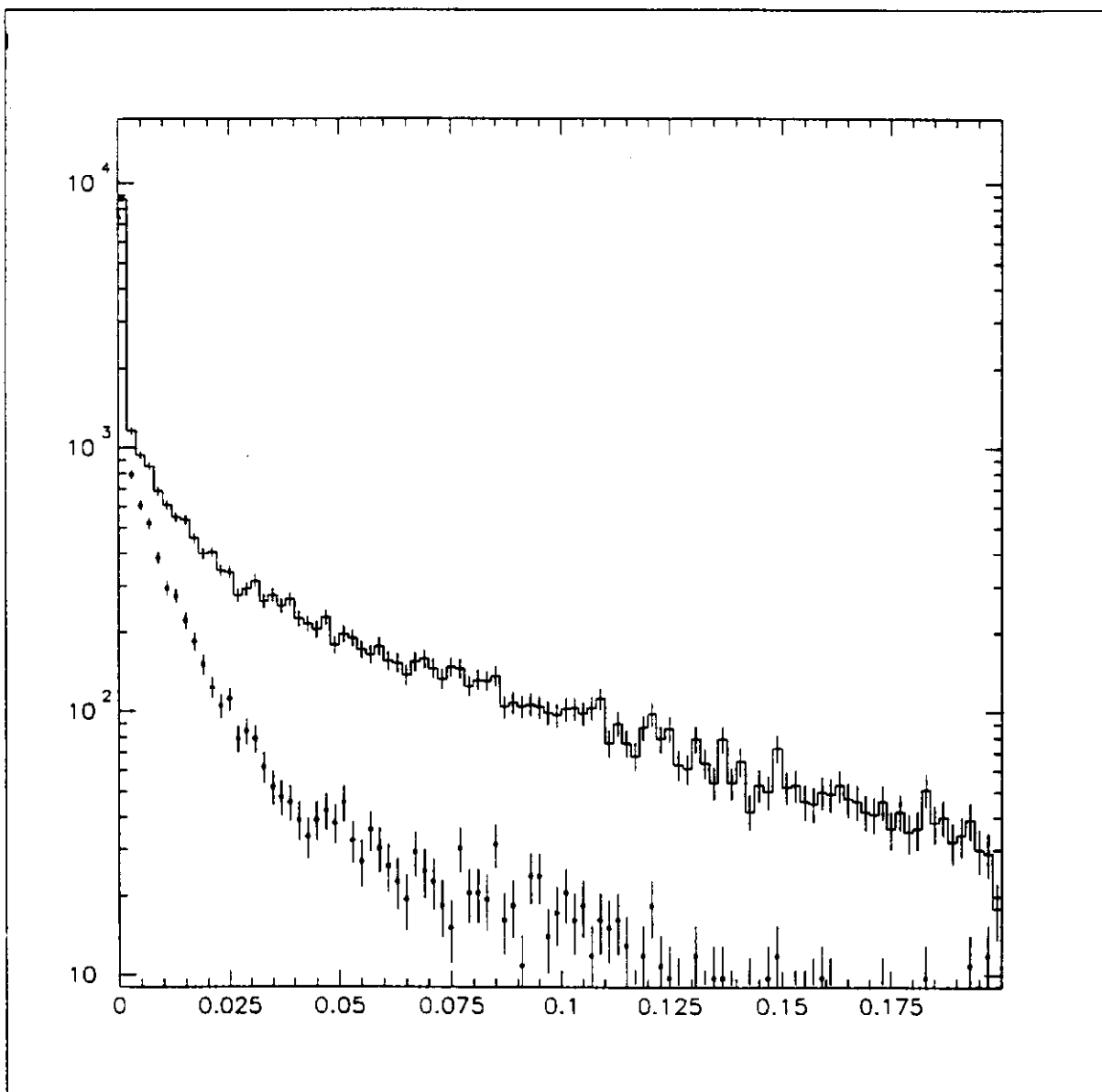


Fig. 4.3.1: A histogram of  $Pt^2$  for  $K_S \rightarrow \pi^+\pi^-$  decays in E773, where the abscissa is in units of  $(\text{GeV}/c)^2$ . A significant reduction in the inelastic background is evident upon the requirement that there be no activity in the active regenerator. The coherent peak remains the same, indicating minimal accidental activity in the device.

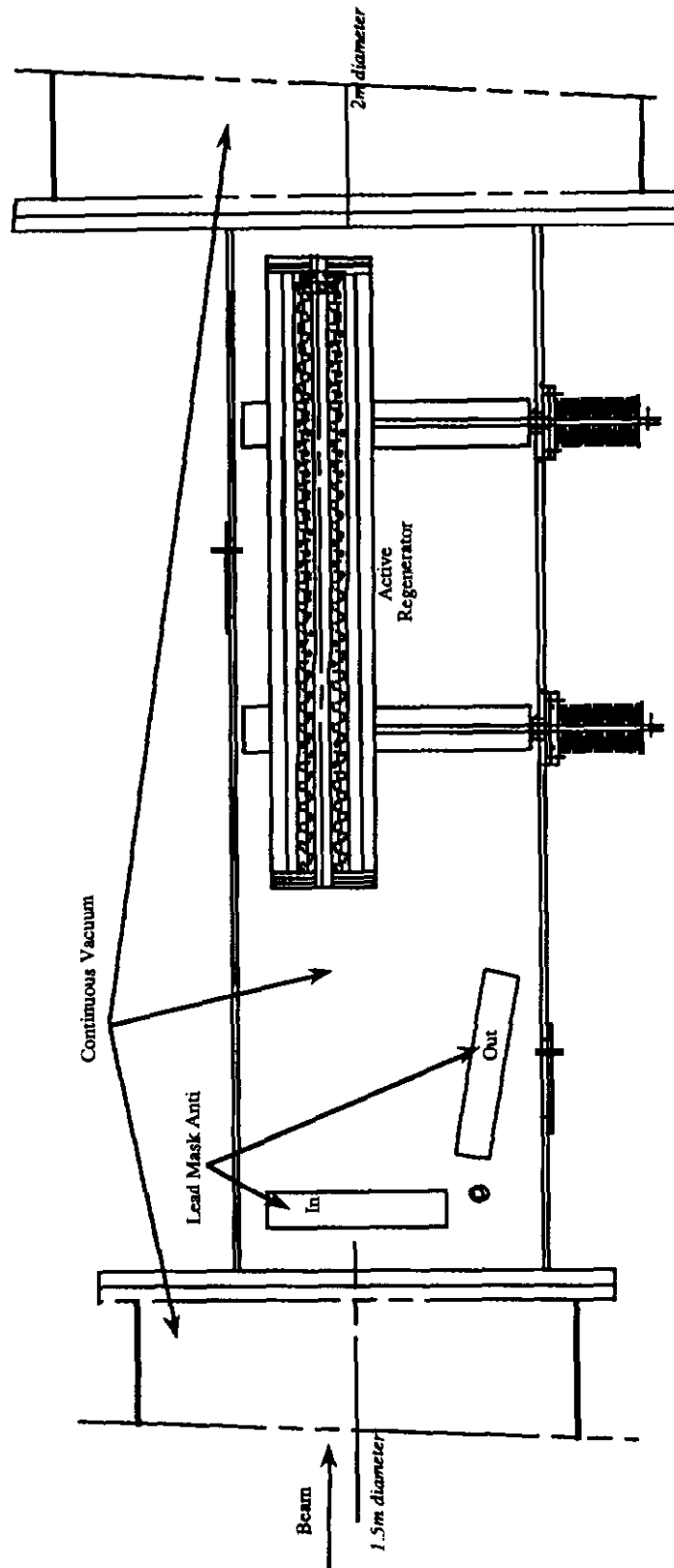


Fig.4.3.2: A view of the proposed regenerator for P832, showing the active mask as well as elements of the vacuum vessel.

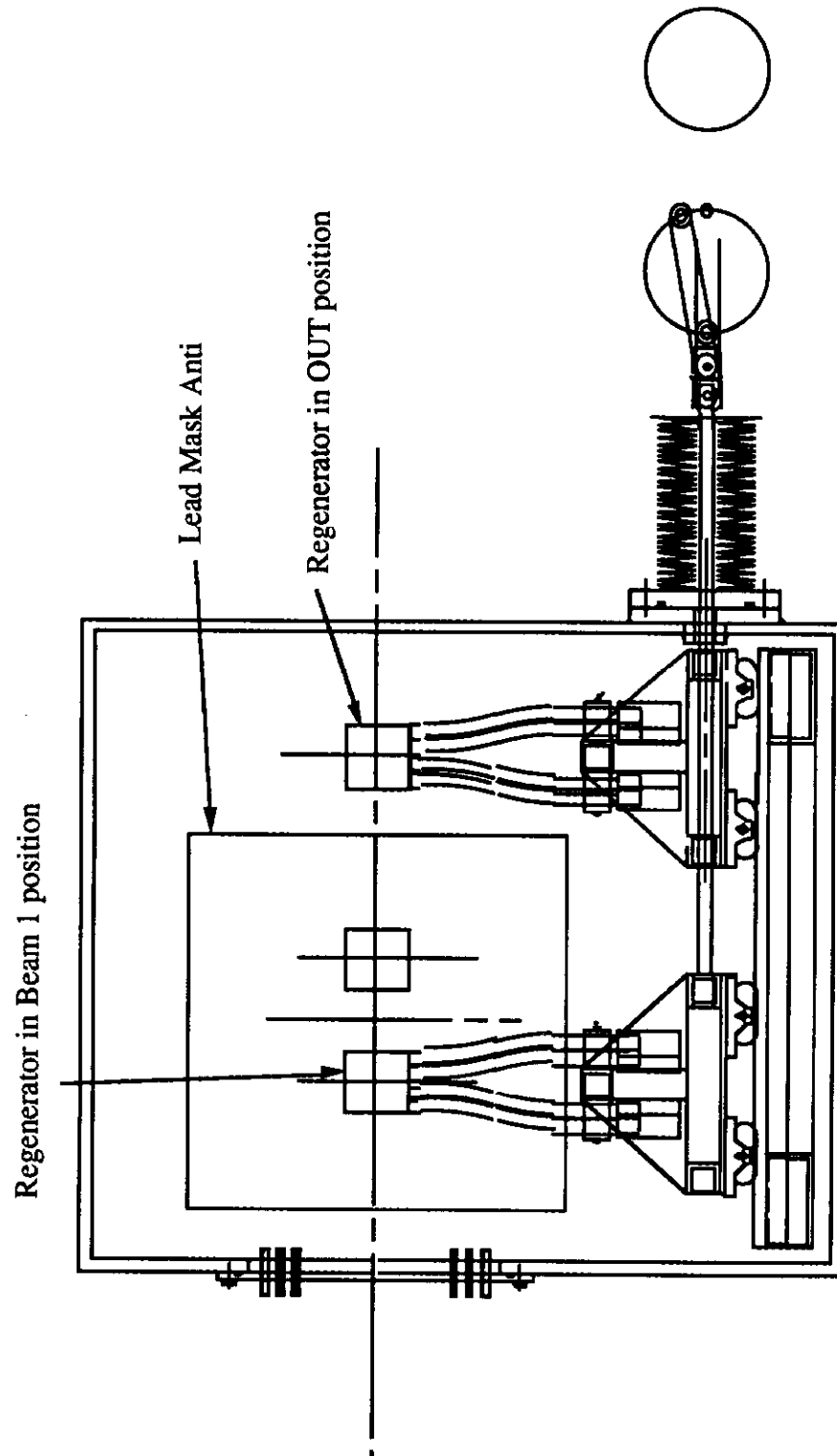


Fig. 4.3.3: Beam view of the proposed regenerator and its mover, showing the three positions of the regenerator mover.

The P832 regenerator will have the segmentation the same as in E773, thus calling for a total of 60 1.31" thick fast (Pilot U or equivalent) scintillator planes, with 120 1-1/8" diameter PMT's. The PMT base will be active as in E773 to maintain low heat dissipation.

Since the regenerator will be in vacuum, there are three special design considerations. First, the heat dissipation from each of the sources has to be kept to a minimum, and the heat has to be carried out. Second, the items in vacuum should be reliable. Third, the regenerator design and fabrication has to be integrated with that of its mover and the vacuum vessel. The regenerator mover has been designed so that it not only allows the spill-by-spill beam to beam motion, but it can be also taken out far enough to allow E799 type of two  $K_L$  beam running.

The cost estimate to build the regenerator, its mover and vacuum tank is \$120 k.

### **The Active Mask**

The purpose of the Active Mask is to sharply define the acceptance upstream of the regenerator and prevent cross-over background of decays from one beam to the other. This Lead-Scintillator sandwich device will have 8 layers of 0.25" thick lead and 0.25" thick scintillator with two 3.6" square beam apertures, and its proposed location is one meter upstream of the regenerator. The beam apertures is designed to be just a little smaller than the size of the regenerator scintillator to avoid the sneak-by decays. The outer dimensions will be 24" by 24" to cover the space between the regenerator and the adjacent photon veto. (See Fig. 4.3.2). Again, the Mask Anti is designed so that it can be swung away from its normal position and be essentially taken out of the beam with no interruption to data taking. This will facilitate E799 style of two  $K_L$  beam running.

The cost estimate to build the active lead mask is \$20 k.

### **The Absorber Mover**

This item includes the mechanical mover itself, mover control, and the position readout. The movement has to be coordinated with that of the regenerator mover spill by spill. The E731/E773 mover itself, or an equivalent item should work just fine. The absorber mover will be only used in P832 running, and be placed just downstream of the the primary collimator and the beam dump.



## 4.4 Chambers

The same drift chambers used in E731 can be used for KTeV experiments. Some upgrades of the current chamber front end electronics (pre-amplifier/amplifier) and chamber gas system to handle the fast drift gas mixture will be needed for the higher singles rate environment at KTeV.

Although slightly larger chamber (up to 2 m by 2 m) is desirable, the current drift chamber system is suitable for the KTeV experiments in terms of the tracking recognition and the space point resolution (better than 100  $\mu\text{m}$  resolution was achieved in '91 run). The sizes of the existing four drift chambers are listed in the detector configuration Table 4.1.1. A 0.635 cm hexagon cell geometry, with offset double layers to resolve the left-right ambiguity in each view is used. Each chamber consisted of 2 horizontal planes ( $x, x'$ ) and 2 vertical planes ( $y, y'$ ) to reconstruct the space points for the charged particles.

For the purpose of this design report, we will assume using the existing chambers with the following upgrades:

- a. Chamber pre-amplifier and/or amplifier system,
- b. Gas system and fast drift gas R&D.

Drift chamber maintenance will require replacement of all broken wires and clean up the chambers before we install them in the new KTeV experimental hall. The chamber refurbishment should take two persons in about 2 days per chamber. The work should be done a few months before the experiment starts.

For the sake of completeness, we note here that the spectrometer regions between the drift chambers will be filled with helium bags, as in the current kaon experiment in MCenter.

### 4.4.1 Drift Chamber Preamps/Amplifiers

The existing E731 drift chambers have cells that are 1.27 cm wide, and also 1.27 cm in the beam direction. They are probably more susceptible to space charge buildup than wire chambers with smaller cell geometry (they do have excellent resolution,

however). Since E799II will require that they work in a higher rate environment than previously, we propose to build a drift chamber preamp system that would have a gain of 10. This gain would replace an equal factor of gas gain, allowing us to run at about 300V lower high voltage. This would create fewer positive ions near the sense wire, and make the chambers capable of handling a rate approximately 10 times higher.

We have built a prototype of this preamp system. It consists of preamp cards, which plug into the drift chamber in the same slots as the existing amplifier cards, and have a gain of 10. They send out the amplified signals differentially on a ribbon cable. The next stage of the preamp system fits in a card cage for Faraday shielding. It consists of receiver cards, which receive the analog differential signals from the preamp cards, and intermediate cards which pass the negative-going signals to the existing amplifier cards. The output of the amplifier cards would then go to TDC's as is currently done.

We have tested this prototype on a chamber that was built in exactly the same way as the chambers in use in our experiment. The test was conducted in Lab 6 at Fermilab using particles from a  $^{90}\text{Sr}$  source. We ran plateau curves using the preamp system, and also using just the existing amplifier cards. The knee of the plateau was indeed 300V lower with the preamps. Two other characteristics of the plateau curves were very encouraging: the rising part was considerably steeper with the preamp system; and the plateau efficiency was 99.5% with the preamps, but only 95% with the regular amplifier cards. The Strontium source provided a chamber rate of 140 kHz, which was shared mostly by two wires, over a length of about 10 cm. While this should not have been the usual rule-of-thumb rate of 20 kHz/cm of wire for the onset of space charge problems, we may have already had a hint of an improvement in the ability of the chamber to handle high rates. The next step is to put this test chamber in the beam, where we will measure the efficiency vs. beam rate, and also measure the chamber resolution at high rates.

We estimate to complete the drift chamber pre-amplifier system would take \$77 k.

## **Drift Chamber Amplifiers**

Just completing the drift chamber preamplifier system will not solve all of our chamber problems, however. Our existing amplifiers use an old LeCroy hybrid for the amplification and discrimination functions, and those hybrids are no longer available. In addition, at high rates, the amplifier cards show several pathologies. They are very noisy

and they put out microsecond-long trains of pulses. These intermittent oscillations are causing inefficiencies in the current run of E799I. We believe that they would not perform well enough to use them in the KTeV phase of E799II. We therefore propose to replace them. We would modify the receiver board of the drift chamber preamp system to include amplification, discrimination, and pulse shaping functions. Additional \$50 k will be needed to install the modified chamber amplifiers.

#### 4.4.2 Drift Chamber and TRD Gas Studies

The higher rate of charged particles in P832 and E799II will lead to an unacceptably high level of accidental hits in the drift chambers and TRDs. In E773 and E799I we have found a strong degradation of the hit-counting trigger rejection with increasing intensity<sup>1</sup>. This degradation can largely be removed with on-line digital mean timing as described in the trigger section of this document, and with faster drift chamber gas mixtures. With the mixture used in E799I, the maximum drift time spanned 8 RF buckets (160 ns). Recent studies<sup>2</sup> of fast mixtures indicate that a factor of two increase in speed can be readily achieved with mixtures that have a component of CF<sub>4</sub> gas.

The structure of conventional TRDs require large gas gaps to ensure high quantum efficiency for the generated X-rays, as well as a large component of xenon gas, which is a notoriously slow gas<sup>3</sup>. The xenon gas mixture employed in E799I had a maximum drift time of 500 nsec, which spanned 25 RF buckets! The mean occupancy of each TRD chamber in E799I was 12 hits out of 200 wires. Since the TRD integrates charge over the full drift length, we can not appeal to mean-timing techniques to reject accidental energy. In order to use the TRDs as a trigger source in E799II, it is essential to reduce the maximum charge collection time to preferably less than 100 nsec. To achieve this, we will embark on studies to search for fast TRD gases,<sup>3</sup> as well as studies of unconventional TRD chamber designs as described in the TRD section of this report.

---

<sup>1</sup> A. Barker, private communication.

<sup>2</sup> Study of Fast Gases, Resolutions, and Contaminants in the D0 Muon System. J.M. Butler et.al., FERMILAB-Pub-89/222-E.

<sup>3</sup> (i) "Gas Mixtures for Transition Radiation Detectors At High Luminosity Colliders.", B. Dolgoshein et al., CERN-EP/89/161.  
(ii) "Xe-Containing Fast Gas Mixtures For Gas-Filled Detectors." L.G. Christophorou et.al., NIM 171 (1980) 491-495.

Gas studies for the drift chamber system will employ an existing full length test chamber of the same cell design. Studies for the TRD system will involve several different test chamber schemes, to search for the fastest practical chamber design. Non-xenon gases will be precisely mixed and monitored with the mixing station component of the TRD gas system employed in E799I. Xenon based test mixtures will be mixed and recirculated with the TRD gas system described in the TRD section of this document. Timing and gain studies will employ cosmic rays and triggerable x-ray sources<sup>4</sup> such as  $^{65}\text{Zn}$ . Electronics and data acquisition equipment required are the following:

- 1) CAMAC system including 10 bit TDCs and ADCs.
- 2) VAX 3200 with Jorway Q-bus CAMAC driver.
- 3) 100 MHz 8-bit flash ADC system for TRD time signature studies.

All this equipment was used in E799I, and can easily be moved to establish a gas test facility. We have used the flash ADC system to read out test wires of the E799I TRDs, and hence will be able to connect our bench measurements to beam measurements with the same system.

---

<sup>4</sup>  $^{65}\text{Zn}$  is a radioactive source that emits an 8 keV x-ray coincident with a 1 MeV gamma that can trigger a scintillator to tag the 8 keV x-ray emission. The transition radiation spectrum of x-ray photons is maximal at 8 keV.

## 4.5 KTeV Spectrometer Magnet

### 4.5.1 Geometry and Field Requirements

One analyzing magnet for KTeV experiments is proposed to measure the momentum of charged particles through the drift chamber tracking system. The magnet is also important in measuring the momentum of the electron from  $K_e3$  decays which are useful in calibrating the CsI calorimeter *in situ*. Therefore a good, steady and uniform field over a 2 m by 2 m area in the gap between the poles is required. In order to meet the objectives of the experiment, the magnet should be designed to meet the following requirements:

- a. Momentum kick: up to 400 MeV/c.
- b. Field Integral Uniformity:  $\pm 5\%$  over a good field aperture 2 m  $\times$  2 m.
- c. Fringe field: < 100 Gauss at the detector 2.5 m from the face.

The magnet shown in Fig. 4.5.1 was found by magnetostatic analysis to meet these requirements while approximately minimizing the sum of the capital and five-year operating costs. The magnet consists of an iron yoke and rectangular poles with "race-track" copper coils wrapped around the poles. In Fig. 4.5.2, the ANSYS magnetostatic study has shown the field integral uniformity meets our requirement. In Fig. 4.5.3, a fringe field study has shown the major field component as a function of z. A preliminary cost estimate with conventional coils gave a total capital cost approximately \$2.5 M and an annual operating cost of about \$200 k.

Studies in the KAMI Conceptual Design Report show that the CCM magnet at the NMUON would also satisfy the above requirements, if it can be regapped from 1.3 m to 2.4 m. After regapping, the field uniformity is still quite good. The option to use the CCM magnet at NMUON has been studied in some detail. Options to build a new KTeV magnet and coil has also been pursued if the CCM option is not available.

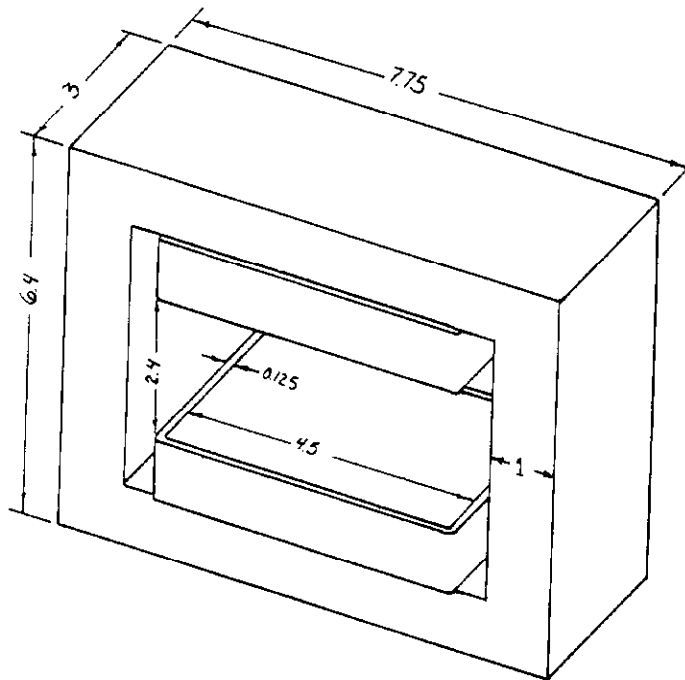


Fig. 4.5.1: Isometric view of a new KTeV analysis magnet. Dimensions are in meters.

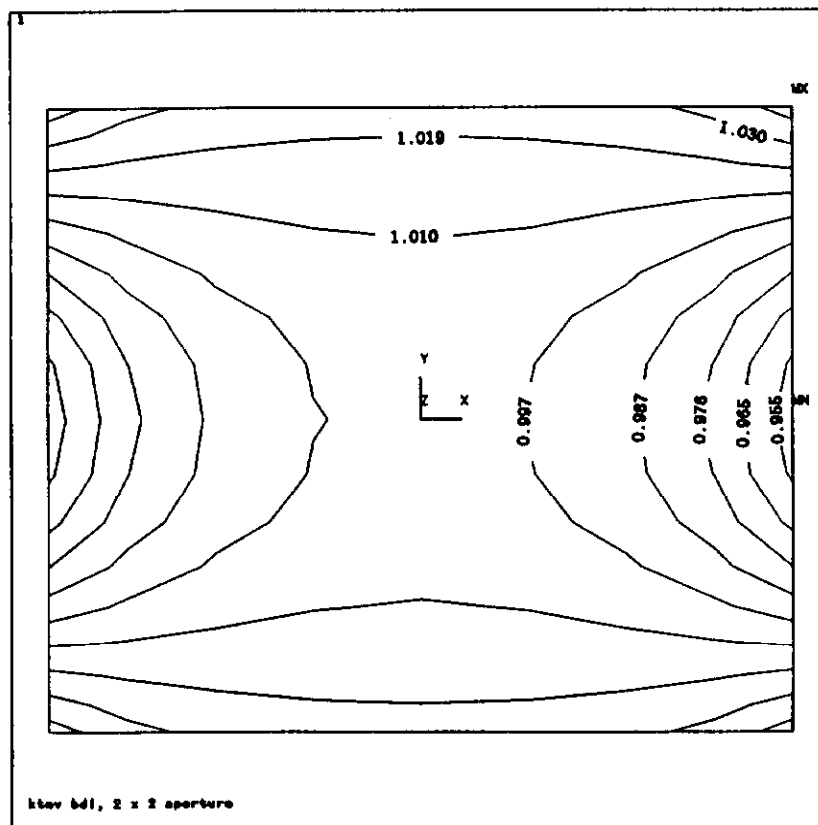


Fig. 4.5.2: Vertical component of the magnetic field, integrated in  $z$  from chamber C2 to C3, as a function of  $x$  and  $y$  over a 2 m high by 2 m wide aperture.

## Fringe Field Along Axis for KTEV Dipole

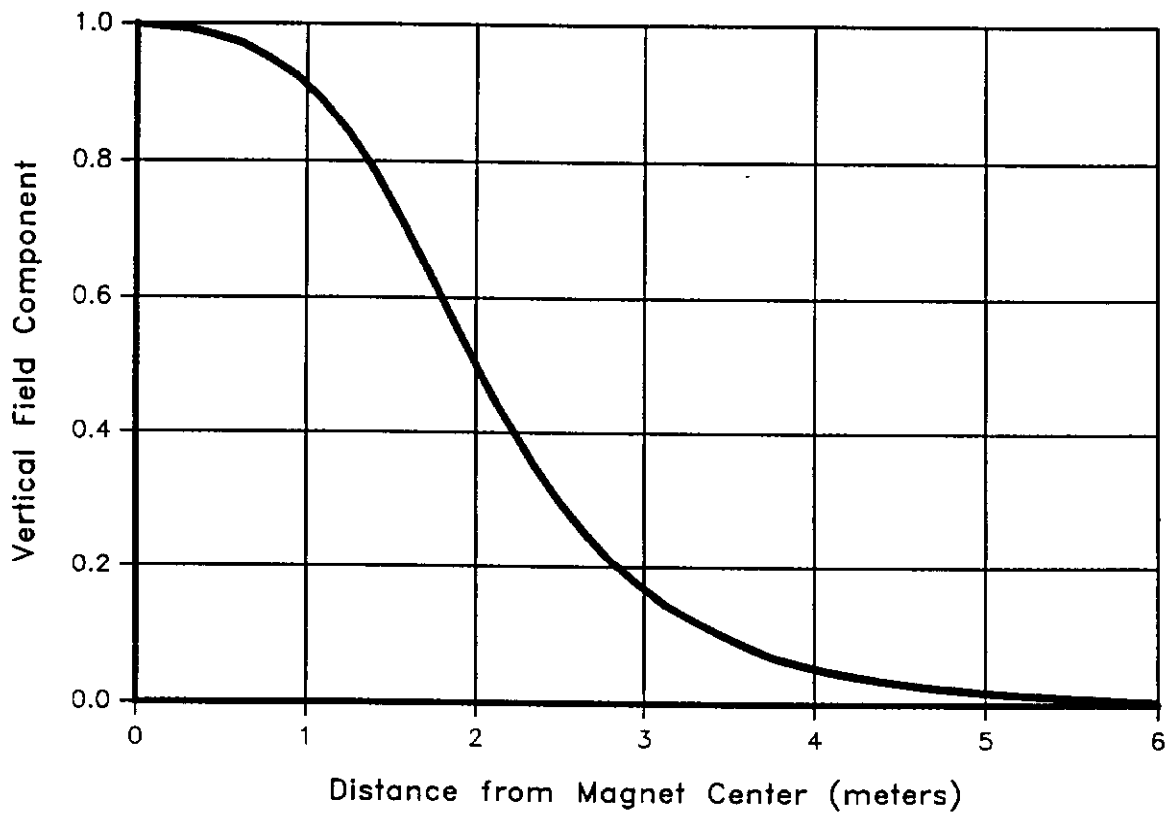


Fig. 4.5.3: Vertical component of the magnetic field as a function of  $z$  along the center line  $x=0$  and  $y=0$ .

## 4.5.2 KTeV Spectrometer Magnet Mapping

The magnetic field mapping requirements are scaled from our E731 experience and E799II/P832 needs. E731 had a systematic uncertainty in the energy scale of  $\pm 0.05\%$  dominated by the neutral energy measurement. This uncertainty gave a systematic error of  $\pm 1.6 \times 10^{-4}$  on  $\epsilon'/\epsilon$ . The magnet field measurement for E731, using Fermilab's ZIPTRACK many year's ago, had an uncertainty of  $\pm 0.1\%$  on the integrated field.

For P832 our goal is to reduce the systematic error in the energy scale of  $\pm 0.005\%$  to give an error of  $\pm 0.5 \times 10^{-4}$  on  $\epsilon'/\epsilon$ . To insure that the momentum measurement or magnet map measurement does not contribute significantly to the systematic uncertainty of the energy scale, we will need a field map measurement with a uncertainty of  $\pm 0.01\%$  from point-to-point on the integrated field measurement.

### ZIPTRACK Feasibility

The ZIPTRACK device that we used was at least one decade old which achieved the precision  $\pm 0.1\%$  on the integrated field measurement for E731. The error on ZIPTRACKing mainly came from the positioning of the Hall probes, the stability of the ADC integrator and the reproducibility of the cart along the length of the ZIPTRACK. With modern alignment equipment and support along with improved ADC stability and sensitivity, to achieve a precision much better than  $0.1\%$  should be doable. A better field uniformity over large aperture of the KTeV magnet will also reduce the measurement errors due to the field gradient. Further investigation on this matter will be pursued in the near future.



## 4.6 Transition Radiation Detectors

Transition radiation photons (TR) are emitted when charged particles cross an interface between two media with different dielectric constants. The phenomena was first predicted by Ginzburg and Frank<sup>5</sup>. Since the total radiated photon energy from a single interface is proportional to the Lorentz factor of the charged particle, a possible application as a particle identification device at high energy was also pointed out<sup>6</sup> and many studies have been performed experimentally<sup>7</sup>. Details of the transition radiation phenomena have been reviewed by many authors<sup>8,9</sup>. We summarize the relevant formulae that are useful for design purposes.

The total yield of TR photon from a single interface is

$$S_0 = \frac{\alpha}{3} \frac{(\omega_1 - \omega_2)^2}{(\omega_1 + \omega_2)} \gamma$$

where  $\omega_i$  = plasma frequency of material  $i$  (assume that the suffix 1 is for a radiator material and 2 for a gas in a gap,  $\omega_1 \gg \omega_2$ ),  $\gamma$  = Lorentz factor ( $E/m$ ) and  $\alpha = e^2/\hbar c$ . The plasma frequency is related to the electron density,  $n_e$  of the material.

$$\omega_{\text{plasma}} = \frac{(4\pi\alpha n_e)^{1/2}}{m_e} \sim \sqrt{\frac{Z}{A}}$$

The TR photon yield from multiple interfaces is affected by an interference effect, and the total photon yield is written as:<sup>9</sup>

$$\frac{dS}{d\omega} = \frac{2\alpha}{\pi} \cdot N \cdot G(\Gamma, \nu, \tau)$$

---

<sup>5</sup> V.L. Ginzburg and I.M. Frank, Z. Eksper. Theor. Fiz. 16, (1946) 15.

<sup>6</sup> G.M. Garibial, Soviet Phys. JETP 10 (1960) 372; 23 (1971) 23..

<sup>7</sup> J.Fisher, et al. NIM, 127 (1975) 525; J Cobb, et al., NIM, 140 (1977) 413; T. Ludium, et al., NIM 180 (1981) 413; C. Fabjan et al., NIM 185 (1981) 119; B. Bauche, et al., Proc. of the Int. Conf. on Instr. for Collider Beam Phys. (1982) June; A. Bungener et al., NIM, 214 (1983) 216.

<sup>8</sup> X. Artru, G.B. Yohl and G. Monessier, Phys. Rev. D12 (1975) 1289;

<sup>9</sup> M.C. Ter-Mikaelian, High Energy Electromagnetic Processes in Condensed Media (Wiley-Interscience, NY 1972).

where  $N$  is a number of interfaces and  $G$  is an interference factor. The interference factor  $G$  is a function of the following variables,

$$\Gamma = \frac{\gamma}{\gamma_1}, \quad v = \frac{\omega}{\gamma_1 \omega_1}, \quad \tau = \frac{l_1}{l_2}, \quad \gamma_1 = \frac{l_1 \omega_1}{2}$$

where  $l_i$  = thickness of medium  $i$ .

Theoretical calculations by Artru et al.<sup>8</sup> shows that the interference factor  $G$  has a peak around  $v = 1/\pi$  for  $\Gamma > 1$ . Then the most probable photon yield in the practical TRD is around  $= l_1 \omega_1^2 / \pi$ . The radiator material must have high plasma frequency, i.e. high  $Z$  to get higher photon yield and energetic photons, but in order to reduce a self absorption effect, the radiator should have low absorption coefficient, i.e. low  $Z$ . These requirements conflicts with each other. However, the plasma frequency is proportional to  $Z^{1/2}$  and the absorption coefficient depends on  $Z^5$ , therefore generally low  $Z$  materials must be chosen as a radiator. A practical radiator, which requires high emission efficiency, has many interfaces because of low efficiency for photon emission ( $\sim 10^{-2}$ ) from a single layer. Polypropylene fiber mats were selected for their ease of fabrication and safety, with rather good efficiency for the emission of TR photons and a moderate absorption coefficient. Since the energies of the TR photons are mainly in the 10 keV X-ray region, Xenon gas was used to detecting the photons with a wire chamber.

#### 4.6.1 TRD Upgrades

TRDs are needed in E799II for the purpose of  $\pi/e$  rejection. The existing leadglass calorimeter has about a rejection factor of 100 combining cuts on  $E/p$  and shape of the shower for particles between 2 to 30 GeV. The proposed CsI calorimeter is estimated to have rejection power of about 500. Here two specific physics issues will demonstrate the necessity of the TRD for electron identification and also its need on the reduction of the trigger rates.

The decay,  $K_L \rightarrow \pi^0 \nu \bar{\nu}$  has essentially direct CP violating amplitude and therefore a single clean event found will suffice to establish the much sought after direct CP violation phenomenon. In E799II, the possible signature of such a decay will be a reconstructed high  $P_t \pi^0 \rightarrow e^+ e^- \gamma$ . Utilizing  $\pi^0$  Dalitz decays to tag the  $K_L$  has the

disadvantage of a reduction of 70 sensitivity, but until we have a truly hermetic photon veto system (see section 4.2.2), the reconstructible quantities of the kaon vertex and  $\pi^0$  mass will provide a cleaner search. However, the Dalitz tag technique has a severe background from  $K_{e3}$ , in which the charged pion is misidentified as an electron. Removing the reconstructed  $e^+e^-$  invariant mass above 35 MeV (Dalitz pair prefers low  $e^+e^-$  mass) gives about a suppression factor of 100, and even with the calorimeter cut this background is still big. Additional TRD  $e/\pi$  rejection will help a great deal. The decay,  $K_L \rightarrow \pi^0 e^+ e^-$  which is the primary goal of the experiment also needs the TRD to suppress backgrounds related with  $K_{e3}$  decay. The details of these  $K_{e3}$  backgrounds are documented in the E799 proposal.<sup>10</sup> Lastly as pointed out in the trigger and data acquisition sections of this report (See Section 4.11 and Section 4.12), we need the TRD as a trigger element to reduce the trigger rate. The "di-electron" trigger rate (projected to be 20 kHz at  $5 \times 10^{12}$  proton/pulse in E799II) has to be prescaled from 2 to 16 depending on the number of the calorimeter clusters (except 4) found. These high rates are all due to  $K_{e3}$  and  $K_L \rightarrow \pi^+ \pi^- \pi^0$ . It is necessary to instrumented the TRD with a trigger capability so that prescale will not be needed, thus significantly increase the physics sensitivity.

In E799I we have built three TRD modules, each uses 10 cm thick polypropylene fiber mat (density of 0.06 g/cm<sup>2</sup>) as radiator and 2.5 cm Xe active chamber volume. The radiator material and its properties, the gas mixture and thickness of the chamber are optimized to give the best photon yield and detection efficiency with Monte Carlo calculation. There are 185 sense wires, all vertical with the cell geometry of a longitudinal drift chamber. The maximum drift time for this chamber with 80/20 mixture of Xe/CO<sub>2</sub> is 500 nsec. The reasons for such a thick chamber (as compare to standard 5 mm to 10 mm PWC) are substantial saving in cost from fewer electronic readout channels, and there is not a need in E799I for trigger rate reduction. We are studying the performance of these modules with E799I data. The different pulse height spectra for electrons and pions identified in the lead glass are shown in Fig. 4.6.1. For the 1994 run, the TRD will be "spread out", i.e., a thinner radiator-chamber combination to decrease charge collection time for triggering purpose, and to take higher rates with less occupancy.<sup>11</sup> We believe with the experience from E799I, we have the know-how to build very thin ( $\approx 1$  cm) large area (2 m  $\times$  2 m) chambers. In addition, we would also like to investigate the possibility of using long low-mass straw tubes as the detection medium. Straw drift tube has the

---

<sup>10</sup> Fermilab E799 proposal, Dec 1988.

<sup>11</sup> D. Errede et al., Fermilab preprint 91/67-E.

advantage of much easier control on gas gain and maintenance.<sup>12</sup> We believe this device to be very attractive, and that some R&D effort should be supported.

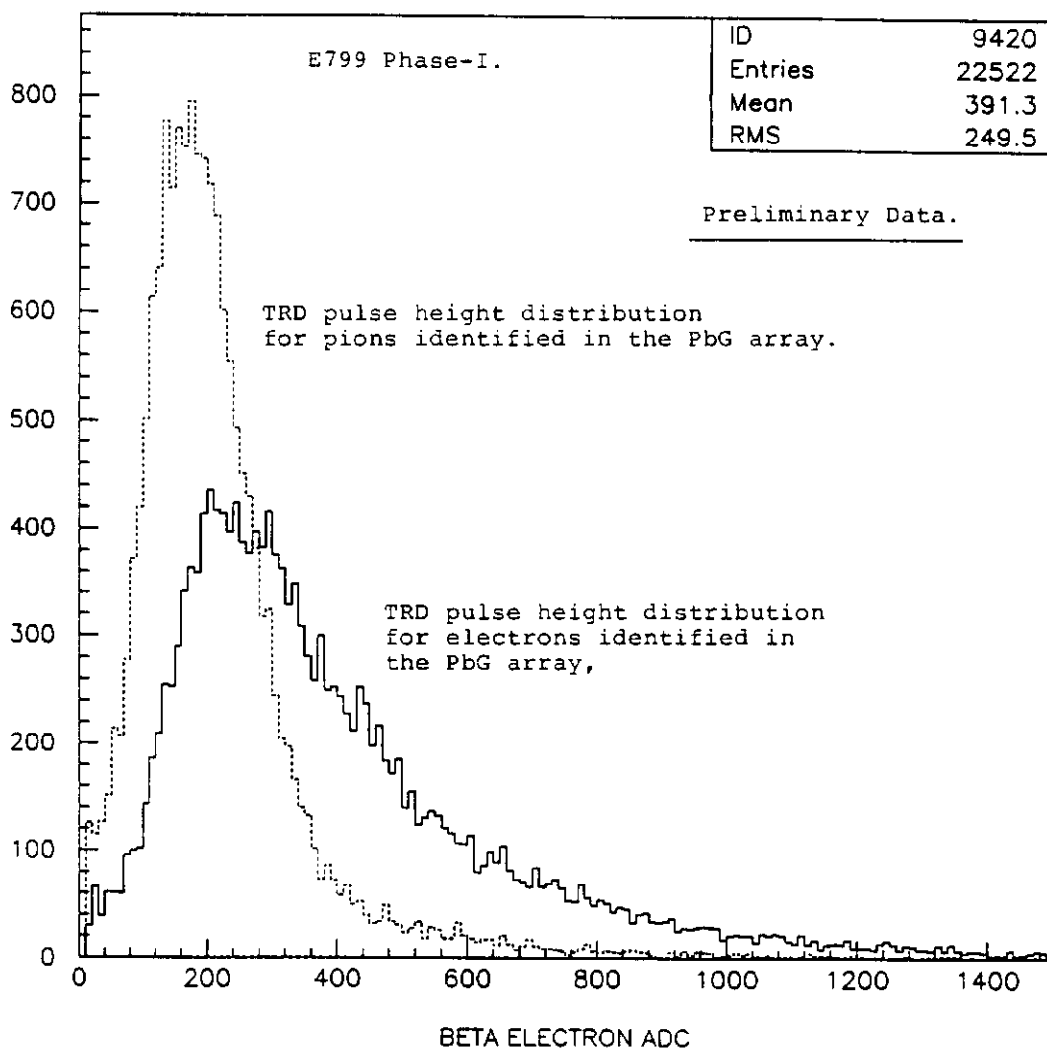


Fig. 4.6.1: E799I TRD pulse height spectra for electrons and pions which were selected by the lead glass.

<sup>12</sup> R. Tschirhart, Proceedings of the Symp. on Particle Identification at High Luminosity Hadron Colliders, 609.

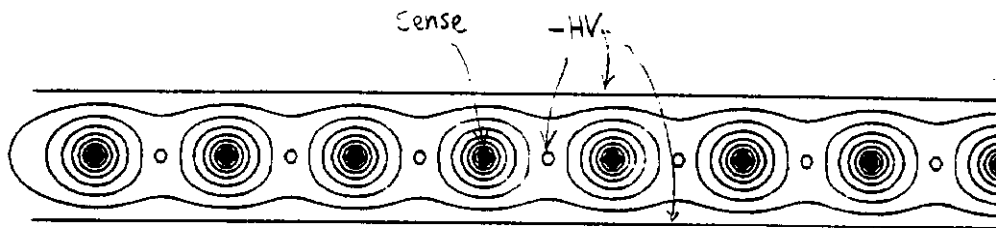
## E799II/P832 TRD Specifications:

### *Physical dimensions:*

Ten modules total; each module composed of:

- a) transition radiation material, most probably polypropylene fiber mats;  
about 3-4 cm thick and density about  $0.06 \text{ g/cm}^2$ .
- b) MWPC with Xe/He/CF<sub>4</sub> mixture, 1 cm thick. Each module will be no more  
than 0.5% radiation length and has an active fiducial region of 2 m x 2 m.

Wire and field geometry are shown below in Fig. 4.6.2.



Expanded view:

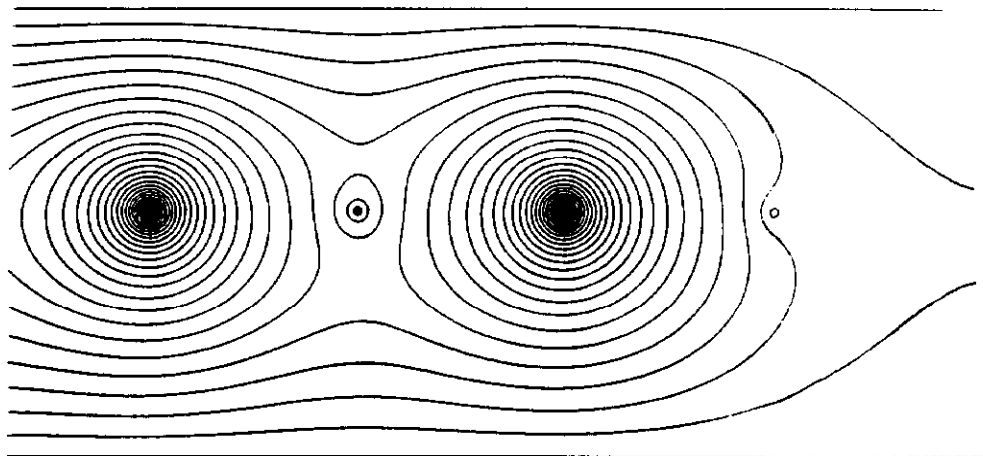


Fig. 4.6.2: TRD's PWC field map and wire geometry.

There will be total of 200 sense wires (.001" Tungsten) and 201 field wires (.004"

Be-Cu). All wires will be vertical. The cathode high voltage windows need to be engineering to maintain its flatness ( $\pm 0.5$  mm) throughout the whole active area.

*Gas:*

With the existing recirculating gas system, there will be an R&D effort to measure the speed of different xenon mixtures. The goal is to achieve 100 nsec total drift time with low gain. One likely candidate is a Xe/CF<sub>4</sub>/He mixture.

*Electronics:*

Each wire will be instrumented with a high band width amplifier, differentiator, a high threshold discriminator with a two bit scaler, a low threshold discriminator for front end. The discriminator outputs will form the inputs for a "TRD Trigger". The raw amplifier pulse need to be digitized with a 12-bit ADC. (The ADC presumably used by the CsI will be more than adequate.)

*Trigger:*

The low and high comparator outputs will be the inputs to memory map lookup units which will determine a) from low threshold hits, charged tracks registered by hit wires, and b) from high threshold hits, whether the track is an electron or pion candidate. Fig. 4.6.3 shows the schematic diagram for TRD electronics and triggers.

We already have all the wire alignment fixtures, mylar stretching machinery etc. from E799I TRD construction, and thus need only raw construction material. The total cost to build the TRD chambers is estimated to be \$73 k. The TRD electronic and trigger system will cost \$170 k in addition.

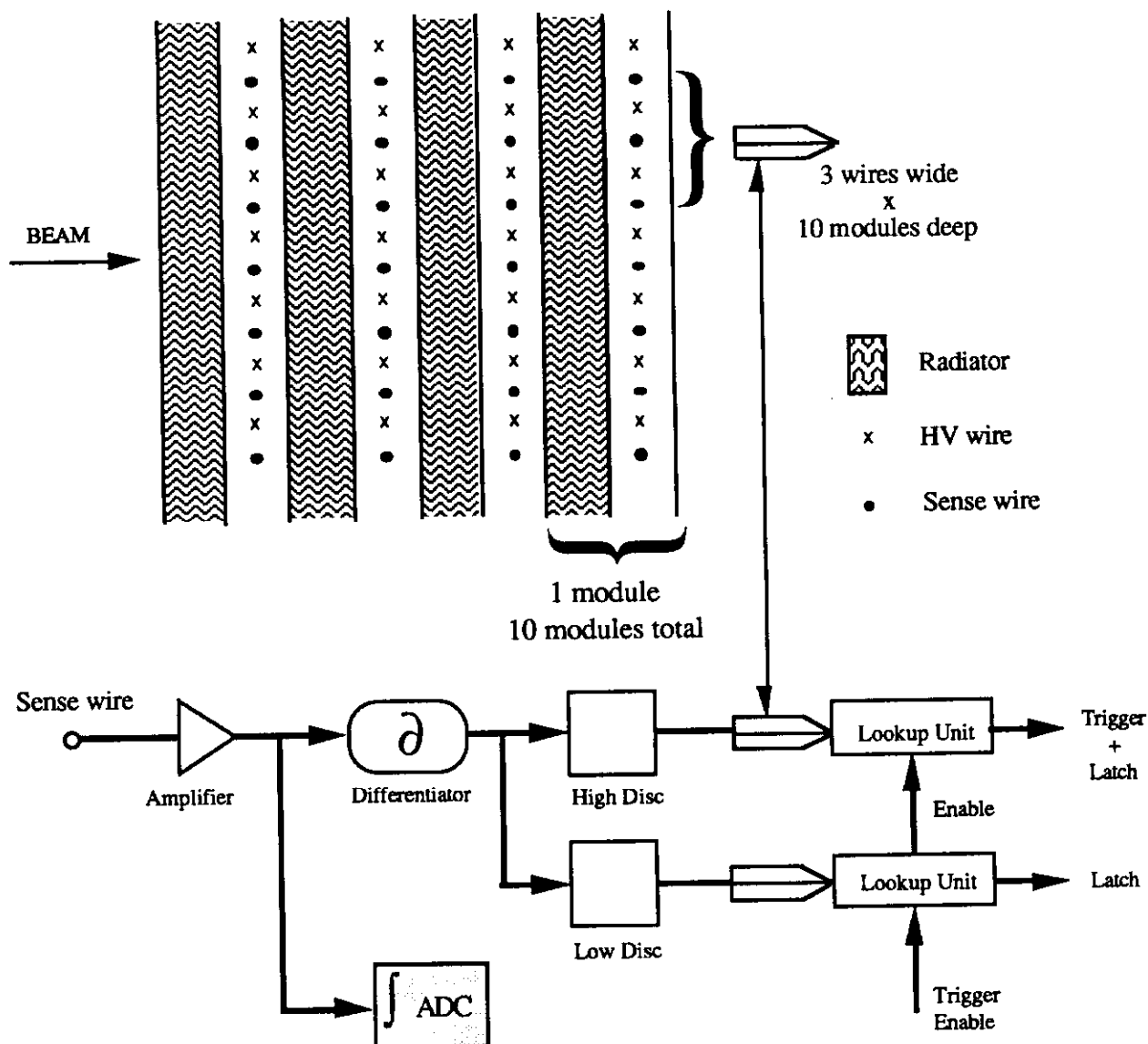


Fig.4.6.3: TRD Electronics and trigger schematics.

## 4.6.2 Recirculating Xenon Gas System

The high cost of xenon gas, (\$11-\$14/liter), prohibits the use of a standard chamber gas system in which gas is exhausted to the atmosphere after passing once through the chambers. For the duration of the P832 and E799II runs, the cost in xenon of a standard single pass system would exceed three million dollars. Hence, the long term use of transition radiation detectors (TRDs) for particle identification requires an attendant

recirculating gas system. Such a system has been designed and built for E799I, and recirculated xenon gas for the three month duration of that run. This system met or surpassed the following design goals, all of which are critical to the successful operation of the TRDs. The architecture and performance of this gas system can be found in the Fermilab technical memo, FERMILAB-FN-574.

1) Differential pressure control:

Since any closed recirculating system is decoupled from the atmosphere, the differential pressure across the large thin mylar windows that separate the atmosphere from the active xenon mixture must be controlled to better than 0.01 inches of water. This upper limit of differential pressure corresponds to a 1 mm displacement of the aluminized mylar cathode planes that define the proportional volume, which in turn translates directly to a 10% change in chamber gain. Atmospheric pressure changes by as much as several inches of water daily, which the gas system must be able to track continuously.

2) Gas contaminant monitoring and purification:

Atmospheric contaminants that diffuse through the thin mylar windows would quickly build up to intolerable levels if there were no mechanism on-line to remove them. Most severe are oxygen and water vapor. Both these contaminants were reduced to negligible levels by passing the mixture through heated metal catalysts and molecular sieve material. The level of oxygen contamination was monitored on-line continuously, and always kept below 60 ppm. In contrast, no effort was made to remove nitrogen, which entered the system at 300 ppm/hour. Every two days the stability of the xenon/quench mixture, as well as the fraction of nitrogen, was monitored offline with a gas chromatography.

3) Xenon recovery:

In order to keep the equilibrium concentration of nitrogen less than 1%, a small fraction of the xenon mixture was continuously bleed to a cryogenic xenon recovery system. Also, when a chamber was in need of internal repair, that chamber's volume of gas was bleed to the cryogenic recovery system. Once a recovery system tank was full, it was sent to a commercial gas supplier for purification back



to xenon stock.

In preparation for the KTeV program, the recirculating gas system will be upgraded so that a single chamber's volume of gas can be recovered quickly, while the other chambers remain in circulation. Currently the recirculating system must be idle while an individual chamber's volume is slowly recovered. In addition, a high sensitivity gas chromatography will be available on-line, so that gas problems related to mixture or contaminants will be discovered and rectified quickly. This gas chromatography will also be able to analyze samples supplied externally for self calibration and monitoring of the drift chamber gas.

The cost of these combined upgrades will be 25K\$-30K\$, and will be paid for by the Fermilab physics department. The system will be maintained by the Fermilab physics department, and will require a 1/4-1/2 time technician for daily maintenance and monitoring.

## 4.7 CsI Electromagnetic Calorimeter

The most important new detector component in the KTeV spectrometer is the precision electromagnetic calorimeter, consisting of bars of pure CsI crystals. The choice of pure Cesium Iodide was motivated by its radiation hardness, speed, and light output. In addition, it is important that there has been considerable experience in the manufacturing of large arrays made of CsI. This is in contrast to BaF<sub>2</sub> which is in addition significantly more expensive. The combination of these features make it the best choice to achieve the required energy resolution in the high rate and moderate radiation environment of the KTeV experiment.

### 4.7.1 General Requirements

We begin by simply listing some of the most important characteristics and design requirements of the elements of the calorimeter.

#### CsI

- Light Yield: 40 photo-electrons/MeV energy deposit
- FWHM: 25 ns
- 2232 2.5 cm × 2.5 cm × 50 cm blocks (120 cm × 120 cm)
- 1024 5 cm × 5 cm × 50 cm blocks (out to 2 m × 2 m)
- 1 muon ≈ 320 MeV ≈ 9 k photoelectrons (p.e.)

#### Phototube/cable

- peak cathode current (80 GeV):  $3.2 \times 10^6$  p.e. ≈ 20 μA
- gain: 8,000 maximum; 4,000 nominal
- peak anode current: 80 mA or 4 V into 50 Ω
- linearity within 1% to 80 mA
- 1 muon: 16 mV
- noise on cable (low frequency): ≤ 10 μV

#### ADC

- dual range 12 bit ADCs
- low range: 2 MeV/count (up to 8 GeV)

- high range: 20 MeV/count (up to 80 GeV)
- low range sensitivity: 50 fC/count (same as LeCroy 2280)
- high range sensitivity: 500 fC/count
- noise level:  $\leq 1/2$  count rms

## Energy Resolution Expected

$$-\frac{\Delta E}{E} = 0.3\%_{\text{const.}} + \frac{0.5\%}{\sqrt{E}}_{\text{stat.}} + \frac{0.9\%}{E}_{\text{noise}}$$

- assumes 30 blocks are read out, incoherent noise

These requirements to achieve an accuracy of  $10^{-4}$  on  $\epsilon'/\epsilon$  are set largely by our experience with lead glass in E731 where the electromagnetic calorimetry limitations have been thoroughly understood. An energy resolution of 1% and a position resolution of 1 mm at the mean photon energy of 15 GeV is required. We are attempting to reduce the systematic error on  $\epsilon'/\epsilon$  by a factor of three and these figures represent a factor of three improvement over that achieved in E731. As is seen above, even better resolution is expected. Since much of the benefit of excellent resolution is lost if significant non-Gaussian tails are present in the energy response, we require a line-shape as close to Gaussian as possible. The energy response of the calorimeter should be linear; when we parametrize the energy response as  $E_T = E_M^{(1-\alpha)}$ , where  $E_{T(M)}$  is the true (measured) energy, then the parameter  $\alpha$  must be less than 0.5%. In E731,  $\alpha$  was typically 3% but became significantly worse for blocks near the beam holes where the radiation damage was the greatest. It is understood that a non-zero  $\alpha$  results from light attenuation in the crystal, a 3% number corresponding to roughly 3% per radiation length effective attenuation. Finally the CsI crystals near the beam holes should show no loss of light after a radiation dose of a maximum of 10 kRads expected in KTeV.

Based upon simulation studies and beam tests, the CsI calorimeter we proposed will meet or exceed these specifications. The EM calorimeter has transverse dimensions of 2.0 meters by 2.0 meters which allows good acceptance for 4-body decays while being well matched to the size of the rest of the KTeV spectrometer. A drawing of the calorimeter is shown in Fig. 4.7.1.

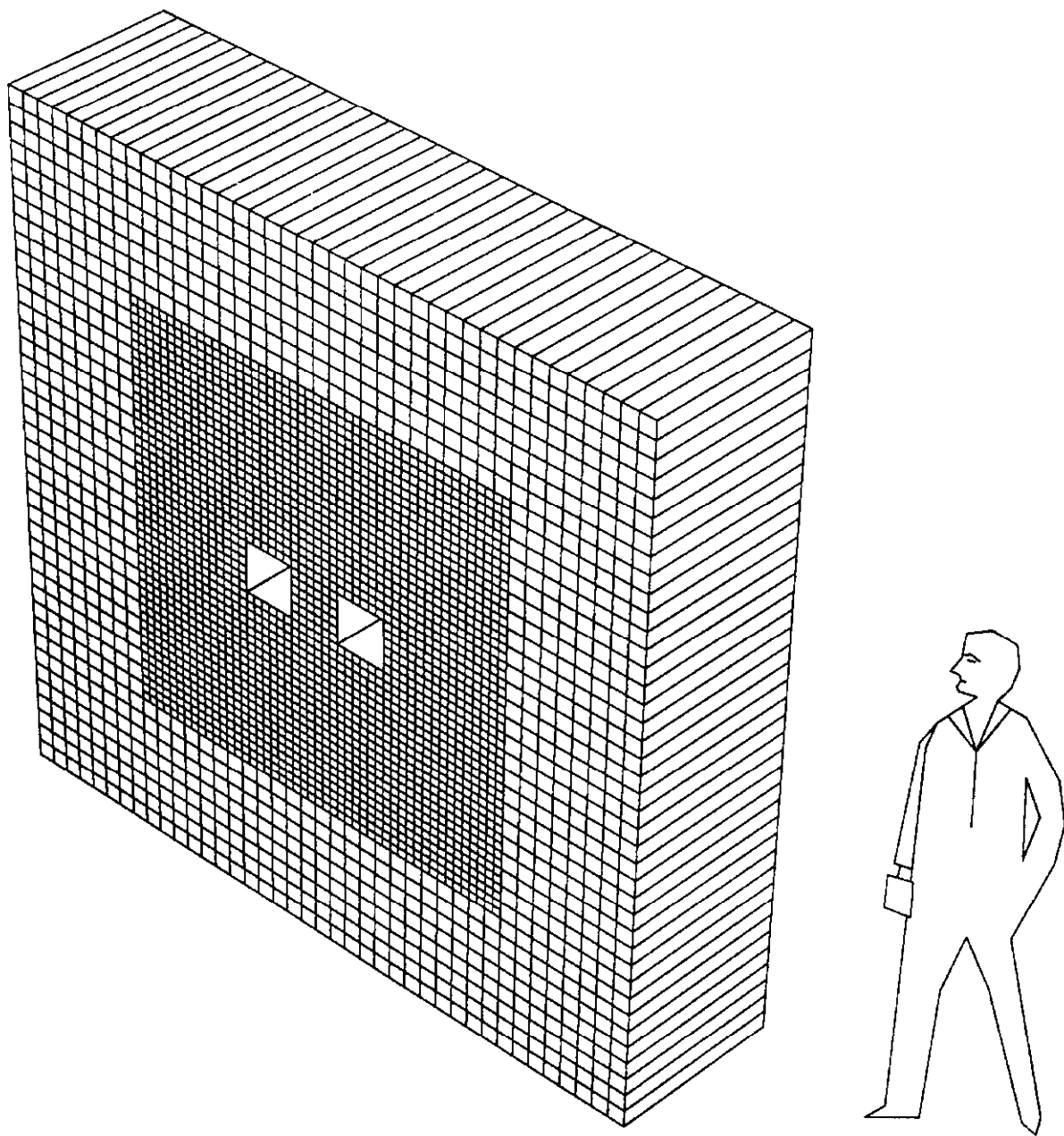


Fig. 4.7.1: Beam view of the KTeV 2 m x 2 m CsI calorimeter array.

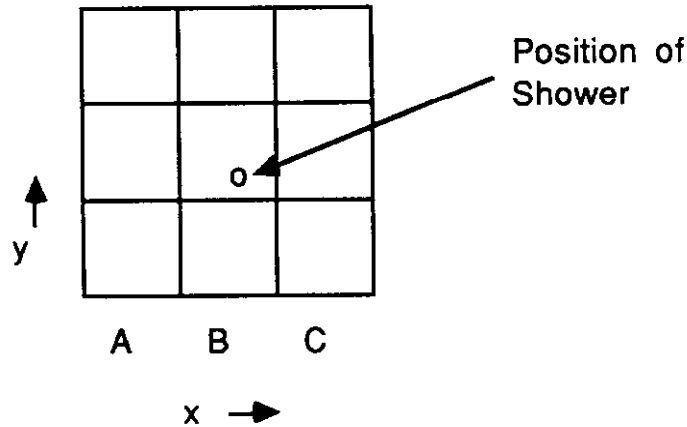
Several of the major deficiencies of the Lead Glass calorimeter will not be problems with the CsI calorimeter. First, CsI has been shown to be radiation resistant. As we will describe in a later section, good samples of CsI crystals show no decrease in light output at exposures of greater than 15 kRads. Second, CsI crystals can be prepared so that the light collection efficiency is a constant over the length of the crystal, removing shower depth fluctuations as a source of energy smearing and non-linearity. Finally, CsI typically can produce 40 photo-electrons per MeV energy deposit leading to an  $0.5\%/\sqrt{E}$  photostatistics term in the resolution; this will be a negligible contribution to the resolution at energies above a few GeV.

In the following sections we will describe the components of the EM calorimeter. The results of Monte Carlo simulations, leading to the dimensions of the CsI crystals, will be given. Then the characteristics of the CsI crystals, photomultiplier tubes and bases, HV supplies and the light flasher monitoring system will be given. The climate controlled environment for the crystals will be discussed and the calibration procedure for the array and its electronics will be given.

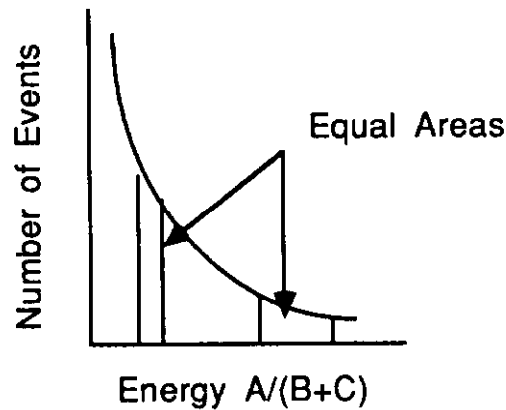
## **GEANT Simulations of Cesium Iodide**

To set the size of the crystals for E799II/P832, we used the GEANT Monte Carlo package to simulate photon showers in cesium iodide. The size of the crystals transverse to the beam direction determines the position resolution for photon showers, with smaller crystals giving better resolution. The length of the crystals is the most important determinant of the energy resolution. Since the energy resolution is determined by how much of an incident photon's energy is deposited in a crystal, the longer a crystal the better the energy resolution. In addition, to minimize tails in the energy distribution, we want to maximize the length of the CsI crystals to reduce the detrimental effects of shower fluctuations on the measurement of  $\epsilon'/\epsilon$ .

In our simulations, we deposited photons of various energies uniformly across the face of a CsI block. To determine the position resolution in blocks of a given size, we sum up the energy in columns of crystals as shown in the following figure.



Since the crystal is uniformly illuminated across the face, when we plot the fraction of energy deposited in column A, equal areas underneath the curve will correspond to equal distances along the face of the crystal.



A lookup table based upon this energy ratio versus impact point along the crystal face is used to give the expected position resolution. Our simulations were run at several energies; Fig. 4.7.2 shows the resulting position resolution as a function of photon energy for two different block sizes, 2.5 cm and 5.0 cm. In P832 the majority of photons are in the energy range from 10 to 40 GeV, which indicates that for 2.5 cm blocks we can achieve better than 1.0 mm resolution.

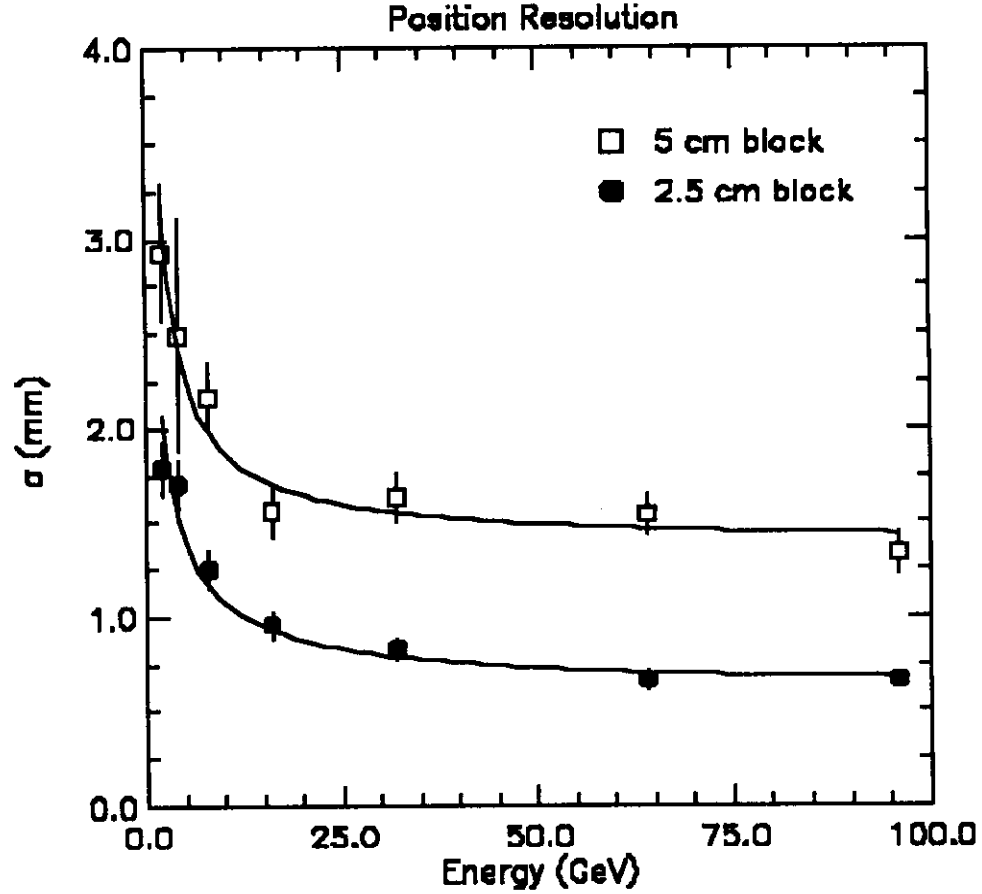


Fig. 4.7.2: Position resolution versus incident photon energy for 2.5 cm and 5.0 cm CsI blocks from GEANT simulation.

Although the cost of the CsI is nearly independent of the crystal dimensions, the other associated costs (phototubes, cables, electronics) directly scale. We have thus investigated using a calorimeter made up of both sized blocks. Since the highest energy photons are deposited nearest the beam holes, we want to concentrate the small blocks in the inner region of the calorimeter. In Fig. 4.7.3 we show the  $K^0$  mass resolution (using 50 cm long crystals) as a function of the extent of the small block region (at 2.0 meters, the 2.5 cm blocks fill up the whole calorimeter; while at 1.0 m, the 2.5 cm blocks would fill the region of the calorimeter within  $\pm 0.5$  m relative to the center of the array and the 5.0 cm blocks would fill the rest array up to 2 m). Based upon this study, we have chosen to equip the central 1.2 m of the array with the smaller blocks. This then leads to a total of 2232 small crystals and 1024 large ones.

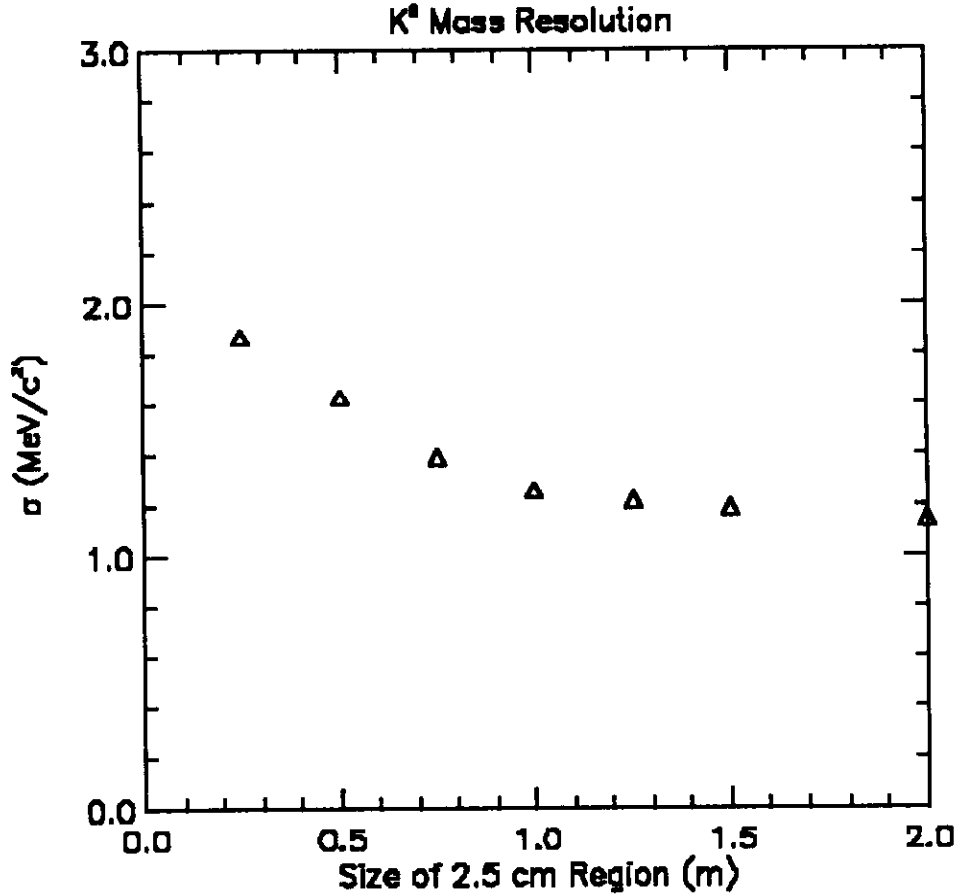


Fig. 4.7.3:  $K^0$  mass resolution as a function of the coverage of 2.5 cm blocks in the central region of a  $2\text{ m} \times 2\text{ m}$  CsI array.

To simulate the energy resolution, we used GEANT and examined the distribution in the energy deposited in a  $7 \times 7$  block array of the small CsI crystals. As shown in Fig. 4.7.4, for 20 radiation length crystals even 16 GeV showers develop a significant low-side tail due mainly to energy leakage out the back of the crystals. In the same figure one can see that if one uses crystals of 25 radiation lengths, at 16 GeV these tails although still present, are significantly reduced.



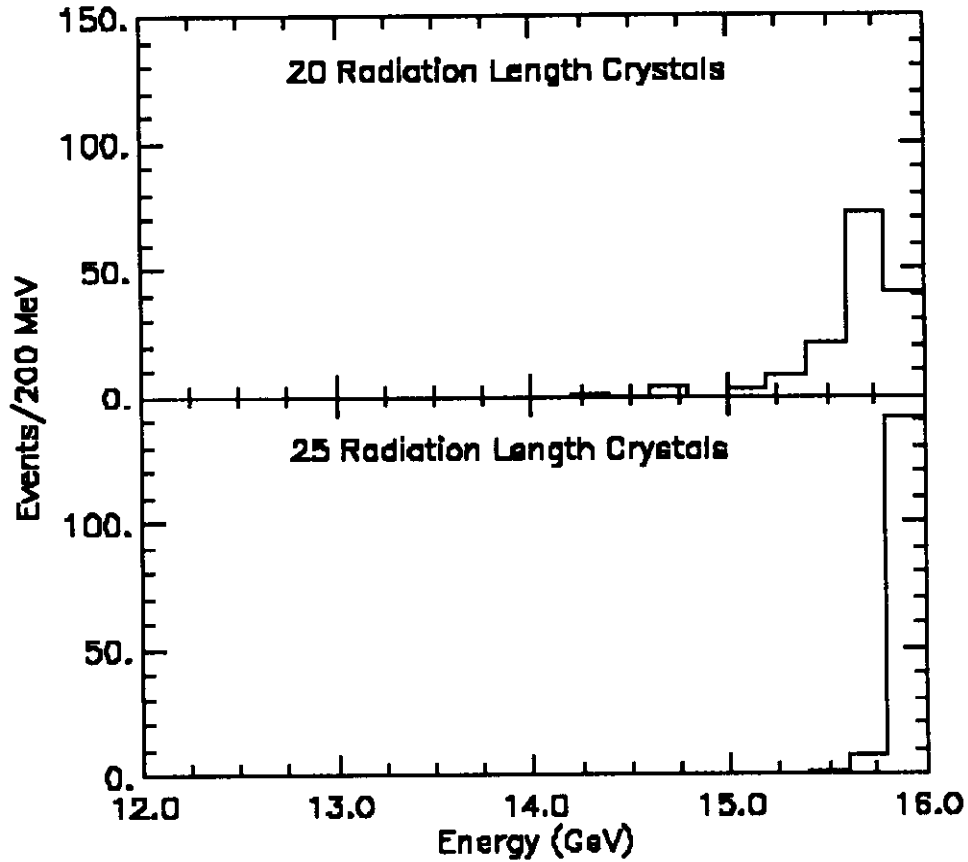


Fig. 4.7.4: The energy deposited in a  $7 \times 7$  blocks CsI array for 16 GeV photons with 20 and 25 radiation length long crystals.

In Fig. 4.7.5 we show the r.m.s. resolution of the CsI calorimeter for a variety of photon energies as a function of the length of the crystals. At the lower energies the resolution is degraded both by leakage out the sides of the crystals as well as out the back of the crystals. At higher energies, most of the resolution degradation occurs through leakage out the back.

## Energy Resolution of CsI Array

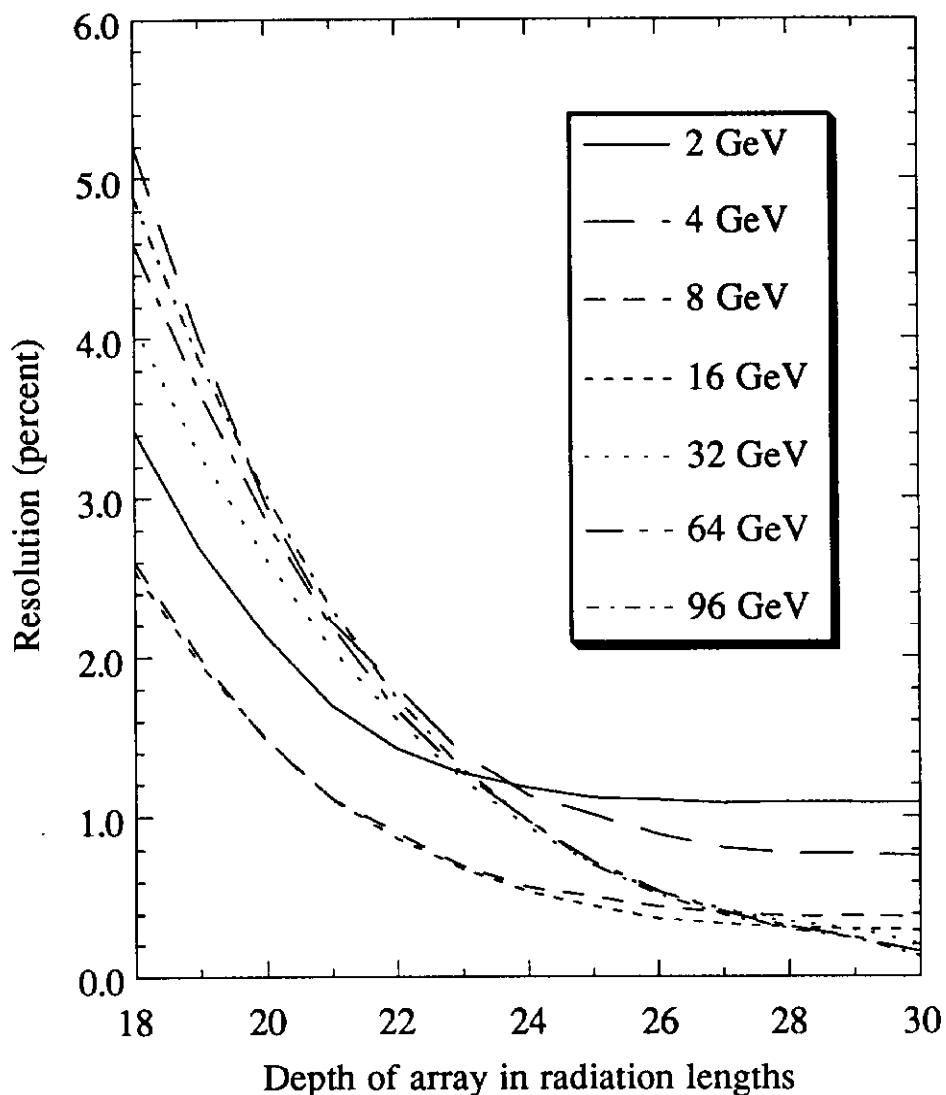


Fig. 4.7.5: Resolution of the CsI calorimeter for a variety of photon energies as a function of the crystal length in radiation lengths.

To better understand what the optimal crystal length would be for P832, we convoluted the distributions in Fig. 4.7.5 by the relative fraction of photons of a given energy expected in P832. The resulting curves are shown in Fig. 4.7.6. We plot the resolution for the vacuum beam as well as for the regenerated beam (they differ only slightly because of the similarity in the energy distributions). From this curve one can see

clearly that 20 radiation length crystals are too short and that at 27 radiation lengths the curves start to level out. We have chosen 50 cm or 27 radiation lengths for the length of our CsI crystals.

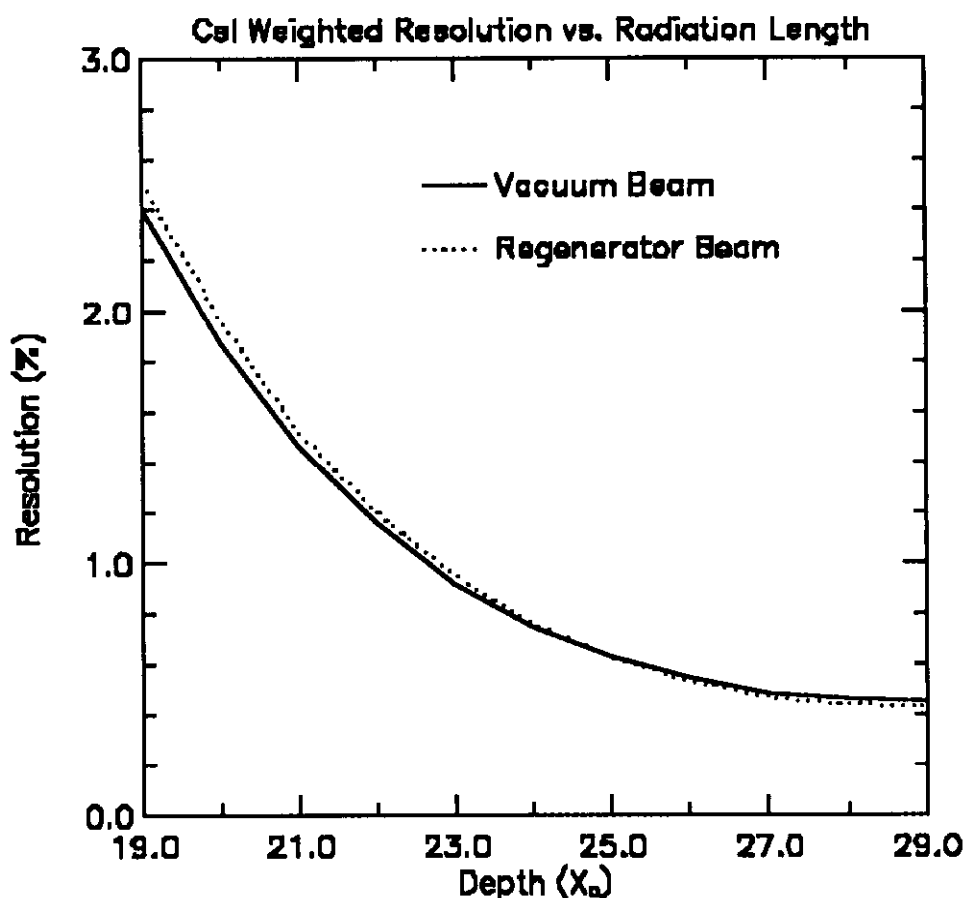


Fig. 4.7.6: Resolution of CsI calorimeter as a function of crystal length when the photon energy distribution of vacuum beam and regenerated beam was convoluted with Fig. 4.7.5.

## 4.7.2 CsI Crystal Specifications

These specifications list the mechanical and scintillation properties required of the CsI crystals in the KTeV CsI electromagnetic calorimeter. The CsI calorimeter we propose is 2.0 meters by 2.0 meters square, with blocks 50 cm or 27 radiation lengths

long. It consists of two sizes of crystals; one with a transverse size of 2.5 cm square, the other with a transverse size 5.0 cm square. Although we are in the process of procuring samples of 50 cm CsI crystals, it is not yet clear if CsI crystals can be grown this long. However, the calorimeter can be constructed using 25 cm crystals which are glued to form 50 cm blocks. Thus these specifications include provisions for either 25 cm long crystals or single 50 cm long crystals.

The physics in the KTeV experiment puts stringent requirements on the resolution and linearity of the CsI calorimeter. To achieve these demands the CsI crystals must have a uniform response along their length, a minimum of material between the crystals, and sufficient light output. Because of fluctuations in the depth of an electromagnetic shower, a non-uniform response along the length of a crystal can degrade the calorimeter's energy resolution. In Fig. 4.7.7 we show the variation in the calorimeter's resolution as a function of the fractional change in response across the length of the crystal. Given this we specify that the response be uniform to within 5% over the length of the crystal. Of course CsI crystals, especially those 50 cm long, do not have an intrinsically flat light response. To achieve this uniformity the crystals are wrapped with a reflector; we will use 0.5 mil thick Aluminized mylar. By selectively wrapping only a part of the crystal the light output can be tuned such that it is uniform along the crystal length. In Fig. 4.7.8 we show a response curve, before and after wrapping, for a glued 40 cm crystal. For this crystal, wrapping the half of the crystal furthest from the photomultiplier tube produces a very uniform response. Typically the optimal wrapping can be quickly found in two or three iterations.

Although some material for wrapping the CsI crystals is a necessity, the amount of material between crystals must be kept to a minimum. Besides the desire to keep the size of gaps in the calorimeter small, dead material can also degrade the energy resolution. In Fig. 4.7.9 we show the variation in the resolution as a function of the wrapping thickness from a GEANT simulation. To keep this contribution to the resolution to a minimum, we allow 2 mils of wrapping around each crystal. This is sufficient to wrap the crystals with Aluminized mylar for tuning, and with an optically opaque material, such as black polyethylene, to ensure that there is no optical coupling between crystals.

To achieve good resolution, we specify that the CsI crystals produce 40 photo-electrons per MeV, with the correct size photo-tubes, a cookie joint between the crystal and PMT (a cookie is a wafer made of an optical glue), and the actual crystal wrapping.

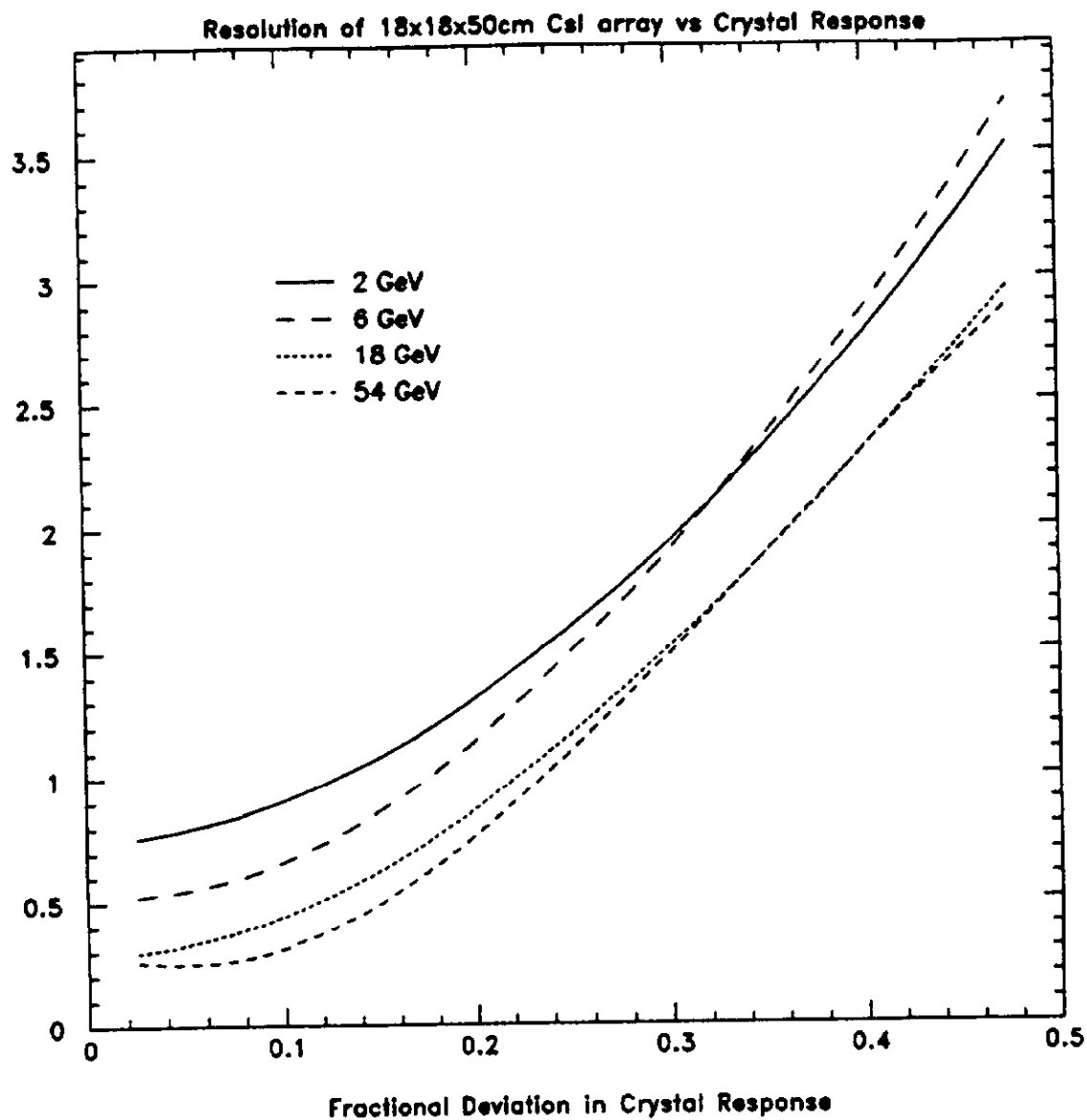


Fig.4.7.7: CsI calorimeter resolution as a function of fractional deviation in crystal response across the length of the crystal.

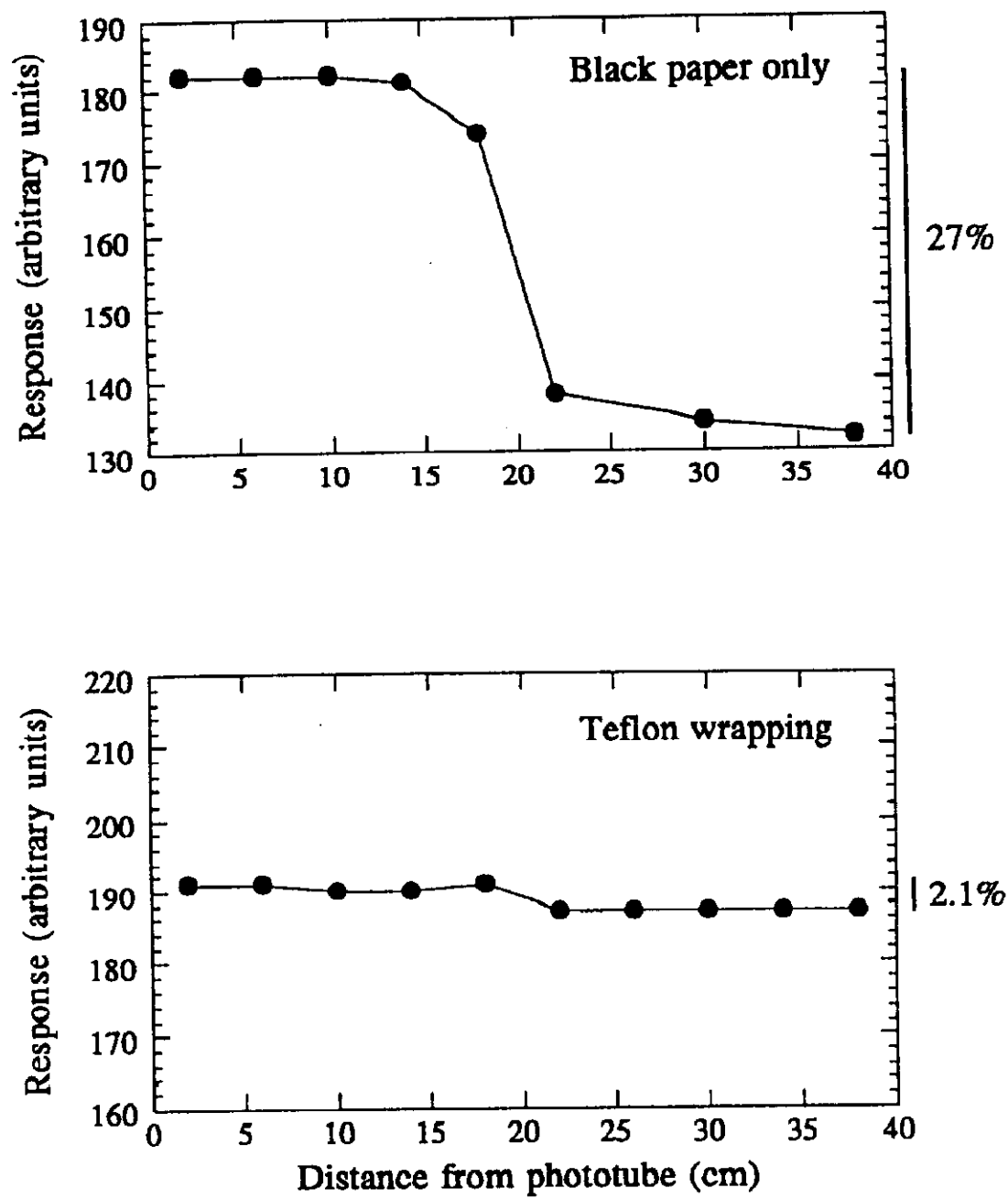


Fig. 4.7.8: CsI crystal response curve before and after wrapping.

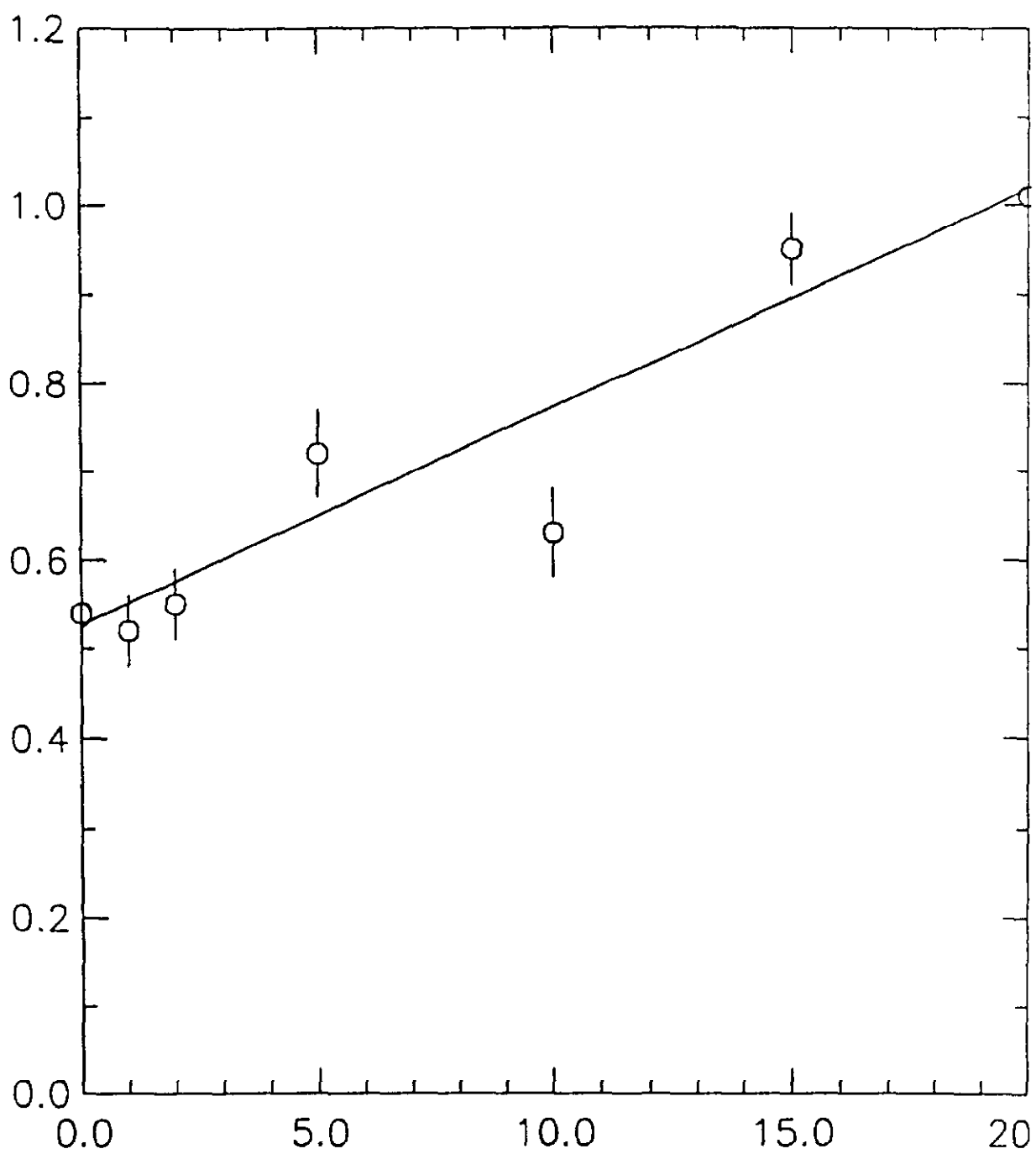


Fig. 4.7.9: GEANT simulation of the resolution in percent as a function of the wrapping thickness in mils of mylar.

CsI has both fast and slow scintillation light components. The fast component is emitted with time constants of 15 and 35 nsec, while the slow component is emitted over a couple of  $\mu$ sec. The amount of light in the slow component must be controlled for two reasons. First, the presence of too much light in the slow component indicates that the crystal contains impurities and will be susceptible to radiation damage. Second, light in the slow component from a previous K decay is a source of accidental energy in the calorimeter. CsI crystals can be routinely grown with a ratio of fast component to total (fast plus slow) of 75%-80%, and samples of such crystals show excellent resistance to radiation damage (see test results on radiation damage study in section 4.8.2). Also a fast to total ratio of ~80% is sufficient to keep accidental energy to an acceptable level. Thus we specify that the CsI crystals have a minimum fast light to total light ratio of 80%. It is also important that this ratio be uniform, to within 5%, along the length of the crystal.

Finally, there will be over 3200 crystals stacked one on top of another in the calorimeter. To maintain the geometrical integrity of the array, the blocks must be uniform in size, with parallel faces and square edges. The mechanical specifications maintain these features to within 2 mils deviation in any linear dimension. The size of the small crystals should be 25 mm by 25 mm by 500 mm or 250 mm, with tolerances of 0.025 mm by 0.025 mm by 0.5 mm or 0.25 mm. The size of the large crystals should be 50 mm by 50 mm by 500 mm or 250 mm, with tolerances of 0.05 mm by 0.05 mm by 0.5 mm or 0.25 mm.

To ensure that the crystals can be stacked parallel to the beam direction and to each other, the opposing and adjacent faces must be sufficiently parallel or square. Opposing side faces must be parallel to 0.5 arc minutes, which corresponds to a deviation of 1.5 mils over 250 mm. Adjacent side faces must be within 1 arc minutes of perpendicular, which corresponds to a deviation of 0.5 mil over 50 mm. Also the end faces should be perpendicular to the side faces to within 1 arc minutes. In the case where we glue two 25 cm crystals, this allows us to maintain the other mechanical specifications. CsI crystals are cut with a bevel at the corners. This bevel region should be uniform and 0.2 mm in size, with a tolerance of 0.1 mm. All together these requirements will allow the CsI to be stacked uniformly to within 1 or 2 mils in any direction.

The cost for the pure CsI crystal of either 25 cm long or 50 cm long bar is estimated to be \$2.5/cc. The total cost for the entire 2.m by 2 m array is then estimated to be \$5 M for the crystal and \$60 k for the wrapping or gluing.



### 4.7.3 CsI Phototube

Although photomultiplier tubes are conventional devices and have a long history in High Energy experiments, the requirement from the proposed precision calorimeter is more challenging than any other applications in the past in terms of linearity and stability.

Basic specifications are summarized in Table 4.7.1. First, a gain is determined by the ratio of the full scale of the ADC and the expected maximum photo electron yields from electromagnetic showers in CsI. We expect a gain of 8000 at less than 2000 V. This rather low gain leads to a new development of fewer dynode stage than conventional PMTs.

Table 4.7.1: Specifications for Phototubes for CsI Calorimeter

Gain .....  $8 \times 10^3$  at  $< 2000$  V

Assuming that the dynamic range of CsI block is  $80 \text{ GeV} = 2000 \text{ pC}$ , and that we get 40 photoelectrons/MeV, then the nominal gain should be :

$$\frac{2000\text{pC}}{80\text{GeV} \times 40 \text{ pe/MeV} \times 1.6 \times 10^{-19} \text{C/e}} = 3900$$

With a safety factor of 2, we expect a gain of 8000 at  $< 2000$  V.

Rate dependence of gain .....  $< 0.5\%$  for 100 kHz  
for 10 mA pulse

Quantum efficiency .....  $> 20\%$  at 320 nm

Pulse linearity .....  $< 1\%$  at  $< 100$  mA

By tuning the nonlinearity to 10% of itself in the base, we should be able to keep the overall linearity to 0.1%, which is smaller than the constant term in the energy resolution.

Cathode linearity .....  $< 1\%$  at  $1 \mu\text{A}$  at cathode

Rise time .....  $< 2$  nsec

Transit time spread for single photo electron .....  $< 1.5$  nsec

Anode uniformity .....  $< \pm 20\%$

Diameter .....	3/4" for 2.5 cm block
	1.5" for 5 cm block

We have been closely collaborating with Hamamatsu Photonics Co. in Japan in developing 6 stages of linear focus type PMT. The 1-1/8" diameter PMT's (R4598) with such structure have already been developed and fifty of them have been manufactured for our beam test last year. The results have been satisfactory so far. Fig. 4.7.10 shows a typical gain curve as a function of high voltage.

The final design of the calorimeter requires two different sizes of PMT's: 3/4" diameter for 2.5 cm blocks and 1.5" diameter for 5 cm blocks. The first five prototypes of each size have recently been manufactured and are now under systematic study.

Among other specifications, anode pulse linearity is the most critical, since it directly affects the constant term of the energy resolution of the calorimeter. A constant term of less than 0.5% suggests that the pulse linearity should be maintained under less than  $\pm 1\%$  deviation over the expected full range of up to 80 mA. The pulse non-linearity is caused by the space charge effect on the later stages of dynodes. To avoid this, the mechanical structure of the dynodes must be carefully optimized to supply a large enough electric field to sweep away secondary electrons emitted from the surface of the dynodes. It is also important to optimize the high voltage ratio between each pair of dynodes. We have been working with Hamamatsu to optimize these parameters to achieve the best performance in linearity.

It should be pointed out that the systematic measurement of linearity with better than  $\pm 0.5\%$  accuracy is not an easy task. At UCLA, a computer controlled system for linearity measurement is now under development. The first result obtained by this system is plotted in Fig. 4.7.11 for 1-1/8" PMT (R4598). By using this system, the first five prototypes of each size will be measured soon.

Other specifications are less demanding and they have already been achieved by existing conventional PMT's. For confirmation, we have measured several basic parameters such as anode gain uniformity and pulse shape. Fig.4.7.12 shows anode uniformity and Fig.4.7.13 shows the pulse shape for a very fast (30 psec) laser signal. The rise time is about 1 nsec and the fall time is less than 2 nsec.

# V-I AND AMPLIFICATION CHARACTERISTICS

TUBE TYPE R4125

1991.10.18

A. TAKAHASHI

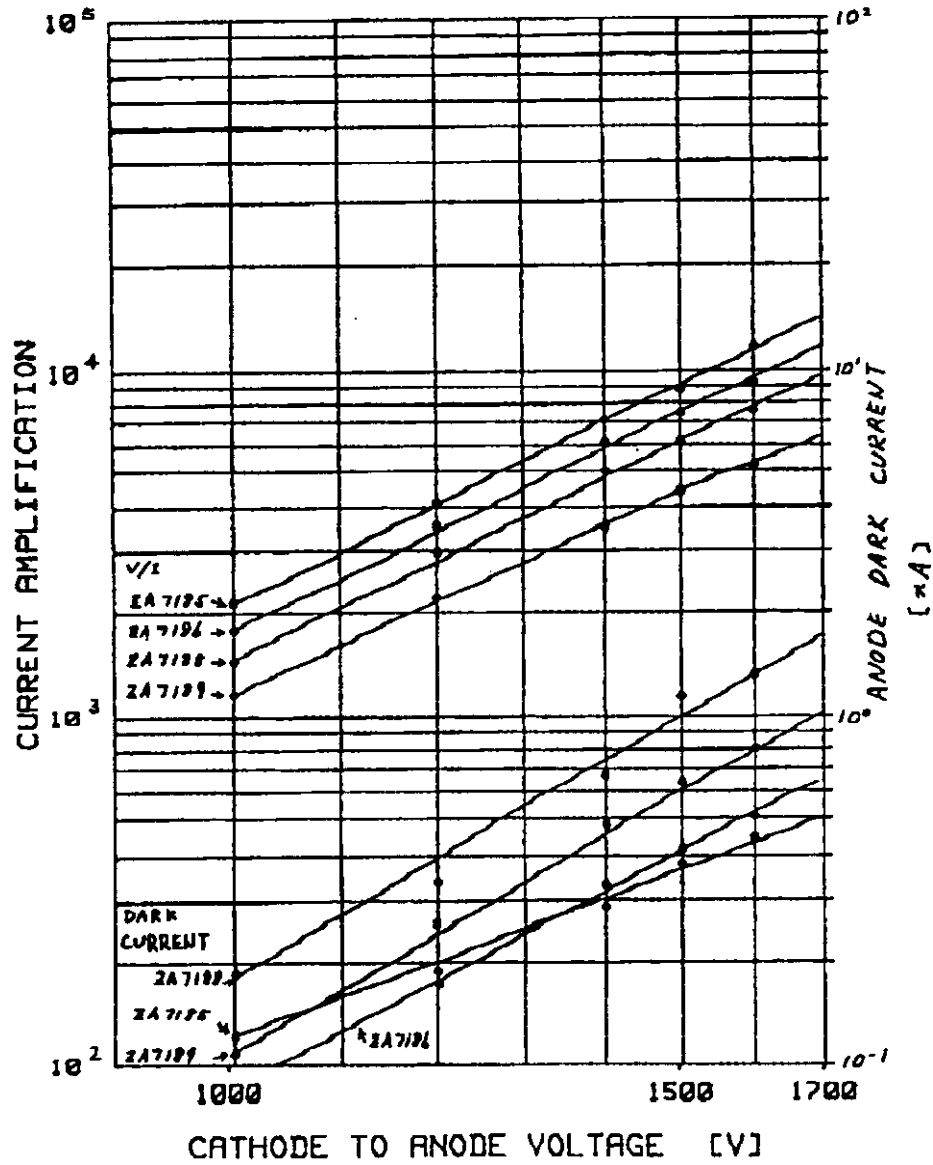


Fig. 4.7.10: A typical PMT gain curve of Hamamatsu R4598 as a function of high voltage.

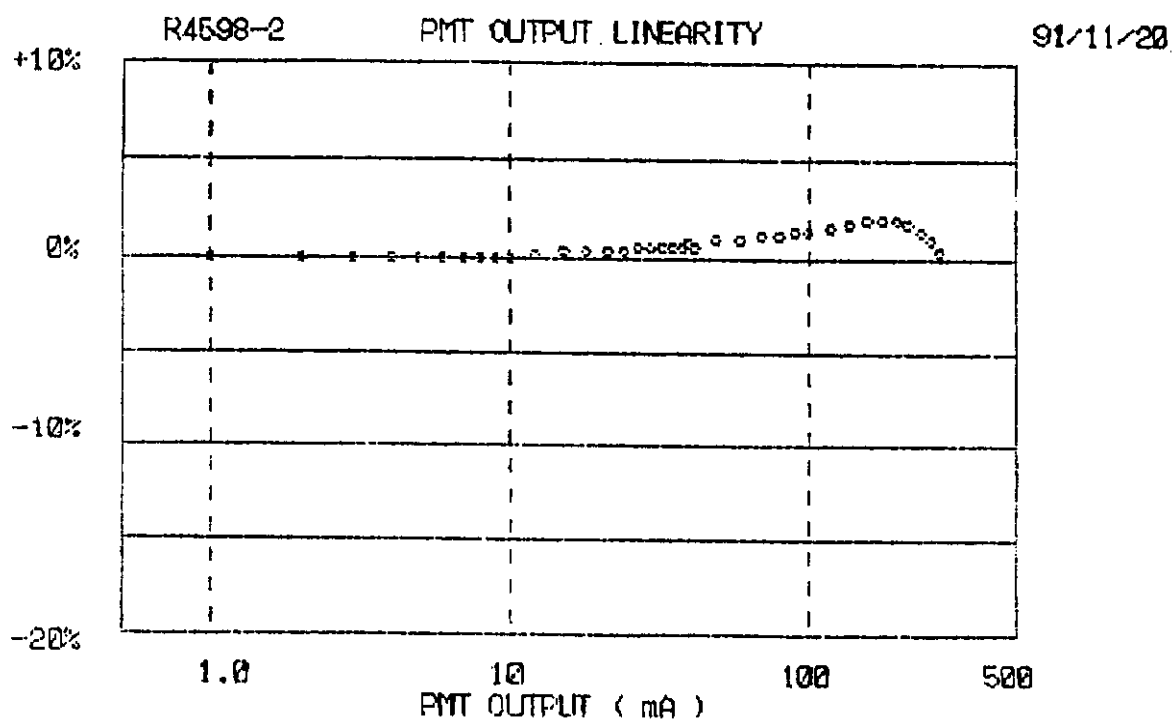
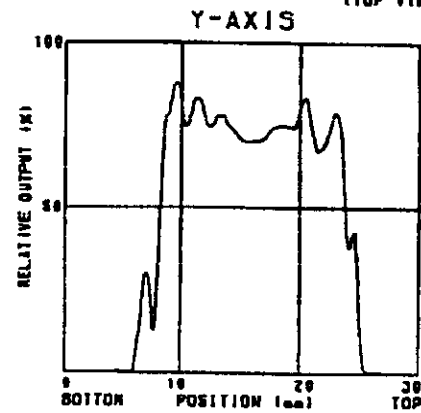
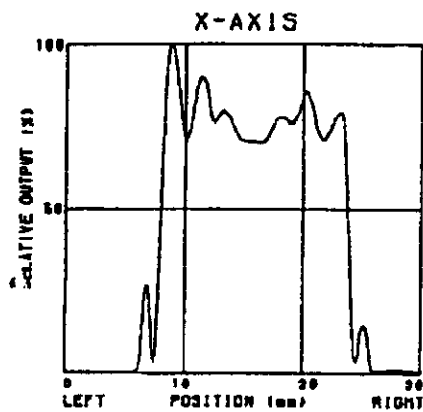
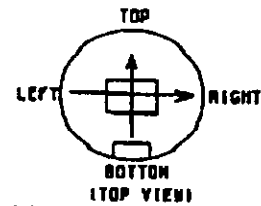


Fig. 4.7.11: PMT linearity measurement of Hamamatsu R4598.

## X-Y UNIFORMITY

TUBE TYPE : R412S  
 SERIAL NUMBER : ZA7186  
 SUPPLY VOLTAGE : -150 (V)  
 WAVELENGTH : 400 (nm)  
 SPOT DIA. : 1.0

DATE : 01/10/17  
 TESTED BY : A.SAKAKOTO  
 COMMENT :  $I_a=250\mu A$



## X-Y UNIFORMITY

TUBE TYPE : R412S  
 SERIAL NUMBER : ZA7186  
 SUPPLY VOLTAGE : -1500 (V)  
 WAVELENGTH : 400 (nm)  
 SPOT DIA. : 1.0

DATE : 01/10/17  
 TESTED BY : A.SAKAKOTO  
 COMMENT :  $I_p=2.02\mu A$

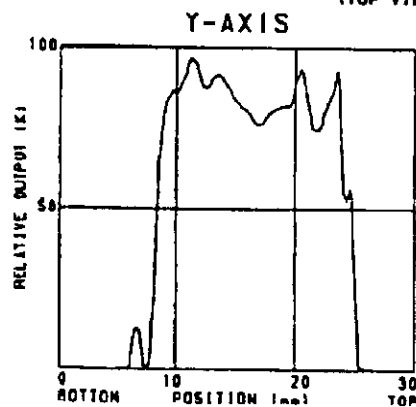
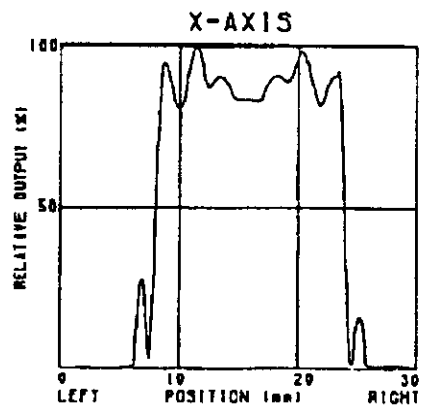
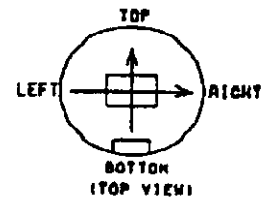


Fig. 4.7.12: Anode Uniformity.

4 - 8 RISE TIME (BLEEDER RATIO 1.5:1:1:1.5:1.6:2.7:2.4)

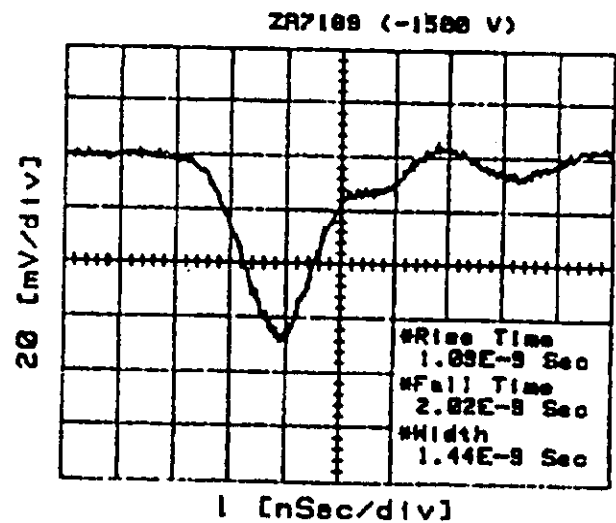
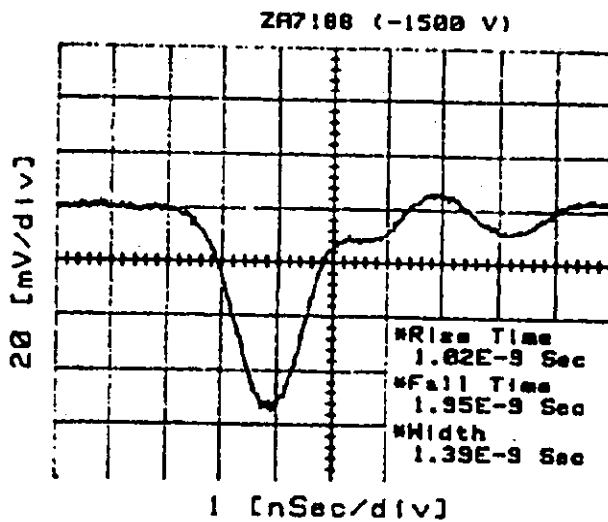
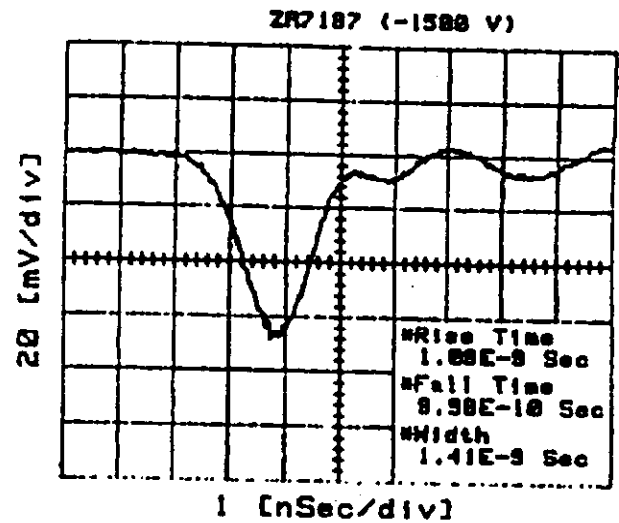
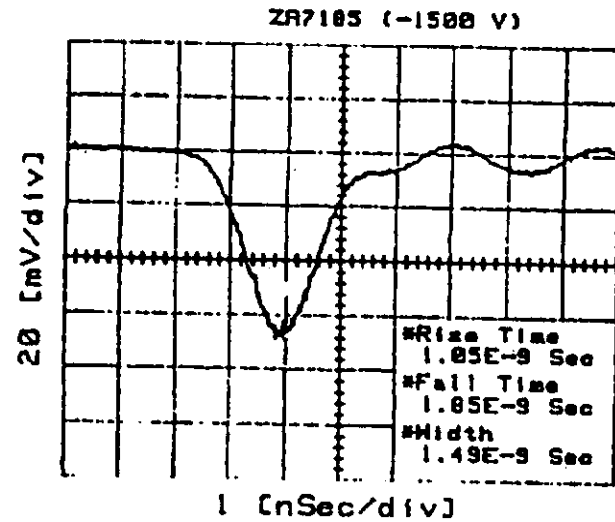


Fig. 4.7.13: Pulse shape from a very fast (30 psec) laser signal. Rise time  $\approx$  1 nsec, fall time  $<$  2 nsec.

#### 4.7.4 CsI PMT Base

The primary purpose of the PMT base is to provide constant voltages for the photo-cathode and for each dynode stage. First, the ratio of voltages must be carefully tuned to achieve the best pulse linearity. Second, to keep the voltages constant with better than 0.5% accuracy, independent of current draw by each stage, a stabilized constant voltage source is necessary particularly for the last few dynodes because of their large currents.

To satisfy this requirement, a new type of transistorized base has been designed by Hamamatsu in collaboration with the KEK-E164 group. Fig.4.7.14 shows the present design for six-stage PMT's (R4598) in which the last three stages are stabilized by transistors. All the parameters have been optimized to achieve the best pulse linearity under the maximum anode current of up to 100 mA, which is expected from the CsI crystals around the beam hole. Our study shows that this base is stable within  $\pm 0.4\%$  variation up to 400  $\mu$ A of DC current. Fifty transistor bases have been manufactured and used for the beam test with R4598 PMT's.

Based on this experience, we will further optimize the base design in terms of performance and cost. Once the final optimization is complete, mass production will be carried out either by Hamamatsu or UCLA/Osaka, depending the final price quoted by Hamamatsu.

#### Cost of Phototubes and Bases for CsI Calorimeter

item	qty.	unit price	cost
1.5" phototube	1024	\$237	\$243 k
3/4" phototube	2232	\$233	\$520 k
phototube base	3254	\$80	\$260 k
Total			\$1023 k

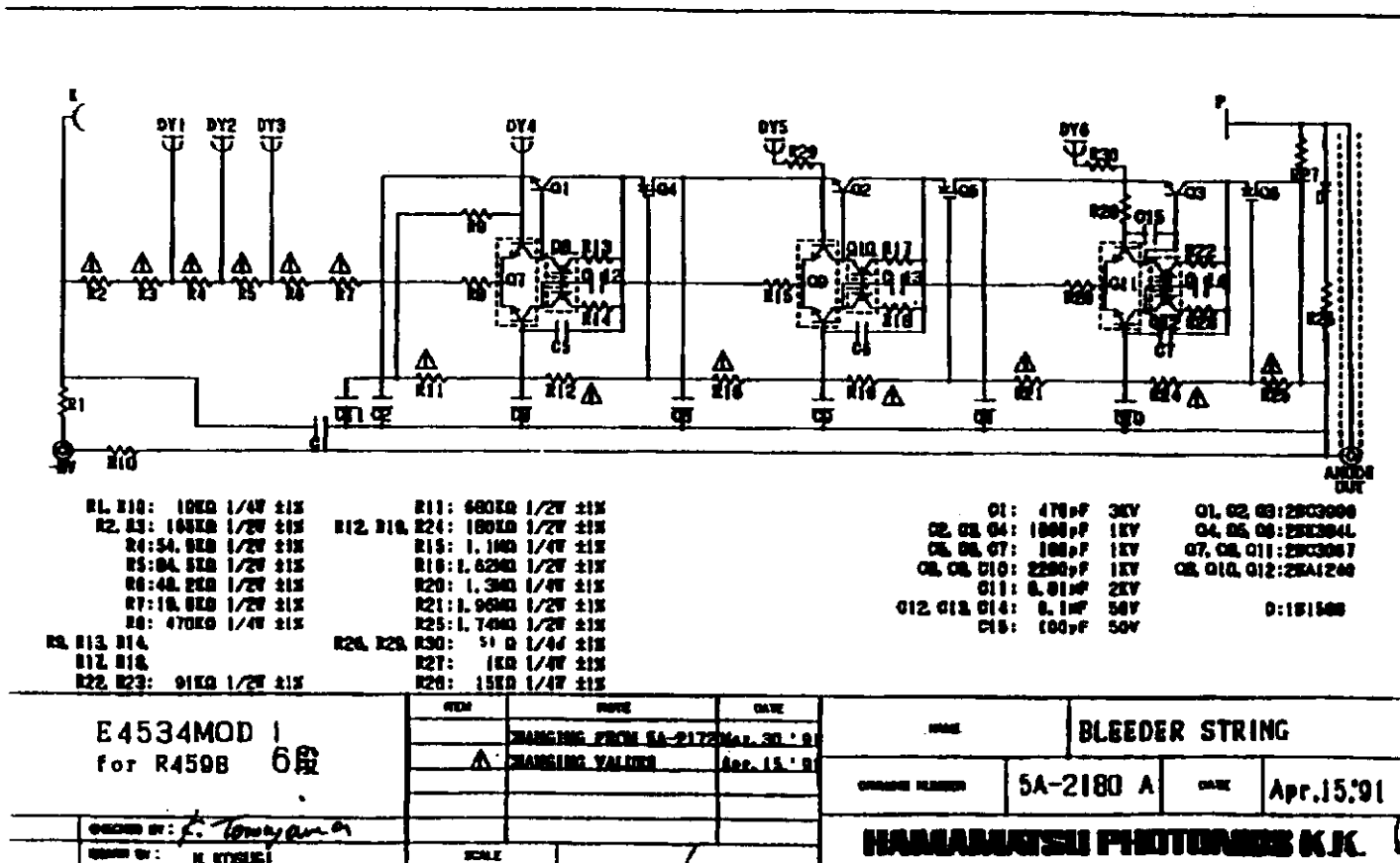


Fig. 4.7.14: Present PMT base design for a 6-stage PMT (R4598).



#### 4.7.5 CsI High Voltage Power Supply

We intend to use the LeCroy 1443/12 PMT HV power supply system for the CsI calorimeter. In this section, we address the effect of HV power supply ripple.

The ripple on the HV power supplies will result in a gain variation on the PMT's which will contribute to the resolution. The fractional change in gain is related to the fractional change in supply voltage by:

$$\frac{dG}{G} = N \frac{dV}{V}$$

where N is the effective<sup>1</sup> number of dynodes in the PMT. In order to attain less than 0.1% noise contribution from the power supply ripple, we require that the ripple be less than  $.001 \times 1800 \text{ V} / 6 \text{ stages} = 300 \text{ mV} (1\sigma)$ .

LeCroy specifies for their 1443/12 16-channel HV module a maximum ripple of less than 250 mV peak to peak (less than 50 mV typical ). This easily meets our requirement.

Other interesting specs on the LeCroy system:

Voltage Regulation:	0.05% of full scale, line and load.
Full Scale:	2500 V, 2047 V, 1500 V.
Programming Step:	0.025% of full scale.
Programming Accuracy:	$< \pm(0.5\% + 2 \text{ V})$ for demand voltages $> 500 \text{ V}$ .
Programming Reproducibility:*	$< 1 \text{ V}$ at constant load and temperature after a 10 min warm up.
Voltage Monitor Accuracy:	$\pm(0.1\% + 1.5 \text{ V})$ channel-to-channel.
Monitor Long Term Stability:*	$< 1.5 \text{ V} / \text{week}$ .
Output Long Term Stability:*	$< 2 \text{ V} / \text{week}$ .

---

<sup>1</sup> In practice, the effective number of dynodes is always less than the actual number. For 10 stage tube the number is commonly 7-8. If we use the actual number of stages here we get a conservative upper bound on the gain variation.

\* The long term stability and programming reproducibility specifications may have some impact on the CsI operations.

Monitor Temperature Coefficient:	Typically 0.005%/° C, Max 0.01%/° C from 500 V to 2500 V (10 - 40° C).
Output Ripple:	< 50 mV peak-to-peak typical; < 250 mV peak-to-peak max.

#### 4.7.6 Laser Calibration System for CsI Calorimeter

The CsI calorimeter proposed for KTeV experiments E-799-II/P-832 has the potential to attain energy resolution better than  $1\%/\sqrt{E}$  with a constant term of less than 1%. To fully exploit this potential in a large array, over 3200 photomultiplier tubes must be individually calibrated to 0.1%. In this section we describe a calibration flasher system that will be used to provide standard light flashes to each photomultiplier tube that match both in spectral content and in timing characteristics the light produced by the CsI calorimeter. The system will allow measurement of photomultiplier/ADC non-linearities over the full dynamic range of the experiment.

The calibration process must address the following problems which contribute to degradation of the resolution

- gain variation of individual photomultiplier tubes with time and with rate
- non-linearity of photomultiplier and ADC response
- change in light output and transparency of individual CsI crystals.

The calibration will be obtained by a combination of

1. special  $e^+e^-$  calibration runs
2. large statistics samples of  $K_{e3}$  decays, and
3. a calibration flasher system.

The  $e^+e^-$  calibration runs will be used to obtain a "snapshot" of the calorimeter performance. Sufficient statistical precision can be obtained in a matter of hours to calibrate each channel. This technique is powerful for the initial setup of the experiment, and for

monitoring changes in individual crystals that may occur due to radiation damage. The ultimate measure of the CsI calorimeter performance will come from the  $K_{e3}$  decays. These events are taken *simultaneously with data running* and measure the calorimeter response under operating conditions that exactly match the data sample, although the offline analysis is needed to produce the required precision. The role of the flasher system is to monitor variations in the photomultiplier response that may occur over a time scale too short to track by the other two methods. In addition, a flasher system that is understood over the full dynamic range of the experiment can independently measure the photomultiplier nonlinearities for each channel and is extremely useful for commissioning and beam-off monitoring of the apparatus.

## N<sub>2</sub> Laser Calibration Systems

The ideal flasher system for a large photomultiplier tube array provides standard light flashes that match both in spectral content and in timing characteristics the light seen by the PMT in its application. Systems have been built for previous Fermilab experiments<sup>2</sup> in which a pulsed N<sub>2</sub> laser was used to excite a plastic scintillator which served as the light source. In these systems, light from the scintillator is distributed to individual photomultiplier tubes using acrylic optical fibers, and the intensity of individual flashes is monitored using a PiN diode<sup>3</sup> mounted directly on the scintillator. The basic scheme is illustrated in Fig. 4.7.15. These systems were designed for use with plastic scintillator calorimeters, and by using the same scintillator as a light source the desired spectral and timing match was attained. Because the intensity of each flash is monitored by a PiN diode, the calibration stability comes from the PiN diode rather than the laser (which is only stable at the 10% level pulse to pulse). PiN diodes have unit gain and are typically linear over several decades. An additional virtue of the system is that the scintillator light is emitted isotropically, and this provides a convenient way to fan out the narrow laser beam to service a large number of separate channels. Calibration is obtained by comparing the PMT response to the PiN diode response. Fig. 4.7.16 shows a typical PMT vs PiN diode calibration curve.

---

<sup>2</sup>H. Haggerty, private communication; M. Crisler, E711 and E774 unpublished reminiscences.

<sup>3</sup>EG&G SGD-160 silicon diffused PIN photodiode.

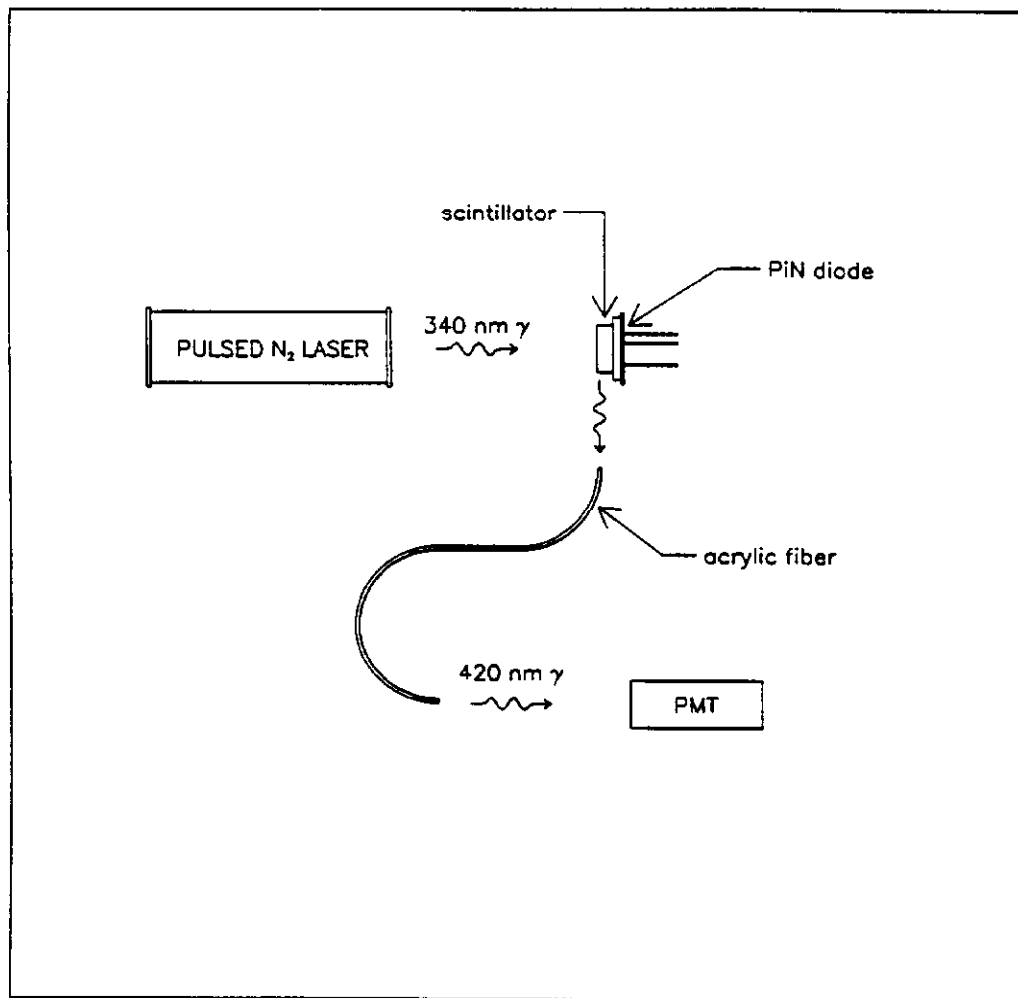


Fig. 4.7.15: N<sub>2</sub> laser calibration system used in Fermilab E711 and E774.

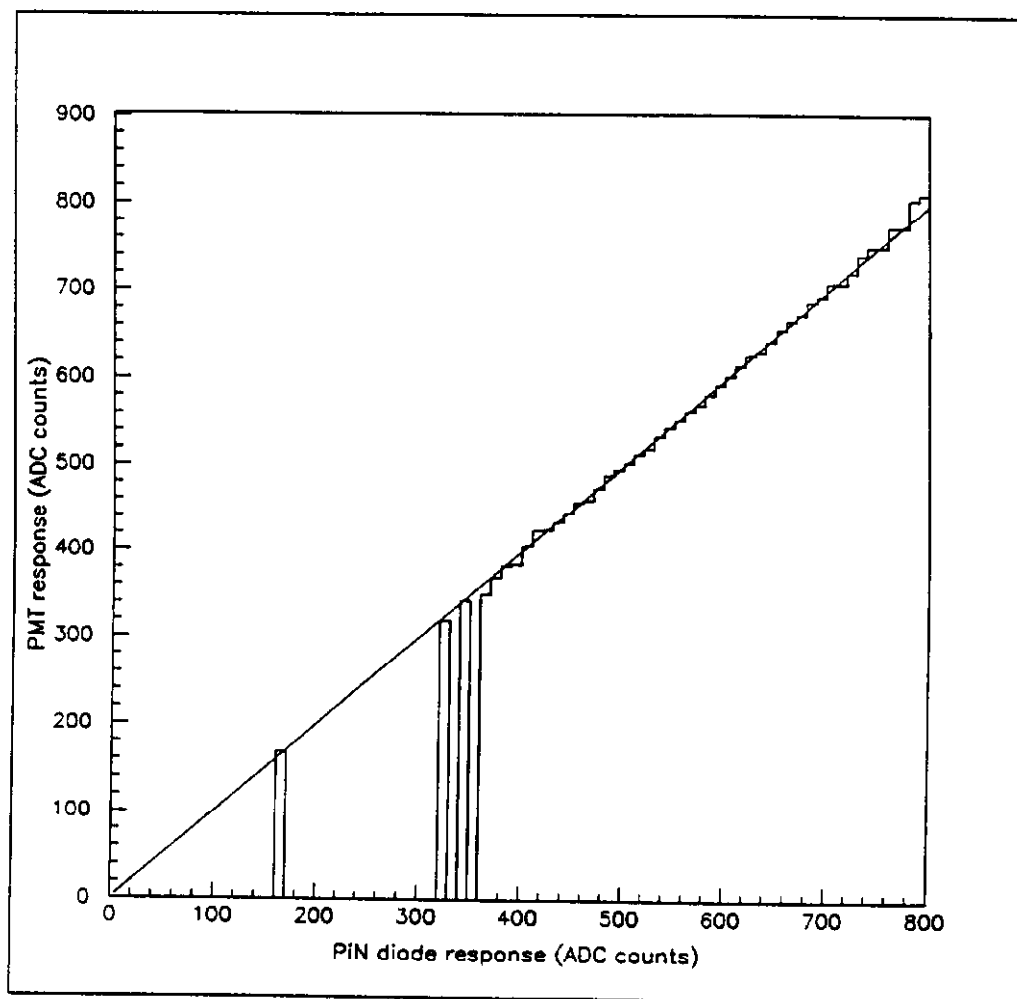


Fig. 4.7.16: Typical calibration curve of photomultiplier vs PiN diode response.

## N<sub>2</sub> Laser Flasher System for CsI Calorimeter

Such a system for the CsI calorimeter would use a CsI crystal as the light source. The technical difficulty is that CsI emits at 310 nm, and in order to excite this emission the laser must operate below the 250 nm absorption edge as shown in Fig. 4.7.17. This is well below the 340 nm frequency of the N<sub>2</sub> laser. Radiation in this frequency can however be obtained using a frequency doubling crystal and a dye laser. The N<sub>2</sub> laser is used to pump a dye laser which is tunable over the spectral range from 360 to 990 nm. The dye laser then drives a frequency doubler which shifts the operating range to 205 - 330 nm. This laser combination is commercially available, and such a system has been purchased by the Fermilab Physics Department from Laser Photonics. Because the 310 nm calibration light will not transmit through plastic, the light distribution must be accomplished using fused silica optical fibers. The system is illustrated in Fig. 4.7.18.

### Engineering Specifications

To cover the dynamic range of the experiment, the system needs to provide flashes of up to  $10^6$  photoelectrons to 3256 photomultiplier tubes. There will be losses due to photomultiplier quantum efficiency and attenuation in the fibers and due to the efficiency of CsI for converting 240 nm light into 310 nm. There are also limitations to the fraction of the CsI light that can be trapped by the fibers (distribution efficiency) and the fraction that can be delivered to the photocathode (photocathode illumination). Some of these factors are well understood, some are not. The following table lists our estimates for factors that go into the laser power calculation. Items that are not well known are indicated with an asterisk\*.

		Note
photons per channel	$10^6$	
total channels	3300	
quantum efficiency	0.20	
photocathode illumination	0.50	*
fiber transmission	0.78	
distribution efficiency	0.10	*
CsI conversion efficiency	0.10	*
photons required per pulse	$4.2 \times 10^{12}$	

energy per photon	5.16 eV	
laser power required	3.5 $\mu$ Joule	
Laser Photonics Specification	5 $\mu$ Joule	

The total cost for the flasher monitoring system is estimated to be \$228 k including \$144 k for fused silica fibers.

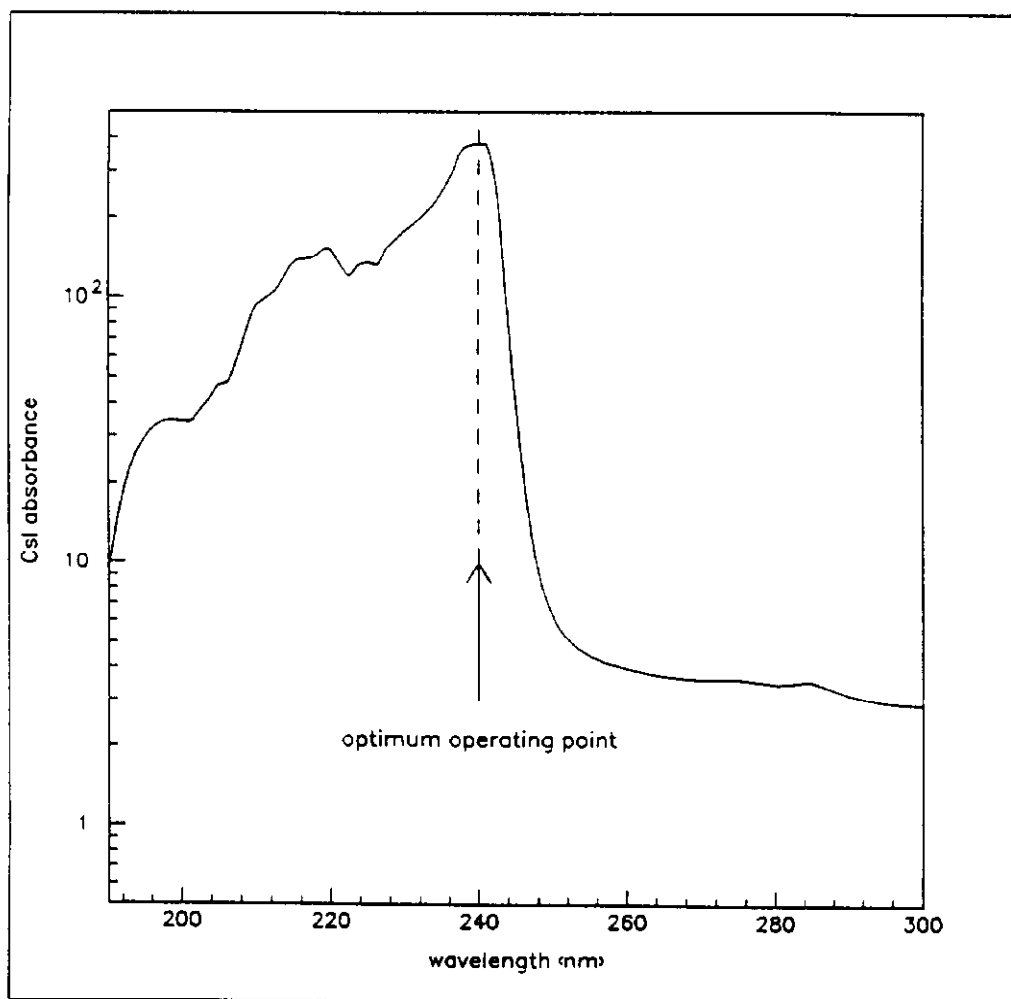


Fig. 4.7.17: CsI absorbance curve showing strong 240 nm absorption edge.

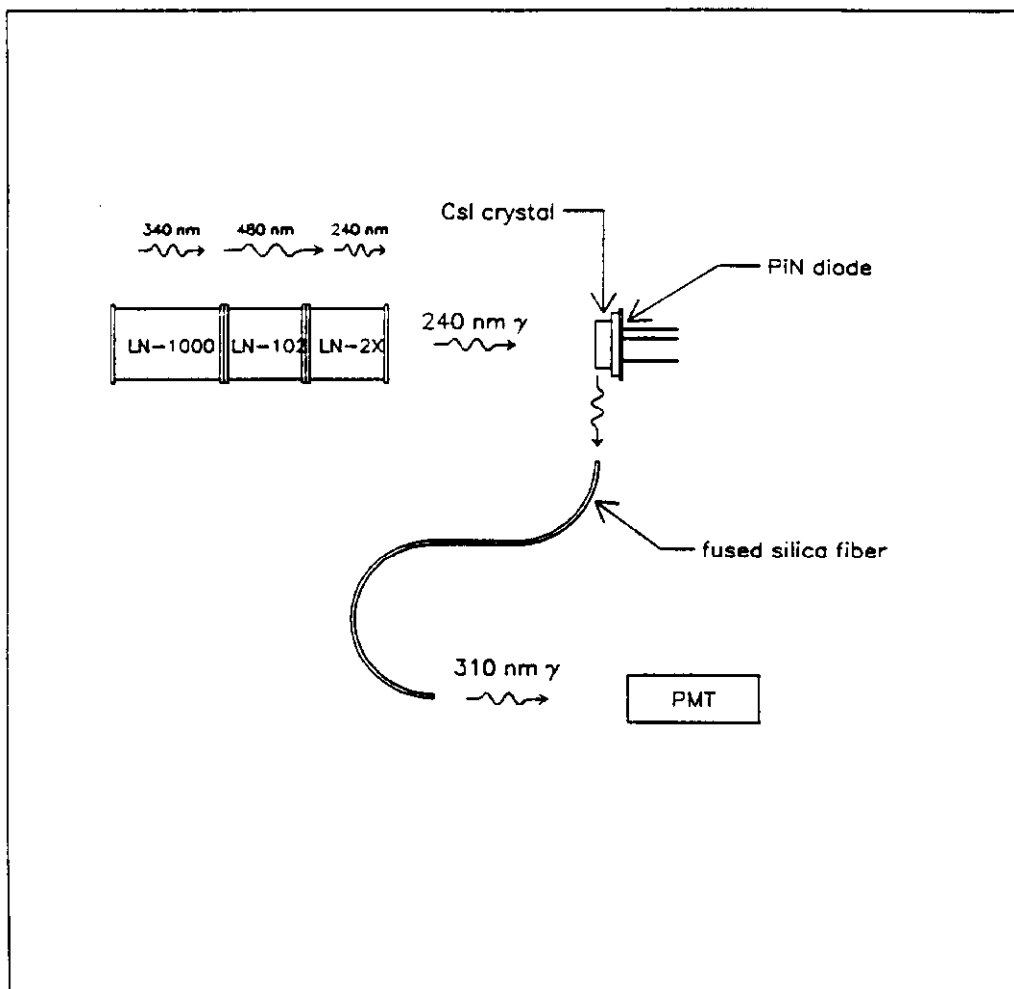


Fig. 4.7.18: Laser calibration scheme implemented for CsI calorimeter.



#### **4.7.7 CsI Calorimeter Blockhouse**

The CsI blockhouse should be heated and air-conditioned. In order to keep the nonuniformity of the crystal response due to temperature effects to within 1.5% (and thus comparable to the variation of response due to light collection effects), a constant temperature gradient of no more than 1°C along the length of the crystals must be maintained. Preliminary results from ANSYS studies by A. Lee indicate that this specification will not be difficult to meet; however, further studies are needed. Time variations in the temperature of any point in the CsI array over a time scale of a few days should be kept within  $\pm 0.5^\circ\text{C}$ , with appropriate temperature measurements to permit temperature-dependent corrections in the data analysis. Time variations on shorter time scales should be as smooth as possible, with  $dT/dt < 0.25^\circ\text{C}/\text{hour}$ , or better if possible. The total heat load from devices inside the house should be assumed to be 10 kW. This allows for a power dissipation of up to 2 watts per PMT base with an additional allowance for contingencies such as heat loads from the exterior of the house in the summer, and the possible inclusion of additional heat sources (e.g., from the flasher system) inside the house. These temperature specifications are based on the figure of  $1.5\%/^\circ\text{C}$  quoted in Woody et al., IEEE Transactions on Nuclear Science, Vol. 37, pg.492 (1990). In addition to the continuation of the ANSYS studies and detailed engineering studies of the temperature control system, measurements of the temperature dependence of the crystals' light output by our collaboration should be made.

The house should have humidity control with humidity less than 5%. Redundancy (the use of passive desiccants as well as a dehumidifier, and perhaps the use of two rather than one dehumidifier units) will be important for this system.

The house should be light tight with a darkroom door or equivalent to facilitate working on the array with high voltages on. An entry area will be needed. An interlock system should be used to insure that bright lights in the house can not be turned on while the high voltage is on. Access to the front of the array is needed; it is not necessary to permit such access in darkness, but humidity control must be maintained while working on the front of the blocks, so the design should allow for this.

The house should be at least 12' high by 15' wide by 15' deep. The dimensions of the house are related to the need to provide good air circulation for the temperature control system, so this consideration should be kept in mind during engineering design of the

temperature control.

The house should have alignment pins through the walls to facilitate surveying. We should consider the use of stereoscopic photography to allow computer-controlled readout of the locations of the crystals; this may provide additional constraints on the blockhouse design which need to be investigated.

The house will require 3300 high voltage feedthroughs, and at least 3300 signal feedthroughs. The options of bringing out the high voltage either on the opposite side of the house from the signal cables, or in pairs of high voltage cable twisted together with signal cable, need further study.

It will be desirable to have a cosmic ray hodoscope above and below the array for monitoring the performance of the crystals, particularly the absorption along the length of each block.

The cost for the temperature and humidity controlled CsI blockhouse is estimated to be about \$190 k.

#### 4.7.8 CsI Calibration

As with the lead glass in E731, E773, and E799I, a set of rigorous calibration and monitoring procedures are required for the CsI calorimeter. This bridges the gap between the precision which can be achieved for reasonable cost on a large scale at the hardware level (1-2%) and the ultimate requirements of the experiment after off-line analysis is completed (overall neutral energy scale uncertainty of 0.01 to 0.02%). To meet the gain matching and calibration requirements of the various stages of triggering and analysis, to ensure efficient detection of malfunctions in the calorimeter subsystems, and to make the procedure robust, we use a multi-stage approach along the lines employed in our previous experiments. We also take full advantage of our beam and detector configuration by performing all calibrations *in situ*. This eliminates the multitude of problems and limitations that plague calorimeters which are not easily accessible during operation and/or which cannot be fully illuminated by adequate fluxes of calibration particles.

## General Requirements

There are four general types of requirements which the CsI calibration procedures must enable us to meet.

- (1) Individual calorimeter channel gains must be matched and controlled during data taking to the accuracy required for hardware cluster finder operation. While a tolerance of  $\pm 5\%$  seems quite adequate for this, we plan to use our laser monitoring system along with periodic electron calibrations and hardware gain corrections to maintain a tolerance of  $\pm 3\%$  thereby ensuring that trigger threshold uncertainties do not pose a significant analysis problem.
- (2) Numerical gain values which are adequate for an analysis precision of about  $\pm 1.5\%$  must be available for use by Level 3 trigger processors.
- (3) For general off-line analysis, gain variation with energy (non-linearity) and with time (drift) must be monitored and numerically corrected for each calorimeter channel to a level that makes contributions from these effects to the calorimeter resolution negligible. Our basic hardware design will limit non-linearity to  $< 1\%$  (primarily from PMTs and ADCs), and time variation to  $< 3\%$  over periods of the order of one week. Periodic calibration and gain monitoring must then reduce these effects below the  $0.25\%$  level to ensure that they do not contribute significant resolution broadening.
- (4) For final physics analysis, the absolute energy scale for neutral events must be *globally determined* well enough to achieve a systematic error appreciably below  $1 \times 10^{-4}$  on  $\epsilon'/\epsilon$ . This implies a contribution of  $< 0.5 \times 10^{-4}$  (better,  $< 0.3 \times 10^{-4}$ ) from a single source, which in turn implies  $< 0.017\%$  ( $< 0.01\%$ ) energy scale uncertainty.

The first three requirements are common to P832 and E799II, while requirement #4 is specific to the determination of  $\epsilon'/\epsilon$  in P832.

## Experience from E731, E773, and E799I

Here we discuss how well we have done with respect to each of the above requirements with the lead glass (PbG) array in E731, E773, and E799I. We now have extensive precision analysis experience with the E731 calibration data. For E773 and E799I, we made a series of incremental improvements in the calibration procedures which improved on-line monitoring analysis and data quality during the run. Off-line physics analysis for these experiments is just now beginning.

It is essential to recognize that the *dominant limitation* on the outcome of our calibration procedures in these experiments is imposed by *light absorption* and *radiation damage* effects in the PbG. After that, the power of a particular calibration procedure is limited by the intrinsic resolution of the glass and by our ability to trigger on appropriately distributed events. During a calibration run, for example, a large number of electrons with a wide range of momenta will strike blocks near the neutral beam axis, but the number striking the outer blocks of the array is much more limited.

- (1) We have generally maintained an on-line gain tolerance of  $\pm 10\%$ , matched to the resolution of the flash ADCs in our hardware cluster finder. The primary difficulty in doing this came from radiation damage to blocks around the beam holes. During E731 the signal level from these blocks decreased by about 4% per week of running. In E773 and E799I, radiation damage effects were somewhat greater than this. Gain drifts in the part of the array **not** subject to substantial radiation damage were  $< 3\%$  over several weeks of normal operation.
- (2) These experiments had no Level 3 trigger processors, but we have been able to quickly produce and use  $e^+e^-$  calibration gains with a precision of  $\pm 1\text{--}2\%$  for E773 and E799I monitor analysis.
- (3) Our typical hardware non-linearity with the PbG is about 8% between 2 GeV and 60 GeV. It is dominated by light absorption in the glass (about 3% per radiation length). We have successfully dealt with radiation damage induced changes in effective gain of order 12% over the three weeks or so between  $e^+e^-$  calibrations. Gain drifts of blocks far from the holes were typically  $< 3\%$ . The  $e^+e^-$  calibrations and our flasher and fiber optic gain monitoring system have enabled us to correct these to below the 0.5% level for three-week data sets.

- (4) The *electron* energy scale is then fine-tuned for each data set to achieve an energy scale good to  $\pm 0.08\%$  using electrons from Ke3 events recorded along with the data samples. To set the photon energy scale, an electron/photon response difference correction ( $\sim 3\%$ , arising from light absorption in the glass) is obtained to a precision of  $\pm 0.2\%$  from events with  $\pi^0$  decays. Finally, the neutral energy (and distance) scale is fine-tuned to better than  $\pm 0.05\%$  by matching to the known position of the regenerator downstream edge.

## KTeV Calibration Procedures

It is important to realize that, to a great extent, the monitoring and calibration of the CsI calorimeter improves right along with its intrinsic performance (in comparison to the present PbG array). The markedly superior transparency and radiation hardness of CsI remove the major limitations on our calibration procedures as discussed above. Likewise, the approximately  $4\times$  improvement in intrinsic resolution proportionately enhances the statistical power of every calibration event and procedure. Thus sample sizes comparable to those which we presently use will be acceptable for procedures in which the array is treated as a whole. Samples which are about  $4\times$  larger will be required when individual channel parameters are determined because the number of channels has been increased by about  $4\times$  from 804 to 3256.

Here we discuss briefly how the planned procedures and systems bear on each of the four stated requirements. Specifications for the required hardware items are discussed in the sections dealing with them.

- (1) Given the radiation hardness of CsI, our experience with our PbG array clearly indicates that we should have no difficulty in achieving the desired  $\pm 3\%$  gain stability over periods of a week or more. Of course, care will have to be exercised about environmental control as well as PMT selection and PMT base design and construction as provided in the hardware specifications. Of course, the laser and fiber optic monitoring system will be essential for ensuring that this requirement is, in fact, being met during actual experimental running.
- (2) We are already able to come close to the stated calibration requirement for the present PbG array. For KTeV, we can take  $e^+e^-$  calibration runs roughly weekly.

With the Level 3 trigger to efficiently suppress electrons hitting blocks where the rates are high and the greater KTeV data acquisition bandwidth, we will be able to obtain 1000 or more useable electron calibration events into each CsI block in two hours of running. We will also use the data acquisition control computer to automatically sequence the magnet changes required for these calibrations to increase the efficiency of the process. The laser monitoring system is more than adequate to interpolate between these calibration runs to the level set in this requirement.

- (3) Here we begin with the dominant hardware parameters improved by a factor of 4-8 or more in comparison to the PbG array, so we should readily be able to achieve the needed factor of 2 performance improvement for this requirement. Our  $e^+e^-$  calibration sample distribution will also be more uniform and much larger for the outer blocks. Further, we are designing the laser monitoring system itself to operate at the 0.1% level for a safety factor of 2.5. If, in fact, we manage to do somewhat better than the minimum requirement at this level, it will serve to ensure our ability to meet the final physics requirements in #4.
- (4) Recording an average of about 40,000  $K_{e3}$  events per block each week simultaneously with the data will enable us to tune the electron energy scale to  $\pm 0.04\%$  or better. Since the transparency of the blocks will be at least  $6\times$  better than the PbG, the electron/photon response difference correction should be less than 0.5%. Events with  $\pi^0$  decays, also recorded simultaneously with the data, will determine this with a precision of at least  $\pm 0.04\%$ . For the final neutral energy (and distance) scale adjustment, we will use the position of a Pb reference sheet, inserted at the downstream end of the decay volume only during special reference runs, as well as the downstream regenerator edge to achieve the needed precision of 0.017% or better.

With the superior resolution of the CsI calorimeter, the greater bandwidth of the KTeV data acquisition system, and the availability of Level 3 trigger selection, we estimate that no substantial increase in beam time devoted to calibration procedures will be necessary.

To carry out the CsI calibration, 20% of a physicist's time will be required to deal with systems integration and planning for the calibration procedures. That can be expected

to increase to 25-30% during data taking and analysis.

#### **4.7.9 Splitting Magnets for $e^+ e^-$ Calibration**

The object of having splitting magnets in the beam line is to facilitate  $e^+e^-$  calibration of the CsI array. This is done by converting photons into  $e^+e^-$  pairs, and splitting the pairs so they illuminate the CsI calorimeter. Traditionally, this was done with the BM109 at the upstream end of the decay region, and a splitting magnet in the decay region. Typically, the energies of the electrons have been up to about 10 GeV at the outside of the glass array. Additionally: These magnets may be used to clean up any low momentum spray/halo coming down the neutral beam

#### **Requirements**

Two magnets, for example BM109's, one X, and one Y. The BM109 magnet can provide up to about 0.9 GeV/c field integral with a standard 8 inch gap. In x, the beams just upstream of the decay region need about 8.5 inches, so that a BM109 should be gapped to 10 inches, in which case the field would be about 0.7 GeV/c. In the distance between the upstream end of the decay region and the CsI, the momentum kick of the BM109 could move an electron of about 70 GeV/c to the outside edge of the CsI array. So in principle two BM109's immediately upstream of the decay region oriented perpendicular to one another would do the job. The physical length of a BM109 is between 80 and 90 inches, depending on the version.

#### **Sweeping**

It is useful to provide sweeping field downstream and/or around the downstream most defining collimator - to clean up charged tracks from scattering in that collimator and in the slab. It may therefore be appropriate to either

- 1) Imbed the final defining collimator in a magnet such as the BM109, or
- 2) To place a BM109 downstream of the final defining collimator.

As it is preferable to have the final defining collimator as far downstream as possible, the preferred option may be to imbed the final collimator in a final sweeping magnet.

#### 4.7.10 Simulation of Radiation Dosage in CsI Calorimeter

The major source of radiation damage to the electromagnetic calorimeter in E731 and E799I came from neutral beam halo. This background can be eliminated by running without an absorber, or by placing the absorber upstream of the initial collimator (see Section 3. Beam Design).

With the new neutral beam design,  $K_L$  decays and neutron interactions in the regenerator (for P832) should be the dominant sources of radiation damage.  $K_L$  decays were modeled with a modified version of the E731 Monte Carlo. The largest damage from decays is estimated to be less than 0.5 rads/week for P832 and at most a few rads/week for E799II (for blocks near the beam hole in the CsI). Damage from beam neutrons and kaons interacting in the P832 regenerator was modeled using GEANT. The model included a 8 cm x 8 cm x 200 cm long plastic scintillator regenerator, a spectrometer magnet with  $P_t = 220$  MeV/c, and a 2 m x 2 m x 0.5 m long CsI array. The momentum spectrum for incident neutrons was based on data from previous experiments,<sup>4</sup> and for incident kaons was based on the Malensek parametrization<sup>5</sup> of E731 data. The results are normalized to  $1.7 \times 10^7$  neutrons per spill and  $1.7 \times 10^7$  kaons per spill for the regenerated beam. The rate of secondaries through the first drift chamber is then  $\sim 1$  MHz. The estimate of radiation damage to the CsI blocks near the beam is 50 rads/block per week (130 hours). The damage to blocks at the outer edge of the array is about 2 rads/block per week.

These figures should pose no major problems in the operation of the KTeV experiments on CsI calorimeter.

---

<sup>4</sup>R. T. Edwards et al, Phy. Rev D18, 76 (1978); J. Engler et al, Nuc. Phy. B84, 70 (1974)

<sup>5</sup>A. J. Malensek, FN-341 (1981)



## 4.8 CsI Test Results

### 4.8.1 CsI Test Array Results

We have assembled a prototype CsI calorimeter which has been tested in an  $e^+e^-$  calibration beam during last year's E799I run. This prototype consists of a 5 by 5 array of CsI blocks which are 40 cm long, corresponding to 22 radiation lengths, and 3.6 cm square. These CsI crystals were manufactured by three vendors. Horiba supplied us with 40 cm long crystals, while Optovac and Solon Technologies supplied 20 cm blocks which we glued to form 40 cm blocks. The crystals were glued with a silicon glue (RTV-615), which has good transparency in the UV. We used Hamamatsu R4598 1<sup>1</sup>/<sub>8</sub> inch diameter photo-multiplier tubes made specially for this test, which have a UV glass window suitable for use with pure CsI. The PMTs are pressure coupled to the CsI crystals using a cookie, a wafer made of the silicon glue, to provide optical coupling between the PMT and the crystal. Finally the crystals were wrapped such that the light output was uniform along their length, as we have described previously.

The calibration beam consists of electrons between 5 and 15 GeV, distributed over the face of the prototype calorimeter. The momentum of the electrons is measured to 0.5% using the drift chambers in the E799I experiment. After each electron calibration, data was taken with muons passing straight through the crystals. The response of the CsI to muons is used to match the gains of the 25 blocks. In Fig. 4.8.1 we show the energy deposition of straight through muons in a single crystal, fitted to a Landau distribution. Such fits are made for all blocks, and the resulting mean number of counts is set equal to the expected deposition of 257 MeV from muons.

To achieve the optimal resolution we adjust the gains calculated from the muon signal. This can be done by minimizing the equation:

$$\Sigma (\Sigma E_i G_i - P) = \chi^2$$

where the first sum is over events and the second sum is over blocks, and  $G_i$  is the gain for each block. From this expression we derive an equation for the  $G_i$ , which is solved to yield the final gains. Typically the gains are only adjusted by a few percent from the muon

result. To measure the energy deposited by the electrons, we simply sum the energies in the 25 blocks. The results from our first calibration are shown in Fig. 4.8.2; we plot the E/P for electrons pointing to the central 2.6 cm square of the center CsI block. We find a resolution of 1.2%. The tracking resolution contributes 0.5% and the pedestals contribute an additional 0.4%, leaving a resolution of about 1.0% due to the CsI alone.

We also measure the position of the electron shower. This is done using the ratio of energy in the center row or column to the nearest adjacent row or column. The mean position as a function of these ratios is measured and fit to a polynomial. Then in turn the fit is used to calculate the shower position given the row or column ratio. In Fig. 4.8.3, we see the difference between the measured position and the actual position; the position resolution is found to be 1.7 mm. This result can be improved by using the correlations between several ratios of adjacent rows or columns, instead of just one ratio.

Unfortunately, in these first tests the crystals were wrapped in several layers of 5 mil thick Teflon, which contributed significantly to the resolution for electrons pointing to the edge of the center block. The thick wrapping also produces the low side tail seen in the E/P plot as verified in a GEANT simulation. In a second calibration we rewrapped the crystals using a thin Aluminized Mylar layer, as we have described previously. With this wrapping, we can improve the energy resolution significantly for electrons over the entire central block. In Fig. 4.8.4 we show the E/P for electrons pointing in the central 2.6 cm of the center CsI block. We again find a resolution of 1.2%, which reduces to 1% when the contributions from pedestals and tracking are removed. Note however, that there is an improvement on low side tail in the distribution. This is a result of the thinner wrapping.

Finally we measure the resolution over the entire center block. In Fig. 4.8.5 we see that the resolution is 1.3% which reduces to a resolution of 1.1% for the CsI alone. The analysis of this data is preliminary and we expect to optimize the analysis for electrons over the entire center block.

Thus we have obtained, after correcting for chamber resolution and pedestal fluctuations, an intrinsic resolution of  $\sim 1\%$  for an average momentum of  $\sim 8$  GeV/c. The pedestal noise was much less for our leadglass array and was larger for the CsI test, because it was a last minute "add-on". The same care, in particular in protecting for ground loops, was not able to be taken. The expected resolution for 22 radiation lengths crystals is around 1% so that we are both near the GEANT limit and our goal of 1%. This is

comforting in that there is more room for improvement, particularly in that the actual crystals will be longer.

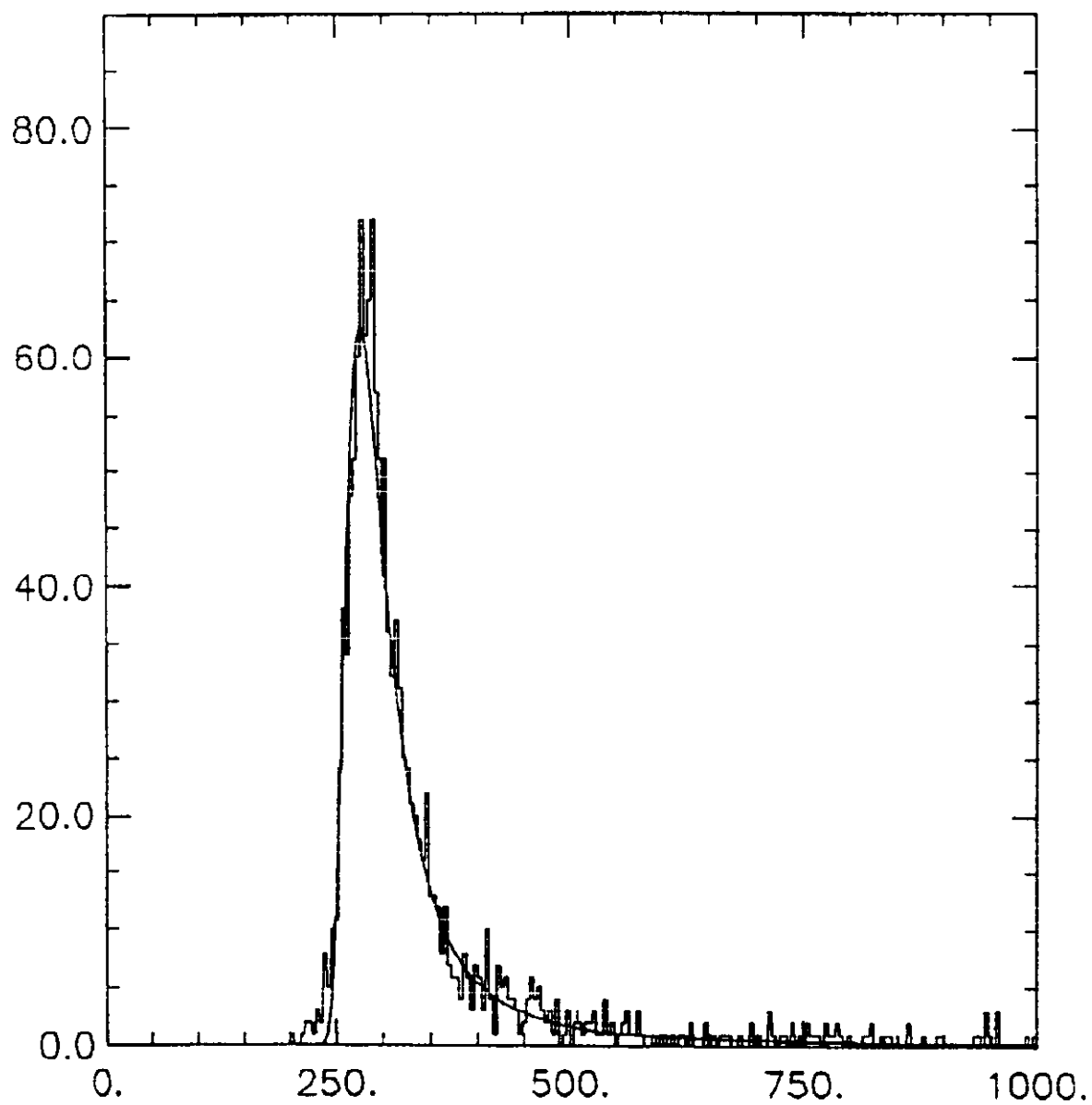


Fig. 4.8.1: ADC counts for straight through muons in a single crystal fitted to a Landau distribution.

11/11/91 11.03

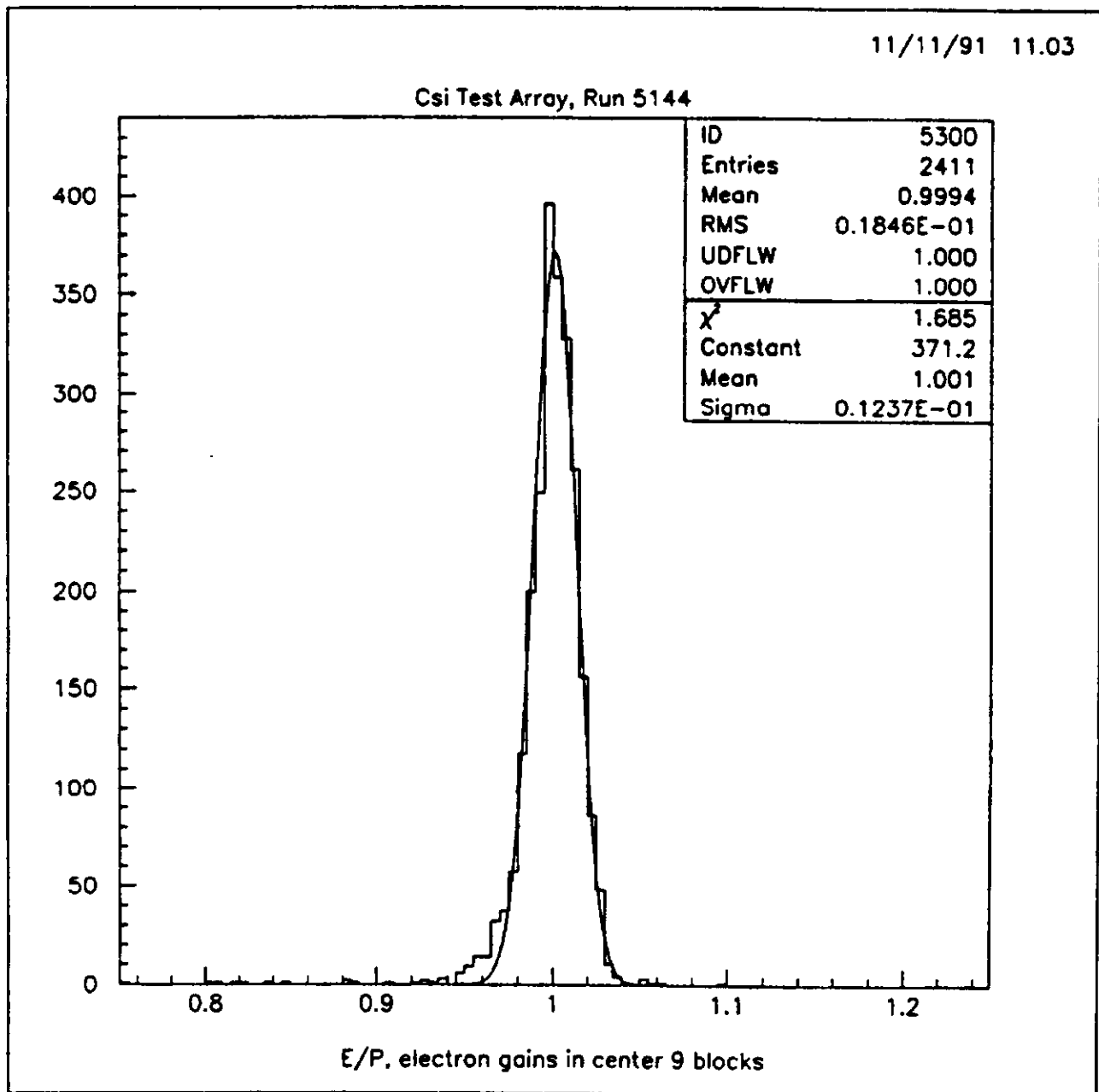


Fig. 4.8.2: E/P for electrons pointing to the central 2.6 cm square of the center CsI block in a 5 x 5 test array from the first electron calibration run.

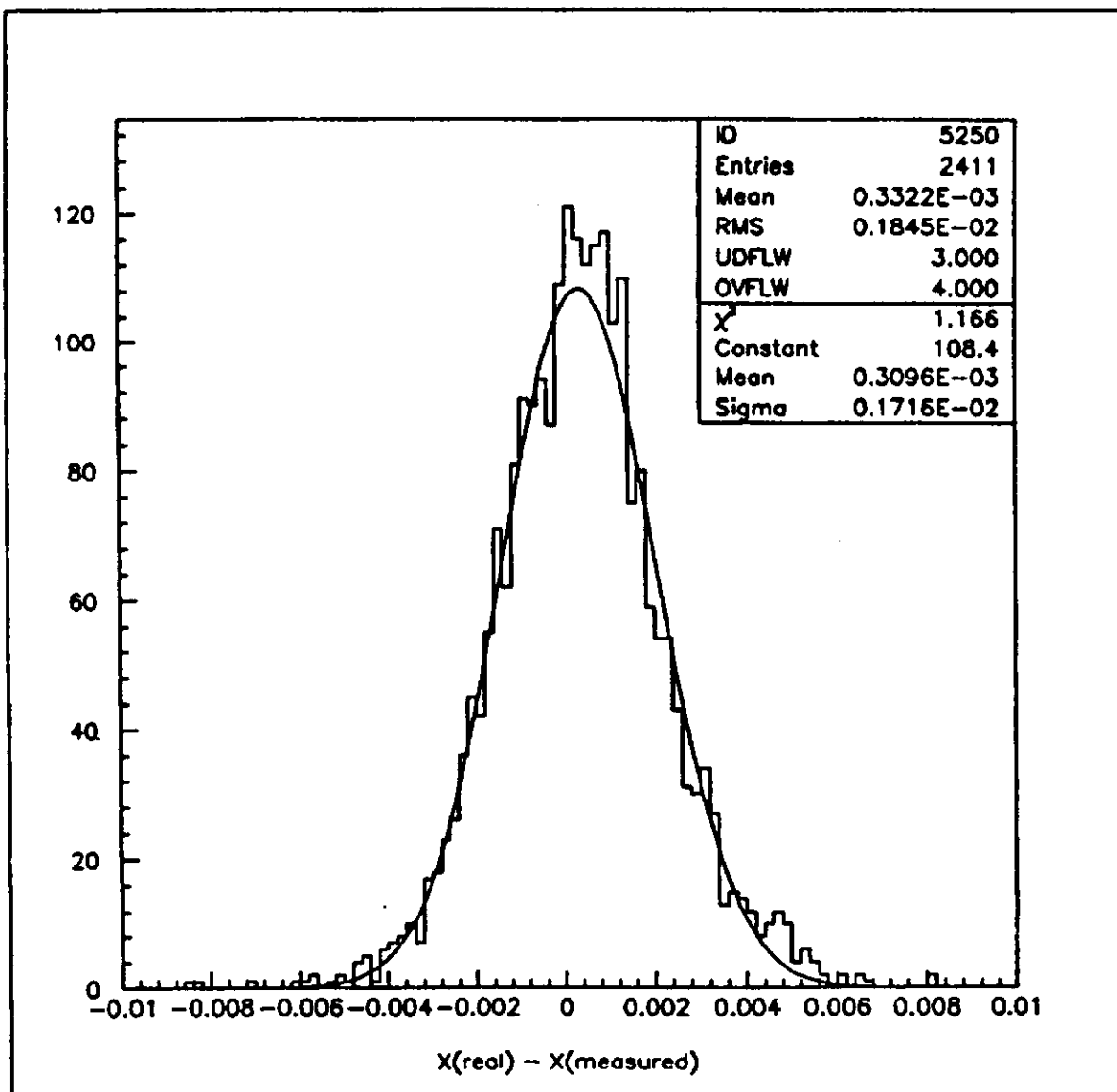


Fig. 4.8.3: Difference between the measured position and the actual position of electrons.  
The position resolution is 1.7 mm.

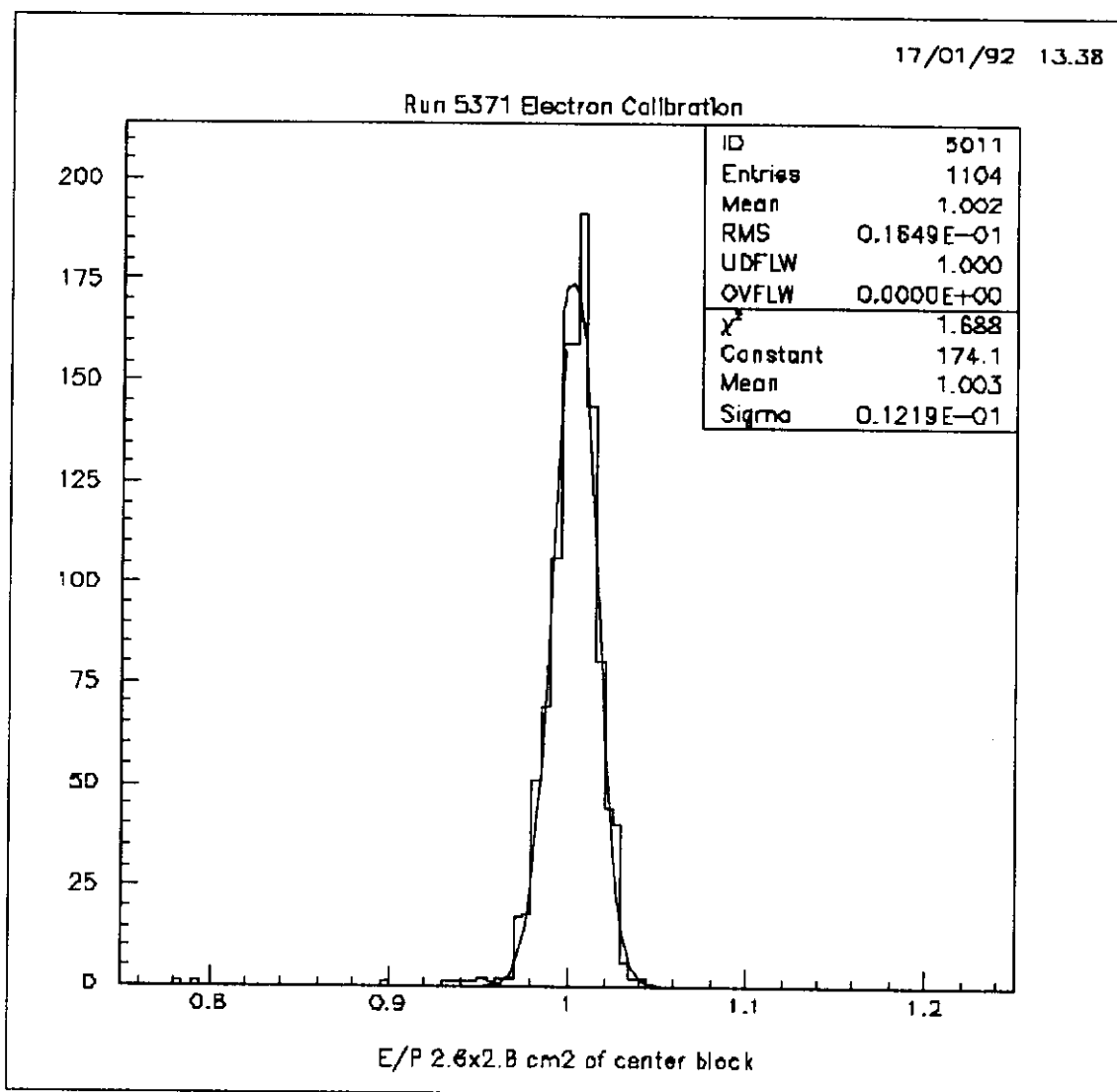


Fig. 4.8.4: E/P for electrons in the center  $2.6 \times 2.6 \text{ cm}^2$  of the center block from the second electron calibration run.

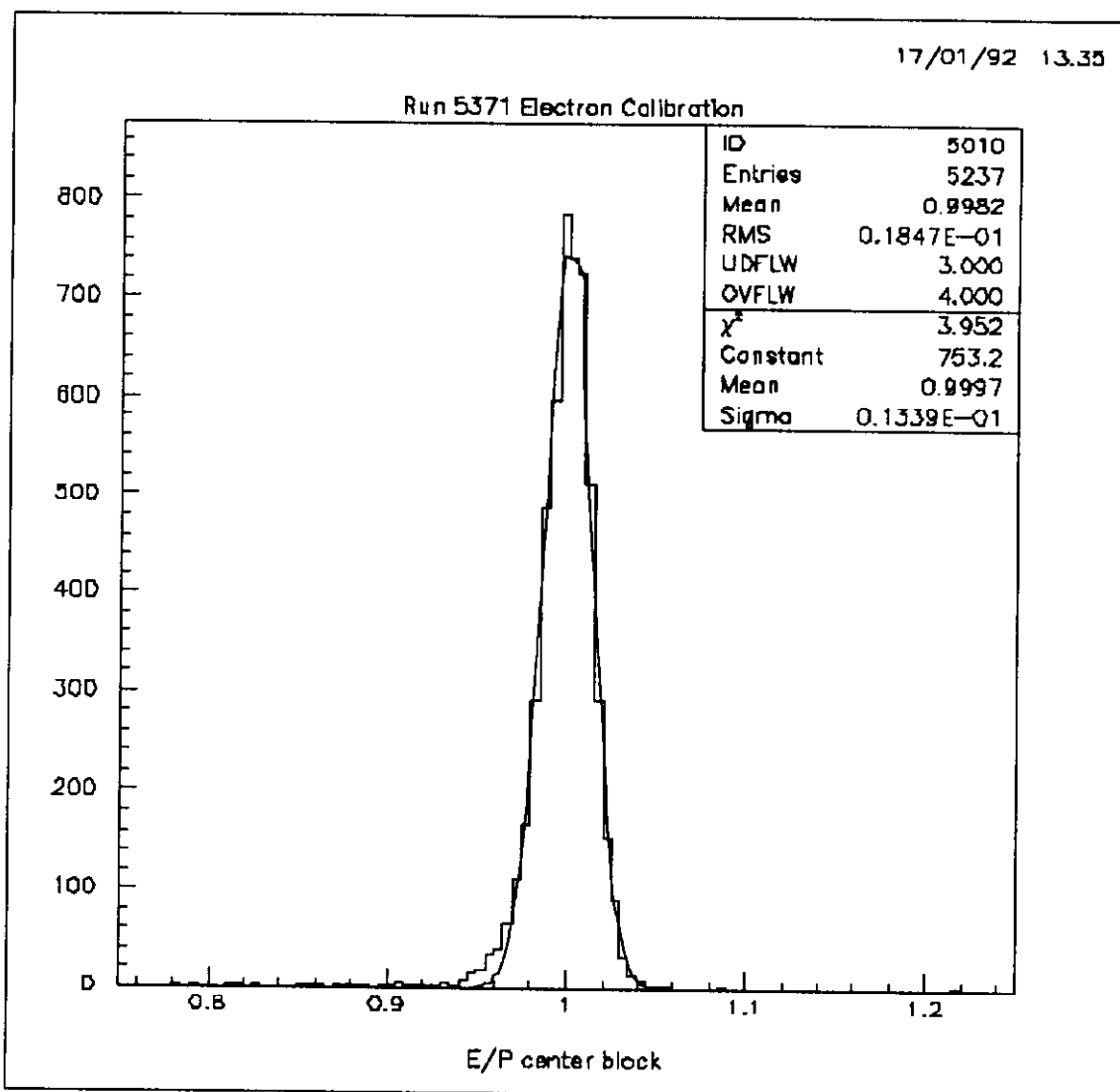


Fig. 4.8.5: E/P for electrons in the center block from the second calibration.

## 4.8.2 Radiation Damage Test Results

To determine how the blocks of cesium iodide will react in a high radiation environment, we mounted some test crystals in the beam line of the current E799I experiment. In E799II and P832 we expect that the integrated radiation dose that the crystals nearest the beam holes must endure will be on the order of 2 kRads or less. This number comes from scaling up the measured radiation from E731 and taking into account the reduced number of neutrons in the beam halo due to beam improvements. The lead glass array used in E731 suffered from many problems related to radiation damage that we would like to alleviate in E799II and P832. In E731/E773/E799I the lead glass blocks surrounding the beam holes suffered significant radiation damage, on the order of 10% for an integrated dose of 50 Rad, which could be partially cured by illuminating the lead glass array with UV light. However, this curing process required significant down time and typically the lead glass recovered only about 95% of its original light output every cure. In addition the lead glass blocks have a measurable attenuation of light along their length which increased as a function of radiation damage. To achieve the desired resolution this attenuation had to be well understood. The parameters which we wanted to test in the CsI blocks were the overall response of the light output as a function of integrated dose, as well as the change in light attenuation with increasing radiation dose.

Initially, we mounted a single Solon crystal transverse to the neutral beams in E799I. This crystal was wrapped with approximately 15 mils of Teflon followed by black paper to provide a light-tight environment. At one end of the crystal was glued a Hamamatsu 1398 phototube which was operated at 1100 volts. The crystal was read out with a LeCroy 1885 ADC and the data was written to the normal data stream. Prior to mounting the crystal in the experiment the crystal was wrapped so that the response along the crystal was sufficiently flat. Aside from the black paper, the crystal was not kept in a special environment. We mounted the crystal directly behind the “back anti-coincidence” counter or BA. This counter is constructed of planes of lead and scintillator and corresponds to a depth of approximately 1.3 interaction lengths. After every spill in which E799I takes data the number of counts in the BA are recorded and we used this data to help determine the integrated dose in the CsI crystal. In addition, we mounted transition radiation dosimeters (TLDs) at various positions on the CsI crystal. These TLDs were removed periodically and helped to give an absolute measurement of the total radiation incident upon the crystal.



To monitor the response of the crystal as a function of the integrated radiation dose, we took special muon runs. A muon which passes transversely through the crystal will deposit approximately 25 MeV and we used single muons which pass through the crystal to provide a simple means of monitoring the test crystal response. Fig. 4.8.6 shows the data from one of these muon runs which shows a clean Landau curve typical of a muon in a scintillating material. To monitor the response of the crystal we fit the data to a Landau distribution and use the peak value as our reference point. In E799I we can use the drift chambers to measure the path of any charged tracks: muons, in particular. Using this information we can project the muon track to the test crystal and determine very accurately where the muon passed through the crystal. This procedure allows us to monitor the test crystal response as a function of distance from the phototube and determine the change in attenuation with increasing radiation dose. Fig. 4.8.7 shows the response of the crystal as a function of distance from the phototube. In the Solon crystal we do not see any appreciable damage up to an integrated dose of approximately 15 kRads. In addition, the linearity of the crystal did not change even at the highest radiation dosage. The fact that the points in subsequent measurements are somewhat higher is due to the systematic uncertainty in our measurement technique. Since these measurements were taken over many weeks, it was difficult to keep all parameters constant in our test setup during the E799I.

For a shorter period of time, we also tested the radiation hardness of crystals from two other manufacturers, Horiba and Optovac. These crystals were prepared in the same manner and mounted next to the Solon crystal for a period of time. The Optovac crystal was subjected to approximately 2 kRads while the Horiba crystal received an integrated dose of approximately 5 kRads. The results of these tests are shown in Fig. 4.8.8 and Fig. 4.8.9. As can be seen, the crystals from these two manufacturers did not fare as well in the radiation tests. While both of these crystals suffered light loss with increased radiation damage, they also exhibited increased attenuation as a function of integrated radiation dose. The results from the Solon crystal more than surpass our requirements for radiation hardness for E799II/P832, but both the Horiba and Optovac crystals would be somewhat marginal. As a comparison, Fig. 4.8.10 shows the response that lead glass would have to radiation damage compared to the Solon crystal over an integrated dose of approximately 2 kRads, assuming that we did not cure the lead glass with UV light.

Our tests, then, show that crystals can be fabricated better than meet our requirement for radiation resistance. We are working with the vendors to improve the

understanding of the appropriate mechanisms.

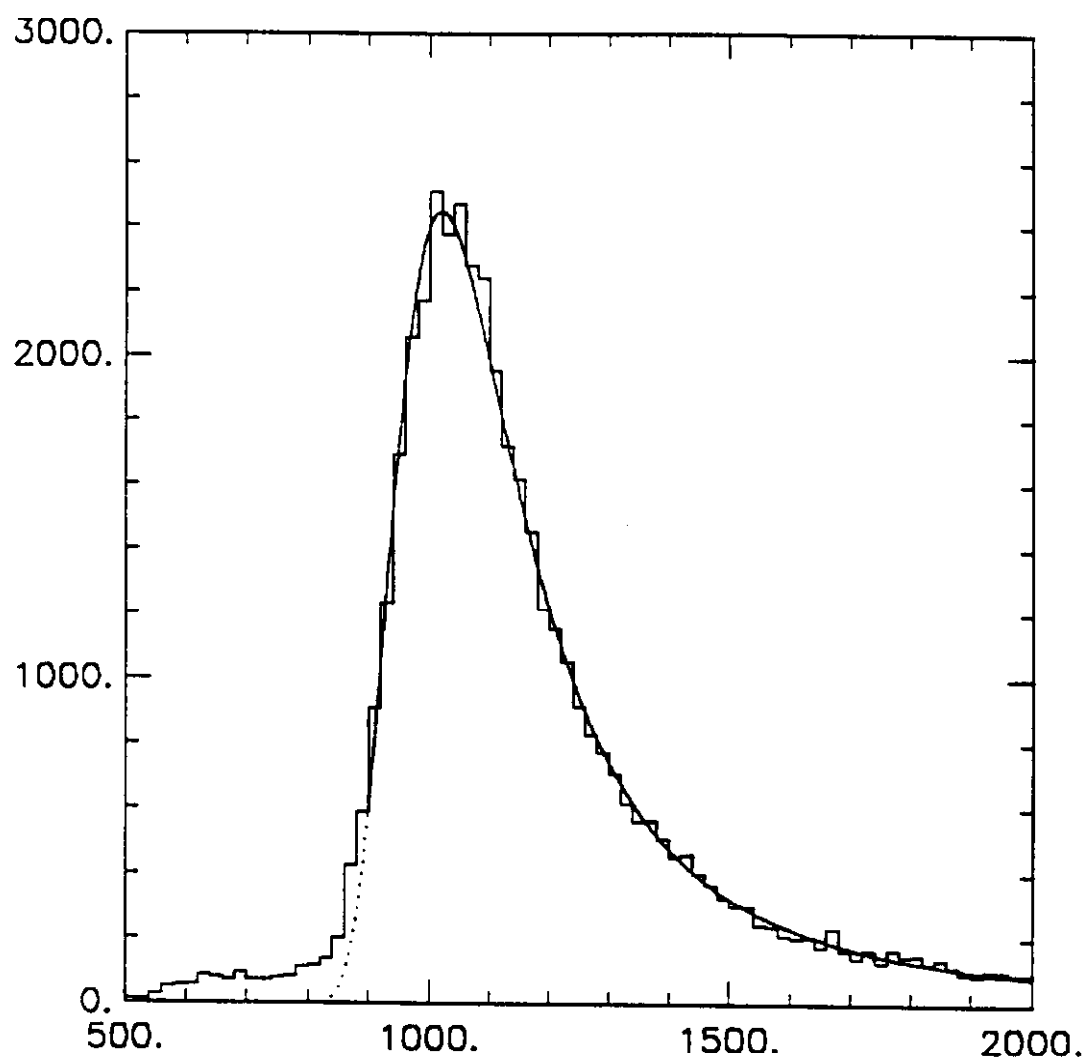


Fig. 4.8.6: Response (ADC counts) of a Solon Crystal for muons transverse to the crystal axis.

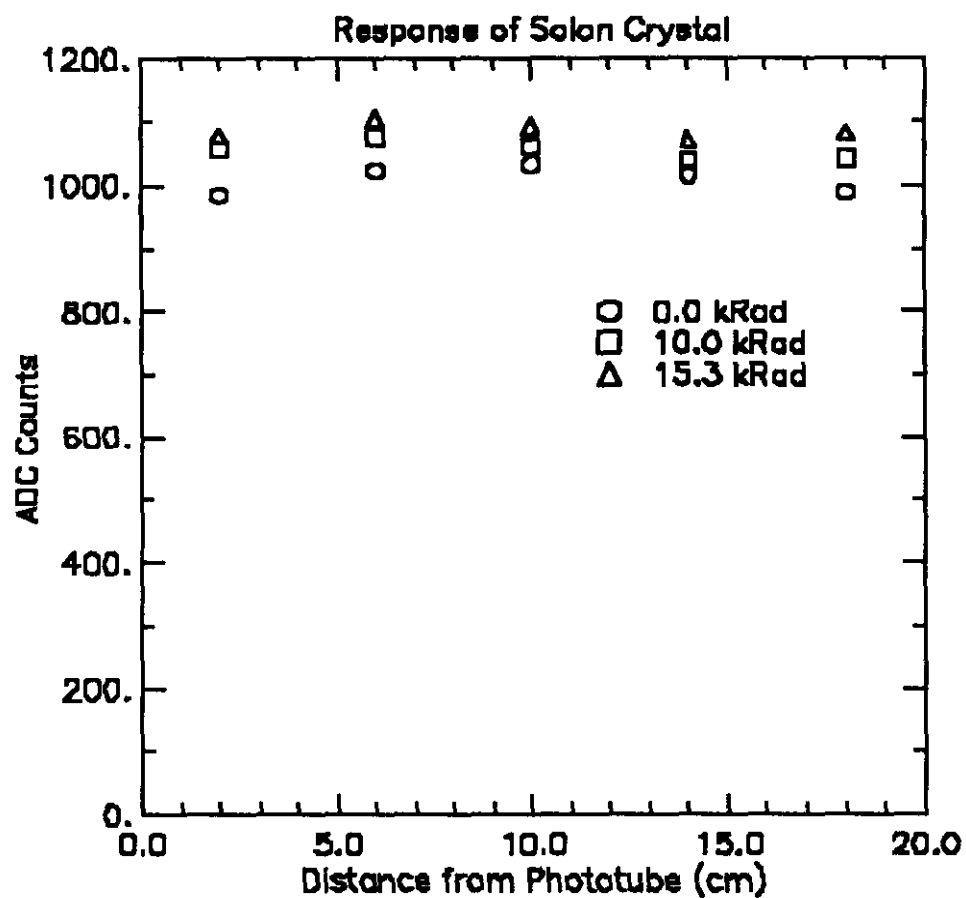


Fig. 4.8.7: Response of the Solon Crystal as a function of Distance from Phototube.

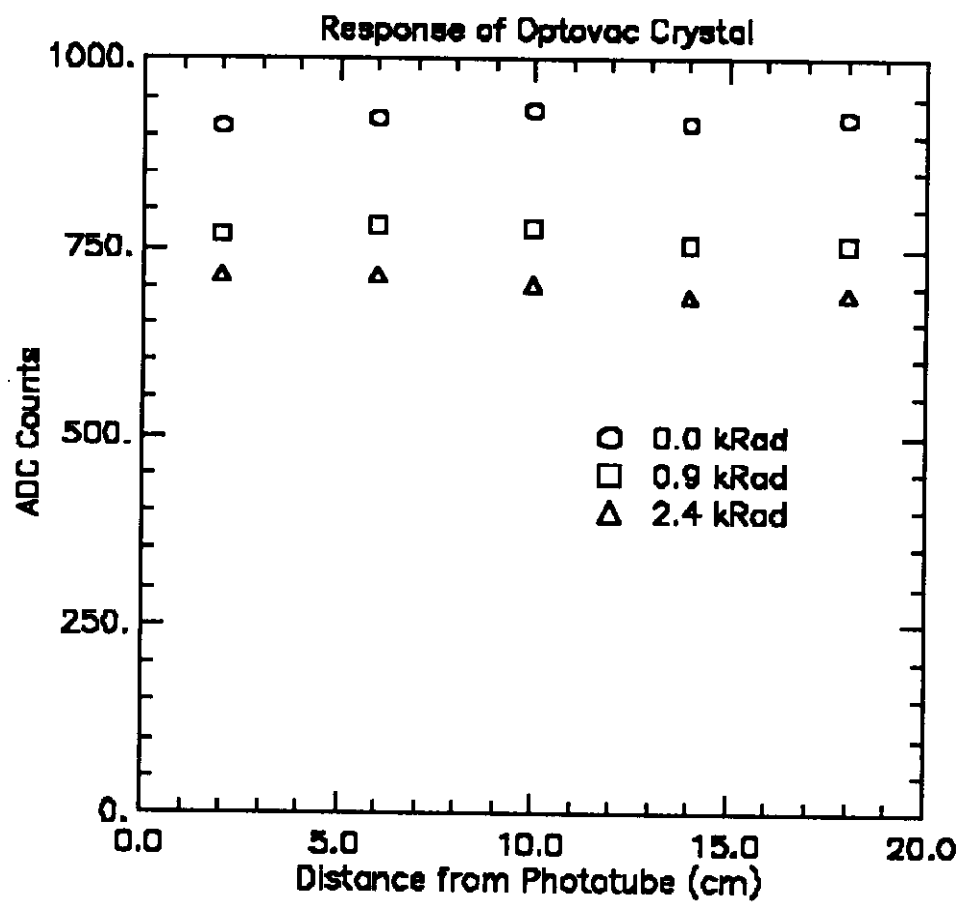


Fig. 4.8.8: Response of the Optovac Crystal as a function of Distance from Phototube.

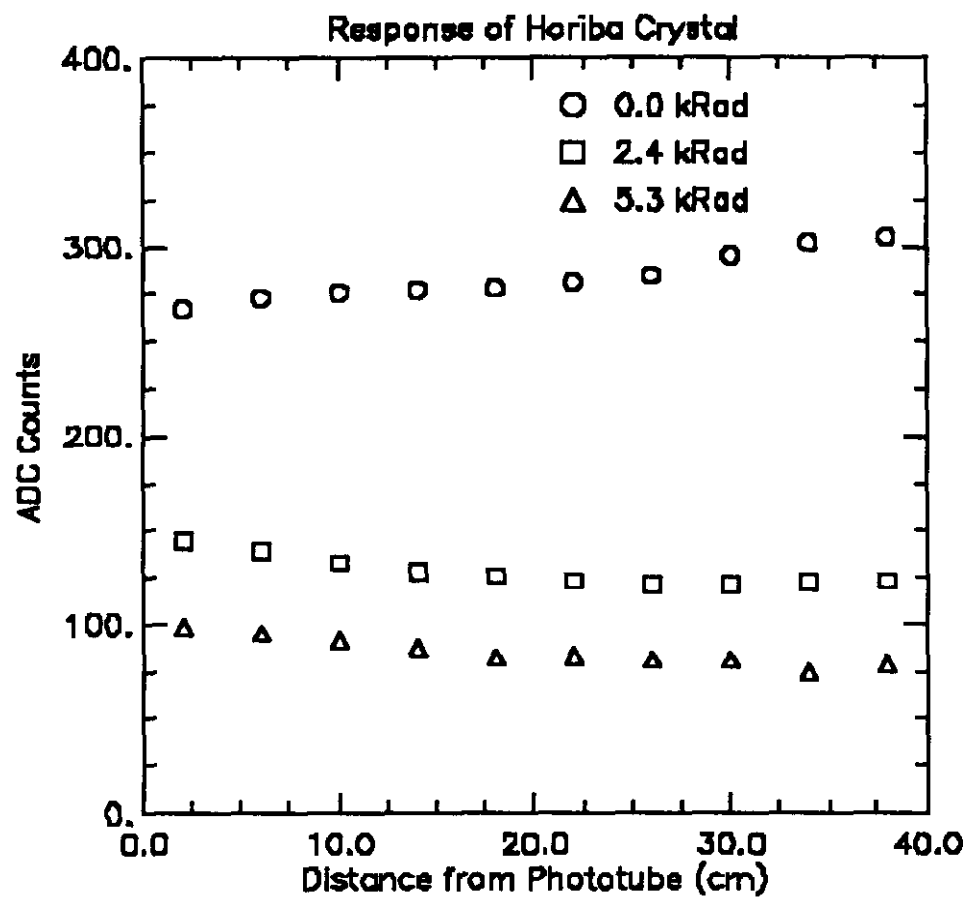


Fig. 4.8.9: Response of Horiba Crystal as a function of Distance from Phototube.

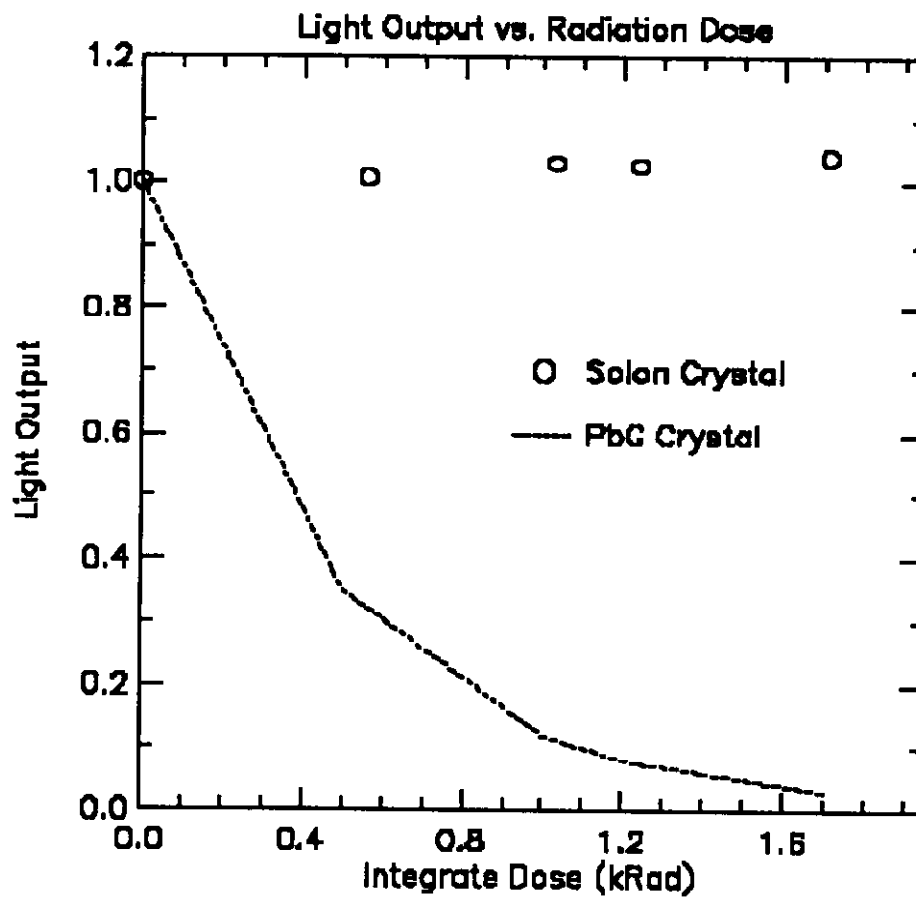


Fig. 4.8.10: Light output of Solon Crystal as a function of integrated dose compare to light output of lead glass crystal.

## 4.9 BEAM HOLE VETO

### Overview

The CsI calorimeter will have beam holes so that it will not be struck directly by the two neutral beams. The size of each beam hole is  $15 \times 15 \text{ cm}^2$ , and they are separated by 15 cm. Special care has to be taken around this region because a) there will be some energy leakage if electrons or photons hit near the hole, and b) the calorimeter is not sensitive to the particles going down the holes.

### *Around the Beam Holes*

If photons hit the CsI very near the beam holes, the event is not usable because the energy resolution degrades due to the lateral leakage. One can always make a software cut on the reconstructed position, but the position resolution with such a leakage is not good enough to make a sharp edge. Without the sharp edge, one has to know the resolution very well to understand the acceptance near the holes, which is not trivial. A good understanding of the acceptance is especially important for P832. In order to make a sharp edge around the holes, E731 and E773 have used a veto counter, called Collar Anti (CA). A new CA will be required for P832.

### *Inside the Beam Holes*

The rate inside the beam holes for E799II is about 10 MHz ( $>5 \text{ GeV}$ ) extrapolating from E799I rates. In P832 we will have 1/5 of these rates because of the lower beam intensity ( $3.5 \times 10^{12}$ ), and one  $K_L$  beam. This means that 20-50% of the buckets will have some activity in the holes. It is extremely difficult to maintain the same level of performance as CsI in such a high rate environment. Therefore if a particle goes down the hole, the event is mostly useless. However, the region inside the beam holes should still be active, to veto background events. In P832, we should veto on photons ( $>5 \text{ GeV}$ ) going down the holes to reduce the background from  $K_L \rightarrow 3\pi^0$  which satisfies 4 cluster trigger. In E799II, the photon veto should be efficient enough to kill background to  $K_L \rightarrow \pi^0 \nu \bar{\nu}$  from  $K_L \rightarrow 2\pi^0$  where one or two of the photons goes down the hole. We name the veto counter in the beam hole as Back Anti (BA), following our tradition.

The following sections will describe BA and CA in further detail.

#### 4.9.1 Collar Anti (CA)

The Collar Anti should have a very sharp edge and a good photon veto efficiency. The size of CA is 2.500 cm wide, with the inner edge aligned with the CsI beam holes within  $\pm 0.1$  mm. The width is based on a GEANT simulation. All the dimensions should be kept to  $\pm 0.1$  mm. In order to eliminate photons sneaking by CA, it is ideal to place it right in front of the calorimeter, almost touching the CsI crystal. Making the thickness as small as possible makes an even sharper edge on the calorimeter.

We will likely make CA by a sandwich of precision machined Tungsten and scintillation tiles with fiber light guides. For 10 radiation length, the tungsten is only 3.5 cm thick and sampling every 2 radiation lengths with 5 mm scintillator brings the total thickness to 6.0 cm. The cost estimate for a new Collar Anti is \$5.8 k.

#### 4.9.2 Back Anti

A lead scintillator stack will be used for the front, electromagnetic section of the Back Anti (BA), and an iron/scintillator stack for the hadronic section. Optimal choices of the parameters: (a) depth of lead, (b) segmentation of lead, (c) depth of iron, and (d) segmentation of iron to do the proposed physics are based on Monte Carlo calculations. For  $\epsilon'/\epsilon$ , the BA will be used on-line to reduce the trigger rate and to suppress background from  $3\pi^0$  decays while the hadronic section will veto the  $\gamma$  veto so that a neutron interacting in the front section will not kill an event. For a  $K_L \rightarrow \pi^0 \nu \bar{\nu}$  search using the Dalitz mode for the  $\pi^0$ , the BA will suppress background from  $K_L \rightarrow 2\pi^0$  decays while the hadronic section will suppress background from  $\Lambda \rightarrow \pi^0 n$ . In both experiments the BA will be used in the on-line trigger and in the offline analysis with tighter cuts.

#### $\epsilon'/\epsilon$

A front section that is too efficient for neutrons could be a mistake for  $\epsilon'/\epsilon$ . In a thick front section which is efficient for photons it is possible that an accidental beam neutron may interact in the same RF bucket with a signal  $K_{L,S} \rightarrow 2\pi^0$ . We would like to keep the false veto rate of BA at the percent level.



In a GEANT simulation of  $K_L \rightarrow 3\pi^0$  background in  $\epsilon'/\epsilon$  the electromagnetic section was taken as a lead/scintillator sandwich  $30X_0$  in length with 30 layers. The scintillator layers were 0.5 cm thick. This segmentation and thickness gave a  $\gamma$  energy resolution of 8% for the generated spectrum shown in Fig. 4.9.1. The hadronic section was an iron/scintillator sandwich of  $5\lambda_I$  length with 8 scintillator layers of 1 cm thickness each. The outer transverse dimensions will be 24 cm by 60 cm which is enough larger than the beams to give total containment of the electromagnetic part of the shower. The total depth is approximately 1.2 meters. The outer transverse dimensions depend slightly on the  $z$  position of the BA and suffice at a point 8 meters from the CsI.

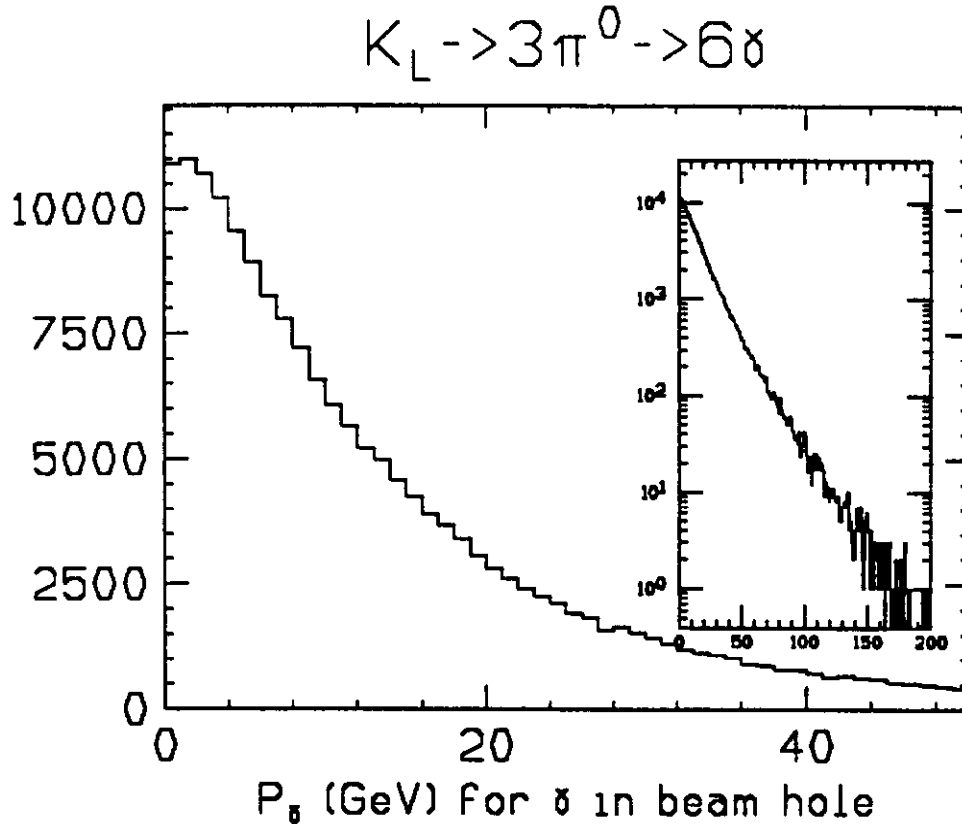


Fig. 4.9.1: Generated  $\gamma$  energy spectrum that hits BA down the beam hole.

Two Monte Carlo runs were made with these specifications: Run 1, gammas with the energy spectrum of  $K_L \rightarrow 3\pi^0$ , and Run 2, beam neutrons from the target. The parameter used to separate neutrons and photons was  $f = E_{Fe}/(E_{Fe} + E_{Pb})$  where  $E_{Fe}(E_{Pb})$  is the energy deposited in the scintillator in the hadronic (electromagnetic) section. The  $f$ -distributions are shown in Fig. 4.9.2. All the photons of Run 1 fell below  $f < .01$  and 142/143 neutrons of Run 2 fell above  $f < .02$ . A cut on  $f$  combined with a threshold cut on  $E_{Pb}$ , the normal way to operate, will improve the discrimination. By constructing the front section in three subsections of  $10X_0$  each, we will keep the option of redefining the electromagnetic section of the BA to be just the first  $20X_0$  of lead.

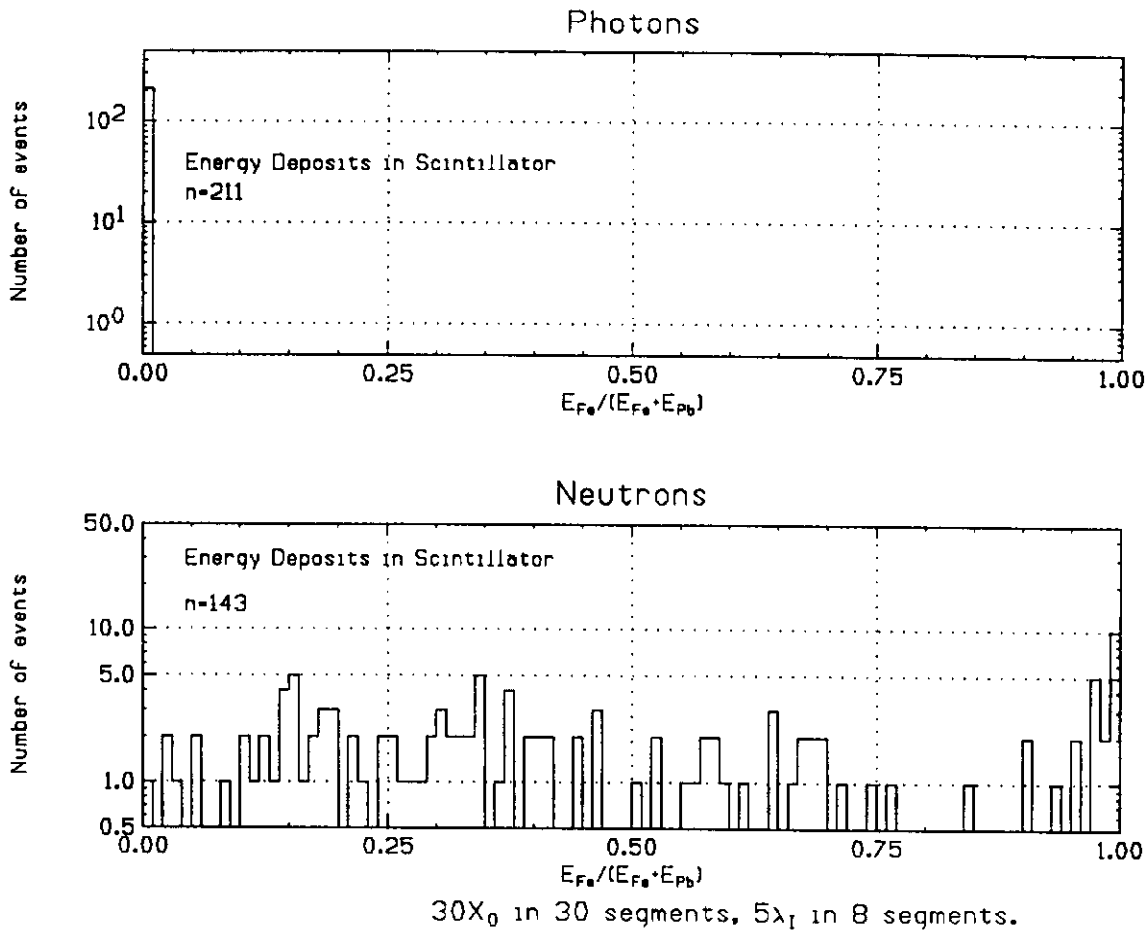


Fig. 4.9.2: Fraction of energy deposit in the scintillator of the hadron section of the BA for gammas and neutrons.

## $K_L \rightarrow \pi^0 \nu \bar{\nu}$ Search

To reduce background below the sensitivity limit of the  $K_L \rightarrow \pi^0 \nu \bar{\nu}$  with  $\pi^0 \rightarrow e^+ e^- \gamma$  experiment ( $\approx 10^{-9}$ ),  $K_L \rightarrow 2\pi^0$  must be rejected at a  $10^{-6}$  level. We learn from a simulation of this background that in events with two  $\gamma$ 's passing through the beam holes of the CsI, the higher energy photon lies in the multi-GeV range. Fig. 4.9.3a shows the distribution from  $1.6 \times 10^7$  simulated  $K_L \rightarrow 2\pi^0$ . There are  $8 \times 10^4$  cases; all exceed 9 GeV. When only one photon falls in the beam,  $1.3 \times 10^6$  cases, the spectrum is softer, as seen in Fig. 4.9.3b, but still the minimum energy found in the run was 700 MeV. Since 8% of the sample give  $e^+ e^- \gamma$  in the CsI and just one of the other photons in the beam hole, these must be rejected at the  $10^{-5}$  level to suppress  $K_L \rightarrow 2\pi^0$  at  $10^{-6}$ . Therefore the requirement on the BA is to be less than  $10^{-5}$  inefficient for photons above 1 GeV. A  $30X_0$  radiator with sampling of  $X_0/2$  is sufficient. This efficiency is more than enough to kill the cases with 2  $\gamma$ 's in the beam hole.

Another background comes from  $\Lambda \rightarrow \pi^0 n$ . This can give a single  $\pi^0$  in the CsI and no photon veto. The neutron from this background always hits the BA. It is possible to achieve a factor of 100 rejection by the BA alone if it is deep enough ( $5 \lambda_I$  is our design value.) When combined with a cut on  $P_t$  to the  $\pi^0$ , which has a 104 MeV/c upper limit for  $\Lambda \rightarrow \pi^0 n$ , this will reduce the level below the single event sensitivity.

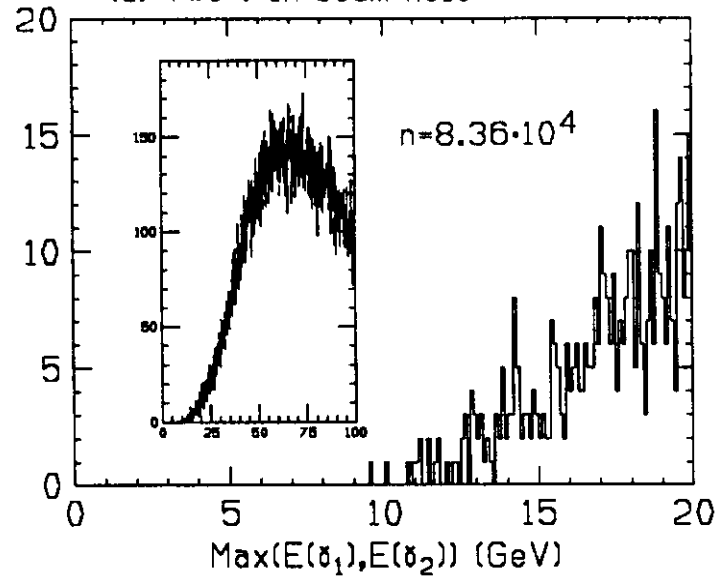
## Location

The location of the BA is critical because it is a dump for the whole neutral beam and is a potential source of background for the CsI calorimeter. A sketch of the simulated positions of the CsI, a Pb wall of thickness  $\approx 30 X_0$ , and the BA is shown in Fig. 4.9.4. The entire downstream part of the detector is involved, in particular, the lead wall following the CsI enclosure. After the wall there is a hadron veto counter plane. As long as the BA is located downstream of this wall some of its background will be prevented from reaching the CsI.

A Monte Carlo simulation was done for this layout and two runs were tried, both with the same locations of components: (1) lead wall 4 meters downstream of the CsI and back-anti another 4 meters downstream of the wall, and (2) lead wall replaced by vacuum to look at what would happen in its absence.

$K_L \rightarrow 2\pi^0 \rightarrow (\gamma_1 \gamma_2) + (\gamma e^+ e^-)$ ,  $\gamma e^+ e^-$  in CsI

(a) Two  $\gamma$  in beam hole



(b)  $\gamma_1$  in beam hole

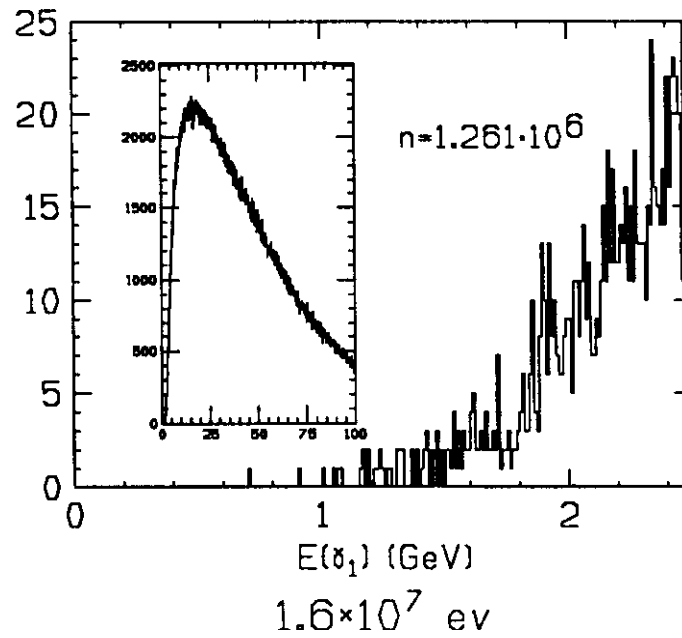


Fig. 4.9.3: Maximum  $\gamma$  energy distribution in BA for the background simulation of  $K_L \rightarrow 2\pi^0 \rightarrow \gamma\gamma e^+ e^-$  with  $\gamma e^+ e^-$  in CsI and a) two  $\gamma$ 's, b) one  $\gamma$  passing through the beam hole.

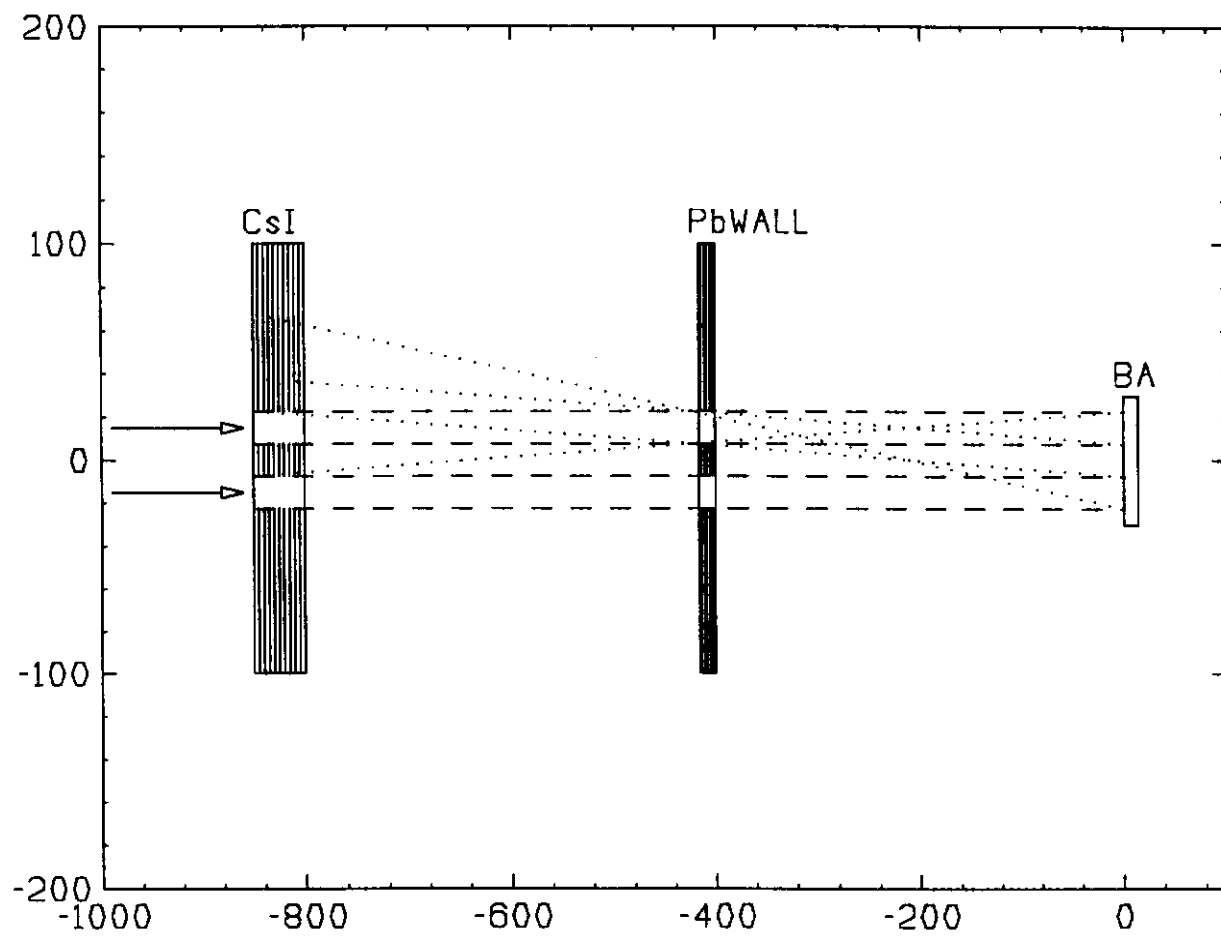


Fig. 4.9.4: BA location 8 meters downstream of the CsI and lead wall.

With the lead wall in place, a run of  $2 \times 10^6$  neutrons having the proper momentum distribution resulted in  $1.5 \times 10^4$  interactions in the wall due to particles scattered back from the BA. There were 700 interactions in the CsI due to separate back-incident particles from 230 separate events, or 0.011% of incident neutron events resulted in at least one backscattered hit in the CsI that produced an average energy deposit of  $\approx 30$  MeV, with an average of 3 back-incident particles in the event. In the vacuum wall run,  $2 \times 10^5$  neutrons resulted in 400 interactions in the CsI from 320 separate events, or 0.16% of incident neutrons eventually led to energy deposit in the CsI. In short, the wall reduced this background by a factor of 14. Without the wall, at  $5 \times 10^8$  neutrons per pulse there would be a bucket occupancy of  $\approx 10^{-3}$  due to this background.

Backscattered particles from the BA are uniformly distributed in the CsI plane out to approximately 4 meters from the beamline. If the BA were located 2 m from CsI with no Pb wall, occupancy in the CsI could rise to 2% of RF buckets, or 1 MHz.

## Segmentation

Transverse segmentation of the front section will be 2 cm x and y strips to be comparable to an average shower width. Transverse segmentation of the hadronic section is determined by the requirement to recover good  $K_L \rightarrow 2\pi^0$  in which all four gammas are absorbed in the CsI, but which would have been vetoed because an accidental neutron was detected in the front section of the BA. This event will be recorded if the neutron gives a big enough signal in the back section of the BA. On the other hand, one wants to cut offline a background  $K_L \rightarrow 3\pi^0$  with four  $\gamma$ 's in the CsI and one in the BA accompanied by an accidental neutron and a missed sixth  $\gamma$ . With a rear section of 10 by 4 segments (6 cm strips) an accidental hadronic shower in this section will overlap the front section photon in  $1/10 \times 1/4 \approx 2.5\%$  of the cases, which is sufficiently low.

The total cost of the Back Anti is estimated at \$90 k with all new materials plus phototubes and bases.

## **4.10 TRIGGER HODOSCOPES, HADRON VETO AND MUON SYSTEM**

### **4.10.1 Trigger Counters**

Because the KTeV trigger counter banks are different sizes from the ones in use currently, and because some serious crazing is developing in several of the existing counters, it is desirable to build new trigger hodoscopes. Based on Monte Carlo simulations of several decays (to 2 charged particle and 4 charged particle final states), we have chosen to build four hodoscopes, of 32 counters each. The individual counters would be 13 cm x 1.10 m x 5 mm, and are arranged to cover an area 2 m x 2 m. The 128 counters would be located 1.5 m upstream of the CsI calorimeter.

Two of the hodoscopes will have their counters standing upright, and each will consist of two sets of 16 counters, arranged one above the other. The tubes and bases will be on the top of the upper set, and below the lower set. The joint will be along the median plane of the experiment. To eliminate the effect of gaps between the counters, and to allow charged particle multiplicities to be measured, the counters of the second hodoscope will be offset 1/2 a counter width (i.e. 6.5 cm) to the side, and offset 5 cm vertically, relative to the counters of the first hodoscope. The particle multiplicity will then be defined as the maximum number of counters firing in one of the banks. The other two hodoscopes would have their counters lying horizontally, and would have similar electronics to determine multiplicities. For a 4 charged particle decay, four hits would be required in the x-measuring hodoscopes, and three or more hits in the y-measuring hodoscopes. The difference is because the analysis magnet does not bend in y, and the particles are closer together.

Since we would use existing phototubes and bases, the cost of constructing these trigger hodoscopes is only that due to scintillators and light guides. The estimate is \$22 k.

### **4.10.2 Hadron Veto**

We will use a scintillator hodoscope located downstream of the CsI for vetoing, in certain of the triggers, decays involving charged pions. In P832, this hodoscope will be

used as a veto in the neutral mode trigger to reject  $K_{\pi 3}$  events. In E799II, it will also be used in the di-electron and di-muon triggers to reject  $K_{\pi 3}$  events.

It is advantageous to locate this hodoscope as far upstream of the neutral beam dump as possible in order to minimize the rate due to backplash neutrons. It will, therefore, be located just outside of the CsI house, 4.5 m downstream of the CsI and 3.5 m upstream of the front of the muon steel. It will be preceded by 6 inches of lead bricks in order to absorb the leakage of electromagnetic showers out of the back of the CsI. GEANT simulations show that, if we require an energy deposit less than 5 minimum ionizing tracks, 80% of  $K_{\pi 3}$  events will be rejected while 99% of  $K \rightarrow 3\pi^0$  events will be accepted.

The cost of hadron veto is estimated to be \$20 k.

### 4.10.3 Muon Detection

#### Scintillator Banks

The primary purpose of the muon detection system depends upon whether the KTeV apparatus is running in the  $\epsilon'$  mode (P832) or in the rare decay mode (E799II). In the  $\epsilon'$  mode, the primary requirement is that  $K_{\mu 3}$  decays be efficiently vetoed both at the level 1 trigger stage and further in the off line analysis. The system used for this purpose in E731 was a scintillator hodoscope located behind 3 meters of steel. The elements of the hodoscope were 20 cm wide and overlapped by about 1 cm to eliminate inefficiencies due to edges. We propose to reproduce this system for KTeV. New scintillator will be used and the dimensions of the hodoscope will be increased to 3.4 m x 2.5 m to accommodate the requirements of the KTeV geometry.

For the rare decay experiment, on the other hand, it is most important to have good muon identification in order to reduce background to the rare decay  $K_L \rightarrow \pi^0 \mu^+ \mu^-$  and  $K_L \rightarrow \pi^0 \mu e$ . The primary background is from  $K_L \rightarrow \pi^0 \pi^+ \pi^-$  in which the charged pions either decay in flight or simulate muons by punching through the steel. In E799I, muons were identified by a scintillator hodoscope which determined the position of particles that exited the steel. From an analysis of preliminary data from E799I, a single event sensitivity of about  $10^{-9}$  will likely be reached in Phase I. In the KTeV experiment, we need to achieve a pion punchthrough probability of less than  $3 \times 10^{-3}$ . GEANT simulations show that this



can be achieved using a hodoscope downstream of 3 m of Fe.

Scintillator hodoscopes with 8.5 cm segmentation will be constructed. There will be both an x-view and y-view hodoscope. The y-view hodoscope will be split at the center both to reduce ambiguities from multiple hits and to reduce the length of the counters. The size of the hodoscope will be 3.4 m by 2.5 m and the total number of counters will be 100.

### **Resistive Plate Chambers**

In order to insure an adequate muon identification, we are investigating a scheme for measuring the particle exit angles with two sets of fine grained hodoscopes. This uses thin chambers operated in the limited streamer mode (resistive plate chambers) instead of scintillators. The advantages of this scheme are that we can achieve either greatly reduced cost or finer segmentation or both. The disadvantage is that we will need to undertake some R&D to learn how to construct these chambers and to make them operate at the necessary rates.

Resistive plate chambers are presently being successfully used as part of the muon detection system and di-muon trigger in the B production experiment E771. They are also being researched by several groups for possible use at the SSC/LHC colliders. A schematic of the layer structure of a chamber is shown in Fig. 4.10.1. Planes of resistive Bakelite plastic,  $\rho = 10^{11} \Omega\text{-cm}$ , define a gas gap of 2 mm across which a voltage of 8 kV is applied. When ionization in the gap occurs, a limited streamer develops which locally discharges the gap and induces a signal on pickup electrodes situated outside of the resistive plastic. The signal induced is large (about 500 mV) and fast (rise time of a few ns and a delay of about 20 ns). The pickup electrodes can be configured in any shape. In our application, we would configure them as strips with x-strips on one side of the gap and y-strips on the other. We would use resistive graphite for both the high voltage and ground electrodes.

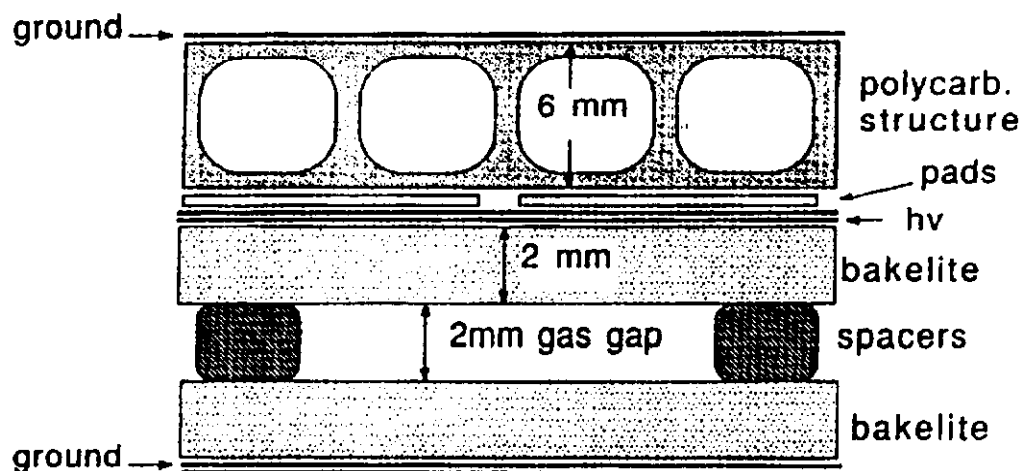


Fig. 4.10.1: A schematic of the layer structure of a resistive plate chamber.

Chambers similar to these have been operating successfully in E771 for over one year. The main drawback of the present chambers is their ability to operate under high rate. When a streamer develops, a region around the streamer of about 3 mm diameter is dead for about 10 msec until the local region can recharge. This time is proportional to the resistivity of the plastic. With a resistivity of  $10^{11}\Omega\text{-cm}$ , the chamber efficiency is reduced to 90% at a flux of  $10^6/\text{m}^2\text{-s}$ . In the rare decay mode of operation of KTeV, the rate of muons from  $K\mu_3$  decays will be about 500 kHz and will be concentrated near the neutral beam axes. We estimate that within a 10 cm radius of the neutral beam axis the flux will be about  $2.5 \times 10^6/\text{m}^2\text{-s}$ . In this region, the chamber would only be about 70% efficient. This problem can be solved by using lower resistivity material. Several groups are presently developing chambers with the Bakelite plastic replaced by glass with a resistivity of  $10^{10}\Omega\text{-cm}$ . These chambers should be able to work efficiently at the required rates.

## **Thickness of Steel**

As determined both by the present data and by GEANT simulation, the rates in scintillators located after 3 m of steel will be about 0.7 MHz in P832 and 4 MHz in E799II due primarily to particle production by the neutral hadron beam interacting in the muon steel. We will, therefore, add another meter of steel making a total of 4 m before the muon detection hodoscopes to lower the rate for E799II to less than 1 MHz. Since the 0.7 Mhz rate in P832 is not large and since we would lose veto efficiency for low momentum muons if the steel were thicker, the muon veto hodoscope will remain at a depth of 3 m.

The estimated cost of steel shielding for the muon filter is \$137 k. The Muon veto will cost \$25 k and muon detection will cost \$70 k for the scintillator bank and \$20 k for the resistive plate chambers.

## **4.11 TRIGGER AND ELECTRONICS**

This section describes a detailed design of the trigger system for KTeV experiments E799II and P832 (Section 4.11.1), the design considerations for CsI calorimeter ADC and its readout system (Section 4.11.2), the front end electronics (TDCs, ADCs and latches) for the rest KTeV spectrometer (Section 4.11.3), the Level 2 trigger processors: the Hardware Cluster Finder II (Section 4.11.4) and the Track Processor Upgrade (Section 4.11.5).

### **4.11.1 Trigger System Design**

#### **Overview**

The trigger system for E799II and P832 will have four levels. The Level 0 Trigger will consist of discriminators and simple logic local to each detector used in the trigger. These electronics will generate a small number of Level 0 Trigger signals from each detector, which will be transmitted via hardline to the Counting House. There, the Level 0 signals will enter the Level 1 Trigger System. The Level 1 Trigger will combine the Level 0 signals from different detectors with a few control signals, and will have the ability to perform fairly complex logic operations. A new Level 1 decision will be made for every RF bucket.

When the Level 1 Trigger fires, ADC and TDC digitizations will begin and the Level 2 Trigger system will be started. If the Level 2 Trigger rejects the event, the ADC's and TDC's will be cleared, and the Level 1 Trigger will be re-enabled. If the Level 2 Trigger accepts an event the Level 1 Trigger will remain disabled until all digitized data have been transferred to the Data Acquisition System's buffer memories. Events stored in the buffer memories will be partially or fully reconstructed by on-line processors. Based on this reconstruction, a Level 3 Trigger algorithm will select a subset of these events to be written onto 8 mm magnetic tape for offline analysis.

This subsection describes the designs of the Level 0 and Level 1 Trigger Systems in

some detail. The following subsections after the front end electronics subsection address the additions and upgrades to the Level 2 Trigger System (the new Hardware Cluster finder, upgrades to the Track Processor, and TRD Electron-Identification Logic) and Section 4.12 discusses the Level 3 Trigger System (which is an integral part of the Data Acquisition System).

Because the logic to be performed by the Level 0 and Level 1 Triggers is generally simple, we have elected to use commercial modules wherever possible to reduce the design and testing effort required. Products from LeCroy Corporation are specified here; however, if necessary or desirable we could substitute equivalent products from other suppliers.

## **Level 0 Trigger Design**

### *Accidental Counters*

Two accidental counters will be placed far upstream of the detector to form a muon telescope pointing toward the target, but away from the detector. These detectors will be used to form a random trigger whose probability of firing is proportional to the instantaneous intensity in each bucket. Such triggers have proven extremely useful in studies of accidental activity in the E731 detector, and have been used to overlay typical accidental activity on Monte Carlo events. To form the Level 0 signals from these counters, a NIM bin containing one LeCroy 623B discriminator module will be required near the location of the more downstream of the two counters.

### *Ring Veto System, Regenerator and Magnet Vetoes*

The logic for these detectors' Level 0 signals will be housed in NIM bins to be located near the vacuum vessel at  $z=114$  m, 126 m, 138 m, 156 m, 174 m, and 185 m.

Signals from each segment of Ring Vetoes 1, 2, and 3 will be sent to the first NIM bin, at  $z=114$  m. Each signal will be discriminated by LeCroy 623B discriminators, and the logic outputs will be combined by LeCroy 429A Logic Fan-In modules to form a single veto signal for each Ring. The trigger signals will be ready within 20 ns of the arrival of phototube pulses at the NIM bin. The latest logic pulses to be ready will be those for RC1, which will be formed no more than 62 ns plus phototube/base transit times after decay

particles pass  $z=114$  m, assuming 16-m long cables.

The second NIM bin will contain the same discriminators and logic fan-ins, and will produce veto signals for RC4, the Regenerator and the Mask Veto. The latest logic pulses here will be those from RC4, which will be available no more than 55 ns plus phototube/base transit times after decay particles pass  $z=126$  m, assuming 11-m long cables.

At  $z=138$  m, a third NIM bin will form Level 0 signals from Ring Vetoes 5, 6, and 7. The last pulses formed here will be those from RC5, at a maximum of 65 ns plus phototube/base transit times after decay particles pass  $z=138$  m, assuming 17 m-long cables. A fourth NIM bin at  $z=156$  m will be used to form the trigger signals from RC8, RC9 and RC10, with similar timing relative to particle passage at  $z=156$  m.

Near the analysis magnet, at 174 m, another NIM bin will be used to form Level 0 Trigger signals from RC11, RC12, and the Magnet Vetoes. Assuming 8 m cables on RC12, its Level 0 signal will be formed no later than 56 ns plus phototube/base transit times after decay particles pass  $z=174$  m.

Level 0 signals from the last Ring Veto, RC13, and from the CsI Collar Anti Counters, will be formed using the same logic in a NIM bin located near the CsI. Signals should be available no more than 56 ns plus phototube/base transit times after particles hit the CsI, assuming 8 m of cable delay before the discriminators.

### *Trigger Hodoscope*

The most complex Level 0 Trigger logic will be that which forms the Trigger Hodoscope signals. The Trigger Hodoscope is the most important element in many charged triggers; it is used to count charged-particle multiplicity and to identify symmetric two-body modes. It is assumed here that the Trigger Hodoscope will consist of four planes of 32 counters, two with counters oriented in the  $x$  direction, the other two in the  $y$  direction.

The Level 0 Trigger Hodoscope Logic will require one CAMAC crate and one NIM bin on the Counting House side of the hodoscope. Signals from all 128 phototube bases will be connected by 5 m-long cables to the inputs of LeCroy 4413 discriminators, which

will be strobed by the RF signal. These discriminators will produce two sets of ECL outputs 41 ns after pulses emerge from the phototube bases. One set of outputs from each 4413 module will be sent via long twisted-pair ribbon cables to the Counting House, where they will be received by FASTBUS TDC modules for readout.

The other set of outputs from each 4413 will be connected by very short jumper cables to the input of a LeCroy 4516 Programmable Logic Unit. Each 4516 will form logical OR's from two sets of 16 counters ( $x$ -Up and  $x$ -Down,  $x'$ -Up and  $x'$ -down,  $y$ -West and  $y$ -East,  $y'$ -West and  $y'$ -East). The 16 outputs of each 4516 will be connected by another short cable to the input of a LeCroy 2365 Logic Matrix, which will form eight logical combinations from the 16 signals. There will be a total of 32 such signals, which will be available 64 ns after pulses leave the phototube bases. These signals will be connected to LeCroy 4616 Level Adapters in the NIM bin. NIM outputs for eight of the 32 signals will be used as Level 0 Trigger signals; these will be available 73 ns after pulses leave the bases.

The 4413 discriminators also produce analog multiplicity signals, which can be daisy-chained. We will connect the outputs from the two 4413's handling each Up-Down or East-West pair of counter banks together. The four signals so formed will be connected to the four analog inputs of a LeCroy 4504 Flash ADC Module, also strobed by the RF. It will produce four 4-bit digital multiplicity signals some 67 ns after pulses leave the PMT bases, allowing for a 5 ns setup time prior to the strobe. These ECL signals will be sent to another Model 4616 Level Adapter for translation to NIM levels, making the 16 Level 0 multiplicity signals available by 76 ns after pulses leave the PMT bases.

### *CsI Calorimeter*

Signals from the 3256 blocks of the CsI Calorimeter will be sampled by Energy-Summing boards which are described in Section 4.11.2. About 200 analog Energy Sum signals will be produced at the wall of the CsI blockhouse, some 30 ns after pulses are produced at the bases of the CsI phototubes. These signals will enter custom-built linear fan-in modules in a rack near the blockhouse, where they will be further summed. The design of these modules is discussed in the section of this report dealing with CsI readout electronics. The linear sum of all the signals for each quadrant of the CsI will be discriminated at two different thresholds by two LeCroy 821 NIM discriminator to produce eight Level 0 Quadrant Energy signals. The linear sum for the entire array must be available

within 55 ns of the time pulses leave the CsI PMT bases. This Total Energy signal will be digitized by a LeCroy 4504 Flash ADC, strobed by the RF. The resulting five signals (four bits plus overflow) will be translated to NIM pulses by a LeCroy 4616 Level Adapter. The five Level 0 Total Energy signals will be available within 84 ns of the CsI PMT pulses. We estimate that this will make them available at the same time as the Trigger Hodoscope multiplicity signals at the point of the hardline feedthrough to the Counting House, since the CsI phototubes will be slightly faster than those on the Trigger Hodoscope because they have fewer stages.

### *Beam Hole Counters, Hadron Veto and Back Anti*

A NIM bin will be supplied at  $z=191$  m near the Hadron Veto. Signals from the Beam Hole Counters, Hadron Veto Bank, and Back Anti will be treated like those from the Ring Veto system, using LeCroy 623B Discriminators and 429 Logic Fan-In Modules. With 8 m-long cables, the Level 0 Trigger signals will be available 56 ns after pulses leave the phototubes on the various counters.

### *Muon Veto and Identification Banks*

A muon veto and a muon identification bank will be located at the far downstream end of the detector. Two CAMAC crates and NIM bins will be located on the Counting House side of this scintillator bank. Signals from each counter will enter LeCroy model 4413 discriminators. One set of ECL outputs from each discriminator will be sent to FASTBUS TDC modules in the Counting House. The analog multiplicity output of muon veto and muon identification bank will go to a LeCroy 821 NIM discriminator, where it will be compared to two different thresholds to produce one-muon and two-muon Level 0 Trigger signals. These signals will be available 57 ns after pulses leave the phototube bases, assuming 5 m long cables.

### *Hardline Transmission*

All the Level 0 Trigger Signals will be transmitted via hardline to the Counting House. The total number of hardlines required for each detector element is shown in the Table below. Assuming that the Muon Identification Bank is located 14 m downstream of the Trigger Hodoscope, the optimum location for the feedthrough of the hardlines from the detector enclosure is 5 m upstream of the Muon Bank, near the upstream end of the Muon



Filter. The Level 0 Trigger Signals from the Trigger Hodoscope, Muon Identification Bank, and CsI Calorimeter should all reach this feedthrough by 100 ns after pulses leave the Muon Bank phototube bases, allowing for 8 m hardline runs in directions transverse to the beam. Table 4.11.1 shows the number of hardlines required for Level 0 Trigger.

Table 4.11.1: Number of hardlines required for Level 0 Trigger.

Detector Element	Hardlines Required
Accidental Counters	2
Ring Vetoes 1-12	12
Mask Regenerator Vetoes	2
Magnet Vetoes	2
Trigger Hodoscope	24
CsI Energy Sums	14
CsI Collar/Edge Vetoes	2
Hadron Veto Bank	2
Beam Hole Counters/Back Anti	4
Muon Veto/Identification Banks	6
<b>Total</b>	<b>70</b>

By placing the Level 1 Trigger Logic as close as possible to the location of the feedthrough, it should be possible for all the Level 0 signals to reach their destinations within 116 ns of the time when pulses emerge from the Muon Bank PMT bases, or about 150 ns after pulses exit the CsI PMT bases.

## Level 1 Trigger Design

The Level 1 Trigger Logic will consist of two racks of electronics located as near as possible to the location of the feedthrough for the Level 0 Trigger signal hardlines from the detector enclosure. One rack will contain a NIM bin and a CAMAC crate, one immediately above the other. These two crates will contain the basic trigger logic, which is described in detail below. The other rack will contain at least one additional NIM bin and one additional

CAMAC crate. These will contain logic to perform less speed-critical functions, including: generation of Detector-Busy vetoes, scalers for all the Level 0 and Level 1 Trigger signals which will be used to monitor rates, and logic for communicating with the Level 2 Trigger and Data Acquisition Systems.

To follow the timing of the Level 1 Trigger, we define  $T=0$  as the time at which CsI signals reach the wall of the CsI blockhouse. In the previous section, we estimated that this was perhaps 25 ns after signals left the CsI PMT bases. Relative to this baseline, the Level 0 Trigger signals reach the Level 1 Logic no later than  $T=125$  ns. The first stage of the Level 1 Trigger Logic consists of 5 LeCroy 4616 NIM-ECL Level Adaptors, which translate the NIM pulses sent via hardline to ECL, and which provide NIM testpoints to check Level 0 Trigger signal timing and integrity.

The ECL outputs of each 4616 will be connected to a LeCroy 4518 Programmable Delay and Fan-Out Unit. These will be used to synchronize the Level 0 signals to within 1 ns of each other. Two of the 16-pair outputs on each 4518 will be used to produce two output cables, each containing eight Level 0 signals repeated on the first eight pairs and the second eight pairs. Only 8 of the 16 channels on the fifth 4518 will be used, so that there will be a total of nine output cables, carrying 72 Level 1 Source signals. The third set of 16 outputs from each of the five 4518's will go to a Fastbus TDC module for readout.

Each of the nine cables from the five 4518's will serve as the input to a LeCroy 4508 Programmable Lookup Unit. These modules will be strobed by the RF signal, and will form programmable logical combinations of eight signals at a time, forming nine sets of 16 Level 1 Trigger bits as outputs. These outputs should be available by  $T=155$  ns. The nine output cables will be combined in three groups of three to be logically OR'ed by LeCroy 4516 Programmable Logic Units. The outputs of each of the three 4516's will likewise be OR'ed by another 4516, producing 16 Level 1 Trigger signals at  $T=180$  ns. These 16 signals will be sent through two LeCroy 4431 Prescalers so that they may be independently and programmably prescaled by factors between 1 and 16. The 16 signals prior to prescaling will continue to a Fastbus latch module for readout. The 16 outputs of the 4431's will form the inputs to a LeCroy 2365 Logic Matrix, which will generate eight Subsystem Beam Triggers by  $T=215$  ns. The cable entering the 2365 will continue to a Fastbus Latch module for readout.

Another LeCroy 2365 module will receive as inputs 16 Calibration and Test Trigger

signals. It will use these to form eight Subsystem Calibration and Test Triggers. The Subsystem Beam Triggers and Subsystem Calibration and Test Triggers will be translated to NIM by LeCroy 4616 Level Adapters. Four LeCroy 365AL Quad Majority Logic Units with a total of eight channels will be used to form eight Subsystem Level 1 Triggers. Each channel of the 365AL has four inputs; a coincidence of two will be required. One of the four will be the Subsystem Beam Trigger and another will be the accelerator RF signal. The other two inputs will both be the Subsystem Calibration and Test Trigger. The Subsystem Level 1 Trigger will then fire immediately if there is a Calibration and Test Trigger, or synchronously with the RF if there is a Subsystem Beam Trigger. A Subsystem-Busy Veto signal will be used to block each Subsystem Level 1 Trigger when necessary.

The Subsystem Level 1 Triggers will be available no later than  $T=255$  ns. The output pulses will be long enough to effectively veto further triggers until the Subsystem-Busy Veto signal can be generated. Some of the Subsystem Triggers will have to be fanned out to many modules, for example the CsI ADC Trigger, which must be distributed to 13 crates of ADC modules. This could be done with a single LeCroy 429A. The outputs of this module would reach the ADC Crate Controllers by about  $T=295$  ns. If the CsI RG-213 cables are 70 m long, and the ADC input ribbon cables are 4 m long, then the CsI pulses from the bucket *before* the trigger will arrive at the ADC inputs at  $T=350$  ns. This means that the ADC Crate Controllers would have to distribute the necessary timing signals to every channel of every ADC module in less than 40 ns.

In addition to the CsI ADC Trigger, Subsystem Triggers may include a Level 2 Trigger Request, a Drift Chamber TDC trigger, a TRD System Trigger, a Ring Veto ADC Trigger, a Trigger Hodoscope Latch Trigger, a Muon System Trigger, and a Data Acquisition Trigger. A copy of each Subsystem Level 1 Trigger will be latched for readout to the Data Acquisition System.

## Level 2 Trigger Overview

When the Level 1 Trigger fires, the Level 2 Trigger systems will be started. These will consist principally of a Cluster Finder which will count the number of in-time energy clusters in the CsI Calorimeter, and a Track Processor which will count the number of in-time hits in each drift chamber plane-pair, and which will search for patterns characteristic

of  $\pi^+\pi^-$  decays. In addition to these two processors, we plan to use the TRD's to identify electrons as part of the Level 2 Trigger in E799II; we may also decide to use the TRD's to reject some  $K_{e3}$  events in P832.

The CsI ADC boards will generate 1600 "Cluster Flag" signals: one for each large CsI block, and one for each group of four small blocks. These flags will be transmitted to the Cluster Finder, which will use them to find clusters. The Cluster Finder must report the number of clusters found back to the Level 2 Trigger Controller within 3  $\mu$ s of the Level 1 Trigger. In the high-intensity environment of E799II and P832, it is particularly important that the Energy Sum boards be designed so that a cluster flag is generated only if there is sufficient *in-time* energy in a given block or group of blocks.

Signals coming from the drift chambers will fire 6-bit TDC's which will be used to determine whether hit pairs are consistent with the hypothesis that they were produced by in-time tracks. Drift chamber signals satisfying this criterion will be sent to the Track Processor electronics used in E773 and E799I. For E799II, the number of hits found in each view of each chamber will be used as a Level 2 Trigger criterion; for P832, the pattern of hits will be examined to select events consistent with the symmetric geometry of  $\pi^+\pi^-$  decays. The Track Processor result must be available to the Level 2 Trigger Controller no more than 3  $\mu$ s after the Level 1 Trigger. In order to keep dead time to a reasonable level, the *average* speed of the Track Processor must be considerably better than this maximum. The pattern-recognition processor used in E773 had a decision time of 0.5  $\mu$ s after the Level 1 Trigger, and this is the speed we anticipate for the charged mode in P832. In E799I the hit counting decision was typically available 1  $\mu$ s after the Level 1 Trigger for events which were rejected. Since digitization proceeds in parallel with Level 2 processing, longer decision times for events which are eventually accepted do not contribute to overall dead time.

The new TRD system will include ten planes of parallel wires running in the vertical direction. Signals from each wire will be discriminated, and majority logic will look for a coincidence of several large pulses among nearby wires in the ten planes. Such a coincidence will be counted as an electron signal. The TRD logic will report whether or not such a coincidence was found within 0.5  $\mu$ s of the Level 1 Trigger.

The Level 2 Trigger Controller will compare the results reported by the Track Processor, the Cluster Finder, and the TRD Electron-Identification Logic to the

requirements imposed for the particular Level 1 Trigger(s) which fired. If the requirements are not satisfied, the event will be aborted, and all ADC and TDC digitizations will be stopped; if the Level 2 Trigger is satisfied, then digitization and the transfer of data to the Data Acquisition system's buffer memories will proceed to completion.

The individual components of the Level 2 Trigger which will be constructed or upgraded for E799II and P832 are described in detail later in the Design Report.

### **Level 3 Trigger Overview**

The Level 3 Trigger will be an integral part of the Data Acquisition system. Digitized data from each of 8 to 16 parallel streams (depending on how much front-end buffering is implemented) will be collected in one of 16 on-line computers. The Level 3 Trigger system must be capable of handling 20 kHz of incoming events, with an average event size of 4 kbyte, during the spill. The on-line computing power and bus bandwidth must be sufficient to execute tracking and cluster reconstruction algorithms on 8,000 events per second, which implies that the average reconstruction time per event per processor must be less than 2 ms. This will allow the up to 460,000 events collected during a spill to be completely processed prior to the beginning of the following spill. The Level 3 Trigger's rejection power will arise from a filtering algorithm which will run in the on-line processors. This algorithm must allow us to reject most  $\pi e \nu$ ,  $\pi \mu \nu$ , and  $\pi^+ \pi^- \pi^0$  decays on-line, while still preserving large samples of these decay modes for normalization, calibration, and studies of systematic errors. The number of events selected by the Level 3 Trigger algorithm to be written to tape should not be greater than 50,000 per spill, which implies that the rejection factor obtained from the Level 3 algorithm must be about 10.

The Level 3 Trigger and Data Acquisition System are described in detail in Section 4.12 in this Design Report.

### **Trigger Timing and Rate Summary**

Table 4.11.2 summarizes estimated rates at the various triggering levels in P832. As noted above, times do not include phototube transit times and base propagation delays.

Table 4.11.2: Estimated trigger rates in P832.

Stage of Processing	Relative Time	Max. P832 Rate
CsI Pulses at Blockhouse Wall	0	---
Level 0 Triggers at Level 1 Trigger Logic	125 ns	1–10 MHz
Level 1 Triggers before Busy Vetoes	245 ns	250 kHz
Gates at ADC's; TDC Common Stop	340 ns	150 kHz
Level 2 Processing Complete	1 $\mu$ s Avg.	20 kHz
ADC and TDC Readout Complete	10 $\mu$ s	20 kHz
Level 3 On-line Filtering	(Buffered)	0.9 kHz to tape

Rates for Level 1 Sources will vary widely; the 1–10 MHz shown should be typical, corresponding to 2--20% occupancy. The estimate for the Level 1 Trigger rate is based on scaling the rate observed in E-773 up to an intensity of  $3.5 \times 10^{12}$  protons per pulse. If beam halo is substantially reduced, this estimate may be pessimistic. No dead time results from the Level 1 Trigger because all signals are “buffered” on delay cables. The Level 2 Processing time will vary considerably from event to event, but for P832 an average of 1  $\mu$ s will be achievable. If the total dead time at a 250 kHz raw Level 1 rate is 40%, then the actual rate of events processed by the Level 2 Trigger will be 150 kHz. Assuming a factor of 7.5 rejection power from the Level 2 Processors, the maximum rate of accepted events will be 20 kHz during the spill. The dead time contribution from the rejected events can be estimated as  $130 \text{ kHz} \times 1.5 \mu\text{s} = 20\%$ , where 1.5  $\mu$ s is taken to be the average total dead time for rejected events, including Level 2 Processing time *and* the time required to reset all ADC's and TDC's in preparation for new data. A 20 kHz readout rate would result in another 20% dead time contribution from the 10  $\mu$ s readout time for events entering the buffer memories, justifying the 40% estimate for total dead time. With a sufficiently large number of parallel data streams and parallel processors on-line, no dead time should result from the Level 3 Trigger processing. In order to obtain dead time near the 20% estimate given in Section 2.3, we will probably have to prescale the charged mode trigger by a factor of two. This will still leave us with 2.5 times more charged than neutral  $2\pi$  events, and so will result in only a minimal loss in sensitivity to  $\text{Re}(\epsilon'/\epsilon)$ .

In E799I, the total rate for  $ee$ ,  $\mu\mu$ , and  $e\mu$  Level 1 triggers was about 20 kHz at an intensity of  $1.4 \times 10^{12}$  protons per pulse. At  $5.0 \times 10^{12}$ , this scales to about 70 kHz. A  $\gamma\gamma$

and  $\pi^0\pi^0$  decay trigger would add some 15 kHz to this rate. The scaled rate for a Dalitz-decay trigger would be about 400 kHz at  $5.0 \times 10^{12}$ , while that for a loose four-track trigger would be about 950 kHz. The accuracy of these estimates depends on differences in the accidental rates between Phase I and Phase II of E799. A trigger system meeting the specifications described here will be sufficient to handle all the  $ee$ ,  $\mu\mu$ ,  $e\mu$ , and  $\gamma\gamma$  triggers, as well as a prescaled sample of Dalitz and Four-Track triggers, with prescale factors to the 10 and 14, respectively, used in E799I for these triggers, while maintaining total live time at the 70% level quoted in the sensitivity estimates of Section 2.3.

The components for the Level 0 and Level 1 Trigger Systems are standard modules which will be obtained from the Fermilab PREP pool. Some of the modules required may already be in the pool; others will have to be purchased.

The total number of CAMAC crates needed for the Level 0 and 1 systems described here is four, containing a total of approximately 60 modules. At \$ 5 k per crate and \$ 2 k per module average, this amounts to \$ 140 k.

In addition, these systems require 12 NIM bins containing a total of approximately 80 modules. At \$2 k per bin and \$450 per module average, this amounts to \$60 k. The total value of the PREP electronics required is therefore estimated to be \$200 k. This does not include Fastbus Latches or TDC's for various trigger counters, but does include scalers for monitoring Level 0 and Level 1 Trigger rates. Costs for hardlines and cable trays are also not included.

#### **4.11.2 CsI ADC Design and Readout Considerations**

In the design of the electronic readout system for the CsI calorimeter, we hope to alleviate some of the problems suffered in the system employed for E731. The ADC's used in E731 were LeCroy 1885 ADC's consisting of a single 12-bit, dual-range A/D converter on each readout card. A total of 96 channels are read in by each ADC card with each output multiplexed into the single A/D converter. In E731 a comparator on the ADC card switches the range of the A/D converter when an input signal exceeds a predetermined value. Since a single A/D converter in the LeCroy design is used for both the high and the low ranges, measuring and monitoring the bilinear gain ratio has been difficult. In addition, analog multiplexing of the input signals contributes to the noise in each channel and creates

rate-dependent problems in the pedestals. In E731 the lead glass readout system used a high-impedance pickoff at the input of the ADC card for generating inputs to the Hardware Cluster Finder. This system generated noise because the flash ADC's connected to these pickoffs generated pulses which fed directly back through the pickoffs into the input of the readout ADC's.

The readout system for the CsI calorimeter will consist of two major components. The first component will be located close to the CsI blocks and will provide an analog sum of the total energy in the calorimeter, called  $E_T$ . The second component of the electronic readout system will be the ADC cards located in the counting room close to the level one trigger system. Fig. 4.11.1 shows a schematic of the readout system for the CsI calorimeter.

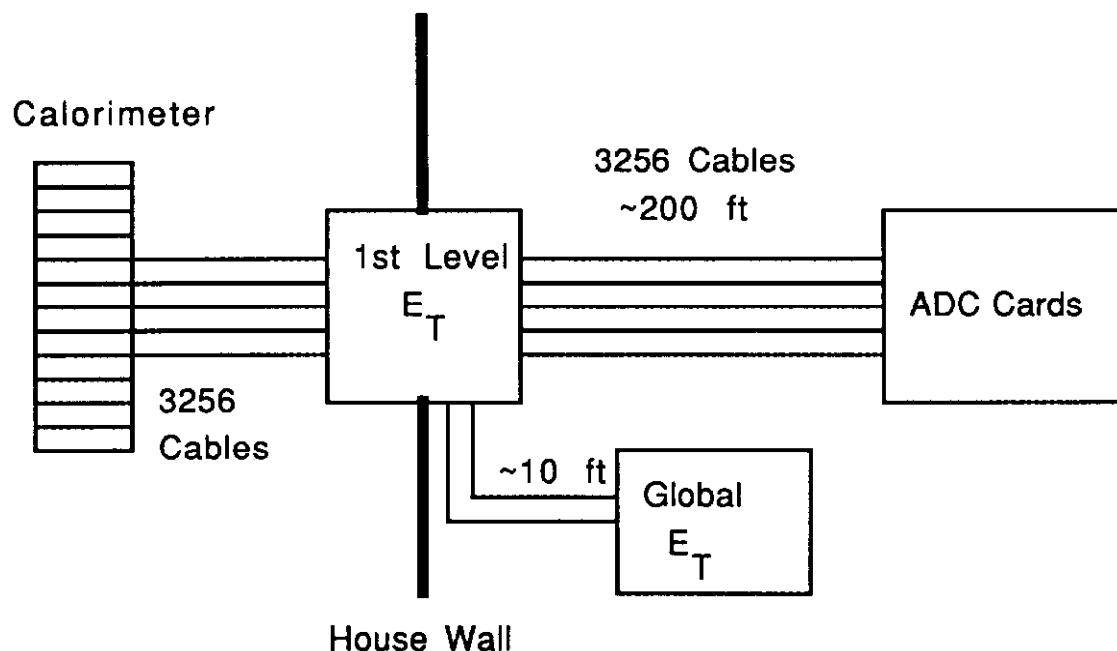


Fig.4.11.1: Schematic of CsI Calorimeter readout.

The analog energy sum modules will consist of approximately 200 cards which will be mounted directly in the wall of the cesium iodide house. Each card will receive the



outputs from 16 crystals. One function of these cards will be to provide feedthroughs from the inside of the house to the outside of the house for the 3256 output signals. In addition, part of the signal from each of the 16 inputs will be tapped off and linearly summed together. On the outside of the cesium iodide house, each card will have 16 analog outputs as well as the output of the linear sum signal. The 200 sum signals will then be connected to the input of the global linear sum module which will provide signals such as the total energy,  $E_T$ , and the measured energy in each quadrant of the calorimeter, will serve as the Level 1 Trigger sources. We estimate that the once a signal appears at the back of the CsI phototubes, the  $E_T$  signal will require approximately 50 ns to form.

The 3256 outputs from the 1st level  $E_T$  modules will be connected by 70 meters of RG213 cable to ADC cards located in the counting room. To digitize this data for the data acquisition system, we need just over 200 total ADC cards assuming that each card can handle 16 channels of input. We plan to put 16 cards in each crate, which corresponds to a total of 13 crates of ADC cards.

The ADC's required for this experiment will need to be very fast and have high precision. Due to the high intensity expected in E799 and P832 the digitization and readout time of the cesium iodide calorimeter must be kept below 10 microseconds. This means that the actual digitization of the data must take place in under 5 microseconds. In addition, to match the expected resolution of the cesium iodide calorimeter, we have determined that the ADC's must have an effective dynamic range of 15 bits. Since no such ADC systems are currently available, we plan to build our own system. To reach the stated precision we plan to use two 12-bit ADC's with one in high range and the other in low range. Having both the high and the low ranges read out simultaneously will reduce some of the problems encountered in E731 since analog switching noise will be reduced and the bilinear gain ratio can easily be measured. There are many 12-bit A/D converters currently available and we have located a vendor who can supply converters with full-range digitization times below 4 microseconds. The noise level for these ADC's must be kept below 1 count r.m.s. ( $\sim 50$  fC) to achieve the best resolution in the cesium calorimeter.

To understand accidental energy which is deposited in the calorimeter just prior to the arrival of a real event, we plan to presample each of the signals in an event. Fig. 4.11.2 shows when the various timing signals will occur relative to the arrival of a pulse. The presample will integrate the difference in charge between times  $t_0$  and  $t_1$ . We expect that the difference in time between these two times will be approximately 20 ns. The output voltage

from the presample will be input to one A/D converter and written to the data stream. The true signal will be the difference in integrated charge which arrives between times  $t_1$  and  $t_2$ , on the order of 100 ns. This signal will be read out by the two ADC's in high and low range. A fourth sampling time,  $t_T$ , about 20 ns after  $t_1$ , will be used to determine whether a given block contained prompt energy for triggering purposes.

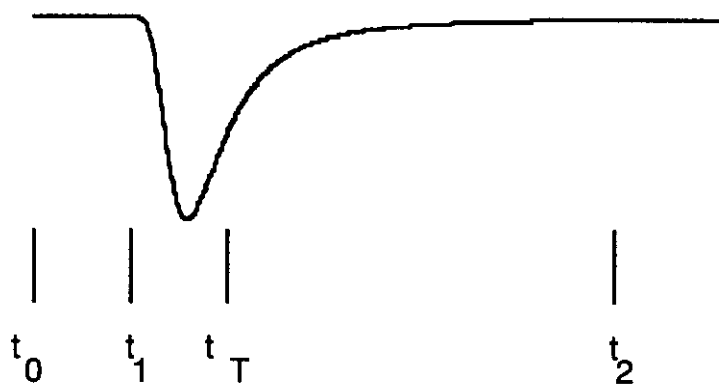


Fig. 4.11.2: Timing structure of ADC's relative to a real CsI crystal pulse.

As shown in Fig. 4.11.3, there will be four sets of switches corresponding to the four sampling times,  $t_0$ ,  $t_1$ ,  $t_T$  and  $t_2$ . At each of these times, the respective switch will close and the voltage corresponding to the current amount of integrated charge will appear on the appropriate capacitor. The output from any two successive times is sent to a differential amplifier which subtracts the early signal from the later signal. The output then corresponds to a real-time, baseline subtraction. This output voltage will then be sent to the input of one of the 12-bit A/D converters. A group at Chicago is currently developing compensating switches to handle the fast switching required for this task.

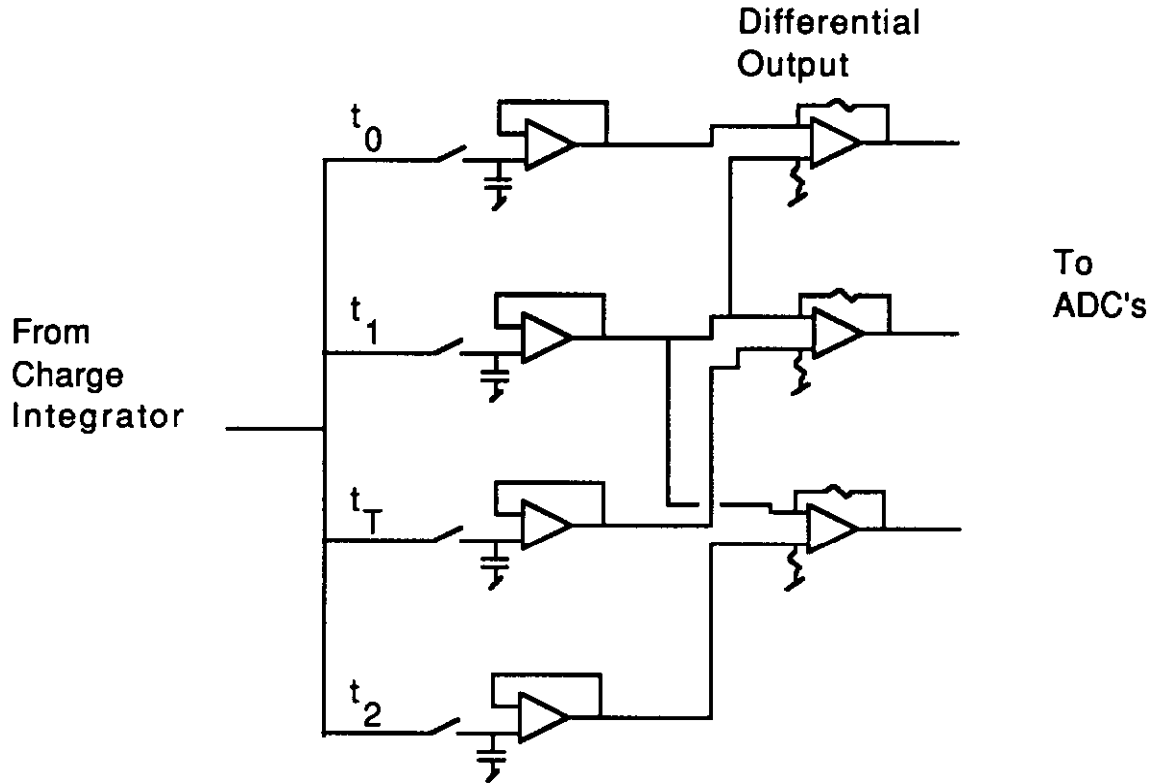


Fig. 4.11.3: Schematic of sample and hold circuit for ADC readout.

As mentioned above, the integrated charge received between times,  $t_1$  and  $t_T$ , will be used to for triggering purposes; namely generate bits for the Hardware Cluster Finder or HCF. If the output signal from this difference exceeds a programmable level, approximately 1 GeV, then a flag will be set on the ADC board to be sent to the HCF. We plan to make the time between  $t_1$  and  $t_T$  for the HCF bit below 20 ns, i.e. the time between successive buckets in a given spill. This will reduce our sensitivity to accidental energy in the calorimeter adding clusters at the trigger level. Although the cesium iodide calorimeter will have both 2.5 and 5.0 cm square crystals, we plan to use the larger 5.0 cm segmentation to define trigger bits for the Hardware Cluster Finder. Therefore, on a large fraction of the ADC boards, the analog signals from four of the small crystals will have to be added together when forming the HCF trigger bits. When a Level 1 Trigger signal is received, these bits will be sent to the cluster finder via four 40 bit-wide busses.

When a Level 1 Trigger signal is received, the ADC Timing Generator will send out signals to close the various switches and start the digitization process in the A/D converters.

The ADC's will be read out if the Level 2 Trigger is satisfied. Reading out the whole calorimeter is not necessary since only a small number of the crystals will contain interesting information. We therefore plan to employ a sparse readout scheme which will be based upon the result of the hardware cluster finder. For each cluster which is identified, we plan to read out all neighboring crystals regardless of the energy they contain. The hardware cluster finder will return 1600 bits of information (corresponding to the 5 cm block segmentation of the calorimeter) setting the flags on the ADC cards signifying which ADC's the data acquisition system needs to read out. For the 2.5 cm blocks, four of these bits will be set for every bit returned by the hardware cluster finder. In addition, it will be possible to read out the ADCs for any block whose energy exceeds an adjustable threshold, whether or not that block belongs to an HCF cluster. This will allow us to retain information for particles that do not deposit large amounts of energy in the calorimeter, such as minimum ionizing tracks. The readout of the ADC's will be programmable so that either or both of the two methods can be used.

We plan to build our own crates for the ADC's so that simplicity can be maintained. The protocol which will be used to transfer the data should use a compact data format and be flexible so that the number of words read out per channel can be programmable. For example, if the low range A/D converter is saturated, it need not be read out. However, for some fraction of events we will want to readout out both high and low range regardless of their values to monitor the bilinear gain ratio. To communicate with the data acquisition system, we plan to transfer data using optical cables, since this will allow us to electrically isolate the ADC's from the rest of the data acquisition system.

The development of CsI ADCs and readout system will be a combined effort between the electronics shop of the Univ. of Chicago and the Fermilab Physics department.

The cost estimate for the CsI calorimeter ADC and readout system is \$796 k which includes \$326 k for cables and \$320 k for the ADC system.

### 4.11.3 Front End Electronics

The TDCs, latches, and ADCs that compose the front end of the data acquisition system must all be able to support an event throughput of 20 kHz while contributing a deadtime of less than 20%. To meet this requirement, all front end modules must effectively be ready for the next event in less than 10  $\mu$ sec. In addition, each ADC and TDC must provide the sensitivity and dynamic range required by the corresponding detector element.

#### TDC Requirements

Detector Element	Sensitivity	Range	Number of Channels
Drift Chambers	500 ps	512 ns	2000 + spares
Photon Veto Sys.	100 ps	100 ns	104 + spares
Hodoscope Arrays	100 ps	100 ns	500 + spares
Trigger Sources & ADC Gates	50 ps	50 ns	128 + spares
Regenerator Sys.	100 ps	100 ns	120 + spares
Beam Calorimeter "Back Anti"	100 ps	100 ns	150 + spares

#### Drift Chamber TDCs

There are three sources of TDCs that can be drawn on to meet the above specifications, two commercially available and one designed by Fermilab. One of the commercial sources, Phillips, would have an effective deadtime of 20-25  $\mu$ sec when used to digitize the drift chambers, and hence is not suitable. The other commercial source is the LeCroy 1877, whose advertised specifications are suitable for the drift chamber readout, but a prototype of this new module will not be available for testing until mid-late 1992. The Fermilab TDC is now in the stage of a mature prototype, whose current configuration is adequate for drift chamber readout. The production of the required 2000 channels using this mature design, would take 50% time of one of the two design engineers in the

Fermilab Physics Department electronics shop for 6 months. In addition, two full time assembly/test technicians would be required for for 4-6 months. In parallel with the assembly and testing of the drift chamber TDC modules, It will be necessary for the equipment pool at Fermilab, "PREP", to receive the modules and establish test and repair fixtures for field support of the drift chamber TDC system. A detailed technical review of the Fermilab TDC's architecture and measured performance can be found in Fermilab conference memo 91/189, July 1991.

## High Resolution TDC

Of the three candidate TDCs, the Phillips and LeCroy modules can both achieve a resolution of 100 ps. As mentioned before, the LeCroy module will not be available for detailed tests until the middle of 1992. The Phillips modules are available now, and with careful architecture of the front end, the Phillips module can be used to digitize the relatively few channels outside of the drift chamber system while maintaining an effective deadtime of less than 10  $\mu$ sec. The Phillips TDCs can share two Fastbus crates with latch modules that will latch each channel that is TDC'ed. Suitable low cost fastbus latch modules are commercially available from several vendors, and will not be described in any detail. After extensive testing and debugging by the E791 group here at Fermilab, the Phillips TDC is quite reliable and well understood. The equipment pool at Fermilab has supported the Phillips module for the last several years. Costing information now follows:

Module	Channels	Cost/Channel	Cost/Module
Fermilab TDC	96	\$30	\$2880
LeCroy TDC	64	\$50	\$3200
Phillips TDC	32	\$60	\$1920
Latch module	96	\$20	\$1920
Readout controller (FB-SCC)(LRS-1821)	--	--	\$3000/\$7000
FB crate/power supply	--	--	\$8000

A drift chamber readout system based on the Fermilab TDC and LRS-1821 readout

controller would cost \$75 k, where the same system employing the LeCroy TDC would cost \$130 k. Hence a reasonable range of cost for the drift chamber readout system is \$75 k to \$130 k. Using the same readout controller and the Phillips TDC, the 100 psec TDC system cost is estimated at \$76 k.

## ADC Requirements

The ADC modules for the CsI calorimeter are described in section 4.11.2 in this report. The following requirements apply to the ADCs used for other detectors in the KTeV spectrometer:

Detector Element	Sensitivity	Range	Number of Channels
Photon Veto Sys.	0.4 pC/count	12-bit	104 + spares
TRD System	0.4 pC/count	12-bit	1480 + spares
Hodoscopes		12-bit	200 + spares
Regenerator Sys.	0.05 pC/count	12-bit	120 + spares
Beam Calorimeter "Back Anti"	0.4 pC/count	12-bit	150 + spares

These requirements can be met in principle by the specifications of either the LeCroy 1879 or Fermilab Fastbus ADC modules. Both modules are now in the prototype stage, with the Fermilab module more mature by 6-8 months. The LeCroy prototype will not be available for testing until mid 1992. A Fermilab prototype is available now for testing. The Fermilab module has an internal pedestal subtraction scheme that greatly simplifies the on-line tracking of pedestals necessary for readout sparsification. Such a scheme would have to be supplied externally for the LeCroy module, making the data acquisition system more complex. If Fermilab produces the 2000 ADC channels outside of the CsI calorimeter system, another 1/2 time design engineer from the Fermilab Physics Department electronics shop will be required, as well as two additional full time assembly/testing technicians. As with production of the Fermilab TDC design, these ADC modules will need to be transferred to PREP for full field support.

A cost estimate of the non-CsI ADC system follows:

Module	Channels	Cost/Channel	Cost/Module
Fermilab ADC	64	\$40	\$2560
LeCroy 1879 ADC	64	\$60	\$3840
CsI Calorimeter ADC	16	\$100	\$1600
Readout Controller (FB-SCC)/(LRS-1821)	--	--	\$3000/\$7000
FB crate/power-supply	--	--	\$8000

The CsI ADC cost is included for completeness, and to illustrate the large cost of using the CsI ADC to digitize all the ADC channels. Such a scheme would exceed \$300 k. The cost of the non-CsI ADC system based on the Fermilab ADC is estimated at \$113 k. The cost of the same system based on the LeCroy ADC is \$155 k. Both commercial and Fermilab ADCs will require extensive testing and debugging at Fermilab.

## Summary

Timely completion of the data acquisition system's front end is essential for the development and debugging of the many new detector systems that compose the KTeV spectrometer. We expect that the development and production of the KTeV front-end electronics will fully use the available resources in the Fermilab Physics Department electronics shop for the next two years. The load on the Fermilab electronics shop could be substantially reduced if the LeCroy TDC becomes available on schedule. If so, the Fermilab electronics shop would focus on producing ADC systems for KTeV, and we would adopt an entirely commercial TDC system. Hence, LeCroy's progress in the first half of 1992 will be closely watched.



#### 4.11.4 Hardware Cluster Finder II

The E799II/P832 hardware cluster finder will count the number of contiguous depositions of energy, or clusters, in the experiment's CsI array. This information will be made available to the Level 2 trigger less than 2  $\mu$ sec after the Level 1 trigger is generated. In addition, the HCF will provide the ADC system with a list of channels whose digitization is to be included in the experiment's data stream. We will discuss the following:

1. Clustering algorithm and Monte Carlo simulation of its effectiveness
2. Xilinx XC3000 logic cell arrays and hardware implementation of the clustering algorithm
3. Sparsification scheme
4. HCF II system architecture; communication with energy summing boards and ADC's

##### Clustering algorithm and Monte Carlo simulation of its effectiveness

We will define a cluster as a set of contiguous CsI crystals which produce signals above a certain threshold. The following are examples of single clusters:

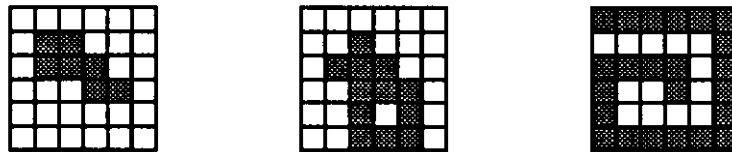


Fig. 4.11.4: single clusters

Depending on details of the shapes of showers, we might want to consider illuminated crystals which only touch corners (corner fusions) to be contiguous:

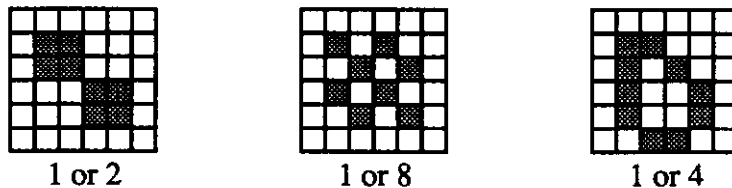


Fig. 4.11.5: corner fusion clusters

The definition of a cluster as a set of contiguous crystals above threshold suggests one algorithm for counting clusters which begins by linking together all lit crystals which share edges (or corners). This linking process might require several iterations to fuse blocks in a cluster like that shown in Fig. 4.11.6:

Fig. 4.11.6: complicated "glue'em" cluster

Another possible algorithm involves counting the number of convex and concave segments encountered traveling around the perimeter of a cluster, as in Fig. 4.11.7.

**Fig. 4.11.7: counting concave and convex segments**

A third algorithm makes use of the fact that a complete clockwise circuit around the

perimeter of a cluster includes four more right turns than left turns, as illustrated below.

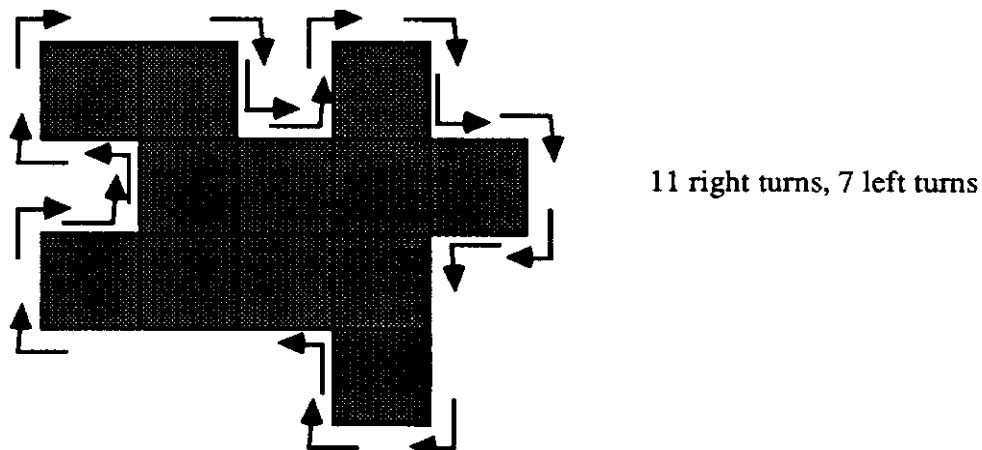


Fig. 4.11.8: counting right and left turns

The difference in the number of right and left turns found in the entire CsI array equals four times the number of clusters. This algorithm can be implemented with logic cell arrays scanning 4-crystal sections of the CsI; the HCF will use this algorithm to count clusters. Hardware implementation of the algorithm will be discussed in the next section. One concern to be addressed is the fact that clusters with holes are not recognized by this algorithm either, as can be seen in the following figure.

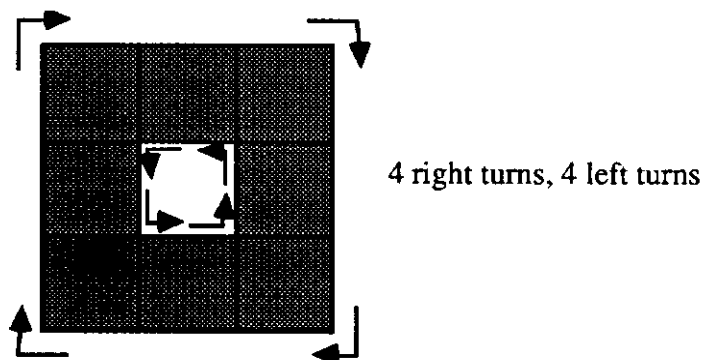


Fig. 4.11.9: a cluster with a hole

We have done Monte Carlo studies of the relative effectiveness of the “glue ‘em” and HCF algorithms in counting clusters in the E799II/P832 photon calorimeter. The Monte Carlo simulation assumed the following geometry:

Table 4.11.3: Monte Carlo geometry		
Detector element	z position	comments
Target	0	point target at 0,0
Decay volume	$99 \text{ m} < z < 159 \text{ m}$	
CsI array	185 m	$2 \text{ m} \times 2 \text{ m}$ ; two holes; $5 \text{ cm} \times 5 \text{ cm}$ block size

The neutral beams were produced at 5 milliradians by an 800 GeV primary proton beam. K mesons were generated using the Malensek energy spectrum (FNAL report FN-341, Oct. 1981), with an additional factor of  $1/E$  included to account for the  $K_L$  decay probability. The beams diverged from the target, and were  $10 \text{ cm} \times 10 \text{ cm}$  wide at the calorimeter, with 10 cm spacing between inner edges. Each beam hole was a square 15 cm on a side, as shown in Fig. 4.11.10 below.

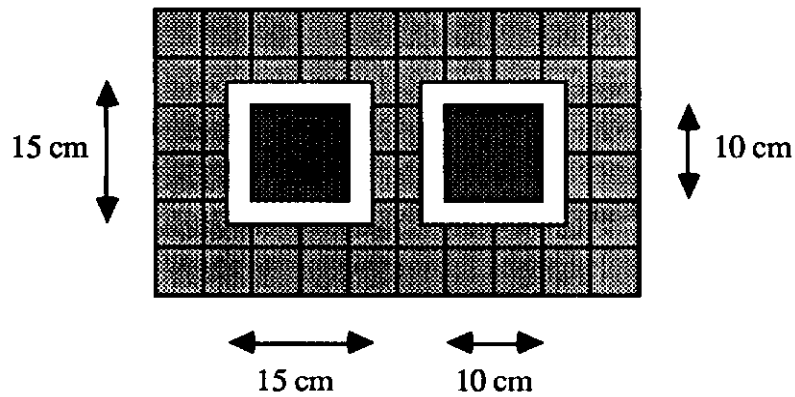


Fig. 4.11.10: hole geometry in Monte Carlo

Kaon decays were generated flat in  $z$  inside the decay volume. The energy spectra of decaying kaons and produced photons are shown in Fig. 4.11.11.

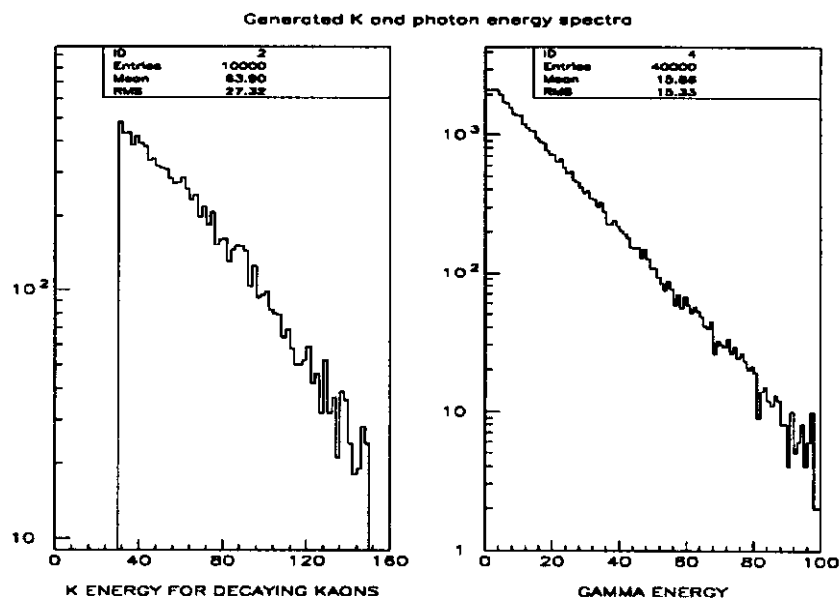


Fig. 4.11.11: K meson and photon energy spectra.

Of 10,000 generated Monte Carlo decays, 3301 had all four photons striking the CsI array. The energy and z spectra for these 3301 events are shown in Fig. 4.11.12.

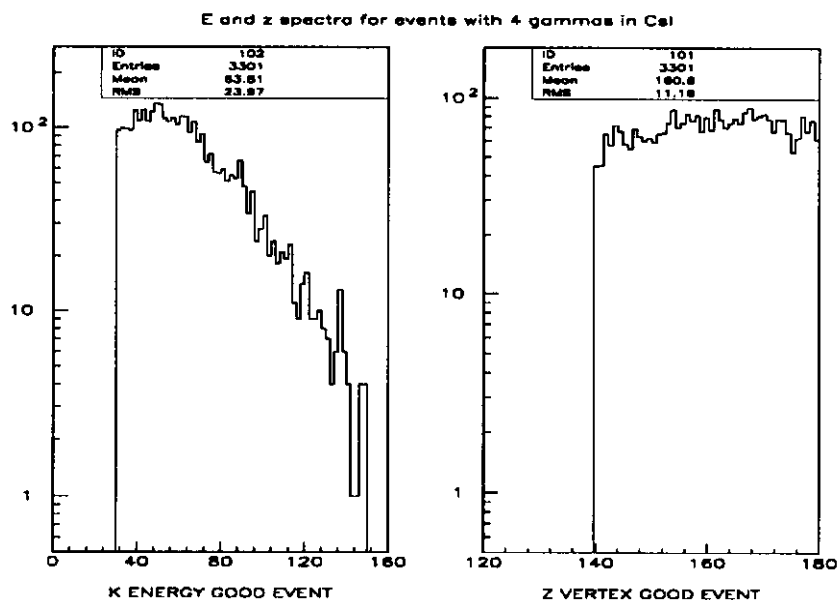


Fig. 4.11.12: Accepted K meson energy and decay position spectra

Photon clusters were generated assuming that the energy per unit area can be described by the function

$$E(r,\theta) = A e^{-r/b} + C e^{-(r/d)^2}$$

where  $A$ ,  $b$ ,  $C$ , and  $d$  are adjustable constants, and  $r$  is the distance from the photon's impact point. Values of the parameters are shown in Table 4.11.4. ( $A$  and  $C$  are rescaled to conserve energy.)

Table 4.11.4: Monte Carlo cluster shape parameters				
	A	b	C	d
"normal"	1	3 cm	1	3 cm
"fat"	1	6 cm	1	6 cm.

Energies deposited in cells on a 5 mm  $\times$  5 mm grid were summed and assigned to the appropriate CsI crystals in the array. To model gain imbalances and noise, the total energy in each crystal was jittered randomly on an event-by-event basis by as much as  $\pm 5\%$ . The cluster finder received a map of the calorimeter with bits set for blocks with apparent signals greater than 500 MeV.

The number of clusters found by the "glue 'em" algorithm is almost always the same as the number found by the HCF algorithm, whether or not corner fusions take place. With "normal" clusters ( $b, d = 3$  cm), most photons are resolved into individual clusters by the "glue 'em" algorithm as shown in the following Table 4.11.5.

Table 4.11.5: clusters vs. photons					
"glue 'em" clusters (3 cm)	photons in the CsI array				
	0	1	2	3	4
4					2201
3				3450	896
2			1834	809	182
1		331	193	61	22
0	8	10	3	0	0

The HCF algorithm usually agrees with the "glue 'em" algorithm:

Table 4.11.6: HCF vs “glue ‘em” clusters					
HCF clusters (3 cm)	“glue ‘em” clusters				
	0	1	2	3	4
4					2201
3				4346	0
2			2821	0	0
1		602	4	0	0
0	21	5	0	0	0.

All events with disagreement between the two algorithms had several photons fusing near a beam hole. Even when “fat” clusters are generated, the agreement between the HCF and “glue ‘em” algorithms is very good, as shown in Tables 4.11.7 and 4.11.8.

Table 4.11.7: clusters vs. photons					
“glue ‘em” clusters (6 cm)	photons in CsI array				
	0	1	2	3	4
4					939
3				1855	1357
2			1277	2027	821
1		279	665	425	184
0	8	62	88	13	0

Table 4.11.8: HCF vs. “glue ‘em” clusters					
HCF clusters (6 cm)	“glue ‘em” clusters				
	0	1	2	3	4
4					939
3				3205	0
2			4047	7	0
1		1429	78	0	0
0	171	124	0	0	0

The number of blocks per cluster is a function of the cluster size parameters, b and d, as

shown in Fig. 4.11.13.

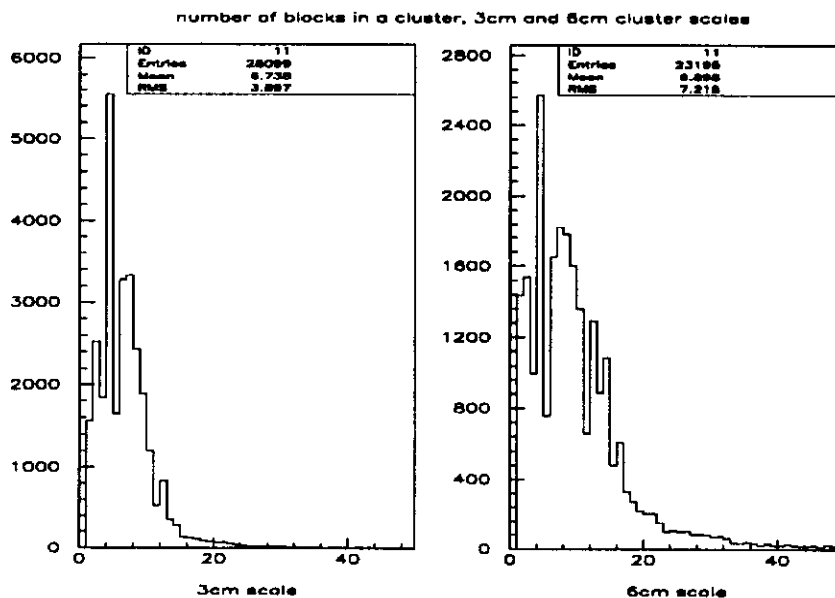


Fig. 4.11.13: blocks per cluster with two different sets of cluster shape parameters

In conclusion, the HCF algorithm almost always agrees with the “glue ‘em” algorithm when applied to  $2\pi^0$  decays, and should work well as part of the level 2 trigger.

## Xilinx XC3000 logic cell arrays and hardware implementation of the clustering algorithm

We will base the architecture of the HCF II around Xilinx CMOS XC3000 family logic cell arrays. Each XC3042 chip contains 96 I/O Blocks and 144 Configurable Logic Blocks (CLB's) in a 132-pin package. Nearly arbitrary interconnections between the chip's input/output pins and CLB's can be established by the I/O Blocks. In addition, interconnect resources on the chip allow complicated logic structures to be built from many CLB's. A schematic diagram of part of an XC3042 and a simplified diagram of a configurable logic block are shown in Fig. 4.11.14 and Fig. 4.11.15.



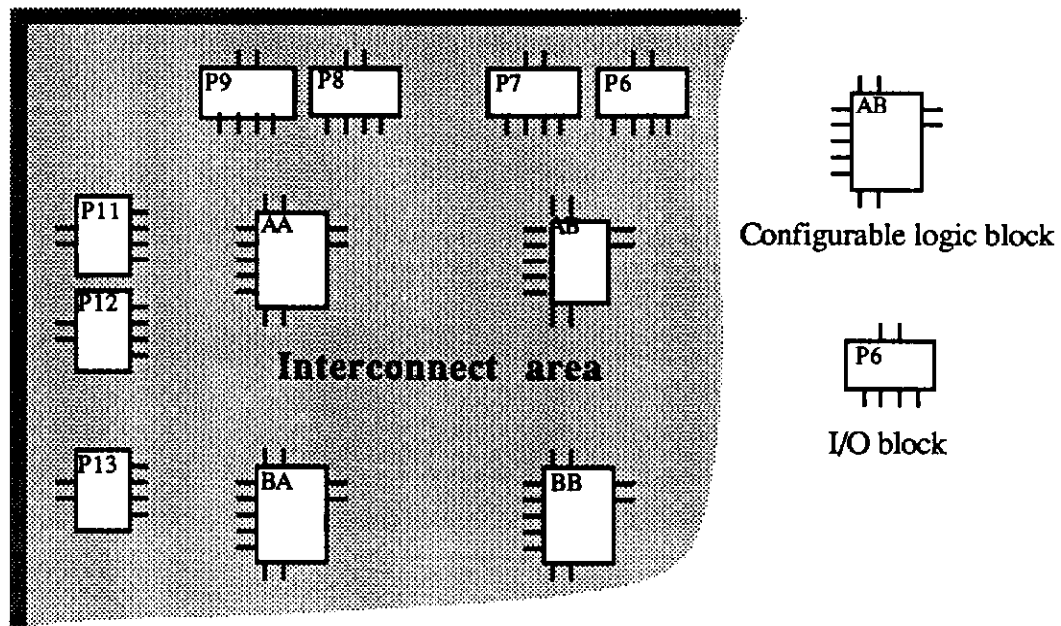


Fig. 4.11.14: Xilinx logic cell array

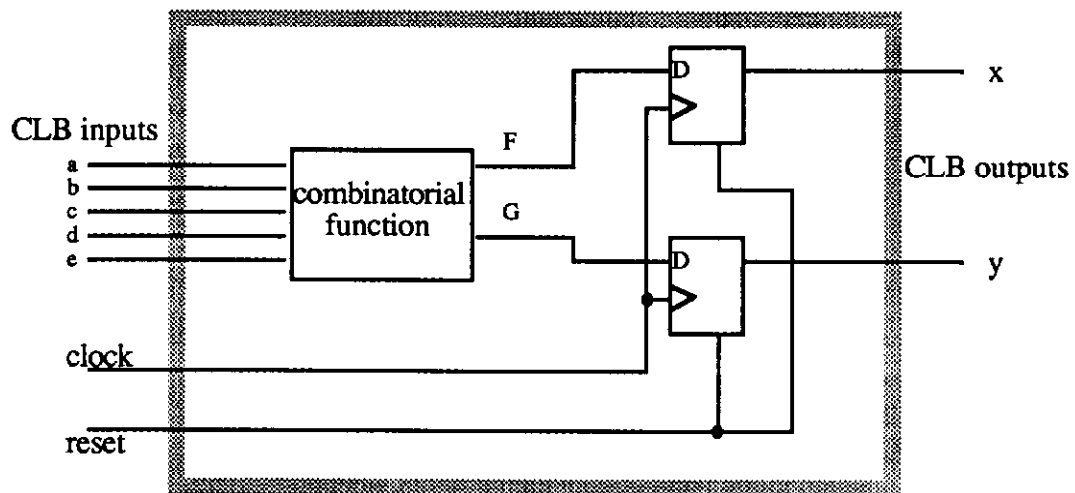


Fig. 4.11.15: configurable logic block

Note that each CLB contains an arbitrary function generator which produces two output bits for patterns of five input bits.

The cluster counting algorithm can be implemented by calculating a “pattern weight”

for overlapping groups of four blocks by presenting a raster scan of the CsI array to the HCF, as indicated in Fig. 4.11.16.

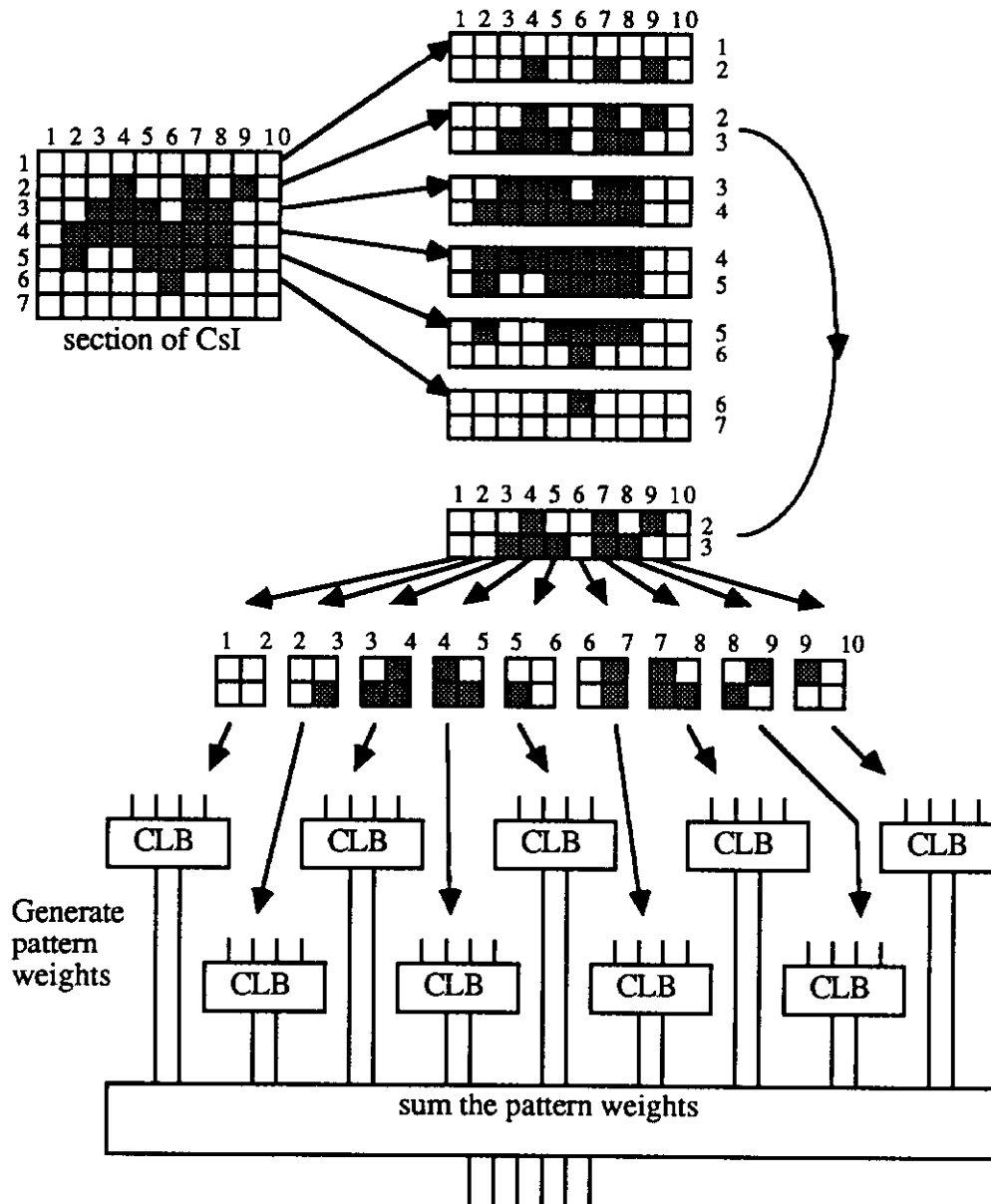








Fig. 4.11.16: cluster counting algorithm

The pattern weights associated with various combinations of “lit” and “unlit” blocks are indicated in Table 4.11.9.

Table 4.11.9: pattern weights	
pattern of struck blocks	pattern weight
	0
	1 (one right turn inside the cell)
	0
	-2 to fuse clusters which touch corners (two left turns inside the cell) +2 to separate clusters which touch corners (two right turns inside the cell)
	-1 (one left turn inside the cell)
	0

Because there are four possible pattern weights, the combinatorial function generator of a single CLB can generate the desired value. After each row is processed, the values are summed and the result is added to the sum from previous rows. By the time data from the entire CsI array is processed, the accumulated sum of pattern weights will equal four times the number of clusters. Two XC3042 chips can process an entire CsI row's worth of data simultaneously. Since the CsI information will be presented in a raster scan, a pair of chips could process the entire CsI array's data in 40 cycles. The HCF algorithm lends itself well to parallel generation of pattern weights, and we plan to build the processor so that it takes about 11 cycles to complete its task. Based on documentation from Xilinx, we estimate that one cycle will require 60 nsec. Tests, to be conducted in the near future, will give us a more accurate picture of the XC3042's performance.

## Sparsification scheme

The HCF will provide the ADC system with a bitmap indicating which CsI channels' digitizations are to be included in the experiment's data stream. Additional Xilinx chips will be used to set bits for one or two rings around blocks which are above threshold, as indicated in the figure below. All blocks in the rings or above threshold will be read out, as indicated in Fig. 4.11.17.

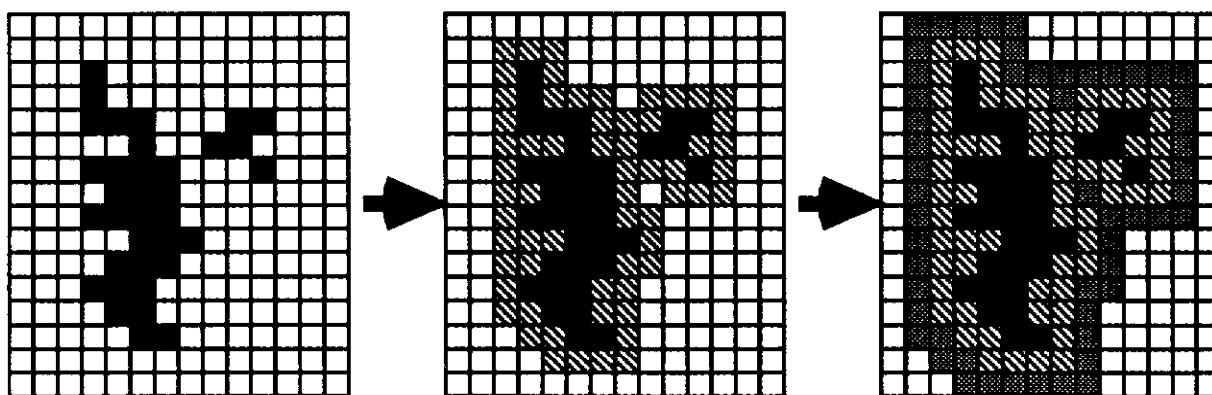


Fig. 4.11.17: sparsification via construction of perimeter rings

The algorithm for building a ring is best described graphically, as shown in Fig. 4.11.18. As with the cluster counting algorithm, sparsification calculations can be done in parallel for different sections of the CsI array; construction of two rings around clusters will take about 14 cycles, each of 60 nsec duration.

## **HCF II system architecture; communication with energy summing boards and ADC's**

The HCF will consist of a router board, four processor boards, and an inverse router board. The router board will receive the bitmap of CsI blocks above threshold and send parts of this bitmap to the processor boards. The processor boards will generate pattern sums for the cluster counting algorithm and sparsification bitmaps. The inverse router board will recombine the sparsification bitmaps from the processors and send the readout bitmap to the ADC system. A diagram of the HCF system's architecture follows, in Fig. 4.11.19.

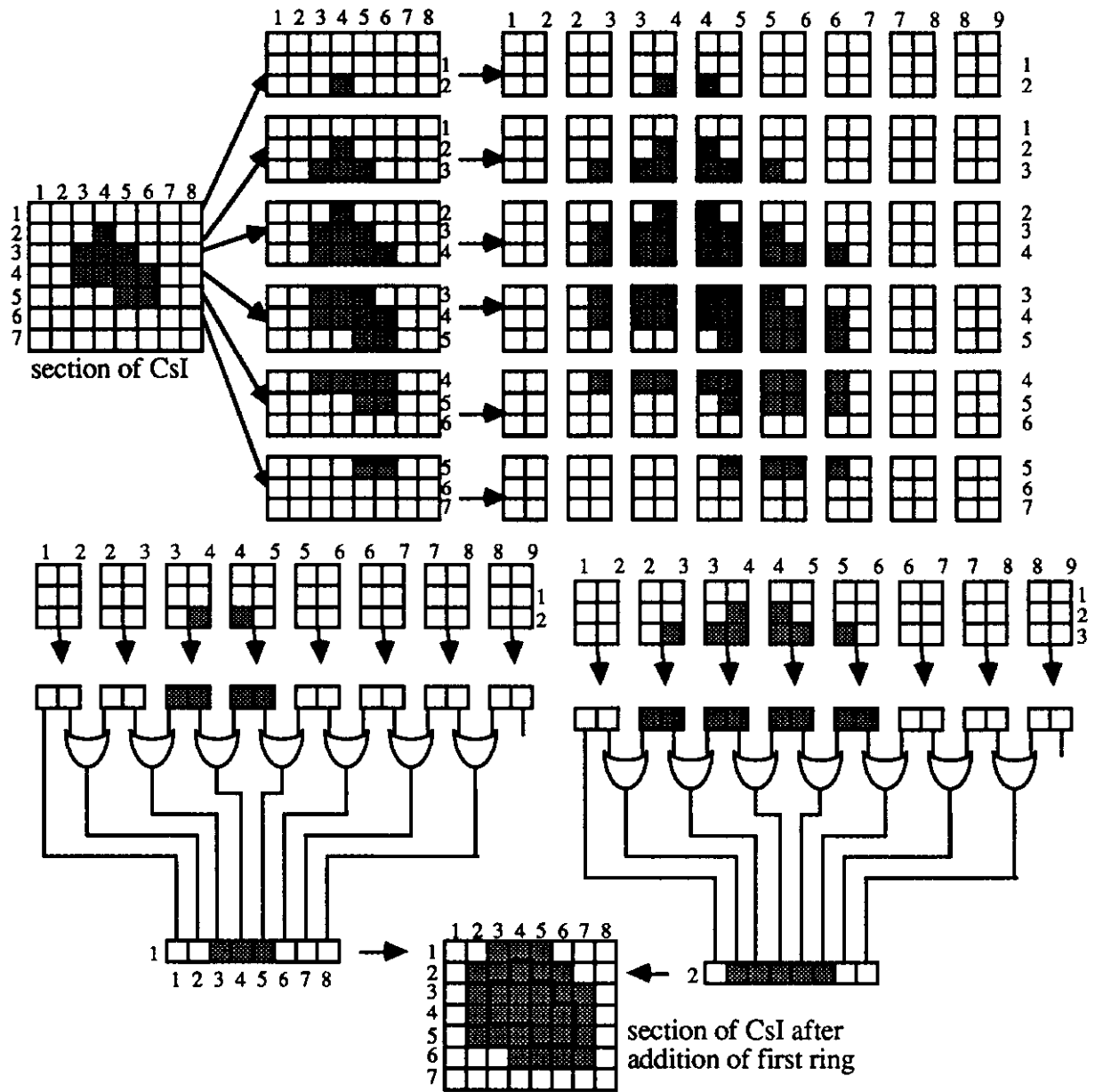


Fig. 4.11.18: ring construction algorithm

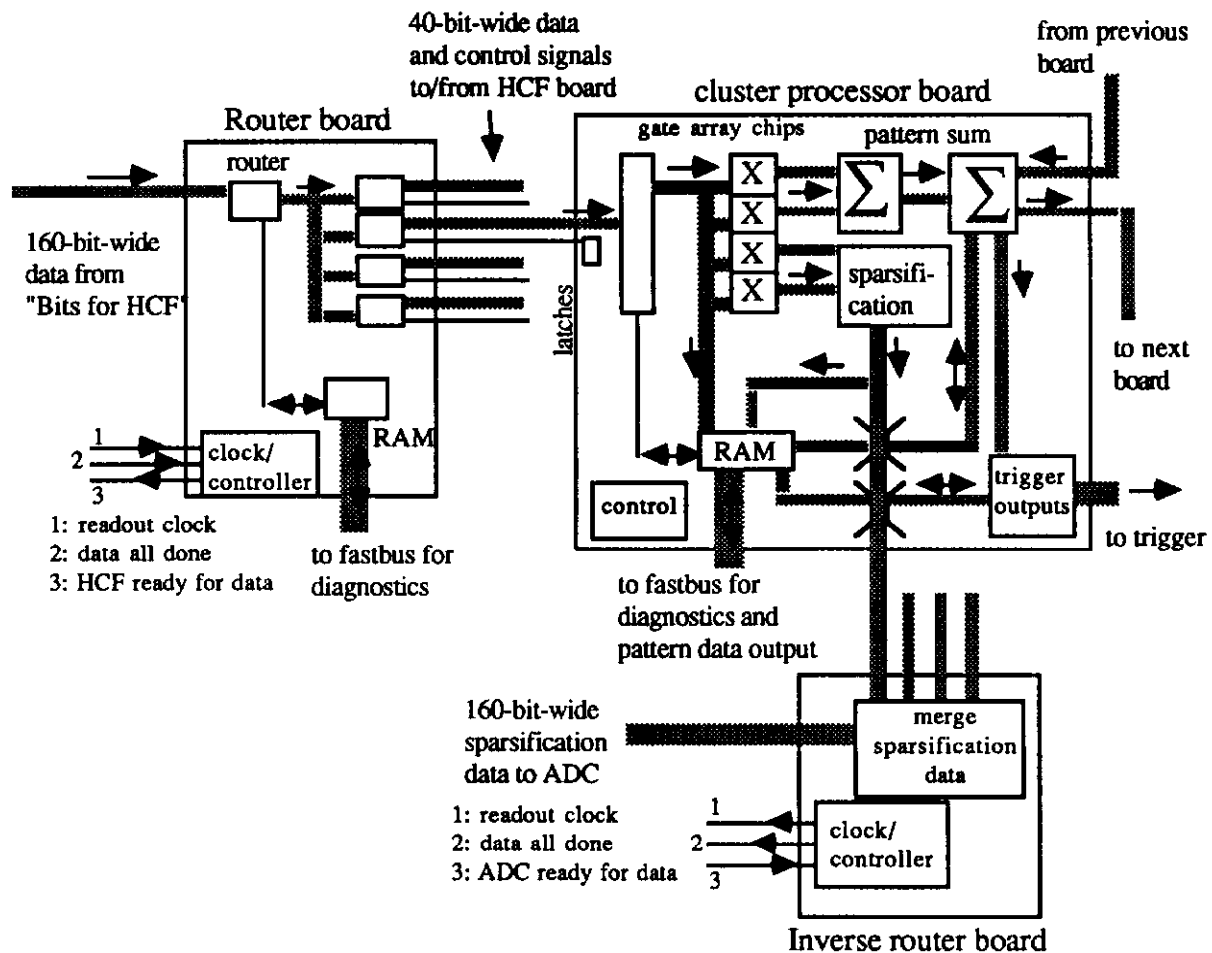


Fig. 4.11.19: HCF II architecture

Communication between the HCF, the ADC's, and the summing circuits which produce the bitmap of blocks above threshold is shown in Fig. 4.11.20. Signals are passed to the HCF on ribbon cables, carrying 160 bits per clock cycle. All data and control signals are differential ECL.

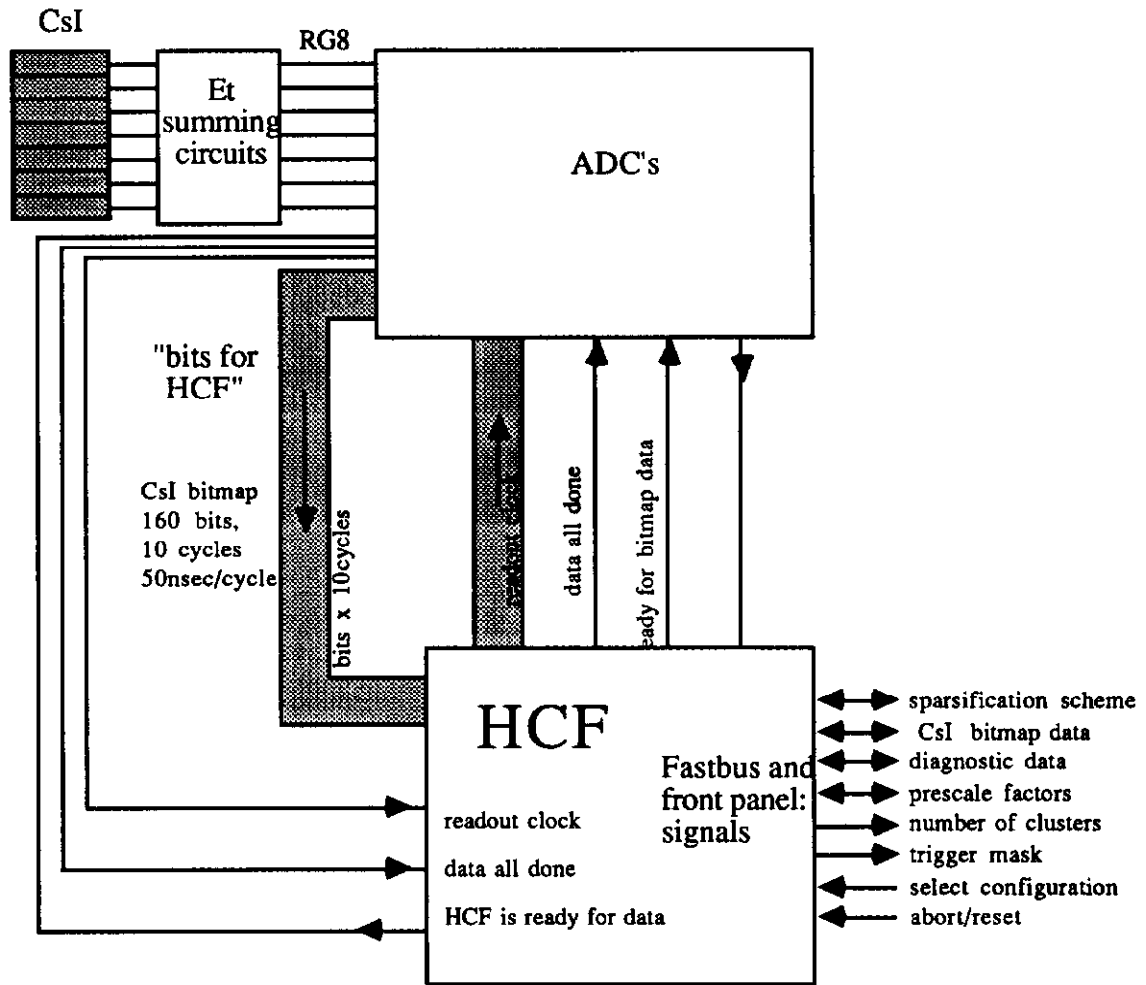


Fig. 4.11.20: HCF - ADC communication

A timing diagram for some of the signals exchanged between the various section of the clustering and ADC systems is shown in Fig. 4.11.21. It will take 600 nsec for the complete CsI bitmap to be delivered to the HCF; cluster counting can take place while data is being received. It is likely that the cluster counting and sparsification will be finished 1μsec after data begins to arrive at the HCF. It seems almost certain that no more than 2μsec will be needed to count clusters.

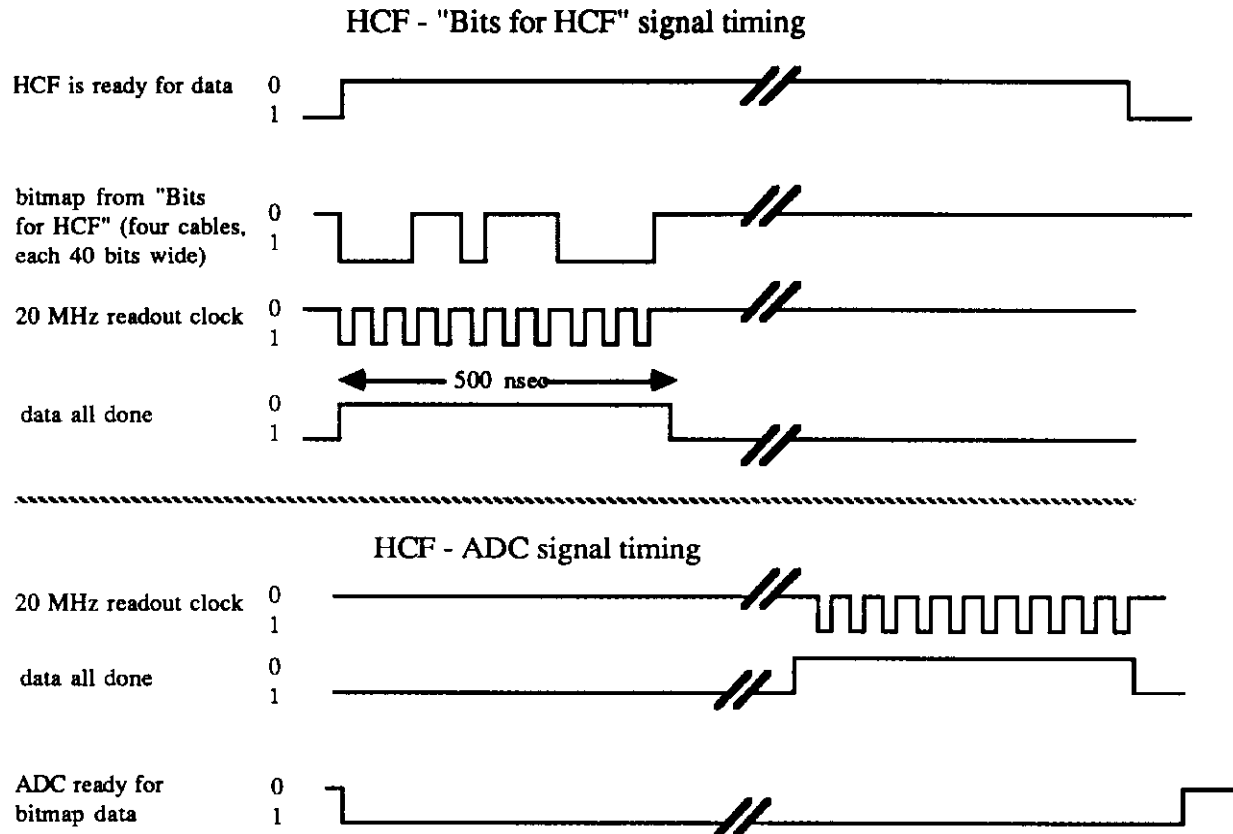


Fig. 4.11.21: HCF system timing

Three different printed circuit boards are required for the HCF II: the router, the cluster processor, and the inverse router. Each of these three board types would be implemented as FASTBUS (IEEE 960) standard boards.

The cost estimate assumes each of these boards to be a fully compliant FASTBUS slave, with logical addressing, broadcast addressing, block transfer capability, and sufficient on-board memory to contain at least one full "image" of data (for diagnostic purposes)

The overall system cost estimate is:

\$10,200	router(s)
\$33,850	cluster processors
\$10,200	inverse router(s)
(\$54,250 total)	



#### 4.11.5 Track Processor Upgrade

In order to use information from the drift chamber system in E773 and E799I, the University of Chicago designed and built a Track Processor system which receives information from each of the approximately 2000 wires in our four drift chambers. In E773, we used a fast lookup table feature of the system to identify events consistent with being examples of the  $\pi^+\pi^-$  decay of the  $K_L$  and  $K_S$ . The rejection factor, defined as the number of Level 1 charged triggers divided by the number of triggers which survived the Track Processor cut, averaged about 7. However, this number was strongly dependent on intensity, varying from about 10 at  $1 \times 10^{12}$  to 5 at  $2 \times 10^{12}$ . The lookup table decision was available less than 500 ns after the time of the Level 1 Trigger.

In E799I, we used the Track Processor system to count the number of hit-pairs in each view ( $X, Y$ ) of each drift chamber. By cutting on these quantities, we obtained a rejection factor of 3 to 5 for our Two-Electron trigger (used for the  $\pi^0 e^+ e^-$  decay mode), and of 40 to 100 for a "Four-Track" trigger (where we required at least four hits in each of the eight views). The Track Processor typically provided this decision less than 1  $\mu$ s after the Level 1 Trigger decision.

In E799II and P832, we will use all the Track Processor electronics built for E773 and E799I. However, the intensity-dependence of the observed rejection factors indicates that accidental hits in the drift chambers were contributing to the satisfaction of Track Processor cuts. In fact, studies of accidental triggers in E799I have shown that some 6% of accidental triggers had enough drift chambers hits to satisfy a Two-Track hit-counting cut, even though less than 1% of those events contained two in-time tracks. These data were collected at an average intensity of  $1.4 \times 10^{12}$  protons per pulse. Since we propose to run P832 at an intensity of  $3.5 \times 10^{12}$ , and E799II at  $5.0 \times 10^{12}$ , it is important that we take action to ameliorate the effect of accidental drift chamber hits on the KTeV triggers.

To do this, we will build a system of six-bit TDC's which will digitize the time of drift chamber hits in 6 ns steps. Immediately upon receipt of a Common Stop signal, the hits times for each pair of wires will address a memory chip containing a map of acceptable  $(t_1, t_2)$  pairs; that is, pairs corresponding to the passage of an in-time track between those wires. This amounts to making an on-line Sum-of-Distances cut on all hit-pairs. When acceptable hits are detected, signals will be sent to the next stage of the Track Processor.

Isolated or out-of-time hits will be blocked, dramatically reducing the probability that accidental hits in the drift chambers could cause an event with too few in-time tracks to satisfy Track Processor requirements.

The use of separate memories for each wire pair endows the system with great flexibility: we will be able to relax or remove timing cuts when one of the wires in a pair is inefficient or hot; we will also be able to adjust for  $t_0$  variations between wires, which are currently as large as 20 ns; we will also be able easily to adjust the memory maps to account for changes in the time-to-distance relationship which may occur as a consequence of variations in the drift chamber gas.

The system will be completely compatible with the existing Track Processor electronics, and will not interfere with the high-precision TDC's to be used for offline tracking. Indeed, the addition of these crude TDC's will allow us to perform useful cross-checks between the precise TDC's and the Track Processor TDC's. The Track Processor TDC times will be read out in the data stream on every event via Fastbus.

The upgrade will consist of 72 Fastbus boards of a single design, including eight spares. Each board will handle 32 wires: 16 each from two complementary planes ( $X, X'$  or  $Y, Y'$ ). A pulse on any of these wires will zero a 6-bit counter which will be continuously clocked at 170 MHz. When a Level 1 Trigger fires, a Common Stop signal will be sent to the TDC board, which will stop all counters. The times of any hits preceding the Common Stop will thus be immediately available at the addresses of the Sum-of-Distances memory maps. Each memory map will supply a single bit specifying whether an acceptable pair of times is present. If so, signals will be repeated on the corresponding wires. Flags signifying hits within the 360 ns full-scale time will be used to perform a sparse readout of the hit times if the event is not aborted by the Level 2 Trigger. In addition to making the Sum-of-Distances cut, the Track Processor TDC's will also reorder the signals in the manner required by the Track Processor, and will generate the logical OR's of groups of 16 adjacent wires which are required by the lookup-table logic to be used in the P832 Level 2 Trigger.

The only effect of this upgrade on the timing of the Track Processor decision is a delay equal to the access time of the memory maps plus the propagation delay of the logic which will use the memory map outputs. This will amount to less than 50 ns, and so will not have a significant impact on the dead time imposed by the Track Processor. It is this

timing consideration which prohibits us from using any commercial TDC chip.

The boards will be built using 100K and 100E ECL logic for maximum speed and density. If we elect to use faster gas in the drift chambers in E799II and P832, then it will be possible to increase correspondingly the clock speed used for the Track Processor TDC's.

All boards will be housed in Fastbus crates, and will be standard Fastbus Slaves. For power dissipation and cooling reasons, and in case daughter boards are required, we will limit the number of modules per Fastbus crate to 12. Six crates will therefore be required. Each crate will be supplied with a LeCroy 1821 Segment Manager/Interface Module or an equivalent Fastbus Master and host computer interface. Each crate will also require a Fastbus power supply and radiator for water cooling. Three relay racks must be modified with the necessary plumbing for water cooling, and an upgraded chiller will be required to handle the additional cooling load.

The University of Chicago will design and purchase the circuit boards and electronic components (estimated at \$235 k), while Fermilab PREP will obtain the required Fastbus crates, power supplies and cooling system (estimated at \$115 k).

## 4.12 Data Acquisition System and Third Level Filter

### 4.12.1 Overview

A. What the Data Acquisition System should do.

- i) It should read out events which were accepted by the 2nd level trigger, and put the pieces together to build an event.
- ii) It should make some cuts to filter the events.
- iii) It should write out to tapes the events which passed the above software filter.
- iv) It should run programs to monitor the detector elements so that we can find problems as soon as possible. If we have enough CPU power, then there will be no need for offline monitoring anymore, since it has much longer turn around time.
- v) It should be able to calibrate the calorimeter on-line. This way, we can check that the gains are balanced, which is important for the HCF, and if necessary we can adjust the phototube gains with a short turn-around time. Producing the calibration files on-line also helps to analyze the data quickly.
- vi) It should allow us to do offline analysis and run Monte Carlos after the run is over.

B. Why we should reduce the event rate.

As described in the Section 4.11, the maximum event rate after the first level and fast second level (cluster finder, chamber logic, and TRD) is estimated to be about 500 k/spill. If we were to write all these events on 8mm cassettes, assuming an average event size of 4 kbytes/event, we would need about 130 drives, and we would have to write

$$500 \text{ k} \times 4 \text{ kbyte} \times 5 \text{ k spills/week} \times 24 \text{ weeks} / 1 \text{ Gbyte/cassette} = 240 \text{ k}$$
cassettes for P832 alone.

However, most of these events are not needed. In P832, they are mostly  $K_{e3}$  events; while some  $K_{e3}$  events are required for calibration and acceptance checks,

the number needed is far smaller than this. In E799II, most of the events passing the Level 2 Trigger are still background, and can be safely removed by Level 3 filtering. We therefore want to implement an on-line filter which will select no more than 10% of the events satisfying the Level 2 Trigger to be written to tape. This will reduce the number of tapes, easing logical problems and speeding the offline analysis.

C. How we should reduce the event rate.

There are two ways to reduce the number of events. One is to build additional specialized Level 2 Processors; the other is to use powerful commercial CPU's with special software at Level 3. The sophisticated 2nd level trigger processor has to collect information from multiple detector elements fast and make a decision. The advantage of this is that the decision is fast, usually within several  $\mu\text{sec}$ . The disadvantages are i) the electronics have to be custom-designed for our experiment, which requires a huge investment in time and manpower to build, design, and debug, ii) it can be maintained only by a few people who designed it..

With a Level 3 filter based on commercial CPU's, the filtering is done after events have been digitized and read out. The advantages of this method are i) we can choose from many high power CPUs available in the market, ii) since the filtering is done by software, it is very flexible, iii) for the same reason, many physicist can maintain or modify the program, and iv) the powerful computers used are available for other purposes after the experiment. The disadvantage is that it is usually slower than the second level trigger processors.

Therefore, the best strategy is to reduce the number of events by 1st and 2nd level trigger logic to the rate which software can handle, and let a Level 3 System handle the rest. For this reason, we have chosen to limit our Level 2 Trigger processors to a Hardware Cluster Finder, a simple hit-counting Track Processor, and TRD Electron-Identification majority logic. More sophisticated filtering will then be performed by the fast and powerful Data Acquisition System described below.

D. How the Data Acquisition System should be made.

As will be summarized in the following specifications, the data acquisition system should be fast and powerful. Besides the numbers listed in the specifications, the data acquisition system should be *simple and reliable*.

The simplicity must apply to both hardware and software. First, the number of hardware elements in the data stream should be minimized. Every additional element is a source of break down, a potential bottle neck and an consumer of manpower. The number of CPUs processing an event has to be minimized, too. Passing events from one CPU to another, it requires a fast data path between them, and communications software on both machines, and synchronization. This adds complexity, so makes the system less reliable and harder to maintain. In software, we should utilize the existing tools as much as possible. If we make the software simple enough, then it will be very easy to develop, debug, and maintain.

#### 4.12.2 DAQ Specifications

Here are the specifications for the data acquisition system.

The number of events to read out..... < 500 k events / spill

This is based on the trigger rate estimates (see spec sheet for triggers);

$$20 \text{ kHz} \times 23 \text{ sec/spill} = 460 \text{ k events / spill} .$$

Event size ..... 4 kbyte / event

The event size is estimated as follows.

CsI calorimeter	$10 \times 10 \text{ blocks} \times 4 \text{ cluster} \times 4 \text{ byte} =$	1.6 kbyte
TRD FADC	$10 \text{ wire} \times 10 \text{ sample} \times 4 \text{ byte} =$	0.4 kbyte
Drift Chamber TDC	$100 \text{ hits} \times 4 \text{ byte} =$	0.4 kbyte
Other ADCs,etc.		0.8 kbyte
Level 2 Trigger Information		0.8 kbyte

---

4.0 kbyte

The number of data streams and data transfer rate ..... dead time < 20%

The number of data streams has to be large enough, and the data transfer rate for the readout must be fast enough to keep the overall dead time caused by digitization and

readout less than 20%. Note that this does not include dead time imposed by the Level 2 Trigger for events which are aborted before readout is complete.

Memory buffer size ..... 1.5 Gbyte

4 kbyte  $\times$  500 k / spill = 2 Gbytes will be read out during the spill, but 1/3 (20s/60s) will be processed by the end of spill; therefore 2 Gbyte  $\times$  2/3 = 1.3 Gbytes of data has to be buffered for off-spill processing.

Third level trigger processing power ..... 1000 MIPS

The on-line monitoring code for E773 which is not optimized for event filtering purpose took 33 msec  $\times$  3.5 MIPS per event. In order to process 500k events/60 sec, we need : 500 k / 60 s  $\times$  33 ms  $\times$  3.5 MIPS = 960 MIPS.

Event reduction by the third level trigger ..... 10

The dominant source of triggers in P832 is Ke3's. Even 40 k Ke3's / spill is good enough for calibration, so we can reduce the number of events to tape by a factor 10.

Tape writing ..... 3.3 Mbyte/sec

4 k byte/event  $\times$  500 k/spill  $\times$  0.1(reduction) / 60 sec = 3.3 Mbyte/sec

Online monitoring CPU power ..... 50 MIPS

In order to monitor 6k events per spill, which is 10 times more than E773, we need 10  $\times$  3.5 MIPS = 35 MIPS.

### Design Requirements

- \* The overall structure and the software of the DA should be so simple that even a physicist can develop, debug, understand, and maintain.
- \* The DA should be flexible so that it is easy to change the number of data streams and processors.
- \* The DA should minimize the number of CPUs which have different tasks, and minimize the need for data links between CPUs which usually require a fast data path and handshaking protocols.
- \* By changing the configuration of memory nodes (by software), it should be able to work as multiple DA system so that different detector groups can work simultaneously.
- \* The DA should not take more than one minute to initialize the system.
- \* It must be possible to use the CPU power of the DA system for offline analysis when the

run is over.

### **4.12.3 Architecture**

Here we will describe the architecture of a data acquisition system which satisfies the requirements listed above. The accepted events will be sent from front end modules (ADC/TDC/...) to a buffer memory, and then to computers for processing (event building, filtering, and logging). The buffer memory forms a FIFO stack stores the events so that the event processing can use 60 seconds per spill, while events come in 20 seconds. The data from multiple front ends come into the buffer in parallel to minimize the dead time due to the data transfer. Total computing power of 1000 MIPS will be achieved by using multiple RISC processors running UNIX. The processors will read out events in parallel, and will also process them in parallel , in order to obtain the maximum possible throughput.

#### ***Front end***

Front end modules (ADC, TDC, latch, and possibly a readout controller) will receive three signals; 1st level event trigger, Fast Clear, and Read. The 1st level trigger should open ADC and latch gates, and start or stop TDCs. If a Fast Clear signal is generated by the second level trigger, the modules should be cleared and get ready for the next event. If the front end modules or the readout controller receives a Read signal, then the data should be sent to the buffer memory, and the modules should prepare for the next event. As described in the Section 4.11.1, the modules should be ready within 10  $\mu$ sec.

For normal events, pedestals should be subtracted from ADC data, and sparsification should be done to reduce the event size. Since information for a particular event will arrive in different data streams from several detectors, a unique event identification number, event\_id, will label this information from each data stream. The event\_id will be used by each Level 3 Processor to construct the data record for that event. The event\_id will be generated by one source, for example, a high resolution calendar/clock and will be latched by the level 0 trigger. The latched event\_id will be copied to each data stream for every event.

#### ***Buffer Memory Matrix***



The buffer memory should receive data from multiple streams in parallel, and send out the events to multiple processors in parallel. In order to minimize the interaction between the multiple processors, we propose to make a memory matrix, as shown in Fig. 4.12.1. The memory modules in one vertical column are connected to one data stream, and the memories in one horizontal row are connected to one processor. The first 1 k events will fill the memories in the first row, and the next 1 k events fills the memories in the second row, and so on. The processor will build an event by reading out data corresponding to the event from all the memory modules in the same row.

The advantage of making a memory matrix is that there are no interactions between multiple processors because each event is allocated to a particular processor when it enters the matrix. Also once a system with  $2 \times 2$  matrix works, then it will be easy to expand the size of the matrix because all the processors run exactly the same code. It will also be simple to configure the matrix so that one processor is connected to one detector element, while other processors are connected to other detectors. Then using the different Subsystem Level 1 Triggers as described in Section 4.11.1, different groups will be able to work simultaneously and independently on different detector subsystems during commissioning, testing and debugging. In addition, with the memory matrix, we will be able to write the same event to multiple rows at the same time. This will allow us to send certain selected events to a CPU dedicated to on-line monitoring and calibration.

The number of columns required in the buffer memory matrix, that is, the number of data streams needed, will depend on whether or not we implement front end buffering. If there is no front end buffering, in other words, if the front end modules are dead while sending out data, then the data transfer has to be done within several  $\mu\text{sec}$  (See CsI ADC Design Considerations in Section 4.11.2). If we assume  $10 \text{ MHz} \times 4 \text{ byte} = 40 \text{ Mbyte/sec}$  transfer rate, then we would need

$$4 \text{ kbyte/event} / ( 40 \text{ Mbyte/sec} \times 6 \mu\text{sec} ) = 16 \text{ data streams.}$$

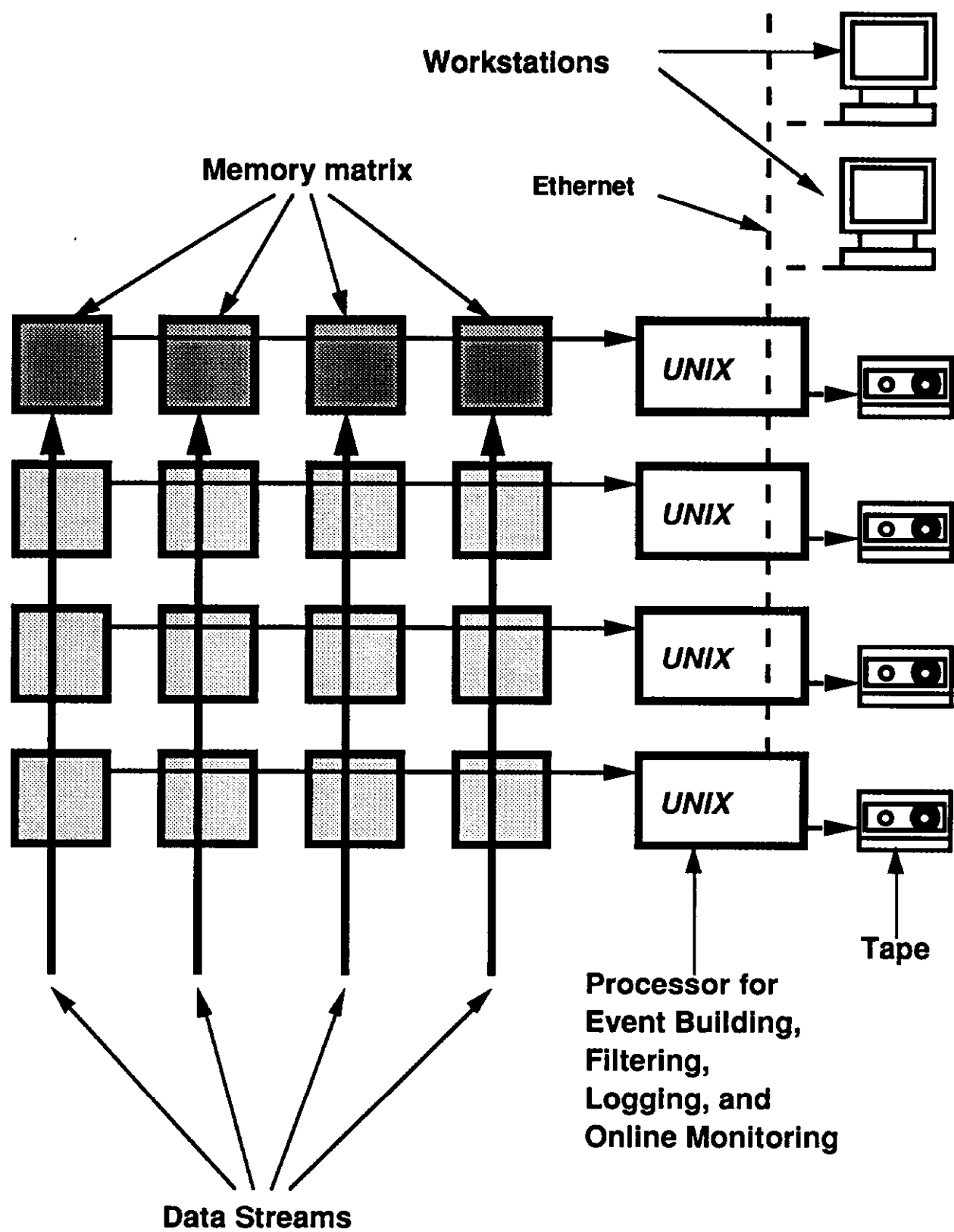


Fig. 4.12.1: Conceptual Design of DA System for KTeV

On the other hand, if the front end modules can take another event while sending the data from the previous event, then we can reduce the number of data streams because the data transfer can take more time. With buffering, there are two ways in which the DA can be dead: first, during digitization of data; and second, after digitization of a second event but before the transfer of data from the first (buffered) event is complete. For example, if the front end is dead for 5  $\mu\text{sec}$  and it takes 15  $\mu\text{sec}$  to send data, and the 2nd level trigger rate is 20 kHz (every 50  $\mu\text{sec}$  on average), then the probability of having the second event within the first 10  $\mu\text{sec}$  of the data transfer is 20%, and since in this case the average time between the end of data transfer of the first event and the end of digitization of the second event is 5  $\mu\text{sec}$  (because it ranges from 10  $\mu\text{sec}$  to 0  $\mu\text{sec}$ , as shown in Fig.4.12.2, the probability of getting additional dead time is about  $20\% \times 5 \mu\text{sec} / 50 \mu\text{sec} = 2\%$ . (The real number is slightly smaller than this, because the timing of the second event follows an exponential distribution.) Therefore allowing 15  $\mu\text{sec}$  for the data transfer is acceptable, and in this case we only need

$$4 \text{ kbyte/event} / (40 \text{ Mbyte/sec} \times 15 \mu\text{sec}) = 7 \text{ data streams.}$$

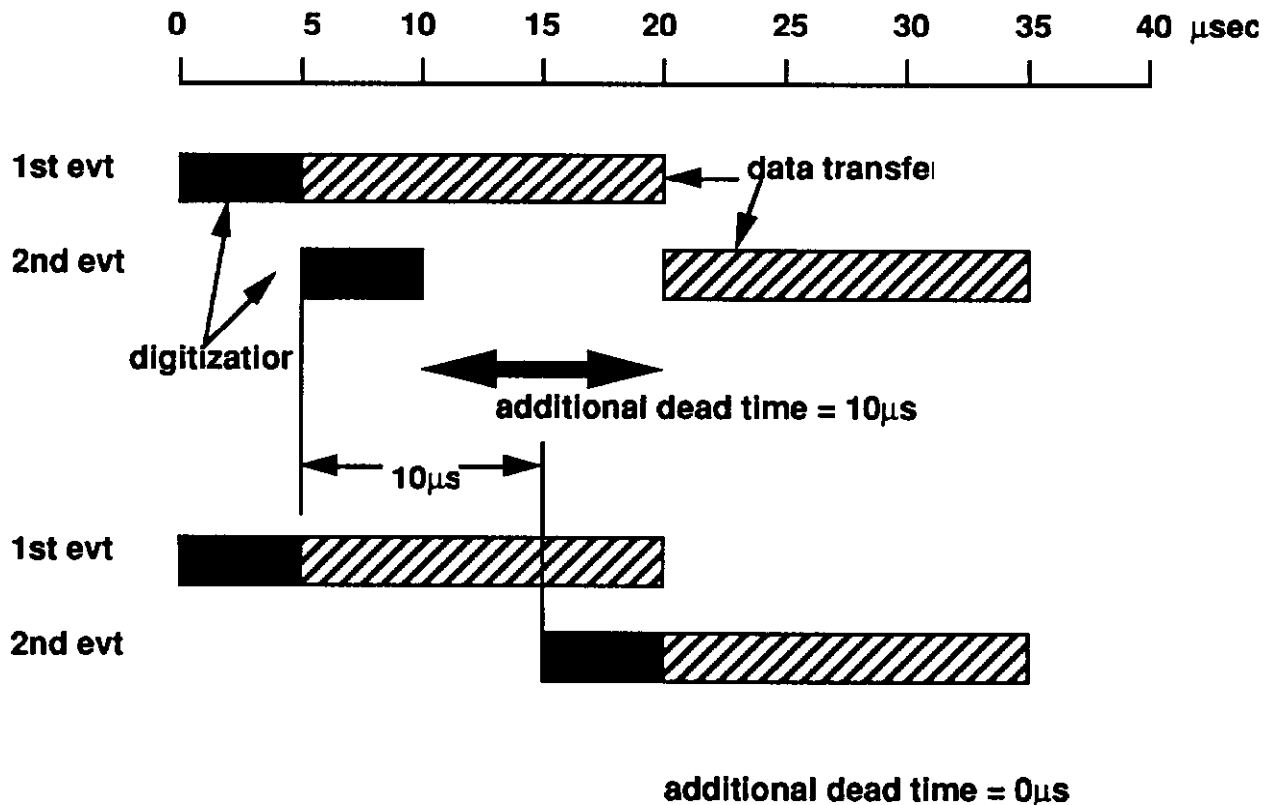


Fig. 4.12.2: When double buffering can be dead

The number of rows required in the buffer memory matrix depends on the processing power of each processor. If we assume 60 MIPS machines, which is less than twice the power of an SGI 4D/35, and slower than some existing HP workstations, then we would need  $1000 \text{ MIPS} / 60 \text{ MIPS} = 16$  rows.

Data are sent from the front end to memory modules either via fan out or by daisy-chaining the memories. In the fan-out scheme, data and data strobes are sent to just one selected memory at a time. In the daisy-chaining case, data are seen by all the memory modules, but only selected memories accept the data. In either case, we should be able to write the same event to multiple rows simultaneously for monitoring and calibration purposes.

Every 1 k events, the row of memories which accepts data is switched from one to the next. The 16th row will then start filling about  $1 \text{ k} \times 16 / 20 \text{ kHz} = 0.8$  sec after the beginning of the spill, so no processor will be idle for long. Switching will work more reliably, because it only happens 400 times per spill, instead of 400,000 times. It also makes the front end digital buffering easier, because by vetoing the triggers for  $< 50 \mu\text{s}$  every time we switch, we can switch all the data streams from one row to another. If we were to switch every event and use front end digital buffering, then switching would have to be done separately for each data stream, complicating the system. If one of the memories in the row fills up, then the system will have to switch to the next available row. If there are full memories in every row, then the DA is dead, and triggers will have to be vetoed until a row becomes available.

Each memory modules could be a linear memory or a FIFO. If it is a linear memory, then the total size should be 33% bigger than the specification. In any case, in order to use the full 60 seconds for event building/filter/logging, we should be able to read data while the memory is receiving data from the front end.

### ***Event Processor Farm***

The event processor farm which will consist of 1000 MIPS of UNIX farm, will do i) event building, ii) on-line filtering, iii) tape logging, and iv) on-line monitoring and calibration.

Most of the machines just do i), ii), and iii). Each machine reads a sub-event from

every memory module, concatenates them, makes an event header, and sets up necessary pointers to sub-events. It also checks that all the sub-events are coming from the same trigger, by checking the event id. The event is then analyzed for the purpose of filtering. The simplest cuts will be done first, and then track reconstruction, mass and  $P_t^2$  cuts, cluster finding, E/p cut, etc. The order in which reconstruction and cuts are performed will be tuned to minimize processing time. The number of MIPS we specified should be the upper limit because the E773 on-line monitoring program on which the specification was based did more than the new filter program has to do.

Events passing the cuts will be written to tape on a drive connected to the particular processor. Every processor has its own tape drive. This avoids further I/O bus traffic and is much simpler than concentrating and merging the events from several processors in order to reduce the number of tape drives. The processors are identical and interchangeable in the event of a failure. If the execution time allows, all these tasks will be done in a single program, and it will not look so different from a simple offline analysis program. If splitting the program into an event-building part and a tape-logging part makes a major overall speed improvement, then we will do so, but this will require us to devise a mechanism to pass events from one task process to another.

One of the machines will be dedicated to on-line monitoring and calibration. The machine will be connected to the memory matrix just like others, and the only difference being that it will run a different program. The assignment of a dedicated processor connected to the memory matrix to monitoring and calibration eliminates the need to transfer data from normal event-building/filtering/logging processors to a special monitoring processor. One could run on-line monitoring processes on all the machines, but we would then need a mechanism to collect histograms from multiple machines. However, the last option is still under consideration.

All the routines will be written in C, and partly in FORTRAN only if necessary.

### ***Central Control Workstation***

There will be a workstation to control the runs. This will accept commands like run/stop/pause/resume, and some other commands to set up run numbers and tape numbers. Depending on the command, it may initialize the front end modules. The commands are sent to UNIX machines either by broadcasting the message or by simply

executing a remote shell command. The central workstation should also be able to collect statistics from UNIX machines.

#### **4.12.4 R&D**

There are several things which we have to test and decide during the DA development.

##### **A. Memory**

This is the biggest unknown factor. There are some candidates, Fermilab VDAS memory, CES ECL/VME memory, dual ported VSB/VME memory, and a memory module built by W. Molzon (U.C. Irvine). Each of them has its own pros and cons, and we have not yet found the module which perfectly fits our need; a VME 4–8 Mbyte FIFO module. We should continue our search and evaluation, by collaborating with Fermilab Computer Division.

##### **B. UNIX machine**

We have to measure the read out speed from a VME module to the machine, measure event building time, on-line filtering time, and tape logging time on candidate UNIX machines.

##### **C. Front end digital buffering**

Can front end digital buffering be done easily? If so, is the cost increase in the front end smaller than the cost reduction in the memory matrix?

##### **D. Front end → memory**

Which data transferring method should we use between the front end and the memory modules? How fast can we drive it? If the transfer is fast enough, then we do not need to worry about the front end digital buffering.

#### **Cost of DA**

The cost of the DA system depends on the size of the memory matrix and which memory we use. Here, we will show the estimate for an  $8 \times 16$  matrix using Fermilab VDAS memories.

item	unit price	qty.	cost
9U crate/ps,bkpln	\$0.6 k	$\times 32$	\$19.2 k
I/O card	\$0.5 k	$\times 128$	\$64.0 k
mem control card	\$0.5 k	$\times 128$	\$64.0 k
4Mb memory	\$1.2 k	$\times 128$	\$153.6 k
EBI	\$0.2 k	$\times 128$	\$25.6 k
VME crate w/ps,bkpln,fan	\$4.0 k	$\times 16$	\$64.0 k
60MIPS CPU w/memory	\$12.0 k	$\times 16$	\$192.0 k
8mm drive	\$2.0 k	$\times 16$	\$32.0 k
Total			\$614.4 k

## 4.13 Offline Computing

Substantial offline computing resources will be required for the KTeV data analysis based on the experience of E731 and the large amount of data required to achieve the experimental goals. The offline analysis consists of: several iterations of the detector calibrations; pass 1 reconstruction and creation of data summary tapes (DSTs); Monte Carlo studies of the detector response and background simulation; pass 2 and 3 reconstruction and the creation of condensed DSTs, final analysis and fitting to extract the physics results, such as  $\epsilon'/\epsilon$ ,  $\tau_S$ ,  $\Delta m$ ,  $\Delta\phi$  from P832 and branching ratio measurements or limits, and form factors for various rare decay modes from E799.

The offline computing needs for E799/P832 for the 94'-95' KTeV run has been estimated using the following method defined by the Fermilab Computing Department in terms of the following parameters:

- a. "Raw Data" Amount of raw data written to tape or other permanent media [Tb =  $10^{12}$  bytes].

- b. "Tape mounts"      Number of operator tape mounts (assumed 8mm tapes).
- c. "Reconstr"          Amount of reconstruction computing (farm, pass 1, Monte Carlo etc.) required in [MIP-Years]
- d. "Analysis"          Amount of analysis computing (general, calibrations, final analysis etc.) required in [MIP-Years]
- f. "Seats"              Number of "analysis seats". An analysis seat is all the resources required to allow a physicist to do analysis (histogramming, cut changes, etc.), for 24 hours a day, 7 days a week.

The following table shows the estimated offline computing specifications for the period from FY93 to FY98.

	FY93	FY94	FY95	FY96	FY97	FY98	Total
Raw Data [Tb]		20	20				40
Tape mounts		5000	10000	10000	7500	2500	35000
Reconstr [MY]		50	150	250	250	200	900
Analysis [MY]	5	25	50	70	70	50	270
Seats	3	6	8	10	10	8	55

The amount of raw data written to tape has been calculated based on the following assumptions: 3.3 Mbytes/sec flat out tape writing throughput estimated in the previous DAQ section and one year KTeV run with 40% data taking efficiencies, i.e.

$$3.3 \text{ Mbyte/sec} \times 1 \text{ year} \times 0.40 \text{ (data taking efficiencies)} = 40 \text{ Tb.}$$

This corresponds to 25,000 8mm data tapes (assuming 1.6 Gbyte/tape).

### ***Cost Estimate***

The offline computing cost based from the Fermilab Computer Department's formula has been estimated to be \$4 M in total, spread out from FY93 to FY98 as follows:

	FY93	FY94	FY95	FY96	FY97	FY98	Total
Cost	\$350 k	\$570 k	\$750 k	\$870 k	\$830 k	\$660 k	\$4.03 M



## **5. COSTS, MANPOWER, AND TIMELINE**

In this section we present more detailed information on costs of the KTeV project. Civil construction requirements are not included here, as accurate estimates of costs associated with different siting options are still being compiled. Manpower requirements for construction of the new spectrometer are summarized, along with available manpower for the project. This is listed by institution, as are project responsibilities. Finally, a timeline is presented showing schedule requirements for components of the detector.

### **5.1 Detector Costs**

A summary of costs to upgrade the currently existing spectrometer to that needed for KTeV is presented in Table 5.1.1. Costs are in current year dollars. Only direct costs are included here, without contingency or EDIA. Total direct spectrometer costs are approximately \$11.4 M.

An additional item not estimated here is the installation cost for the new spectrometer, as well as removal of the existing kaon experiment from MCenter. These costs are currently under detailed consideration. On the other hand, the value of some existing equipment - such as phototubes and bases, existing electronics, etc. - has not been deducted from costs presented here.

Detailed costs for each spectrometer component are listed in Table 5.1.2. Also included in this table are labor estimates in person-years to build each system, with separate breakdown of types of people required. The cost of labor is estimated and included in the dollars needed only when it is normally a direct charge, such as for machining. The total manpower needed to build the new spectrometer, beyond such directly charged labor and prior to installation, is projected to be nearly 100 person-years.

Table 5.1.1

KTeV Spectrometer Costs Summary	
Project	Cost ( \$ K )
Vacuum Decay Tank and Window	475
Vacuum Veto System	454
Spectrometer Veto System	178
Regenerator System	161
Chamber Upgrades	207
Spectrometer Magnet	
TRD System	274
EM Calorimeter	
Crystals	5160
Phototubes and Bases	1428
Electronics	796
Flasher System	228
Blockhouse	189
Hardware Cluster Finder	89
Collar Anti	6
Back Anti	120
Trigger Counters	112
Hadron Veto	27
Muon Detection	322
Trigger Logic	213
Track Processor Upgrades	348
DAQ and Level 3 filter	614
Total	11402

Table 5.1.2

KTeV Spectrometer Costs								
Item or System	Unit	No. of Units	Cost/ unit(k)	Ref	Cost \$K	Labor Est. (person-YR)		
						Phy	Eng	Other
Vacuum System						0.3	1.0	2.0
Vacuum Tank	system	1	300.00	1	300.0			
Right angle valve	each	1	20.00	2	20.0			
Pumping System	system	1	0.00	3	0.0			
5 large flanges	each	5	4.00		20.0			
Rail System	system	1	30.00		30.0			
Instrumentation	system	1	10.00		10.0			
Instrument Air System	system	1	10.00		10.0			
16 Inch upstream pipe	each	1	15.00		15.0			
Vacuum Windows	each	2	5.00	4	50.0		0.3	0.5
Install pumps, elect...		1	15.00		15.0			
Z Calibrator	each	1	5.00	5	5.0			
Sub Total					475.0	0.3	1.3	2.5
Veto System ( Vacuum )						0.7		
RC - 1...4	system	4	22.50	6	90.0		0.1	0.5
RC - 5...7	"	3	33.60		100.8		0.1	0.4
RC - 8..10	"	3	42.60		127.8		0.1	0.4
PMT's and Bases (16/ring)	each	160	0.45	7	72.0			
ADC's	channel	160	0.10	8	16.0			
TDC's	channel	160	0.10	9	16.0			
High Voltage	channel	160	0.10	10	16.0			
Cables, Connectors...	channel	160	0.05	11	8.0			
Assembly					7.0	0.5	0.5	1.0
Sub Total					453.6	1.2	0.8	2.3
Veto System ( Spectrometer )						0.5		
RC - 11	system	1	52.00	6	52.0		0.1	0.2
RC - 12	system	1	47.50		47.5		0.1	0.2
RC - 13	system	1	37.40		37.4		0.1	0.2
PMT's and Bases (16/station)	channel	48	0.45	7	21.6			
ADC's	channel	48	0.10	8	4.8			
TDC's	channel	48	0.10	9	4.8			
High Voltage	channel	48	0.10	10	4.8			
Cables, connectors	channel	48	0.05	11	2.4			
Assembly					3.0	0.5	0.5	1.0
Sub Total					178.3	1.0	0.8	1.6
Regenerator				12		0.5	0.5	2.0
Scintillator	blocks	60			4.0			
Phototubes and bases	each	60	0.50		30.0			
Vacuum Tank	system	1			55.0			
Light Guides	each	60			8.0			
High Voltage	channel	60	0.10	10	6.0			
Structure	system	1			12.0			
ADC's	channel	60	0.10	8	6.0			
TDC's	channel	60	0.10	9	6.0			
Cables(RG 213), connectors	channel	60	0.08		4.8			
Readout/Control Elect.	system	1			9.0			
Mask Anti	system	1			20.0			
Regenerator Sub Total					160.8	0.5	0.5	2.0

Item or System	Unit	No. of Units	Cost/ unit(k)	Ref	Cost \$K	Labor Est. (person-YR)		
						Phv	Eng	Other
General Upgrades								
Chambers - New TDC's				13	130.0	0.5	0.5	1.0
Chambers - new preamps/disc					77.0	1.0	1.5	2.0
Trigger Processor Upgrade				14		0.5	0.2	1.0
Processor Circuits	system				235.0			
Fastbus Crates & Power Sup.	each	6	8.00		48.0			
Chiller Upgrade					10.0			
Lecroy 1821 Manager/Interfaces					55.0			
Trigger Electronics						0.5	0.0	0.5
CAMAC Modules	each	60	2.00		120.0			
CAMAC crates	each	4	5.00		20.0			
NIM Modules	each	80	0.45		36.0			
NIM Crates	each	12	2.00		24.0			
Trigger Sources	channel	128	0.10		12.8			
TRD's				15		2.0	1.0	4.0
Mechanical					73.0			
Electronics					137.0			
Trigger System					34.0			
Gas System Upgrade					30.0			
Trigger Hodoscopes				16		0.5	0.5	2.0
Scintillator					21.0			
Light Guides					0.5			
Misc. Labor					0.7			
PMT's and Bases	channel	128	0.45		57.6			
High Voltage	channel	128	0.10		12.8			
Cables	channel	128	0.05		6.4			
TDC's	channel	128	0.10		12.8			
General Sub Total					1153.6	5.0	3.7	10.5
Collar Anti						0.2	0.2	1.0
Tungsten	cm^3	1225	0.00		4.3			
Scintillator	m^3	8.75	0.10		0.9			
Fibers	meter	20	0.00		0.0			
PMT's, bases..	channels	2	0.45		0.9			
Electronics/Readout	channels	2	0.10		0.2			
Cables	channels	2	0.05		0.1			
High Voltage	channels	2	0.10		0.2			
					0.0			
CA subtotal					6.1	0.2	0.2	1.0
Back Anti						0.5	0.5	1.8
Scintillator					3.0			
Iron					4.5			
Lead					1.1			
Light Pipes					1.4			
PMT's (1.125 inch ) & Base	each	150	0.35		52.5			
Mech Supports					5.0			
High Voltage	channel	150	0.10		15.0			
Cables( sig, hv )	channel	150	0.05		7.5			
ADC's	channel	150	0.10		15.0			
TDC's	channel	150	0.10		15.0			
Shipping					5.0			
Back Anti Subtotal					120.0	0.5	0.5	1.8

Hadron Calorimeter								
Hadron Veto						0.5	0.5	1.0
Scint	m^2	5.3	1.50		8.0			
PMT's and Bases	channel	24	0.45		10.8			
ADC's	channel	24	0.10		2.4			
TDC's	channel	24	0.10		2.4			
High Voltage	channel	24	0.10		2.4			
Cables	channel	24	0.05		1.2			
Muon Veto						0.5	0.5	2.0
Scintillator	m^2	8.5	1.50		12.8			
PMT's and bases	channels	24	0.45		10.8			
Latch+Disc.	channels	24	0.12		2.9			
TDC's	channels	24	0.10		2.4			
ADC's	channels	24	0.1		2.4			
High Voltage	channels	24	0.10		2.4			
Cables	channel	24	0.05		1.2			
Steel	tonn	275	0.50		137.5			
Muon Detection						0.5	0.5	2.0
Scintillator	m^2	15.4	1.50		23.1			
PMT's and Bases	channels	100	0.45		45.0			
Latch+Disc.	channels	100	0.12		12.0			
TDC's	channels	100	0.10		10.0			
ADC's	channel	100	0.1		10.0			
High Voltage	channels	100	0.10		10.0			
Cables ( HV+Signal)	channels	100	0.03		3.2			
Resistive Plate chambers						1.0	0.5	3.0
Chambers					20.0			
High Voltage					4.0			
Disc. Cards	channel	320			6.4			
Latches	channel	320			6.4			
Hadron Subtotal					349.6	2.5	2.0	8.0

Item or System	Unit	No. of Units	Cost/ unit(k)	Ref	Cost \$K	Labor Est. (person-YR)		
						Phy	Eng	Other
DAQ/On-Line Comp						3.5	2.0	2.0
Processors (RISC)					192.0			
9U/craate					19.2			
I/O Card					64.0			
Memory Control					64.0			
4 Meg Memory cards					153.6			
EBI					25.6			
VME Crates...					64.0			
8mm Drives					32.0			
ADC & TDC system integration						0.5	1.0	0.5
DAQ Subtotal					614.4	4.0	3.0	2.5

Page 3 / 4

Item or System	Unit	No. of Units	Cost/ unit(k)	Ref	Cost \$K	Labor Est. (person-YR)		
						Phy	Eng	Other
EM Calorimeter								
CsI Xtals	cm^3		0.0025	17	5100.0	3.0	1.0	12.0
Wrap, Glue....					60.0			
Phototubes - 1.25 inch	each	1024	0.237		242.7	1.2	1.0	3.0
Phototubes - 0.75 inch	each	2232	0.223		497.7			
PMT Bases	each	3254	0.095		307.5			
High Voltage	channel	3300	0.10		330.0			
PMT support/mounting					50.0			
Electronics						2.0	2.0	2.0
Cables					326.0			
ET Trig Module					49.0			
Timing Generator					5.0			
Cables to HCF					1.5			
Optical cable to DA					6.5			
Controller Cards					39.0			
Crates and Power Supplies					39.0			
ADC's					320.0			
Testing Card					10.0			
Electronics sub subtotal					796	2.0	2.0	2.0
Hardware Cluster Finder						0.5	1.0	1.5
Simulation/Demo.					30.0			
Fastbus Crate	each	1	5.00		5.0			
Routers					10.2			
Cluster Processors					33.8			
Inverse Routers					10.2			
HCF sub subtotal					89.2	0.5	1.0	1.5
CsI House								
Design ( ANSYS )					11.4	0.5	0.5	
Instur. and Control					68.5		0.2	0.5
Heat/Cool/Ducts					64.5		0.2	0.5
Building & insulation					30		0.1	0.5
Supports					15		0.1	0.5
CsI House sub subtotal					189.4	0.5	1.1	2.0
Monitoring ( Laser, fibers...)						1.0	0.5	1.0
LN-1000 N2 laser					11.5			
LN-2x Freq Doubler					5.0			
LN-102 dye laser					3.5			
BBO xtal					1.8			
Mic acc					10.0			
Fused Silica Fibres					143.6			
Fiber Terminations					33.0			
Assoc Electronics					20.0			
Laser sub sub tot					228.4	1.0	0.5	1.0
EM Sub Total					7890.9	8.2	6.6	21.5

Spectrometer Total					11402.3	23.4	19.4	53.7
							96.5	

References for Table 5.1.2

- 1 Vacuum Tanks estimated cost based on quote from Ability Engineering Technology.
- 2 Valve is a standard catalog item.
- 3 All vacuum pumps salvaged from bubble chambers.
- 4 Vacuum windows to be tested - those R & D costs included.
- 5 Preliminary estimate
- 6 Costs based on engineering studies by Don Goloskie - Physics.
- 7 PMT's including bases, shields etc costed at \$450 each - Steven Pordes - Physics.  
Though many tubes and bases exist in the MCenter experiment, these have not been deducted from the total costs presented here.
- 8,9 ADC's and TDC's are \$40 to \$60 per channel. Including crates, powersupplies, Misc. data cables, we assume \$ 100 / channel.
- 10 High voltage assumed Lecroy 1440 system at \$25,000/256 channels.
- 11 Assumes one signal ( RG-58 ) and one High Voltage cable per channel.
- 12 Regenerator in vacuum, so special bases for PMT's
- 13 New TDC's for high rate faster gas - Lecroy 1877's.
- 14 Trigger processor - chamber mean timing.
- 15 TRD's upgrade includes modification of existing chambers  
plus two additional TRD's, and faster electronics
- 16 Replacement of existing old scintillator, more and better coverage.
- 17 Verbal Quote, Long crystals may require additional processing costs.

## 5.2 Manpower Availability

Institutional responsibilities as projected for KTeV are summarized by project in Table 5.2.1. Some projects requiring joint efforts span two institutions and are so listed. A similar dual listing for Fermilab Divisions also indicates a joint effort.

Table 5.2.2 presents a summary of the currently projected manpower available for KTeV. Listings are initially given of the actual number of individuals involved. These numbers were then converted to Full Time Equivalents (FTEs) on an individual basis. This sum of FTEs is presented as total FTEs. For the more permanent staff of each institution, the persons listed are those currently at that institution and expected to be available for KTeV efforts. For research associates and students, the numbers include projections.

The total of FTEs in Table 5.2.2 is 83 person-years per year. In a comparison with the Table 5.1.2 listing of spectrometer manpower requirements, it should be noted that additional people beyond those requirements listed here will be needed for technical beam, magnet, and facility construction not itemized here. Additionally, manpower requirements for installation of the experiment in a new area are not compiled here.



Table 5.2.1

KTeV Project Responsibilities - By Institution	
Project	Institution(s)
Vacuum Decay Tank and Window	Fermilab - RD
Vacuum Veto System	Fermilab - Phys/UCLA
Spectrometer Veto System	Fermilab - Phys/UCLA
Regenerator System	Chicago/Fermilab - RD
EM Calorimeter	
Crystals	Chicago/Fermilab - Phys & RD
Phototubes	Osaka
Bases	Osaka/UCLA
ADC's	Chicago/Fermilab - Phys
Flasher System	Fermilab - Phys
Blockhouse	Fermilab - Phys & RD
Hardware Cluster Finder	Illinois
TRD's	
Mechanical	Fermilab - Phys & RD
Mechanical	Fermilab - Phys
Electronics	Chicago
Drift Chamber Upgrades	Rutgers
Muon/Hadron System	
Counters	Rutgers
Resistive Plate Chambers	Rutgers
Shield Iron/Pb	Fermilab - RD
Trigger Logic	Chicago
Non-EMcal ADC's, TDC's...	Fermilab - Phys
Track Processor Upgrades	Chicago
DAQ and Level 3 filter	Fermilab - Comp/Osaka
Back Anti	UCLA
Collar Anti	Osaka
Off-line Computing	Fermilab Computing / All
Spectrometer Magnet	Fermilab - Acc & RD

Table 5.2.2

KTeV Available People-Power Estimates							
Institution	Faculty Level	Research Assoc.	Grad. Student	Tech	Eng. or Programmer	Under Grad.	
Fermilab - Res. Div	9	0	0	8	16	0	
Fermilab - Physics	0	4	0	10	2	0	
Fermilab - Computing	0	0	0	2	3	0	
Chicago	3	3	5	2	1	4	
Elmhurst	1	0	0	0	0	1	
Illinois	1	1	2	1	1	2	
UCLA	2	1	3	1	1	4	
Rutgers	2	4	3	1	1	4	
Osaka (Japan)	1	2	4	0	0	2	
Total People	19	15	17	25	25	17	
Total FTE's	8.7	15	17	25	14.0	4.3	
Grand Total FTE's	83 Person-Years per Year						

## 5.3 Beam Technical Costs

Full costing of the technical beam components needed for KTeV is dependent on final site selection for the experiment. Here we list in Table 5.3.1 those beam components which are largely independent of siting, beginning with the final primary beam targeting quadrupoles. As in other sections, required components are listed as new rather than existing whenever they have not been specifically identified for KTeV use. In many cases use of existing equipment may be feasible. As example, it may be possible to use the E8 hyperon magnet for the target sweeping magnet; similarly 4Q120 quads may be available.

Costing of the spectrometer magnet is highly dependent on experiment siting. Here a new magnet is estimated by scaling from the cost of existing large magnets. However, it is possible that the existing Chicago Cyclotron Magnet can be utilized, with a required regapping, if the experiment is staged in the NMuon hall.

Table 5.3.1

KTeV Beam Technical Costs						
Item	Unit	No of units	Exist	\$ K each	\$ (K) Total	Ref
<b>Primary Beam</b>						1
Target Area						2
Dipoles 4-4-240 B2	each	2	0	60	120	
Power Supply for B2	each	2	0	60	120	
Trim Dipoles & PS	each	2	0	24	48	
Collimators	each	1	0	50	50	
Quadrupoles ( 4q120 )	each	8	0	50	400	
Quad Power Supplies	each	2	0	60	120	
Control/Monitor						3
Micro-Swic	each	1	0	8	8	4
Other Swics	each	2	0	6	12	
Swic Scanners	each	11	0	3	33	5
BPM with electronics	each	2	0	5	10	
Sem	each	1	0	13	13	
Current Digitizers	each	2	0	2	4	
Primary Beam subtotal					938	
<b>Secondary Beam</b>						
Target Magnet						
Magnet	each	1	0	500	500	6
Power Supply	each	1	0	80	80	
Copper Absorber	each	1	0	10	10	7
Target/Absorber						7
Target Assembly	system	1	0	5	5	
Stationary Absorber	system	1	0	2	2	
Moving Absorber	system	1	0	5	5	
Dump Magnet						8
Magnet	each	1	0	400	400	7
Collimators	system	1	0	50	50	
RAW cooling system	system	1	0	20	20	
Secondary Collimators	each	1	0	50	50	
"Slab" Collimator	each	1	0	20	20	
BM109 (e+e- Cal.)	each	2	1	50	50	
Secondary Beam Subtotal					1192	
<b>Spectrometer ( Facility )</b>						
Spectrometer Magnet	each	1	0	2500	2500	9
Total Technical Costs					4630	

## References and Notes ( Beam Technical Costs )

- 1 Applies to final focus region only. There will be additional costs that are site dependent for primary transport to this point.
- 2 Magnets are costed as new. This assumption is significantly site dependent
- 3 "Beam Line Instrumentation" revised March 1988.
- 4 The "micro swic" is being newly developed for the KTeV project.
- 5 New SWIC scanners are under development.  
These new versions will be used for KTeV.
- 6 Target Magnet could be the E8 hyperon magnet, currently in MCenter
- 7 Very approximate costs.
- 8 The 'Dump Magnet' is at a preliminary stage of design. More detailed design awaits comprehensive muon flux simulations.
- 9 The cost of a new spectrometer magnet is very preliminary.  
Depending on siting, other options using an existing magnet may be available.

## 5.4 Detector Timeline

Shown below is a timeline projection for construction of the KTeV detector indicating estimates in calendar months required for design, prototype testing, procurement, assembly, and installation of each component.

KTEV TIME-LINE:	D=Design
	T=Prototype tests
	P=Procurement
	A=Assembly
	I=Installation
SYSTEM	1992 1993 1994
	JFMAMJJASONDJFMAMJJASONDJFMAMJJASON
CsI	
crystals	TTTTTT PPPPPPPPPPPPPPPPPP AAAAAAAAAAAAAAAA IIIIII
phototubes	TTTTTT PPPPPPPPPPPP AAAAAAAAAAAAAAAAIIII
bases	DDDDTTTTPPPPAAAAA IIII
flasher	
blockhouse	DDDDDD..... AAAA
ADC	DDDDTTTTTTPPPPPAAAAAII
cluster finder	
processor board	DDDDATTT I
router boards	DDDDDATTTI
Vacuum System	DDD PPPPPPPPP III
Vacuum Photon Veto	
detectors	DDDDDD TTTTTT PPPPPPPPPPPP AAAAAAAAAAAAAAAAIIII

SYSTEM	1992		1993		1994	
	JFMAMJJASOND	JFMAMJJASOND	JFMAMJJASOND	JFMAMJJASOND	JFMAMJJASOND	JFMAMJJASOND
Regenerator detectors vacuum				DDDTPPPT	.AAI	
		TTTDDPPPPPIII				
Drift Chambers amps preamps gas TDCs		DDDTTTPPAAAAII				
		TTTPPAAAAII				
		TTTTTT				
		DDTTPPAAAAAI				
Non-CsI ADCs		DDDDTTPPAAAA I				
Track Processor Upgrade		DDDDATTTTTPPPAAATTII				
Scintillator Hodoscopes	D TPP			AAAIIII		
Resistive Plate Chambers		DDDTTDDDTTPPPAAAAII				
TRD chambers  electronics gas		DDDDDDDDDAATTTTTTTTTTAAAAAAAAAII				
		PPPPPP				
		DDDDDDTTDDDDTTTPAAAAAI				
Back-Anti		DDDDDDDTTDDDTTDDPPPPPPPPAAAAII				
Trigger Level 0..		PP		IITTTTT		
Trigger Level 1..		PPPPIITTTT				
Data Acquisition		DDDPTTTTTTTTTTPPPII				

## **APPENDIX A. EXPERIMENT SITING AND ENVIRONMENTAL SAFETY**

As indicated previously, environmental safety and health concerns preclude the continuation of the higher intensity KTeV program in the current MCenter location. In this regard, a survey of other existing experimental areas has been conducted to determine potential options for siting the KTeV [and ultimately KAMI] programs.

The requirement for a below grade location of the targeted primary and secondary beam, to enable protection from intense muon fluxes, effectively precludes an existing location in either the Meson or Neutrino experimental areas. This led to consideration of siting options in the Proton area or NMuon. Discussion in A.1 focuses on siting options and the status of the engineering effort to analyze comparative costs for appropriate sites. Detailed in A.2 are additional environmental safety and health concerns which are being addressed in the design of the KTeV facility.

### **A.1. Experiment Siting**

The best existing facility match to KTeV requirements is the Wide Band hall downstream of the PB primary beam line. However, programmatic considerations precluded this as an option for KTeV, leading to a detailed evaluation of the alternate choice in NMuon.

For NMuon, two siting options are being considered. The first or upstream site would position the KTeV target in an extended NM2 target hall, making use of the existing NM primary beam transport. Besides the new target hall section, required civil construction would include new secondary beam enclosure, experimental hall, and counting rooms. Additionally, a new large analysis magnet would be required.

For the second or downstream site option in NMuon, the KTeV detector would be positioned in the existing NMuon experimental hall. The experiment would also utilize the counting rooms which are located above and to the east of the detector pit. The existing muon beam line would need to be upgraded in shielding to primary intensity capability. Additionally, a new target hall and secondary beam enclosure would be required. Detailed



studies are underway to understand costs for regapping the Chicago Cyclotron Magnet, around which the experimental hall was constructed, for use as the KTeV analysis magnet.

Figure A.1.1 shows a conceptual design for the generic (site independent) experimental hall, decay enclosure, and counting house needed for the KTeV program. The design shown is intended to be a general guide with some latitude for flexibility and compromise; e.g. the counting rooms could be multi-story if necessary provided distances to the fast electronics remain short to minimize cable lengths. Crucial design components are the below-grade detector pit and the option for hadron shielding between the detector and counting room areas.

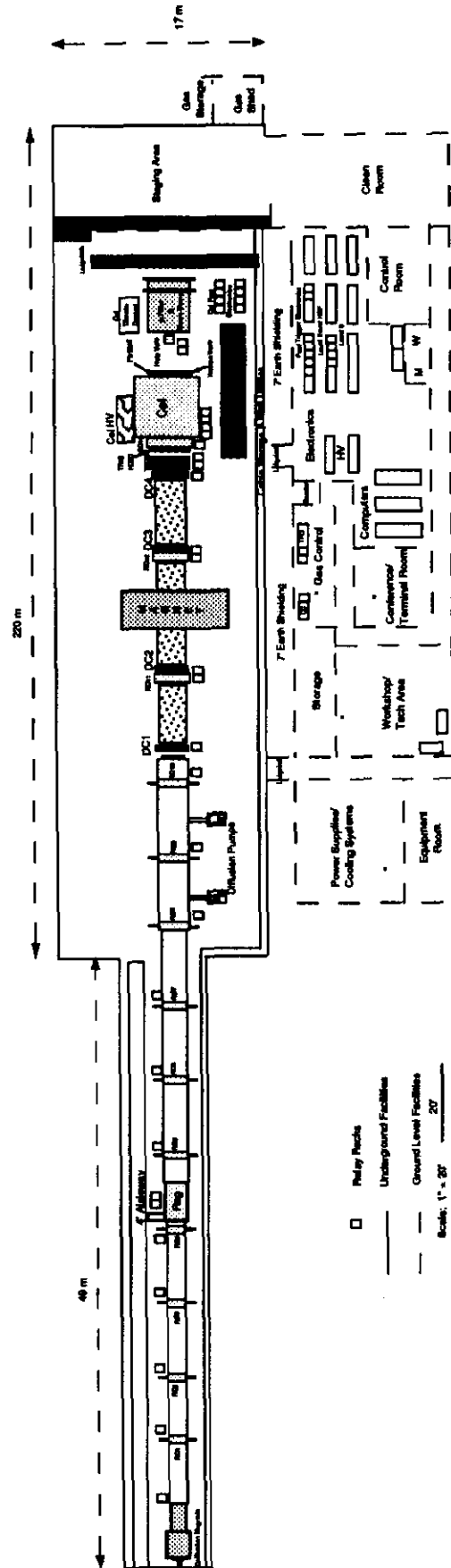
The experimental hall illustrated has a floor area of approximately 12,000 ft<sup>2</sup> (not including decay enclosure), and the counting rooms, about 8400 ft<sup>2</sup>. Based on current knowledge, this design does provide adequate space for the KAMI upgrade. For comparison, the Wide Band experimental hall has approximately 11,500 ft<sup>2</sup> and 9200 ft<sup>2</sup> for the experimental hall and counting rooms respectively, not including enclosure.PB6. The NMuon hall has about 19,700 ft<sup>2</sup>, excluding NMR, plus 10,600 ft<sup>2</sup> for the counting rooms.

Significant work has been accomplished by the Fermilab Facilities Engineering Section in analyzing the civil construction requirements for the two possible KTeV sites in the NMuon area. However, costs and design details are not yet available for release. Present efforts are focused on obtaining preliminary but comprehensive comparative costing information which can facilitate a final siting choice for KTeV. The current estimate is that this level of data should be available by March of this year.

Figure A.1.1

R. Ford  
1/18/92

# KTeV Experimental Hall Layout (Conceptual)



## **A.2. ES&H Issues**

This section describes the environmental, safety, and health (ES&H) issues associated with the KTeV project. In general, they are not different in kind from those existent in previous Fermilab Tevatron fixed-target experiments. The magnitude of the radiation safety issues will be somewhat larger, however, due to the anticipated increase in beam intensities for KTeV, as well as increased beam intensity capability and primary beam energy expected from the Tevatron for the next fixed target run. This requires considerable attention to the proper amount of passive shielding, fencing, and/or interlocked radiation detectors. Additionally the large vacuum window required for the kaon decay pipe must be carefully evaluated for integrity due to its diameter and the requirement of minimal thickness.

### **A.2.1. Radiation Safety**

Radiation safety issues are naturally divided into those due to prompt (beam-on) radiation and residual activation.

The prompt radiation of most concern consists of two components:

- neutrons arising from the deliberate dumping of the primary and secondary beams, or accidental or unavoidable beam losses in the beam transport systems;
- muons produced by the target station.

Residual activation is an issue that must be addressed for the major target station components (targets, sweeping magnet, and dump magnet). Levels of activation on the order of 100 rem per hour can be expected for target station components, requiring careful planning and handling in the event of component failure.

Residual levels associated with the surrounding target station steel shielding are also important from the point of view of safe and efficient beam-off accesses into the target station enclosure. The target station steel shielding will be designed to keep the calculated

beam-off dose rates within the enclosure to less than 100 mrem per hour at one foot from the shield surface.

Primary and secondary beamline shielding for neutrons will consist of a combination of dirt, concrete, and steel, to reduce dose rates from both normal running and accident conditions to levels consistent with the requirements of the Fermilab Radiation Guide<sup>1</sup>. The methodology of the 1991 Research Division shielding assessment<sup>2</sup> will be used to calculate dose rates and specify the amount of shielding required. As an example, an experimental hall with 25 feet of clear space between the beamline and the side wall would require at least 6 feet of earth-equivalent shielding between it and a continually occupied counting room immediately beyond that shielding. Inputs for this calculation are a worst-case accidental loss of a secondary hadron beam of  $6 \times 10^9$  particles per spill (per  $3 \times 10^{13}$  primary protons), 60 spills per hour, and an effective secondary beam energy of 80 GeV. An additional contribution to the dose from muons passing through the counting room could require greater reduction of the hadron dose.

Muon dose rates are a potential issue for both on and off the Fermilab site. For the on-site case, muon fluxes and trajectories are being taken into consideration in designing the target station, secondary beamline and experimental halls to ensure that above ground muon dose rates do not exceed Radiation Guide criteria. In particular, counting rooms for the KTeV experiment must be located in regions of low muon flux such that the muon dose rate, when combined with neutron rates does not exceed limits for continually occupied areas of 0.25 mrem per hour during normal operation. Other, minimally occupied, areas are allowed higher dose rates, with suitable barriers and other controls in place depending on the actual dose rates. Achieving these limits is still a major design task for KTeV, as illustrated in Section 3.

The annual dose rate at the site boundary must also be less than 10 mrem. Locating the target station and secondary beam line below grade level is an important factor in keeping the muon dose rate within acceptable limits both on-site and off-site because of the additional shielding provided in the forward direction. For this reason, the KTeV target station and secondary beam line will be located below grade.

---

<sup>1</sup>Fermilab Radiation Guide - Fifth Edition, Chapter 6 (March, 1988).

<sup>2</sup>Fermilab Research Division Shielding Assessment Methodology (1991).

Another important issue is the level of activation produced in unprotected soil surrounding the target station and subsequently transported into the groundwater beneath it. The two leachable isotopes of concern are  $^3\text{H}$  and  $^{22}\text{Na}$ . The standard Fermilab model<sup>3</sup> for calculating radioactive isotope concentrations in ground water can be used to estimate the required target station shield thickness for ground water protection. Approximately five feet of steel followed by two feet of concrete (the enclosure walls) should be sufficient to reduce concentration in the ground water to acceptable levels.

Since the primary beam will pass through air-filled regions of the target station the potential for air activation exists. This activation consists primarily of short-lived isotopes ( $^{11}\text{C}$ ,  $^{13}\text{N}$ ,  $^{15}\text{O}$ ) which will be monitored when released through a stack to ensure that released concentrations and site boundary doses do not exceed EPA limits or DOE limits.

Cooling water for the dump magnet, and probably for the sweeping magnet, will be circulated through a closed-loop system due to the high levels of activation that occur. Retention pits for the collection of leaking or spilled radioactive water will be incorporated into the target hall design to prevent the release of this water to the environment.

### **A.2.2. Conventional/Occupational Safety**

Items of special conventional safety interest include the following to be used by the KTeV experiment:

- high voltage electronics (>5 kV)
- high-current low-voltage electronics
- flammable gases (argon-ethane in drift chambers)
- exotic/toxic metals (beryllium/beryllium oxide targets, beryllium and lead beam absorbers and tungsten collimators)
- commercially available lasers (for gain calibration and monitoring of the CsI calorimeter)
- cryogenics (LN<sub>2</sub> for the xenon recovery system for the TRDs)
- active regenerator inside decay pipe

---

<sup>3</sup>Peter J. Gollon, *Soil Activation Calculations for the Anti-proton Target Area*, Fermilab report TM-816; and J. D. Cossairt, *Derived Concentration Guide for Accelerator-Produced Radionuclides in Surface Water Discharge and Drinking Water*, Fermilab Environmental Protection Note #1 (March 13, 1990).

- confined spaces (the decay pipe)
- large vacuum windows for the decay pipes

Insuring the safety of the large (up to 1.8 meter diameter) vacuum window on the decay pipe will require particularly careful analysis and review.